# DISSERTATION

Titel der Dissertation

## Combined First-Principles and Model Hamiltonian study of RMnO$_3$ (R=La, Pr, Nd, Sm, Eu, Gd)

Verfasserin

### Sowmya Sathyanarayana Murthy, M.Sc.

angestrebter akademischer Grad

### Doktorin  der Naturwissenschften (Dr. rer. nat.)

Wien, 2013

# Abstract

Perovskite transition metal oxides (TMOs) which fall under the so-called "strongly-correlated" systems exhibit an interplay of structural, electronic and magnetic phenomena which lead to complex orbital- and spin-ordered states which have attracted a lot of attention, theoretically and experimentally. Among this class of TMOs the orthorhombic $R\text{MnO}_3$ perovskites (where $R^{3+}$ is a rare-earth cation), are mainly known as the parent compounds of colossal-magneto resistance (CMR) manganites. Theoretically, these compounds have been historically studied using *(a)* First-principles simulations *(b)* Model Hamiltonians. First principles simulation studies are based on two main theories namely the Hartree-Fock (HF) and Density Functional Theory (DFT) in which the intractable many-body problem is mapped into a simplified one-electron theory. Model Hamiltonians are typically based on Hubbard Hamiltonians or tight-binding (TB) Hamiltonians. Another approach to study these compounds are based on combination of both First-principles simulations and the Model-Hamiltonians, as done for instance in DFT+DMFT (Dynamical mean field theory) schemes.

In this thesis, we investigate the electronic and magnetic properties of the parent compounds of manganites $R\text{MnO}_3$ (R = La, Pr, Nd, Sm, Eu and Gd), by performing first-principles calculations and downfold the physically important $3d$ $e_g$ bands by means of maximally localized Wannier functions (MLWFs) by using the VASP2WANNIER90 interface. The *ab initio* analysis was conducted at different levels of theory for what concern the treatment off the exchange-correlation interaction: (i) DFT in the Perdew-Burke-Ernzerhof (PBE) approximation; (ii) PBE+U, where U is the on site Hubbard-like electron-electron repulsion; (iii) Hybrid Functionals, a suitable mixing of DFT and HF via the inclusion of a portion (1/4) of exact HF exchange in the PBE functional and (iv) GW. We calculate the tight binding parameters for an effective $e_g$ tight-binding Model Hamiltonian using two types of model parametrization: (a) el-el interaction is treated implicitly: the changes in the beyond-DFT treatment are incorporated and reflected in the TB parameters. (b) el-el interaction is treated explicitly and the value for Hubbard-U is obtained.

We have first investigated the ground state electronic and magnetic properties at PBE, PBE+U, HSE and GW level of the whole $R\text{MnO}_3$ series and then we have mapped the obtained *ab initio* bandstructure into a TB description. The $e_g$ TB dispersion at all levels of calculations (PBE, PBE+U, HSE, $GW_0$) are found to

match closely the MLWFs. We provide a complete set of TB parameters, including both on-site and hopping interactions, which should serve as a guidance for the interpretation of future studies based on many-body Hamiltonian approaches. In particular, we found that the Hund's coupling strength ($J_H$), the Jahn-Teller coupling strength and Hubbard-U remain nearly constant in all members of the $R\text{MnO}_3$ series (and this reflects the fact that the band gap and the screening properties do not change much from $\text{LaMnO}_3$ to $\text{GdMnO}_3$, and that all $R\text{MnO}_3$ compounds remain in a Mott-Hubbard insulating state), whereas the nearest neighbour hopping amplitudes shows a monotonic attenuation as expected from the trend of the tolerance factor.

In addition to this, by mapping the first principles total energies for different magnetic configurations into a classical Heisenberg Hamiltonian we have computed the most relevant exchange parameters and derived a mean field estimation of the Néel temperatures ($T_N$) across the $R\text{MnO}_3$ series. We show that the evolution of the computed $T_N$ follows very closely the corresponding measured values. The observed monotonic decrease of $T_N$ can be nicely correlated with the modulation of the structural properties, and in particular with the progressive rectification of the Mn-O-Mn angle which is associated with the quenching of the volume and the decrease of the tolerance factor due to the reduction of the ionic radii of $R$ going from La to Gd.

# Zussamenfassung

Perovskite sind Übergangsoxide (TMO, kurz für Transition Metal Oxides), gehören zu den so genannten stark-korrelierten Systemen und zeigen ein Wechselspiel von strukturellen, elektronischen und magnetischen Phenomänen. Dieses Wechselspiel führt zu komplexen Orbital- und Spin-geordneten Zuständen, welche große theoretische und experimentelle Beachtung finden. Zu dieser Klassse der TMO gehört zum Beispiel der orthorhombische $R\text{MnO}_3$ Perovskite, der auch als Ausgangsstoff für die sogenannten colossal-magneto resistance (CMR) Manganite dient. Aus theoretischer Sicht wurden diese Verbindungen mittels ab initio Methoden und Model-Hamiltonians behandelt. Ab initio Simulationen basieren auf zwei wesentlichen Theorien: der Hartree-Fock (HF) und der Dichte-Funktional-Theorie (DFT). Letztere beruht auf der Abbildung des vollständig wechselwirkenden Vielteilchen-Problems auf ein vereinfachtes nichtwechselwirkendes Einteilchen-Problem. Auf der anderen Seite basieren Model-Hamiltonians typischerweise auf modifizierte Hubbard-Hamiltonians oder Tight-Binding-Hamiltonians. Ein weiterer Ansatz ist die Kombination von ab-initio Methoden und Model-Hamiltonians, wie es zum Beispiel in der Dynamical-Mean-Field Theorie (DFT+DMFT) verwendung findet.

In dieser Dissertation untersuchen wir die elektronischen und magnetischen Eigenschaften der Ausgangsstoffe folgender Manganite $R\text{MnO}_3$ ($R =$ La, Pr, Nd, Sm, Eu and Gd). Mit Hilfe von ab initio Berechnungen betrachten wir insbesondere die 3d $e_g$ Bänder im Sinne von maximal lokalisierten Wannier-Funktionen (MLWFs, Maximal Localized Wannier Functions). Diese wurden mittels dem VASP2WANNIER90 Interface bestimmt. Zur Bestimmung der Austausch- und Korrelationsenergie werden folgende Approximationen angewendet: (i) DFT mittels Perdew-Burke-Enzerhof (PBE), (ii) PBE+U, mit U als on-site Hubbard Elektron-Elektron Abstoßung, (iii) Hybrid Funktionale, mit einer Mischung aus DFT und HF durch Hinzunahme von $\frac{1}{4}$ des exakten Austauschbeitrags aus HF im PBE Funktional, sowie (iv) die GW-Methode. Desweiteren berechnen wir Parameter für einen effektiven $e_g$ TB-Hamiltonian über folgende zwei Model Parametrisierungen: (a) implizite Elektron-Elektron Wechselwirkung (WW): der Effekt durch die beyond-DFT Methoden reflektieren sich in veränderten TB Parametern; (b) explizite Elektron-Elektron WW ergibt den Hubbard-U Parameter.

Nach der Bestimmung von den elektronischen und magnetischen Grundzustandseigenschaften der $R\text{MnO}_3$ Reihe auf dem Level von PBE, PBE+U, HSE und GW wurden die ab-initio Bandstrukturen in eine TB Beschreibung übergeführt.

Die $e_g$ TB Dispersion aus allen Methoden stimmt gut mit denen aus der MLWF überein. Wir stellen einen kompletten Satz von TB Parametern zur verfügung, welche on-site und hopping-Parameter beinhalten und als Richtlinie für zukünftige Untersuchungen von Vielteilchen-Hamiltonians dienen. In unserer Untersuchung stellen wir fest, dass die Hund'sche Kopplungsstärke ($J_H$), die Jahn-Teller Kopplungsstärke und der Hubbard-U Parameter nahezu in allen Elementen der $R$MnO$_3$ Reihe konstant bleiben. Das spiegelt sich in der Tatsache wieder, dass sich die Bandlücke und die Abschirmeigenschaften nicht stark zwischen LaMnO$_3$ und GdMnO$_3$ unterscheiden und dass alle $R$MnO$_3$ Elemente die Eigenschaft eines Mott-Hubbard Isolators aufweisen. Außerdem beobachten wir eine monotone Abnahme der Hopping-Amplitude für die am nächsten benachbarten Mn Atome. Dies wird auch durch die Veränderung des Toleranzfaktors bestätigt. Es wurden Gesamtenergien von verschiedenen magnetischen Konfigurationen in einen klassischen Heisenberg Hamiltonian abgebildet. Die daraus berechneten Austauschparameter dienten zur Ableitung der Nèel Temperatur ($T_N$) in einer mean-field Abschätzung für die komplette $R$MnO$_3$ Serie. Wir zeigen, dass sich die Nèel Temperatur entlang der $R$MnO$_3$ Serie genauso entwickelt wie im Experiment festgestellt wird: Die monotone Abnahme von $T_N$ korreliert mit der Modulation der strukturellen Eigenschaften. Dies zeigt sich in der ganzen $R$MnO$_3$ Reihe durch die Abnahme der korrigierten Winkel zwischen Mn-O-Mn, des Volumens und des Toleranzfaktors.

# Acknowledgements

# Contents

# CONTENTS

# List of Figures

# List of Tables

# LIST OF TABLES

# Acronyms

| | |
|---|---|
| TMOs | Transition Metal Oxides |
| FP | First-Principles |
| MH | Model-Hamiltonian |
| TB | Tight-Binding |
| HF | Hartree-Fock |
| DFT | Density Functional Theory |
| LDA | Local Density Approximation |
| LSDA | Local Spin Density Approximation |
| MC | Monte Carlo |
| LDA+U | Local Density Approximation + Coulombic U |
| PSIC | Pseudo Self-Interaction Correction |
| CMR | Colossal Magneto-resistance |
| GMR | Giant Magneto-resistance |
| MLWFs | Maximally Localized Wannier Functions |
| el-el | Electron-electron |
| SE | Schrödinger Equation |
| BO | Born-Oppenheimer |
| CI | Configuration Interaction |
| MP | Møller Plesset |
| HK | Hohenberg-Kohn |
| KS | Kohn-Sham |
| OFDFT | Orbital-Free Density Functional Theorem |
| GGA | Generalized Gradient Approximation |
| PBE | Perdew-Burke-Ernzerhof |
| B3LYP | Becke-3 parameter-Lee-Yang-Parr |
| VWN | Vosko-Wilk-Nusair |
| GWA | Green's Function -G, Screened Coulomb potential-W Approximation |
| LCAO | Linear Combination of Atomic Orbitals |
| SK | Slater-Koster |
| WFs | Wannier Functions |
| BZ | Brillouin Zone |
| DMFT | Dynamical Mean-Field Theory |
| VMC | Variational Monte Carlo |

| IR | Ionic Radii |
|-----|------------------|
| FM | Ferromagnetic |
| AFM | Antiferromagnetic |

# Introduction

Strongly correlated systems are a class of materials that have been known to challenge the theory of electronic structure. In these systems, the state of each electron depends on the state of one another or in other words, the correlation between electrons in these systems often determine the physics. Perovskite Transition Metal Oxides (TMOs) are a class of compounds that fall under these so-called strongly correlated systems. They exhibit an interplay of structural, electronic and magnetic phenomena that lead to the formation of complex orbital- and spin-ordered states, polaronic formation, spin-charge separation, non-Fermi liquid behaviour etc. These compounds pose a challenge to the theory and consequently to the computations due to their strongly correlated nature [1], [2], [3], [4]. The theoretical study of TMOs include understanding these underlying complexities and to come up with efficient description of their properties.

The electronic structure of TMOs are usually studied using 2 different approaches: (1) First-Principles (FP)/*ab-initio* methods (2) Model Hamiltonians (MH) typically based on tight-binding (TB) models. The most representative FP methods are Hartree-Fock (HF) theory and Density Functional Theory (DFT). HF theory is a wavefunction-based variational approach in which the many-body wavefunction is approximated by a single Slater determinant. The other widely-used FP approach, DFT is a density-functional based approach in which the ground state is obtained from the charge density.

The most difficult term in the many-body Hamiltonian is the exchange and correlation of the electron. The HF theory treats exchange in an exact way whereas the correlation part is completely neglected. DFT treats both the exchange and correlation in an approximate way. The mother of all exchange-correlation potentials used in DFT is the Local Density Approximation (LDA). In LDA, the exchange correlation potential is replaced by the results of a uniform electron gas suitably derived from quantum Monte Carlo (MC) calculations. This gives good results when the electron density does not have large spatial variations,

which is found in metallic systems. But, in strongly correlated electron systems, the electrons become nearly localized wherein the electron density fluctuations are quite high with large spatial dependence, and so LDA does not work well. However there are more elaborate FP methods such as the Local Density Approximation + Coulombic U (LDA+U), Pseudo Self-Interaction Correction (PSIC), Hybrid Functionals and GW to improve over conventional DFT.

Another way to study the theory of electronic structure is by using Model Analysis which is based on the well-known Hubbard Hamiltonian. The field of model condensed matter has made a great progress in treating this many-body problem related to the strongly-correlated systems. The model systems which had to deal with a limited number of parameters proved to work, but when the complexity of the problem increased it became necessary to evaluate the model in terms of the choice and the number of parameters.

A way to overcome this difficulty is to combine FP and MH approaches through a procedure called the **downfolding**. In strongly-correlated systems, there exists a well-defined group of bands, isolated from the rest of the bands and located near the Fermi level, which predominantly determines the ground state properties. The basic idea of downfolding is to construct the Hamiltonian for this subset of bands from the first principles by making it free of any adjustable parameters. MH could be then solved by solvers such as Dynamical Mean-Field Theory (DMFT), Variational Monte Carlo (VMC), path-integral renormalization group etc. Thus downfolding method would enable us to deal with the many-problem confined to a restricted subspace of the Hilbert space i.e. we would have a solution to an "effective" many-body problem. The model analysis would help in understanding the underlying physics of materials at the microscopic level.

A class of TMOs called the Manganite systems which possess the formula $R_{1-x}A_x\text{MnO}_3$ ($R$ = trivalent rare earth cation, $A$ = Divalent alkaline earth cation e.g. $\text{La}_{1-x}\text{Ca}_x\text{MnO}_3$, $\text{Pr}_{1-x}\text{Sr}_x\text{MnO}_3$, $\text{Nd}_{1-x}\text{Sr}_x\text{MnO}_3$ etc.) has been an area of active research for many decades since its discovery in the late 1940s [5], owing to its rich phase diagram and technological importance. These compounds exhibit very rich phase diagram as a function of temperature and doping. A phenomena called the "Colossal magneto-resistance" (CMR) which paves way to the possibility of replacing the Giant magneto-resistance (GMR) materials in the hard disk drives with CMR materials has been observed in these manganite systems. The magnetoresistance is the change in the resistance in the presence of a magnetic field. The understanding of manganite systems could also help in understanding the fundamental physics behind these interesting observations.

A widely studied compound is $LaMnO_3$ which is also the parent compound for the CMR manganites. This compound is a well-known example for strongly correlated systems in which the electronic and magnetic properties are controlled by the $Mn^{3+}$ $e_g$ states that lie near the Fermi level. The theoretical model for manganites is based on an effective two-band tight-binding model for the $Mn^{3+}$ $e_g$ electrons. The corresponding TB Hamiltonian typically contains the kinetic energy term, local terms like the Jahn-Teller coupling terms and Hund's coupling term that describes the coupling of the $t_{2g}$ spins with the $e_g$ spins and the electron-electron (el-el) Coulomb repulsion term. It has been shown in [6] that using such a model where the parameters are partly obtained from the first-principles and partly from the experiments, a phase diagram as a function of doping and temperature found in manganites systems could be reproduced.

The combination of FP and the TB Hamiltonian in the case of $LaMnO_3$ have been explored by the authors of [7] where the validity of the TB model was tested by comparing the energy dispersion calculated for the TB model with the full KS bandstructure calculated with the Local Spin Density Approximation (LSDA) to DFT. In [8], the authors demonstrated that Maximally Localized Wannier Functions (MLWFs) (via WANNIER90 code) based on KS bandstructures provide a systematic way to construct realistic, materials-specific TB models. The obtained parameters were compared to the commonly used TB models for the manganites. Using this approach, the parameters of the model can be simply read off and no fitting procedure is required. This approach thus allows to identify any discrepancies that arise from the simple models and the full DFT band structure.

In this thesis, we will discuss the mapping procedure (FP $\Rightarrow$ MLWFs $\Rightarrow$ TB) using the VASP2WANNIER90 interface for $LaMnO_3$ using different FP schemes. These include conventional DFT with and without additional on-site Hubbard U term, hybrid functionals and partially self-consistent GW. The method dependent changes of the calculated TB parameters and their interplay with the el-el interaction term (U) will be discussed and interpreted. Two alternative model parametrizations are introduced: one in which the effects of the el-el interaction are implicitly incorporated in the otherwise non-interacting TB parameters and the other one includes an explicit mean-field el-el interaction term in the TB Hamiltonian. We will also explore the evolution of the electronic, structural and magnetic properties of $RMnO_3$ where $R$ = La, Pr, Nd, Sm, Eu, Gd in order to understand the phase diagram shown by Kimura et al. in [9]. The obtained parameters are discussed, compared and interpreted. This study gives an indepth

insight of the effects due to the structural and the magnetic configurations of $R$MnO$_3$.

The thesis is organized as follows: The theory part employed in this work is discussed elaborately in Chapter 1. The construction of the TB Hamiltonian is discussed for the widely studied compound LaMnO$_3$ and the results obtained through the mapping procedure (DFT/beyond-DFT $\Rightarrow$ MLWFs $\Rightarrow$ TB) is explained for LaMnO$_3$ in Chapter 2. In Chapter 3, we will discuss the application of the mapping procedure to $R$MnO$_3$ ($R$=La, Pr, Nd, Sm, Eu, Gd) and the evolution of the structural, electronic and magnetic properties and the changes in the calculated TB parameters as a function of ionic radii (IR) of $R^{3+}$. The thesis ends with Summary and Conclusions presented as Chapter 4.

# Chapter 1

# Theory

## 1.1  Introduction

TMOs have been studied theoretically during the past few decades by two historically distinct solid state communities namely MH and FP approaches. MH approaches are based on the celebrated Hubbard model which has its origin in the seminal work by Anderson, Kanamori and Hubbard in which the many-body problem is solved by using a small set of bands and short-ranged interactions [10],[11],[12]. The FP methods are classified into two categories: HF and DFT. In HF theory (which is a variational wavefunction-based theory), an explicit form for the wavefunction is written in terms of a single Slater determinant and the solutions are arrived at by using this wavefunction. The other widely used FP approach is DFT which is a density-based theory in which the ground state is obtained from the charge density. There are more elaborate treatments available for these complex TMOs such as LDA+U, PSIC, Hybrid Functionals and GW. Another useful way to study the complex TMOs is by combining the two distinct methods i.e. FP and the MH by a downfolding procedure. While there are many ways to downfold the relevant bands, in this work, the downfolding procedure is carried out via MLWFs in order to map the FP with an effective TB MH.

## 1.2  The Schrödinger equation

The fundamental equation that describes the behaviour of energy and matter at atomic level is the Schrödinger equation (SE). By solving this problem of in-

teracting particles moving in an external potential, equilibrium properties such as crystal structure, cohesive energy, charge density, elastic constants, magnetic properties, phonons, etc and excited state properties such as excitation, optical properties, transport etc. could be studied. But, analytical solution is possible only for very few systems such as the Hydrogen atom, Harmonic oscillator, particle in a box etc. For many other systems of interest that involve many interacting particles, numerical methods have to be employed.

The full Hamiltonian for a system of electrons and nuclei (interacting system) (adopting Hartree units) is given as,

$$
\hat{H} = \underbrace{-\frac{1}{2}\sum_{i}\nabla_i^2}_{\hat{T}_e} \underbrace{-\frac{1}{2}\sum_{I}\nabla_I^2}_{\hat{T}_N} \underbrace{-\sum_{i,I}\frac{Z_I}{|\mathbf{r}_i - \mathbf{R}_I|}}_{\hat{U}_{e-N}} + \underbrace{\frac{1}{2}\sum_{i\neq j}\frac{1}{|\mathbf{r}_i - \mathbf{r}_j|}}_{\hat{U}_{e-e}} + \underbrace{\frac{1}{2}\sum_{I\neq J}\frac{Z_I Z_J}{|\mathbf{R}_I - \mathbf{R}_J|}}_{\hat{U}_{N-N}}
$$

(1.1)

where the indices i and I stand for electrons and nuclei respectively. $\hat{T}_e$ and $\hat{T}_N$ denote the kinetic energy of the electrons and nuclei respectively. $\hat{U}_{e-N}$ is the potential due to the electron-nucleus Coulombic interaction which involves one electron at a time. $\hat{U}_{e-e}$ is a Coulombic interaction involving a pair of electrons. The el-el Coulombic interactions are very difficult to deal with in practice. Almost all the electronic structure calculations employ approximations to treat this difficult term.

For more than 3 particles, the solution to the above equation becomes impossible. It therefore becomes important to introduce some approximations. One such useful approximations is the Born-Oppenheimer (BO) approximation [13] that decouples the electronic and nuclei degrees of freedom. The concept of BO approximation is that the degrees of freedom connected with the motion of the nuclei can be separated from those of the electron because the nuclei are much heavier than the electrons. The full Hamiltonian is now given as,

$$
\hat{H}_e = \hat{T} + \hat{U}_{e-N} + \hat{U}_{e-e}
$$

(1.2)

A stationary electronic state (for $N$ electrons) is then described by a wavefunction $\psi(\mathbf{r}_1, \mathbf{r}_2, \cdots, \mathbf{r}_N)$ fulfilling the many-body SE given as,

$$
\hat{H}_e|\Psi\rangle = (\hat{T} + \hat{U}_{e-N} + \hat{U}_{e-e})|\Psi\rangle
$$

(1.3)

The wavefunction $\Psi$ must be antisymmetric (fermionic property) , i.e. $\Psi(\mathbf{r}_1, \mathbf{r}_2, \cdots, \mathbf{r}_N) = -\Psi(\mathbf{r}_2, \mathbf{r}_1, \cdots, \mathbf{r}_N) = -\Psi(\mathbf{r}_1, \mathbf{r}_N, \cdots, \mathbf{r}_2)$ etc.

In the next section, we will discuss the two alternative ways under the FP approach to solve the SE namely the HF theory and the DFT.

## 1.3 Hartree-Fock theory

HF theory assumes that the exact $N$-body wavefunction could be approximated by a Slater determinant which by variational principle leads to a set of $N$-coupled equations for the $N$ one-electron wavefunctions [14]. Thus the starting point for the HF theory is a set of approximate one-electron wavefunctions (spin-orbitals). In this theory it is assumed that the electron feels the presence of the other electrons in an average manner. Slater determinant which satisfies the antisymmetric property of electrons is given as

$$\Psi_{AS} = \frac{1}{\sqrt{N!}} \begin{pmatrix} \psi_1(\mathbf{r}_1, s_1) & \psi_2(\mathbf{r}_1, s_1) & \cdots & \psi_N(\mathbf{r}_1, s_1) \\ \psi_1(\mathbf{r}_2, s_2) & \psi_2(\mathbf{r}_2, s_2) & \cdots & \psi_N(\mathbf{r}_2, s_2) \\ \vdots & \vdots & \ddots & \vdots \\ \psi_1(\mathbf{r}_N, s_N) & \psi_2(\mathbf{r}_N, s_N) & \cdots & \psi_N(\mathbf{r}_N, s_N) \end{pmatrix} \tag{1.4}$$

Variational method applied to Eqn. 1.3 ($\langle \Psi_{AS} | \hat{H}_e | \Psi_{AS} \rangle$) leads to Fock operator which is given as $\hat{F} = \hat{h} + \hat{J} - \hat{K}$ where $\hat{h}$ is the single-particle operator, $\hat{J}$ is the Coulomb operator and $\hat{K}$ is the exchange operator. These operators are given as,

$$\hat{h}\psi(\mathbf{r}) = \left[ -\frac{1}{2}\nabla^2 - \sum_n \frac{Z_n}{|\mathbf{r} - \mathbf{R}_n|} \right] \psi(\mathbf{r}) \tag{1.5}$$

$$\hat{J}_{\mathbf{k}}(\mathbf{r})\psi(\mathbf{r}) = \int \psi_{\mathbf{k}}^*(\mathbf{r}') \frac{1}{\mathbf{r}_{12}} \psi_{\mathbf{k}}(\mathbf{r}')\psi(\mathbf{r}) d\mathbf{r}' \tag{1.6}$$

$$\hat{K}_{\mathbf{k}}(\mathbf{r})\psi(\mathbf{r}) = \int \psi_{\mathbf{k}}^*(\mathbf{r}') \frac{1}{\mathbf{r}_{12}} \psi(\mathbf{r}')\psi_{\mathbf{k}}(\mathbf{r}) d\mathbf{r}' \tag{1.7}$$

The Fock operator is an effective one-electron Hamiltonian. The Coulomb operator $\hat{J}$ corresponds to the classical interaction of the electron distributions and the exchange operator $\hat{K}$ which has no classical analog is a direct result of the antisymmetry property of the wavefunction.

Thus the HF equation that is to be solved is an eigenvalue equation given as $\hat{F}\psi_{\mathbf{k}} = \varepsilon_{\mathbf{k}}\psi_{\mathbf{k}}$. Since the Fock operator depends on the orbitals used to construct the Fock matrix, the eigenfunctions of the Fock operator are in turn new orbitals which can be used to construct a new Fock operator. Thus, the HF orbitals

are optimized iteratively until the difference between the total energies of two successive iterations reaches a value that is below a given threshold. Thus, a set of self-consistent one-electron orbitals are calculated. According to Koopman's theorem, each eigenvalue of the Fock operator gives the energy required to remove an electron from the corresponding single-electron states (ionization potential). The total HF energy is given as

$$E_{\mathrm{HF}} = \sum_{\mathbf{k}} \left[ \varepsilon_{\mathbf{k}} - \frac{1}{2} \langle \psi_{\mathbf{k}} | \hat{\mathrm{J}} - \hat{\mathrm{K}} | \psi_{\mathbf{k}} \rangle \right] \tag{1.8}$$

In practice, the one-particle wavefunctions have to be expanded in a finite basis $\chi_p$ (Slater type orbitals or Gaussian orbitals or plane waves) as

$$\psi_{\mathbf{k}}(\mathbf{k}) = \sum_{p=1}^{M} C_{p\mathbf{k}} \chi_p(\mathbf{r}) \tag{1.9}$$

Thus $\hat{F}\psi_{\mathbf{k}} = \varepsilon_{\mathbf{k}}\psi_{\mathbf{k}}$ becomes $\mathbf{FC_k} = \varepsilon_{\mathbf{k}}\mathbf{SC_k}$ (in matrix notation) (Roothaan equation).

The HF calculations are widely used by the chemistry community. HF theory could be used for geometry optimizations, for studying chemical reactivity, to calculate vibrational and molecular properties. In HF theory, all correlations are neglected except those required by the Pauli Exclusion Principle. However there are other methods which are based on wavefunctions that include the correlation effects such as CI (Full and truncated CI) and perturbation theory based approaches such as MP (MP2, MP3, MP4).

## 1.4 Density Functional Theory

DFT has been a popular theory used in solid-state physics since 1970s. Till 1990s, DFT was not considered as an accurate theory for certain quantum chemical calculations, but it started becoming popular after attempts were made to refine the exchange and correlation interactions.

The basic idea of DFT is that any property of a system of many interacting particles can be written as a functional of the ground state density $n_0(\mathbf{r})$ i.e. in principle, $n_0(\mathbf{r})$ (a function of the positions $\mathbf{r}$) gives all the information in the many-body wavefunctions for the ground state. This idea greatly simplifies the problem of solving the full many-body SE that involves $3N$ degrees of freedom for $N$ electrons.

Although DFT has its roots in the Thomas-Fermi model, theoretically it is firmly rooted on the famous Hohenberg-Kohn (HK) theorems [15]. The formulation of DFT by Hohenberg and Kohn applies to any system in an external potential $V_{ext}(\mathbf{r})$ and could be applied to the problem of interacting electrons and fixed nuclei in the BO approximation described by the Hamiltonian as given below:

$$\hat{H}_e = -\frac{\hbar^2}{2m_e}\sum_i \nabla_i^2 + \sum_i V_{ext}(\mathbf{r}_i) + \frac{1}{2}\sum_{i\neq j}\frac{e^2}{|\mathbf{r}_i - \mathbf{r}_j|} \qquad (1.10)$$

In Eqn. 1.1, the term $\hat{U}_{e-N} = \sum_i V_{ext}(\mathbf{r}_i)$.

The HK theorems are stated below:

**Theorem 1** *For any system of interacting particles in an external potential $V_{ext}(\mathbf{r})$, the potential is determined uniquely, except for a constant, by the ground state particle density $n_0(\mathbf{r})$*

**Corollary 1** *All properties of the system are completely determined given only the ground state density $n_0(\mathbf{r})$.*

**Theorem 2** *A universal functional for the energy F[n] in terms of the density can be defined, valid for any $V_{ext}(\mathbf{r})$. A variational principle exists such that the global minimum value of this functional is the exact ground state energy. The density that minimizes this functional is $n_0(\mathbf{r})$.*

**Corollary 2** *The functional F[n] alone is sufficient to determine the exact ground state energy and density.*

The energy functional that is mentioned in the theorem 2 is given as,

$$E_{HK}[n] = F_{HK}[n] + \int d^3r V_{ext}(\mathbf{r})n(\mathbf{r}) \qquad (1.11)$$

Where $F_{HK}[n] = \langle\psi[n]|\hat{T} + \hat{U}_{e-e}|\psi[n]\rangle$, $V_{ext}$ is the external potential and $\psi[n]$ is the ground state wave function that has $n$ as its ground state density. The functional $F_{HK}[n]$ must be universal since it does not depend explicitly on the external potential but depends only on the electronic density.

### 1.4.1 Kohn-Sham approach

The practical implementation of HK theorems has been realized by the Kohn-Sham (KS) approach. Though there have been other formulations like the OFDFT (Orbital-Free Density Functional Theory), KS approach is more popular and widely used. In 1965, Kohn and Sham proposed the idea of replacing the intractable many-body problem of the interacting electrons in a static external potential into a tractable problem involving an auxiliary system of non-interacting electrons moving in an effective potential. The KS construction of an auxiliary system is based on 2 assumptions: (i) The exact ground state density can be represented by the ground state density of an auxiliary system of non-interacting particles ("V-representability"). (ii) The auxiliary Hamiltonian consists of the usual Kinetic operator and an effective *local* potential acting on an electron at a given position and spin.

Kohn and Sham derived a coupled set of differential equations so that the ground state density $n_0(\mathbf{r})$ could be found. The KS approach to the full many-body interacting system is to rewrite the energy functional (Eqn.1.11) as,

$$E_s[n] = T_s[n] + \int d^3r V_{s,ext}(\mathbf{r}) n(\mathbf{r}) \tag{1.12}$$

Where the subscript 's' refers to non-interacting electron system. The above equation is minimized using Lagrange's multipliers, such that,

$$\frac{\delta E_s[n]}{\delta[n]} = \frac{\delta T_s[n]}{\delta[n]} + V_{s,ext}(\mathbf{r}) = \lambda n(\mathbf{r}) \tag{1.13}$$

Where $\lambda$ is the Lagrange multiplier constraint that leads to $\int d^3r \, n(\mathbf{r}) = N$. One can solve KS equations of the auxiliary non-interacting system:

$$\left[ -\frac{1}{2}\nabla^2 + V_{s,ext}(\mathbf{r}) \right] \phi_k = \varepsilon_k \phi_k \tag{1.14}$$

Which yields the orbitals that reproduces the density $n(\mathbf{r})$ of the original system:

$$n(\mathbf{r}) \overset{def}{=} n_s(\mathbf{r}) = \sum_{k=1}^{1} |\phi_k(\mathbf{r})|^2 \tag{1.15}$$

For the many-electron system which is non-interacting system + el-el interaction, the energy functional is given as,

$$E[n] = T_s[n] + \int d^3r V_{s,ext}(\mathbf{r}) n(\mathbf{r}) + \frac{1}{2}\int d^3r \int d^3r' n(\mathbf{r}') \frac{1}{|\mathbf{r}-\mathbf{r}'|} n(\mathbf{r}) + E_{xc}[n] \tag{1.16}$$

Where,

- $T_s[n] \rightarrow$ kinetic energy functional of the non-interacting electron gas

- $\int d^3 n(\mathbf{r}) \, V_{s,ext}(\mathbf{r}) \rightarrow$ External energy

- $\int d^3(\mathbf{r}) \int d^3(\mathbf{r}') \, n(\mathbf{r}') \frac{1}{|\mathbf{r}-\mathbf{r}'|} \, n(\mathbf{r}) \rightarrow$ Hartree energy

- $E_{xc}[n] \rightarrow$ unknown correlations.

Now we need to vary this equation w.r.t. the density under the condition that $\int d^3 r \, n(\mathbf{r}) = N$. Using the method of Lagrange's multipliers, we obtain,

$$\frac{\delta E[n]}{\delta[n]} = \frac{\delta T_s[n]}{\delta[n]} + \frac{\delta E_{xc}[n]}{\delta[n]} + \int d^3 r' n(\mathbf{r}') \frac{1}{|\mathbf{r}-\mathbf{r}'|} + V_{s,ext}(\mathbf{r}) = \lambda n(\mathbf{r}) \qquad (1.17)$$

The above equation is similar to the non-interacting case, the only difference being the "effective" potential which is given as,

$$V_{eff}(\mathbf{r}) = \frac{\delta E_{xc}[n]}{\delta[n]} + \int d^3 r' n(\mathbf{r}') \frac{1}{|\mathbf{r}-\mathbf{r}'|} + V_{s,ext}(\mathbf{r}) \qquad (1.18)$$

Where $V_{xc}[n] = \frac{\delta E_{xc}[n]}{\delta[n]}$. The corresponding KS independent particle SE can now be solved.

$$\left[ -\frac{1}{2} \nabla^2 + V_{eff}(\mathbf{r}) \right] \phi_k = \varepsilon_k \phi_k \qquad (1.19)$$

with

$$V_{eff}(\mathbf{r}) = \frac{\delta E_{xc}[n]}{\delta[n]} + \int d^3 r' n(\mathbf{r}') \frac{1}{|\mathbf{r}-\mathbf{r}'|} + V_{s,ext}(\mathbf{r}) \qquad (1.20)$$

which yields the orbitals $\phi_k$ that reproduce the density $n(\mathbf{r})$ of the original many-body system:

$$n(\mathbf{r}) \stackrel{def}{=} n_s(\mathbf{r}) = \sum_{k=1}^{N} |\phi_k(\mathbf{r})|^2 \qquad (1.21)$$

The sum of the eigenvalues of the Eqn. 1.19 leads to:

$$\sum_{k=1}^{N} \varepsilon_k = \mathrm{T}_s + \int d^3r \mathrm{V}_{xc}[n](\mathbf{r})n(\mathbf{r}) + \int d^3r \int d^3r' n(\mathbf{r}')\frac{1}{|\mathbf{r}-\mathbf{r}'|} + \int d^3r \mathrm{V}(\mathbf{r})n(\mathbf{r}).$$
(1.22)

Comparing the above equation with the energy-functional of the many-body system (Refer to Eqn. 1.16), we obtain,

$$\mathrm{E} = \sum_{k=1}^{N} \varepsilon_k - \frac{1}{2}\int d^3r d^3r' n(\mathbf{r}')\frac{1}{|\mathbf{r}-\mathbf{r}'|}n(\mathbf{r}) - \int d^3 \mathrm{V}_{xc}[n](\mathbf{r}n(\mathbf{r}).$$
(1.23)

$\mathrm{V}_{xc}$ in Eqn.1.23 is mostly approximated within the LDA, GGA or meta-GGA within DFT.

In LDA, it is assumed that the density can be treated locally as an uniform homogenous electron gas (HEG); the exchange-correlation energy at each point in the system is the same as that of an uniform electron gas of the same density. The local exchange-correlation energy is a simple function of the local charge density $\varepsilon_{xc}(\mathrm{n})$, given as

$$\mathrm{E}_{xc}^{LDA}[n] = \int d^3r \varepsilon_{xc}[n(\mathbf{r})](\mathbf{r})$$
(1.24)

In practice, it is important to determine the exchange-correlation energy for an uniform electron gas of a given density. The $\epsilon_{xc}(n)$ is given as,

$$\varepsilon_{xc}(n) = \varepsilon_x(n) + \varepsilon_c(n)$$
(1.25)

The exchange term takes on a simple analytical form for the HEG:

$$\mathrm{E}_x^{LDA}[n] = -\frac{3}{4}\left(\frac{3}{\pi}\right)^{1/3}\int n(\mathbf{r})^{4/3}d\mathbf{r}$$
(1.26)

The correlation term is given as

$$\mathrm{E}_c = \int d^3r \varepsilon_c[n(\mathbf{r})](\mathbf{r})$$
(1.27)

The analytic forms for the correlation energy in the case of HEG is not known except for the high and the low density limit given as,

High density limit : $\varepsilon_c = \mathrm{A} \ln(\mathrm{r}_s) + \mathrm{B} + \mathrm{r}_s(\mathrm{C} \ln \mathrm{r}_s + \mathrm{D})$

Low density limit : $\varepsilon_c = \frac{1}{2}\left(\frac{\mathrm{g}_0}{\mathrm{r}_s} + \frac{\mathrm{g}_1}{\mathrm{r}_s}^{3/2} + \cdots\right)$ Where $\frac{4}{3}\pi \mathrm{r}_s^3 = \frac{1}{\mathrm{n}}$. Intermediate values for the density could be obtained by using accurate Monte-Carlo

simulations and interpolation [16, 17, 18, 19]. LDA works for finding properties such as structure, phase stability and vibrational frequencies. Usually, the lattice constant is underestimated, binding energies are overestimated. However LDA reasonably works due to the cancellation of errors resulting from the underestimation of the exchange energy and the overestimation of the correlation energy, but it doesn't work for the "so-called" strongly correlated systems.

The other exchange-correlation potentials within DFT are Generalized Gradient Approximation (GGA) and meta-GGA. Non-locality is introduced into exchange and correlation by the gradient of density. The GGA functional is defined as follows,

$$\mathrm{E}_{xc}^{GGA}[n^{\uparrow}, n^{\downarrow}] = \int d^3 r \varepsilon_{xc}[n(\mathbf{r}), \nabla n(\mathbf{r})](\mathbf{r}) \tag{1.28}$$

Meta-GGA functional is a developed form of the GGA functional that includes a dependence on the kinetic energy density ($\tau$), i.e. on the Laplacian of the orbitals, apart from the dependence on the density and the gradient of density. Meta-GGA functional is given as,

$$\mathrm{E}_{xc}^{MGGA} = \int d^3 r \varepsilon_{xc}[n(\mathbf{r}), \nabla n(\mathbf{r}), \tau_s(n(\mathbf{r}))](r) \tag{1.29}$$

The form of the exchange-correlation potential used in the present work is the PBE potential which is a form of GGA functional.

## 1.5   Hybrid functionals

The hybrid approach to constructing density functional approximations was introduced by Axel Becke in 1993 [20]. The idea of Hybrid functionals proposed by Becke has its origins in the adiabatic connection formula which is a rigorous formula for the exchange-correlation energy $\mathrm{E}_{xc}$ of KS DFT. The most convenient of all possible forms is given as,

$$\mathrm{E}_{xc} = \int_0^1 \mathrm{U}_{xc}^{\lambda} d\lambda \tag{1.30}$$

where $\lambda$ is an interelectronic coupling-strength parameter that "switches on" the $1/\mathrm{r}_{12}$ Coulomb repulsion between electrons and $\mathrm{U}_{xc}^{\lambda}$ is the potential energy of exchange correlation at intermediate coupling strength $\lambda$. $\lambda = 0$ represents the non-interacting KS reference system while $\lambda = 1$ represents the full interacting

real system. So this formula connects the KS reference system with the full interacting real system through a continuum of partial interacting systems all of which have the same density. This equation is very important in the KS DFT for it provides the foundation for the construction of the approximate exchange-correlation functionals. Approximating the $\lambda$ dependence of the integrand in Eqn.1.30 by linear interpolation, $E_{xc}$ becomes

$$E_{xc} \approx \frac{1}{2}U_{xc}^0 + \frac{1}{2}U_{xc}^1 \tag{1.31}$$

Where $U_{xc}^0$ is the exchange-correlation potential energy of the non-interacting reference system and $U_{xc}^1$ is the exchange-correlation potential energy for the fully-interacting real system. It could be observed that $U_{xc}^0$ is nothing but the pure exchange energy of the KS Slater determinant and therefore could be evaluated exactly. On the other hand, it was proposed by Becke that $U_{xc}^1$ be estimated by a LSDA given as,

$$U_{xc}^1 \approx U_{xc}^{LSDA} = \int \varepsilon_{xc}[n_\alpha(\mathbf{r}), n_\beta(\mathbf{r})]d^3\mathbf{r} \tag{1.32}$$

Where $n_\alpha$ and $n_\beta$ denote the spin densities, $\varepsilon_{xc}$ is the exchange-correlation potential-energy density of a spin-polarized electron gas.

Equation 1.30 is modified to obtain the hybrid form which is given as,

$$E_{xc} \approx \frac{1}{2}E_x + \frac{1}{2}U_{xc}^{LSDA} \tag{1.33}$$

The above equation represents a true hybrid because it is impossible to decide if it is an exact-exchange correction to LSDA or an LSDA correction to exact exchange. Using HF theory, the band gap is large because it includes full exchange and no correlation, whereas DFT includes approximate exchange and correlation. Combination of HF exchange and DFT's approximate exchange and correlation should therefore give a better value for the band gap.

Thus, a hybrid exchange-correlation functional can be in principle constructed as a linear combination of the HF exact-exchange functional $E_x^{HF}$ given as,

$$E_x^{HF} = \frac{1}{2}\sum_{i,j} \int \int \psi_i^*(\mathbf{r}_1)\psi_j^*(\mathbf{r}_1)\frac{1}{\mathbf{r}_{12}}\psi_i(\mathbf{r}_2)\psi_j(\mathbf{r}_2)d\mathbf{r}_1 d\mathbf{r}_2 \tag{1.34}$$

and any number of exchange and correlation explicit density functionals.

A popular hybrid functional used in the quantum chemistry community is B3LYP (Becke-3 parameter-Lee-Yang-Parr) exchange-correlation functional [21],[22] which is given as,

$$\mathrm{E}_{xc}^{B3LYP} = \mathrm{E}_{xc}^{LDA} + \mathrm{a}_0(\mathrm{E}_x^{HF} - \mathrm{E}_x^{LDA}) + \mathrm{a}_x(\mathrm{E}_x^{GGA} - \mathrm{E}_x^{LDA}) + \mathrm{a}_c(\mathrm{E}_c^{GGA} - \mathrm{E}_c^{LDA}) \quad (1.35)$$

Where $\mathrm{a}_0 = 0.20$, $\mathrm{a}_x = 0.72$, $\mathrm{a}_c = 0.81$. $\mathrm{E}_x^{GGA}$ and $\mathrm{E}_c^{GGA}$ are GGA functionals (Becke 88 exchange functional [23] and the correlation functional of Lee, Yang and Parr for B3LYP [24] and $\mathrm{E}_c^{LDA}$ is the VWN (Vosko-Wilk-Nusair) LDA to correlation functional [16]. The three parameters were taken from [25].

Other widely used Hybrid functionals are PBE0 and HSE functionals. The PBE0 functional [26], [27] mixes $\frac{1}{4}$ of exact (HF) exchange with $\frac{3}{4}$ of PBE exchange, and describes correlation in the GGA (PBE),

$$\mathrm{E}_{xc}^{PBE0} = \frac{1}{4}\mathrm{E}_x^{HF} + \frac{3}{4}\mathrm{E}_x^{PBE} + \mathrm{E}_c^{PBE} \quad (1.36)$$

The HF calculations under periodic boundary conditions are quite expensive due to the fact that the decay of the exchange interaction with distance is very slow. Heyd et al. [28] proposed an idea to overcome this difficulty, i.e. to separate the Coulomb kernel into short-range and long-range parts, i.e.

$$\frac{1}{r} = \frac{erfc(\omega r)}{r} + \frac{erf(\omega r)}{r} \quad (1.37)$$

where $\frac{\mathrm{erfc}(\omega\mathrm{r})}{\mathrm{r}}$ denotes the short-range part which is a complementary error function of $\omega\mathrm{r}$ and $\frac{\mathrm{erf}(\omega\mathrm{r})}{\mathrm{r}}$ denotes the long range part which is an error function of r. $\omega$ is an adjustable parameter. The HSE functional which is used in the present work is given as,

$$\mathrm{E}_{xc}^{HSE} = \frac{1}{4}\mathrm{E}_x^{sr,HF} + \frac{3}{4}E_x^{sr,PBE} + \mathrm{E}_x^{lr,PBE} + \mathrm{E}_c^{PBE} \quad (1.38)$$

The optimum range separation parameter $\omega \approx 0.2$ Å$^{-1}$ is said to be a good choice [29].

## 1.6   LDA+U

LDA and GGA fails for strongly correlated systems, i.e. systems with localized d and f electrons. Localization in these systems is due to the fact that electrons cannot come close to each other due to the presence of strong repulsion in

short-ranged part of the Coulomb interaction. LDA treats the distribution of the interacting electrons as that averaged over the space. However, it does not treat the electron configuration avoiding each other and so consequently predicts an incorrect metallic solution for systems such as Mott insulators. In antiferromagnetic systems and orbital-ordered systems, there is a symmetry breaking and the electron distribution of each spin or orbital loses its uniformity. If these symmetry breaking is taken into account then the localization could be described. LDA+U is one of the corrective approaches that aims at improving the accuracy of the DFT functionals in describing the ground state of correlated systems. It is based on using Hubbard Hamiltonian to describe the "strongly correlated" electronic states (localized 'd' or 'f' electrons) while the rest of the valence electrons are treated at DFT level of approximation.

The Hubbard Hamiltonian is given as,

$$\text{H}_{Hub} = t \sum_{\langle i,j \rangle, \sigma} (\text{c}_{i,\sigma}^{\dagger} \text{c}_{j,\sigma} + h.c.) + U \sum_{i} n_{i,\uparrow} n_{i,\downarrow} \tag{1.39}$$

where $\langle i,j \rangle$ represents the nearest-neighbour atomic sites, $\text{c}_{i,\sigma}^{\dagger} \text{c}_{j,\sigma}$ represent the creation and annihilation operators for electrons of spin $\sigma$ at sites i,j respectively and $n_{i,\sigma}$ denotes the number operator (spin $\sigma$ and site $i$).

Within LDA+U, the total energy of the system is given as,

$$\text{E}_{LDA+U}[n(\mathbf{r})] = \text{E}_{LDA}[n(\mathbf{r})] + \text{E}_{Hub}[n_{mm'}^{I\sigma}] - \text{E}_{dc}[n^{I\sigma}] \tag{1.40}$$

Where $\text{E}_{Hub}$ is the term that contains the el-el interactions as modeled in the Hubbard Hamiltonian and $m$ labels the localized states of the same atomic site $I$. When $\text{E}_{Hub}$ is added, the Coulomb interaction that is already counted in the exchange correlation potential in LDA is doubly counted and $\text{E}_{dc}$ models the contribution to the DFT energy from correlated electrons as a mean-field approximation to $\text{E}_{Hub}$. The Hubbard correction is applied only to the localized states of the system. It is a functional of the occupation numbers that are defined as the projections of occupied Kohn-Sham orbitals ($\psi_{k,b}^{\sigma}$) on the states of a localized basis set ($\phi_{m}^{I}$) which is given as

$$\text{n}_{m,m'}^{I\sigma} = \sum_{k,b} \text{f}_{kb}^{\sigma} \langle \psi_{kb}^{\sigma} | \phi_{m'} \rangle \langle \phi_{m}^{I} | \psi_{kb}^{\sigma} \rangle \tag{1.41}$$

Where $\text{f}_{kb}^{\sigma}$ represents the Fermi-Dirac occupations of the KS states and k and b represent the k-point and the band indices.

Equation 1.40 gives the general structure of the LDA+U energy functional. Anisimov et al. [30], [31], [32] were the first to introduce LDA+U and it consists of an energy functional that can be written as

$$E = E_{LDA} + \sum_I \left[ \frac{U^I}{2} \sum_{m,\sigma \neq m',\sigma'} n_m^{I\sigma} n_{m'}^{I\sigma'} - \frac{U^I}{2} n^I (n^I - 1) \right] \qquad (1.42)$$

Where $n_m^{I\sigma} = n_{mm}^{I\sigma}$ and $n^I = \sum_{m,\sigma} n_m^{I\sigma}$. The second and the third terms represent the Hubbard and the double counting terms of Eqn.1.40 respectively. The action of the Hubbard corrective potential on the Kohn-Sham wavefunctions needed for the minimization process can be defined using the atomic orbital occupations given in Eqn.1.41. It is given as,

$$V|\psi_{k,b}^\sigma\rangle = V_{LDA}|\psi_{k,b}^\sigma\rangle + \sum_{I,m} U^I \left( \frac{1}{2} - n_m^{I\sigma} \right) |\phi_m^I\rangle\langle\phi_m^I|\psi_{k,b}^\sigma\rangle \qquad (1.43)$$

The KS equations obtained from Eqn.1.42 will thus yield the ground state one-body density matrix of the system. If $n_m^{I\sigma} < 1/2$ i.e. for half-filled orbitals, the Hubbard potential is repulsive and for others it is attractive. This favours fully occupied or fully unoccupied states and opens a gap of the order $U^I$. The difference between the potential acting on the occupied and unoccupied states gives the measure of the energy gap opening between their eigenvalues. Therefore, the explicit account of on-site el-el interactions favours the electronic localization and may lead to the band gap opening in the KS spectrum, provided the on-site Coulomb repulsion prevails on the kinetic energy , minimized through delocalization.

The LDA+U approach described above has a discrepancy that is, the formulation given by Eqn.1.42 is not invariant under rotation of the atomic orbital basis set that is used to define the occupation of $d$ states $n_m^{I\sigma}$ which produces an undesirable dependence of the results on the specific choice of localized basis set. A. Liechtenstein and coworkers [33] introduced a formulation which is a rotationally-invariant formulation in which the $E_{Hub}$ and $E_{dc}$ are given a more

general expression borrowed from the HF method, which is given as,

$$
\begin{aligned}
\mathrm{E}_{Hub}[(\mathrm{n}^I_{mm'})] &= \frac{1}{2} \sum_{m,\sigma,I} [\langle m,m''|\mathrm{V}_{ee}|m'm''\rangle \mathrm{n}^{I\sigma}_{mm'} \mathrm{n}^{I-\sigma}_{m''m'''} \\
&\quad + (\langle m,m''|\mathrm{V}_{ee}|m'm'''\rangle - \langle m,m''|\mathrm{V}_{ee}|m''',m'\rangle)\, \mathrm{n}^{I\sigma}_{mm'} \mathrm{n}^{I\sigma}_{m''m'''}] \\
\mathrm{E}_{dc}[(\mathrm{n}^I_{mm'})] &= \sum_I \left( \frac{U^I}{2}\mathrm{n}^I(\mathrm{n}^I-1) - \frac{J^I}{2}[\mathrm{n}^{I\uparrow}(\mathrm{n}^{I\uparrow}-1) + \mathrm{n}^{I\downarrow}(\mathrm{n}^{I\downarrow}-1)] \right)
\end{aligned}
$$

Though this formulation proves to be the most complete formulation of LDA+U based on a multi band Hubbard model, in many occasions, a much simpler expression of the Hubbard correction ($\mathrm{E}_{Hub}$) introduced by Dudarev et al. [34] is actually implemented and adopted. The energy functional is given as,

$$
\mathrm{E}_U\left[\mathrm{n}^{I\sigma}_{mm'}\right] = \mathrm{E}_{Hub}[\mathrm{n}^I_{mm'}] - \mathrm{E}_{dc}[\mathrm{n}^I]
$$

$$
= \sum_I \frac{U^I}{2}\left[(\mathrm{n}^I)^2 - \sum_\sigma Tr[(\mathrm{n}^{I\sigma})^2]\right] - \sum_I \frac{U^I}{2}\mathrm{n}^I(\mathrm{n}^I-1)
$$

$$
= \sum_{I,\sigma} \frac{U^I}{2}Tr[\mathrm{n}^{I\sigma}(1-\mathrm{n}^{I\sigma})]
$$

This simplified version of the Hubbard correction has been successfully used in several studies and will be the one adopted in the present thesis.

## 1.7 GW method/approximation

In the DFT formulation, the ground state energy is written as a functional of the ground state density which gives a minimum when variational theorem is applied w.r.t that density. Once this energy functional is known or approximated, the solution of the many-body problem is given by a set of self-consistent solution of effective one-particle equation. One of the practical computational schemes is the LDA functional as the exchange correlation functional. The obtained KS eigenvalues have no physical meaning. They are often considered as single particle excitation energies i.e. energy needed to remove an electron or add an electron to the system. There are no theoretical justification for this consideration. Moreover in the KS approach we map the interacting system to a non-interacting system. Though the interactions are incorporated through exchange and correlation terms, still the description is a one-particle description. The electrons

could be more accurately described when they are considered to be quasiparticles. So the proper treatment for calculation of the quasiparticle excitation energies is required. One of the best methods available at present for calculating the quasiparticle energies is the GW approximation [35], [36]. The basic idea of the GW approximation is the expansion in the series of the screened Coulomb interaction for the proper treatment of the screening effects in solids [35], [37], [38]. The initial works on GW method include the study of the electron gas by Quinn and Ferrel in which they attempted to include the correlation effects and work on electron gas in the high density region. In 1965, Hedin derived an exact closed set of equations for the self-energy in which the self- energy was expanded in powers of the screened Coulomb potential. Lundquist did extensive calculations of the electron gas self-energy and spectral functions [39]. Hybertson and Louie performed GW calculations on semiconductors and found that the band gap problem of DFT is cured [40]. The all-electron GW calculations were done by Aryasetiawan in 1990's. GW calculations can now be performed for systems containing more than 50 atoms [41],[42].

For an inhomogenous system, the quasiparticle energies and wavefunctions are calculated by using the equation,

$$(\text{T} + \text{V}_{ext} + \text{V}_H)\psi_{\mathbf{k}n}(\mathbf{k}) + \int d\mathbf{r}' \sum(\mathbf{r}, \mathbf{r}'; \text{E}_{n\mathbf{k}})\psi_{\mathbf{k}n}(\mathbf{r}') = \text{E}_{\mathbf{k}n}\psi_{\mathbf{k}n}(\mathbf{r}) \qquad (1.44)$$

Where $\sum$ is the self-energy which can be evaluated by using the Green's function based formula given by Hedin [35]. The basic quantity of the GWA is the one-particle Green's function given as,

$$\text{G}(1, 2) = i\langle \text{N}|\text{T}[\hat{\psi}(1)\hat{\psi}^\dagger(2)]|\rangle, \qquad (1.45)$$

where $|\text{N}\rangle$ is the ground state of the $N$ electron system, T is the time-ordered product, $\hat{\psi}$ and $\hat{\psi}^\dagger$ are field operators and 1=$(\mathbf{r}_1, t_1)$ is the composite space-time variable. Starting from the equation of motion of the Green's function, Hedin derived a set of equations between the Green's function G, self-energy $\sum$, screened Coulomb interaction W, polarization function P and vertex correction $\Gamma$:

$$\sum(1, 2) = i \int \text{G}(1, 3^+)\text{W}(14)\Gamma(3, 2, 4)d(34), \qquad (1.46)$$

$$\text{W}(1, 2) = \text{v}(1, 2) + i \int \text{v}(1, 3)\text{P}(3, 4)\text{W}(4, 2)\text{d}(34), \qquad (1.47)$$

$$P(1, 2) = -i \int G(1, 3)\Gamma(3, 4, 2)G(4, 1^+)d(34), \qquad (1.48)$$

$$\Gamma(1, 2, 3) = \delta(1-2)\delta(1-3) + \int \frac{\delta \sum(1, 2)}{\delta G(4, 5)}G(4, 6)G(7, 5)\Gamma(6, 7, 3)d(4567), \quad (1.49)$$

$$G(1, 2) = G_0(1, 2) + \int G_0(1, 3)\sum(3, 4)G(4, 2)d(34), \qquad (1.50)$$

To solve the above equations, one must find the self-energy $\sum$. In the GWA, the vertex correction is approximated as

$$\Gamma(1, 2, 3) = \delta(1-2)\delta(2-3), \qquad (1.51)$$

which leads to the self-energy that is given as,

$$\overset{GW}{\sum}(1, 2) = iG(1, 2)W(1, 2), \qquad (1.52)$$

In real materials, the GW calculations can be carried out non self-consistently on top of the DFT solution as well as partially self-consistent (in G) or fully self-consistent (in G and W). The starting Green's function equivalent to Eqn.1.45 is

$$G_0(\mathbf{r}, \mathbf{r}'; \omega) = \sum_v^{occ} \frac{\psi_v(\mathbf{r})\psi_v^*(\mathbf{r}')}{\omega - \varepsilon_v - i\delta} + \sum_c^{unocc} \frac{\psi_c(\mathbf{r})\psi_c^*(\mathbf{r}')}{\omega - \varepsilon_c - i\delta}, \qquad (1.53)$$

where $\psi_v$ and $\psi_c$ are the eigenstates of the KS equation. The polarizability from which the W is computed is given as,

$$P_0(\mathbf{r}, \mathbf{r}'; \omega) = \sum_v^{occ} \sum_c^{unocc} \left[ \frac{\psi_v(\mathbf{r})\psi_c^*(\mathbf{r})\psi_c(\mathbf{r}')\psi_v^*(\mathbf{r}')}{\omega - (\varepsilon_c - \varepsilon_v) + i\delta} - \frac{\psi_v^*(\mathbf{r})\psi_c(\mathbf{r})\psi_c^*(\mathbf{r}')\psi_v(\mathbf{r}')}{\omega - (\varepsilon_c - \varepsilon_v) + i\delta} \right]$$
$$(1.54)$$

By substituting W in Eqn.1.52, $\sum$ is computed. Once the self-energy is computed, the Green's function is obtained by solving the Dyson equation 1.50. Its spectral function, $A(\mathbf{k}, \omega)$, is given as

$$A(\mathbf{k}, \omega) = \frac{1}{\pi} \sum_n |\langle \psi_{\mathbf{k}n} | Im G(\omega) | \psi_{\mathbf{k}n} \rangle|, \qquad (1.55)$$

$A(\mathbf{k}, \omega)$ is the one-electron excitation spectrum for electron addition or removal. This is the quantity that is to be compared with the photoemission

measurements. The peak position of the spectral function i.e. the quasiparticle energy is given as

$$\mathrm{E}^{QP}_{\mathbf{k}n} = \varepsilon_{\mathbf{k}n} + Re\langle\psi_{\mathbf{k}n}|\sum(\mathrm{E}^{QP}_{\mathbf{k}n}) - \mathrm{v}_{xc}|\psi_{\mathbf{k}n}\rangle \tag{1.56}$$

Since it is often assumed that the self-energy is weakly frequency dependent, it is safely expanded around the Kohn-Sham eigenvalue. Eqn. 1.56 is reduced to

$$\mathrm{E}^{QP}_{\mathbf{k}n} = \varepsilon_{\mathbf{k}n} + \mathrm{Z}_{\mathbf{k}n}Re\langle\psi_{\mathbf{k}n}|\sum(\varepsilon_{\mathbf{k}n}) - \mathrm{v}_{xc}|\psi_{\mathbf{k}n}\rangle, \tag{1.57}$$

where the renormalization factor Z is defined by

$$\mathrm{Z}_{\mathbf{k}n} = \left(1 - \frac{\partial Re\sum_{\mathbf{k}n}}{\partial\omega}|_{\omega=\varepsilon_{\mathbf{k}n}}\right)^{-1} \tag{1.58}$$

# 1.8 Tight-Binding model and Maximally Localized Wannier Functions

## 1.8.1 Tight-binding method

TB model is a one-electron model which is based on the idea that atomic-like orbitals could be used as a basis to expand the crystal wavefunctions. "Tight-binding" refers to the tightly-bound electrons in solids. This model works very well for the electrons that are tightly-bound to the atom. TB method is also very closely related to the LCAO (Linear Combination of Atomic Orbitals) which is widely used in chemistry. TB method provides a basis for the construction of many-body theories such as the Hubbard model and the Anderson impurity model.

After the establishment of the idea of an orbital by Robert Mulliken in 1928, LCAO for molecules was developed by Finklestein and Horowitz whereas LCAO for solids was developed by Bloch [43]. In 1954, a parametrized tight-binding method which involves a simpler interpolation scheme for studying the electronic structure (especially for the d-electrons of the transition metals) was conceived by J.C.Slater and G.F.Koster [44]. Slater and Koster call it a "tight-binding" or the "Bloch" method and their celebrated paper provides a systematic procedure for formulating a tight-binding model. Their paper provides the famous "Slater-Koster" table that is used to build a TB Hamiltonian. There are fundamentally 3

ways in which TB fomulation plays an important role in electronic structure. (1) It provides the simplest understanding of the fundamental features of electronic bands. (2) Empirical TB methods: In this, a form for the Hamiltonian and overlap matrix elements are assumed without any specification regarding the orbitals except for the symmetry. The values of the matrix elements may be derived approximately or could be found by fitting with the experimental data or other theory. (3) Using local orbitals like Gaussians to carry out a full self-consistent solution of independent-particle equations. We will now move on with the detailed discussion of the TB method.

Let us consider a crystal where the atoms in the unit cell are at positions $\tau_{\kappa,j}$ where $\kappa$ indicates the type of atoms and $j$ indicates the number of atoms of type $\kappa$. Consider a set of orbitals that form a basis $\chi_\alpha(\mathbf{r} - \mathbf{R}_I)$, each associated with an atom at position $\mathbf{R}_I$. Letting $m$ denote the composite index $[\kappa, j, \alpha]$ we allow the entire basis to be specified by $\chi_m(\mathbf{r} - (\tau_m + \mathbf{T}))$, where $\mathbf{T}$ is a translational vector. Within this atomic-like Bloch basis, we can solve the Schrödinger equation by computing the Hamiltonian and the overlap matrix elements $H_{m,m'}$ and $S_{m,m'}$. The matrix elements of the Hamiltonian of a state $m$ in the cell at the origin and state $m'$ in the cell labelled by the translation vector $\mathbf{T}$ is given as,

$$\mathrm{H}_{m,m'}(\mathbf{T}) = \int d\mathbf{r}\chi_m^*(\mathbf{r} - \tau_m)\hat{H}\chi_{m'}[\mathbf{r} - (\tau_{m'} + \mathbf{T})], \qquad (1.59)$$

The above equation applies to any orbitals $m$ and $m'$ in cells that are separated by the translation $\mathbf{T}$, since the crystal is translationally invariant. The overlap matrix is given by

$$\mathrm{S}_{m,m'}(\mathbf{T}) = \int d\mathbf{r}\chi_m^*(\mathbf{r} - \tau_m)\chi_{m'}[\mathbf{r} - (\tau_{m'} + \mathbf{T})] \qquad (1.60)$$

According to Bloch's theorem, the basis state with wavevector $\mathbf{k}$ can be written as,

$$\chi_{m\mathbf{k}}(\mathbf{r}) = \mathrm{A}_{m\mathbf{k}}\sum_{\mathbf{T}} \mathrm{e}^{i\mathbf{k}\cdot\mathbf{T}}\chi_m[\mathbf{r} - (\tau_m + \mathbf{T})], \qquad (1.61)$$

where $\mathrm{A}_{m\mathbf{k}}$ is a normalization factor. Wavevector $\mathbf{k}$ is restricted to the first Brillouin zone and this is sufficient because when reciprocal lattice vector is added the phase factor $\mathrm{e}^{i\mathbf{k}\cdot\mathbf{T}}$ is unchanged. The translational invariance of the Hamiltonian

## 1.8 Tight-Binding model and Maximally Localized Wannier Functions

shows that the matrix elements of the Hamiltonian with the basis functions $\chi_{m\mathbf{k}}$ and $\chi_{m'\mathbf{k}'}$ are non-zero only for $\mathbf{k} = \mathbf{k}'$, with

$$H_{m,m'}(\mathbf{k}) = \int d\mathbf{r}\,\chi_{m\mathbf{k}}^*(\mathbf{r})\hat{H}\chi_{m'\mathbf{k}}(\mathbf{r}) = \sum_{\mathbf{T}} e^{i\mathbf{k}\cdot\mathbf{T}} H_{m,m'}(\mathbf{T}), \qquad (1.62)$$

and

$$S_{m,m'}(\mathbf{k}) = \int d\mathbf{r}\,\chi_{m\mathbf{k}}^*(\mathbf{r})\chi_{m'\mathbf{k}}(\mathbf{r}) = \sum_{\mathbf{T}} e^{i\mathbf{k}\cdot\mathbf{T}} S_{m,m'}(\mathbf{T}), \qquad (1.63)$$

Since the Hamiltonian conserves $\mathbf{k}$, an eigenfunction of the SE in a basis can be written in the form

$$\psi_{i\mathbf{k}}(\mathbf{r}) = \sum_{m} c_m(\mathbf{k})\chi_{m\mathbf{k}}(\mathbf{r}), \qquad (1.64)$$

and the secular equation for wavevector $\mathbf{k}$ is given as,

$$\sum_{m'}[H_{m,m'}(\mathbf{k}) - \varepsilon_i(\mathbf{k})S_{m,m'}(\mathbf{k})]c_{i,m'}(\mathbf{k}) = 0 \qquad (1.65)$$

Local orbitals are different from other basis because the locality of $\chi_m(\mathbf{r} - (\tau_m + \mathbf{T}))$ causes $H_{m,m'}$ and $S_{m,m'}$ to decrease and become negligible for large distances $|\tau_m\text{-}(\tau_{m'}+\mathbf{T})|$.

The Hamiltonian and the overlap matrix elements (Eqns. 1.59 and 1.60) can be divided into one-, two-, and three-center terms. The Hamiltonian matrix elements arise from a Hamiltonian that has the form ,

$$\hat{H} = -\frac{1}{2}\nabla^2 + \sum_{\mathbf{T}\kappa j} V^{\kappa}[|\mathbf{r} - (\tau_{\kappa j} + \mathbf{T})|], \qquad (1.66)$$

where the first term is the kinetic energy term and the second term is the potential decomposed into a sum of spherical terms centered on each site $\kappa$, $j$ in the unit cell. The kinetic part of the Hamiltonian matrix element always involves one or two centers. But the potential terms may depend on the positions of other atoms and they can be divided into the following:

- One-center - where both the orbitals and the potential are centered on the same site and these terms have the same symmetry as an atom in free space.

23

- Two-center - The orbitals are centered on different sites and the potential is on one of the two and these terms have the same symmetry as the other two-center terms.

- Three-center - The orbitals and the potential are all centered on different sites.

The two-center matrix elements play an important role in calculations involving local orbitals. The orbitals can be classified in terms of the azimuthal angular momentum about the line between the centers, i.e. the value of $m$ with the axis chosen along the line, and the only non-zero matrix elements are between the orbitals with the same $m=m'$. Slater and Koster proposed that the Hamiltonian matrix elements could be approximated with the two-center form and fitted to theoretical calculations. Within this approach, all the matrix elements have the same symmetry and this is a very useful approach to understanding electrons in materials. Examples for two-center matrix elements of $s$ and $p_i = \{/p_x, p_y, p_z/\}$ orbitals separated by displacement vector $\mathbf{R}$ are shown in Fig.1.1. Matrix elements are related to $\sigma$ and $\pi$ integrals by the transformation to a combination of orbitals that are aligned along $\mathbf{R}$ and perpendicular to $\mathbf{R}$. These two-center matrix elements are given in SK table shown in the Tab.1.1. The table gives the transformation of the matrix elements (Eqn. 1.59) in terms of $V_{mm'}$ where $m$ and $m'$ refers to the orbitals at different sites (for example $V_{ss\sigma}$). In the table, this is referred to as $E_{n,m}$ where $n,m$ represents $s$, $x$ ($p_x$), $y$ ($p_y$) , $z$ ($p_z$), $xy$ ($d_{xy}$) etc. and the integrals could be expressed as

$$E_{n,m}(p,q,r) = \int \psi_n^*(\mathbf{r})H\psi_m(\mathbf{r} - pa\mathbf{i} - qa\mathbf{j} - ra\mathbf{k})dv \qquad (1.67)$$

The above equation is taken from the original paper by Slater and Koster [44] which are given using a different notation in this section by Eqns. 1.59, 1.62. If the atoms are located at the vector positions $pa\mathbf{i}+qa\mathbf{j}+ra\mathbf{k}$, where $p$, $q$, $r$ are integers, $a$ is the lattice constant and $l$, $m$ and $n$ are the direction cosines and $l=p(p^2+q^2+r^2)^{-\frac{1}{2}}$, $m=q(p^2+q^2+r^2)^{-\frac{1}{2}}$ and $n=r(p^2+q^2+r^2)^{-\frac{1}{2}}$.

To obtain the Hamiltonian matrix elements in k-space, Eqn. 1.59 has to be multiplied by the Bloch phase factors (Fourier-transformed) as given by the Eqn. 1.62.

| | |
|---|---|
| $E_{s,s}$ | $V_{ss\sigma}$ |
| $E_{s,x}$ | $lV_{sp\sigma}$ |
| $E_{x,x}$ | $l^2 V_{pp\sigma} + (1 - l^2)V_{pp\pi}$ |
| $E_{x,y}$ | $lmV_{pp\sigma} - lmV_{pp\pi}$ |
| $E_{x,z}$ | $lnV_{pp\sigma} - lnV_{pp\pi}$ |
| $E_{s,xy}$ | $\sqrt{3}lmV_{sd\sigma}$ |
| $E_{s,x^2-y^2}$ | $\frac{\sqrt{3}}{2}(l^2 - m^2)V_{sd\sigma}$ |
| $E_{s,3z^2-r^2}$ | $[n^2 - (l^2 + m^2)/2]V_{sd\sigma}$ |
| $E_{x,xy}$ | $\sqrt{3}\ l^2 mV_{pd\sigma} + m(1 - 2l^2)V_{pd\pi}$ |
| $E_{x,yz}$ | $\sqrt{3}lmnV_{pd\sigma} - 2lmnV_{pd\pi}$ |
| $E_{x,zx}$ | $\sqrt{3}l^2 nV_{pd\sigma} + n(1 - 2l^2)V_{pd\pi}$ |
| $E_{x,x^2-y^2}$ | $\frac{\sqrt{3}}{2}l(l^2 - m^2)V_{pd\sigma} + l(1 - l^2 + m^2)V_{pd\pi}$ |
| $E_{y,x^2-y^2}$ | $\frac{\sqrt{3}}{2}m(l^2 - m^2)V_{pd\sigma} - m(1 + l^2 - m^2)V_{pd\pi}$ |
| $E_{z,x^2-y^2}$ | $\frac{\sqrt{3}}{2}n(l^2 - m^2)V_{pd\sigma} - n(l^2 - m^2)V_{pd\pi}$ |
| $E_{x,3z^2-r^2}$ | $l[n^2 - (l^2 + m^2)/2]V_{pd\sigma} - \sqrt{3}ln^2 V_{pd\pi}$ |
| $E_{y,3z^2-r^2}$ | $m[n^2 - (l^2 + m^2)/2]V_{pd\sigma} - \sqrt{3}mn^2 V_{pd\pi}$ |
| $E_{z,3z^2-r^2}$ | $n[n^2 - (l^2 + m^2)/2]V_{pd\sigma} + \sqrt{3}n(l^2 + m^2)V_{pd\pi}$ |
| $E_{xy,xy}$ | $3l^2 m^2 V_{dd\sigma} + (l^2 + m^2 - 4l^2 m^2)V_{dd\pi} + (n^2 + l^2 m^2)V_{dd\delta}$ |
| $E_{xy,yz}$ | $3lm^2 nV_{dd\sigma} + ln(1 - 4m^2)V_{dd\pi} + ln(m^2 - 1)V_{dd\delta}$ |
| $E_{xy,zx}$ | $3l^2 mnV_{dd\sigma} + mn(1 - 4l^2)V_{dd\pi} + mn(l^2 - 1)V_{dd\delta}$ |
| $E_{xy,x^2-y^2}$ | $\frac{3}{2}lm(l^2 - m^2)V_{dd\sigma} + 2lm(m^2 - l^2)V_{dd\pi} + lm(l^2 - m^2)/2V_{dd\delta}$ |
| $E_{yz,x^2-y^2}$ | $\frac{3}{2}mn(l^2 - m^2)V_{dd\sigma} - mn[1 + 2(l^2 - m^2)]V_{dd\pi} + mn[1 + (l^2 - m^2)/2]V_{dd\delta}$ |
| $E_{zx,x^2-y^2}$ | $\frac{3}{2}nl(l^2 - m^2)V_{dd\sigma} + nl[1 - 2(l^2 - m^2)]V_{dd\pi} - nl[1 - (l^2 - m^2)/2]V_{dd\delta}$ |
| $E_{xy,3z^2-r^2}$ | $\sqrt{3}\,[lm(n^2 - (l^2 + m^2)/2)V_{dd\sigma} - 2lmn^2 V_{dd\pi} + lm(1 + n^2)/2V_{dd\delta}]$ |
| $E_{yz,3z^2-r^2}$ | $\sqrt{3}\,[mn(n^2 - (l^2 + m^2)/2)V_{dd\sigma} + mn(l^2 + m^2 - n^2)V_{dd\pi} - mn(l^2 + m^2)/2V_{dd\delta}]$ |
| $E_{zx,3z^2-r^2}$ | $\sqrt{3}\,[ln(n^2 - (l^2 + m^2)/2)V_{dd\sigma} + ln(l^2 + m^2 - n^2)V_{dd\pi} - ln(l^2 + m^2)V_{dd\delta}]$ |
| $E_{x^2-y^2,x^2-y^2}$ | $\frac{3}{4}(l^2 - m^2)V_{dd\sigma} + [l^2 + m^2 - (l^2 - m^2)^2]V_{dd\pi} + [n^2 + (l^2 - m^2)^2/4]V_{dd\delta}$ |
| $E_{x^2-y^2,3z^2-r^2}$ | $\sqrt{3}\,[(l^2 - m^2)[n^2 - (l^2 - m^2)/2]V_{dd\sigma}/2 + n^2(m^2 - l^2)V_{dd\pi} + (1 + n^2)(l^2 - m^2)/4V_{dd\delta}]$ |
| $E_{3z^2-r^2,3z^2-r^2}$ | $[n^2 - (l^2 - m^2)/2]^2 V_{dd\sigma} + 3n^2(l^2 + m^2)V_{dd\pi} + \frac{3}{4}(l^2 + m^2)V_{dd\delta}$ |

**Table 1.1:** Table of two-center matrix elements proposed by Slater-Koster [44]
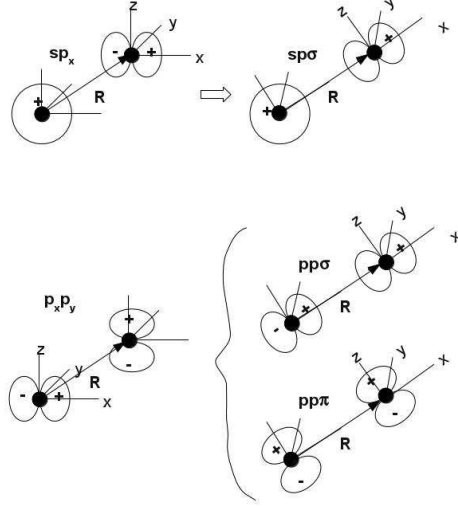
**Figure 1.1:** Schematic representation of the two-center matrix elements of s and $p_i = \{/p_x, p_y, p_y/\}$ orbitals separated by the displacement vector $\mathbf{R}$.

## 1.8.2  Maximally Localized Wannier Functions

MLWFs provide an alternative representation of the electronic structure in terms of the functions localized in real space. These functions are obtained by the Unitary transformation from the energy eigenfunctions, thus providing the full equivalent description. MLWFs provide an insightful physical picture through their center, their extension and their shape. The electron orbitals can be visualized. We will discuss the formulation in detail in the following section.

In the independent particle approximation, the eigenstates of a solid (crystal) are represented in the form of Bloch functions which are written as a periodic function times a phase factor (plane wave) [43],

$$\psi_{n\mathbf{k}}(\mathbf{r}) = u_{n\mathbf{k}}(\mathbf{r})e^{i\mathbf{k}\cdot\mathbf{r}} \tag{1.68}$$

The Bloch functions at different $\mathbf{k}$ points have different phase factor or the envelope function. Wannier functions could be obtained using the following expression:

$$w_0(\mathbf{r}) = \frac{V}{(2\pi^3)} \int_{BZ} d\mathbf{k}\psi_{\mathbf{k}}(\mathbf{r}) \tag{1.69}$$

Where V is the Real-space primitive cell volume.

## 1.8 Tight-Binding model and Maximally Localized Wannier Functions

More generally, by including a phase factor $e^{-i\mathbf{k}\cdot\mathbf{R}}$ (where $\mathbf{R} \rightarrow$ lattice translation vector), WFs can be constructed by using the equation below:

$$|\mathbf{R}n\rangle = \frac{V}{(2\pi)^3}\int_{BZ} d\mathbf{k}e^{-i\mathbf{k}\cdot\mathbf{R}}|\psi_{n\mathbf{k}}\rangle \tag{1.70}$$

Where the Dirac notation $|\mathbf{R}n\rangle$ refers to the WF $w_{n\mathbf{R}}$ in cell $\mathbf{R}$ associated with band $n$.

The Bloch functions and the Wannier functions are related by Fourier transform:

$$|\psi_{n\mathbf{k}}\rangle = \sum_{\mathbf{R}} e^{i\mathbf{k}\cdot\mathbf{R}}|\mathbf{R}n\rangle \tag{1.71}$$

The problem is that the WFs that are obtained via the above formula are not unique, because of the fact that $\psi_{n\mathbf{k}}$ possesses "gauge freedom" which means that a certain Bloch function could be constructed by any real function that is periodic in the reciprocal space. So while Fourier transforming from Bloch function to Wannier function, for the same wavevector, it could be possible that there exists different WFs.

The task of constructing $N$ WFs from a set of isolated bands becomes greatly difficult. The expression for WFs for this case can written as shown below:

$$|\mathbf{R}n\rangle = \frac{V}{(2\pi^3)}\int_{BZ} d\mathbf{k}e^{-i\mathbf{k}\cdot\mathbf{R}}\left[\sum_{m=1}^{N} U_{mn}^{(\mathbf{k})}|\psi_{m\mathbf{k}}\rangle\right] \tag{1.72}$$

But there are infinitely many Unitary transformations. This "non-uniqueness" posed a great challenge making the construction of the WFs very difficult.

To solve this problem of non-uniqueness, many localization procedures were introduced to fix U. A widely used approach to localize the WFs has been developed by Marzari and Vanderbilt and the resulting functions are termed as "Maximally Localized Wannier Functions" [45]. There are other approaches to obtain a well-localized WFs like the WFs by projection technique [46, 47, 48].

The broad picture is that, a quantity that measures the sum of the quadratic spreads of the $N$ MLWFs in the unit cell around their centers, called the Localization functional is defined. The goal is to find the Unitary matrix that minimizes this localization functional. The localization functional is defined as given below:

$$\Omega = \sum_{n}\left[\langle\mathbf{0}n|r^2|\mathbf{0}n\rangle - \langle\mathbf{0}n|\mathbf{r}|\mathbf{0}n\rangle^2\right]$$

$$= \sum_n \left[ \langle r^2 \rangle_n - \mathbf{r^2}_n \right] \tag{1.73}$$

The localization functional measures the sum of the quadratic spread of the WFs around their centers. The choice of the localization functional is in such a way that it is decomposed into a "gauge-invariant" part and a "gauge-variant" part. Gauge invariance means that the quantity is invariant under any Unitary transformation. Hence, the minimization means that it is the "gauge-variant" part that is actually minimized. For practical purposes, the localization functional has to be converted into its equivalent Bloch space representation.

The localization functional is written as :

$$\Omega = \Omega_I + \tilde{\Omega} \tag{1.74}$$

Where $\Omega_I \rightarrow$ Gauge-invariant part and $\tilde{\Omega} \rightarrow$ Gauge-variant part and they are written as shown below:

$$\Omega_I = \sum_n \left[ \langle \mathbf{0}n|\mathbf{r}^2|\mathbf{0}n \rangle - \sum_{\mathbf{R}m} |\langle \mathbf{R}m|\mathbf{r}|\mathbf{0}n \rangle|^2 \right] \tag{1.75}$$

$$\tilde{\Omega} = \sum_n \sum_{\mathbf{R}m \neq \mathbf{0}n} |\langle \mathbf{R}m|\mathbf{r}|\mathbf{0}n \rangle|^2 \tag{1.76}$$

For practical purposes, it is important to convert the useful quantities into equivalent Bloch representation. The matrix elements of the position operator between WFs take the form as shown by Blount are given as [49]:

$$\langle \mathbf{R}n|\mathbf{r}|\mathbf{0}m \rangle = i\frac{V}{(2\pi)^3} \int d\mathbf{k} e^{i\mathbf{k}\cdot\mathbf{R}} \langle u_{n\mathbf{k}}|\nabla_{\mathbf{k}}|u_{m\mathbf{k}} \rangle \tag{1.77}$$

and

$$\langle \mathbf{R}n|\mathbf{r}^2|\mathbf{0}m \rangle = -\frac{V}{(2\pi)^3} \int d\mathbf{k} \int d\mathbf{k} e^{i\mathbf{k}\cdot\mathbf{R}} \langle u_{n\mathbf{k}}|\nabla_{\mathbf{k}}^2|u_{m\mathbf{k}} \rangle \tag{1.78}$$

Where $\langle u_{n\mathbf{k}}|$ stands for Bloch orbitals that were calculated on a regular k-point mesh. The important step now is to determine the reciprocal space derivatives. The information on the reciprocal space derivatives are encoded in the overlaps $M_{mn}^{(\mathbf{k},\mathbf{b})}$ between the Bloch orbitals at neighbouring k-points,

$$M_{mn}^{(\mathbf{k},\mathbf{b})} = \langle u_{m\mathbf{k}}|u_{n,\mathbf{k}+\mathbf{b}} \rangle \tag{1.79}$$

## 1.8 Tight-Binding model and Maximally Localized Wannier Functions

The different terms involved should be expressed in terms of the overlaps. The Marzari-Vanderbilt expressions for $\mathbf{r}_n$ and $\langle \mathrm{r}^2 \rangle_n$ are given as,

$$\mathbf{r}_n = -\frac{1}{N} \sum_{\mathbf{k},\mathbf{b}} \mathrm{w}_b \mathbf{b} Im \ln \mathrm{M}_{nm}(\mathbf{k}, \mathbf{b}) \tag{1.80}$$

$$\langle \mathrm{r}^2 \rangle_n = \frac{1}{N} \sum_{\mathbf{k},\mathbf{b}} \mathrm{w}_b \left( \left[ 1 - |\mathrm{M}_{nn}^{(\mathbf{k},\mathbf{b})}|^2 \right] + \left[ Im \ln \mathrm{M}_{nn}^{(\mathbf{k},\mathbf{b})} \right]^2 \right) \tag{1.81}$$

The gauge invariant and the gauge-variant terms are written as:

$$\Omega_I = \frac{1}{N} \sum_{\mathbf{k},\mathbf{b}} \mathrm{w}_b \left( J - \sum_{mn} |\mathrm{M}_{mn}^{(\mathbf{k},\mathbf{b})}|^2 \right) \tag{1.82}$$

Where the band indices $m$,$n$ run from 1 to $J$. and

$$\tilde{\Omega} = \frac{1}{N} \sum_{\mathbf{k},\mathbf{b}} \mathrm{w}_b \sum_{m \neq n} |\mathrm{M}_{mn}^{(\mathbf{k},\mathbf{b})}|^2 + \frac{1}{N} \sum_{\mathbf{k},\mathbf{b}} \mathrm{w}_b \sum_n \left( -Im \ln \mathrm{M}_{mn}^{(\mathbf{k},\mathbf{b})} - \mathbf{b} \cdot \mathbf{r}_n \right)^2 \tag{1.83}$$

The main goal is to find the Unitary matrix that minimizes the localization functional. This involves an updating of the Unitary matrices in order to reach the minimum. To begin with, all the $\mathrm{U}_{mn}^{\mathbf{k}}$ are initialized to $\delta_{mn}$. Through the steepest descent procedure, $\Delta \mathrm{W}$ (infinitesimal anti-Hermitian Unitary matrix) is calculated for a small step in the direction opposite to the gradient defined by

$$\mathrm{G}^{\mathbf{k}} = \frac{d\Omega}{d W^{\mathbf{k}}} = 4 \sum_b \mathrm{w}_b \left( \mathbb{A} \left[ \mathrm{R}^{(\mathbf{k},\mathbf{b})} \right] - \mathbb{S} \left[ \mathrm{T}^{(\mathbf{k},\mathbf{b})} \right] \right) \tag{1.84}$$

Where $\mathbb{A}$ and $\mathbb{S}$ are superoperators defined as $\mathbb{A}[B] = (B-B^\dagger)/2$ and $\mathbb{S}[B]=(B+B^\dagger)/2i$. After each step described above, the Unitary matrices are updated according to ,

$$\mathrm{U}^{(\mathbf{k})} \rightarrow \mathrm{U}^{\mathbf{k}} \exp[\Delta \mathrm{W}^{(\mathbf{k})}] \tag{1.85}$$

and the overlaps are also updated accordingly as,

$$\mathrm{M}^{(\mathbf{k},\mathbf{b})} = \mathrm{U}^{(\mathbf{k})\dagger} \mathrm{M}^{(0)(\mathbf{k},\mathbf{b})} \mathrm{U}^{(\mathbf{k}+\mathbf{b})} \tag{1.86}$$

It could be possible that the localization functional could display multiple local minima. In order to avoid these, Marzari-Vanderbilt procedure involves the preparation of a set of reference Bloch orbitals $|u_{n\mathbf{k}}^{(0)}\rangle$ by projection from a set of initial trial orbitals $g_n(\mathbf{r})$ corresponding to some very rough initial guess $g_n(\mathbf{r})$ for the WFs.

The above procedure outlined is when we are starting with a set of isolated bands. But there is another case where we start with a set of entangled bands. Entangled bands are those bands which lie within a limited energy range but overlap and hybridize with other bands which extend further out in energy.

The entangled bands are difficult to treat because, it is not clear exactly which states to choose initially that could form the correct set of WFs. In this case, before applying the localization procedure, some prescription for constructing $N$ WFs from a large band-manifold for each k-point is to be formulated. The computation of constructing well-localized WFs starting from entangled bands are broken down into 2 steps: 1. Subspace selection [50] 2. Gauge selection. In the subspace selection step, a smooth Bloch manifold is constructed. In the gauge selection step, the constructed subspace is represented using a set of $N$ Bloch functions (now smooth functions of $\mathbf{k}$ ) such that the corresponding WFs are well localized.

To choose smoothly varying Bloch-like states, starting from a larger set of Bloch bands, we employed energy windows. The procedure is as follows: Starting from a set of $N$ localized trial orbitals $g_n(\mathbf{r})$, they are projected onto the space spanned by the chosen eigenstates at each $\mathbf{k}$,

$$|\phi_{n\mathbf{k}}\rangle = \sum_{m=1}^{Q_{\mathbf{k}}} |\psi_{m\mathbf{k}}\rangle\langle\psi_{m\mathbf{k}}|g_n\rangle \tag{1.87}$$

$(Q_{\mathbf{k}} \geq N)$
The resulting orbitals are then orthonormalized to produce a set of N smoothly-varying Bloch-like states across the BZ,

$$|\tilde{\psi}_{n\mathbf{k}}\rangle = \sum_{m=1}^{N} \frac{|\phi_{m\mathbf{k}}\rangle}{\langle\phi_{m\mathbf{k}}|\phi_{n\mathbf{k}}\rangle^{1/2}} \tag{1.88}$$

This procedure simultaneously achieves the goals of subspace selection and gauge selection. The gauge selection can be further refined by minimizing $\tilde{\Omega}$ within the projected subspace.

## 1.8.3 Downfolding

Combination of the FP and MH involves the construction of effective Hamiltonian from first principles. The basic idea of the **downfolding** method is to calculate the renormalization effect to the low-energy degrees of freedom caused by the
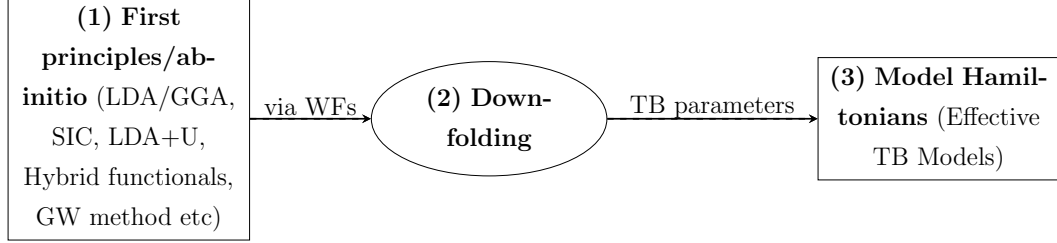
**Figure 1.2:** Schematic flowchart showing the scheme used in this work to combine the FP and MH approaches.

elimination of the high-energy ones. In many strongly correlated materials, there exists a well-defined group of bands near the Fermi level which are isolated from the bands away from the Fermi level. In TMOs, this group consists of the bands whose main component is $3d$ orbitals at the transition metal atoms. The low energy degrees of freedom may be further restricted to either $t_{2g}$ or $e_g$ orbitals only, if the crystal-field splitting is large as in many cases with perovskite TMOs like $SrVO_3$ or $LaMnO_3$. In general, a complete basis set can be constructed from the basis functions of the Hamiltonian obtained by ignoring the el-el interaction. In this basis, the second quantized total Hamiltonian of electrons equivalent to the electronic part of the full Hamiltonian is written as,

$$H[c^\dagger, c] = \sum_{\mu,\nu} h_K(\mu, \nu)c_\mu^\dagger c_\nu + \sum_{\mu,\mu',\nu,\nu'} h_V(\mu, \mu', \nu, \nu')c_\mu^\dagger c_{\mu'}^\dagger c_\nu c_{\nu'} \qquad (1.89)$$

The above Hamiltonian is nothing but the Hubbard Hamiltonian written using a different notation (Refer to Eqn.**??**). The first term represents the kinetic energy which includes the one-body term and the second term is the Coulomb interaction in the present basis representation with the electronic degrees of freedom $\mu$. If one employs the basis of LDA eigenfunctions for KS equation, then $\mu$ denotes a LDA band, spin and momentum. The first step of the downfolding procedure i.e. to derive the low-energy effective model, we have to construct a set of localized orbitals that span the Hilbert space of the low energy electronic states. There are many ways to obtain these localized orbitals, one of which is MLWFs [45], [50] which was discussed in the previous section. An alternative approach to finding the Wannier orbitals is the Anderson Wannier orbitals. MLWFs are more general because it does not depend on any particular bandstructure calculation method. Although Wannier orbitals could be chosen in an arbitrary way, it is better to find

maximally localized orbitals to make the range of transfers and interactions in the effective lattice models as short as possible. Once the bands are downfolded and the effective Hamiltonian is obtained, the last step is to solve this Hamiltonian. For solving the Hamiltonian, DMFT, VMC etc. are usually employed.

A schematic representation of the whole procedure (as employed in this thesis) is illustrated in the Fig.1.2. The illustration provided in the Fig.1.2 could be described as follows: Electronic structure methods are basically divided into two categories: FP and MH approaches. Starting from FP methods like the PBE, PBE+U, Hybrid functionals and GWA, a set of bands (for eg. the *3d* correlated subspace of $Mn^{3+}$ of $R$MnO$_3$) are downfolded via MLWFs. TB parameters corresponding to an effective TB model Hamiltonian are extracted from the MLWFs.

In this thesis, we will discuss the TB parametrization obtained by starting from DFT, DFT+U, Hybrid functionals and GW. The reason for this is explained in the follwoing: The quality and characteristics of the Wannier representation inevitably depend on the underlying Kohn-Sham states. It is well known that the mean-field-type one-particle description of the electronic structure within the standard LDA [51] or GGA [27] approximations to DFT is incapable to correctly describe exchange and correlation effects in the so called *strongly-correlated materials*, resulting, among other failures in much too small band gaps and magnetic moments [1]. It has been noted that the underestimation of the band gap and related failures are of course also partly due to the intrinsic limitation of the KS approach, which is not meant to describe quasi-particle excitations correctly. For this reason, the DFT-derived subset of orbitals is typically employed as reference for the one-electron (i.e. non-interacting) part of the effective Hamiltonian, where all approximated contributions coming from LDA/GGA exchange-correlation effects are subtracted in order to avoid double-counting. For example, in the DFT+DMFT method [52], the effective Hamiltonian can be written as $\hat{H} = \hat{H}_{DFT} - \hat{H}_{dc} + \hat{H}_U$, where $\hat{H}_{DFT}$ is the KS Hamiltonian, $\hat{H}_{dc}$ accounts for the double-counting correction, and $\hat{H}_U$ represents the Hubbard-like term which describes the electronic interactions in the strongly correlated bands. A critical issue of the DFT+DMFT approach is that a well defined expression for the double-counting potential is not known and several forms have been suggested. Karolak and coworkers have recently addressed this issue by treating the double-counting term as an adjustable parameter and suggested that the best agreement with experiment is achieved by setting the double-counting potential in the middle of the gap of the impurity spectral function [53]. Within this context, it is therefore justified to construct effective Hamiltonians starting from band structures

obtained using different schemes, such as e.g. LDA+$U$ [54] or hybrid functionals, which usually provide much better gaps for semiconducting materials than conventional DFT approximations and could therefore represent a more appropriate "non-interacting" reference for model calculations.

### 1.8.4 MLWFs $\Rightarrow$ TB parameters

In this section we will discuss how the MLWFs and TB Hamiltonian are connected so that we could obtain the TB parameters from the MLWFs.

A set of $N$ localized WFs $|w_{n\mathbf{T}}\rangle$ corresponding to a group of $N$ bands that are described by delocalized Bloch states $|\psi_{m\mathbf{k}}\rangle$ is defined by the following transformation:

$$|w_{n\mathbf{T}}\rangle = \frac{V}{(2\pi)^3} \int_{BZ} \mathrm{d}\mathbf{k} \left[ \sum_{m=1}^{N} U_{mn}^{(\mathbf{k})} |\psi_{m\mathbf{k}}\rangle \right] \mathrm{e}^{-i\mathbf{k}\cdot\mathbf{T}} , \qquad (1.90)$$

where $\mathbf{T}$ is the lattice vector of the unit cell associated with the WF, $m$ is a band index, $\mathbf{k}$ is the wave-vector of the Bloch function, and the integration is performed over the first Brillouin zone (BZ) of the lattice. Different choices for the unitary matrices $\mathbf{U}^{(\mathbf{k})}$ lead to different WFs, which are thus not uniquely defined by Eqn.1.90. A unique set of MLWFs can be generated by minimizing the total quadratic spread of the Wannier orbitals as already discussed in Sec.1.8.2 [45].

After obtaining a set of MLWFs, the corresponding Hamiltonian matrix, $\mathrm{H}^{(W)}(\mathbf{k})$ is constructed by a Unitary transformation,

$$H^{(W)}(\mathbf{k}) = (U^{(\mathbf{k})})^{\dagger} H^{(B)}(b)(U^{(\mathbf{k})}) \qquad (1.91)$$

from the diagonal Hamiltonian matrix in the Bloch basis, $\mathrm{H}_{nm}^{(B)}(\mathbf{k}) = \varepsilon_{n\mathbf{k}}\delta_{nm}$ with the eigenvalues $\varepsilon_{n\mathbf{k}}$.

Once the transformation matrices $\mathbf{U}^{(\mathbf{k})}$ are determined, a TB representation of the Hamiltonian in the basis of MLWFs is obtained:

$$\hat{H} = \sum_{\mathbf{T},\Delta\mathbf{T}} h_{nm}^{\Delta\mathbf{T}} \hat{c}_{n\mathbf{T}+\Delta\mathbf{T}}^{\dagger} \hat{c}_{m\mathbf{T}} + \mathrm{h.c.} , \qquad (1.92)$$

with

$$h_{nm}^{\mathbf{T}} = \frac{V}{(2\pi)^3} \int_{B} Z\mathrm{d}\mathbf{k} \left[ \sum_{l} \left( U_{ln}^{(\mathbf{k})} \right)^{*} \epsilon_{l\mathbf{k}} U_{lm}^{(\mathbf{k})} \right] \mathrm{e}^{-i\mathbf{k}\cdot\mathbf{T}} . \qquad (1.93)$$

Here, $\epsilon_{l\mathbf{k}}$ is the eigenvalue corresponding to Bloch function $|\psi_{l\mathbf{k}}\rangle$. We note that $\mathbf{T}$ and $\Delta\mathbf{T}$ in Eqns.1.90-1.93 indicate lattice translations, whereas for crystal

structures with more than one atom per unit cell, $n$ and $m$ generally represent combined orbital, spin, and site indices, specifying the various orbitals at all sites within the primitive unit cell.

## 1.9 Electronic structure calculations using VASP

All the calculations (PBE,HSE and GW) presented in this work has been done using VASP (Vienna Ab-initio Simulation Package). VASP is a complex ab-initio simulation package that performs simulation using pseudopotentials or the projector-augmented wave (PAW) method within a plane wave basis set [55], [56], [57], [58]. In VASP, the four essential input files are INCAR, POSCAR, POTCAR and KPOINTS. INCAR file is a tagged free-format ASCII file that determines "what to do and how to do it". POSCAR file contains the position of the ions. KPOINTS file determines the kpoint settings. POTCAR contains the pseudopotential and the information about the atoms. VASP uses a self-consistent cycle with a Pulay mixer and iterative matrix diagonalisation scheme to calculate the KS ground state. At each electronic step the wavefunctions are iteratively improved and the charge density is refined.

We will discuss the basic ideas behind implementation of the theory in practise and PAW method under this section. In a one-particle theory like KS-DFT or HF, the task of finding the solution to the many-body problem i.e. $\psi\left(\mathbf{r}_1, \mathbf{r}_2, \cdots, \mathbf{r}_N\right)$ is reduced to calculating $\psi_{n\mathbf{k}}\left(\mathbf{r}\right)$ at a discrete set of kpoints $\mathbf{k}$ in the first BZ, for a number of bands that are of the order of the number of electrons in a unit cell. Each electronic state $|\psi_{n\mathbf{k}}\rangle$ obeys the Bloch theorem which is given as,

$$\psi_{n\mathbf{k}}(\mathbf{r} + \mathbf{R}) = \psi_{n\mathbf{k}}(\mathbf{r})\mathrm{e}^{i\mathbf{k}\cdot\mathbf{R}} \tag{1.94}$$

Where $\mathbf{R}$ is the translational lattice vector that leaves the Hamiltonian invariant. Therefore the problem is transferred from the real space to the reciprocal space (momentum space/k-space). The problem of infinite number of electrons in the real space is now mapped on to the problem of expressing the wavefunction in terms of an infinite number of reciprocal space vectors within the first Brillouin zone $\mathbf{k}$. In practice, it is not possible to deal with an infinite number of vectors. This problem could be solved by sampling the BZ at special set of kpoints. Sampling of k-points could be done by various methods, popular methods being the

Monkhorst-Pack and the Chadi-Cohen methods [59, 60]. The total wavefunction at each point is expressed in terms of a discrete plane-wave basis set given as,

$$\psi_{n\mathbf{k}}(\mathbf{r}) = \frac{1}{\Omega^{1/2}} \sum_{\mathbf{G}} C_{\mathbf{G}} n\mathbf{k} e^{i(\mathbf{G}+\mathbf{k})\mathbf{r}} \qquad (1.95)$$

where $\psi_{n\mathbf{k}}(\mathbf{r})$ is the Bloch wavefunction, $\Omega$ is the volume of the first BZ, $\mathbf{k}$ is the wavevector and $\mathbf{G}$ the reciprocal lattice vector. Other important quantities are the charge density of an electron which is given as,

$$n(\mathbf{r}) = \sum_{\mathbf{G}} n_{\mathbf{G}} e^{i\mathbf{G}\mathbf{r}} \qquad (1.96)$$

and the potential

$$V(\mathbf{r}) = \sum_{\mathbf{G}} V_{\mathbf{G}} e^{i\mathbf{G}\mathbf{r}} \qquad (1.97)$$

which also are expanded in a plane-wave basis set. In principle, the plane-wave basis set must be infinite in number, but it could be considered converged for large values of $(\mathbf{G}+\mathbf{k})$ in practise by introducing an energy cut-off, given as

$$\frac{1}{2}|\mathbf{G} + \mathbf{k}| < E_{cutoff} \qquad (1.98)$$

The energy cut-off depends on the system that one is working with and therefore it becomes necessary to test the convergence of the energy for a given cut-off value. Using plane waves, both the vacuum and the high-density regions have been forced to be described with high accuracy and therefore a large number of plane waves are necessary. There are 2 distinct regions in an atom/molecule/solid: (1)Region near the nuclei (large potential): where the one-electron wavefunction $\psi$ oscillates rapidly (2) Interstitial region (small potential) : where $\psi$ oscillates slowly. Plane waves are convenient but they fail to describe the region efficiently where the one-electron wavefunction oscillates rapidly and too many plane waves are needed in order to circumvent this problem. To treat these regions while solving DFT equations, two different traditional approaches have been introduced:

- All-electrons approaches (using exact potentials) such as the augmented plane wave methods (Eg. Full potential Linear Augmented Wave (FLAPW) method) which is very accurate but expensive.

- Pseudopotential approach which is less accurate but inexpensive.

In the FLAPW method, the region near the nuclei is described by radial function and spherical harmonics, whereas PW are used in the interstitial part. The partial solutions of the different regions are matched with value and derivative at the interface between atomic and interstitial regions.

The pseudopotential approach was first introduced by Hans Hellmann in 1934. The basic idea of pseudopotentials is to replace the strong Coulomb potential of the nucleus and the effects of the tightly bound core electrons by an effective ionic potential acting on the valence electrons (Fig.1.3). This idea is justifiable because in most materials the core electrons do not contribute to bonding. The
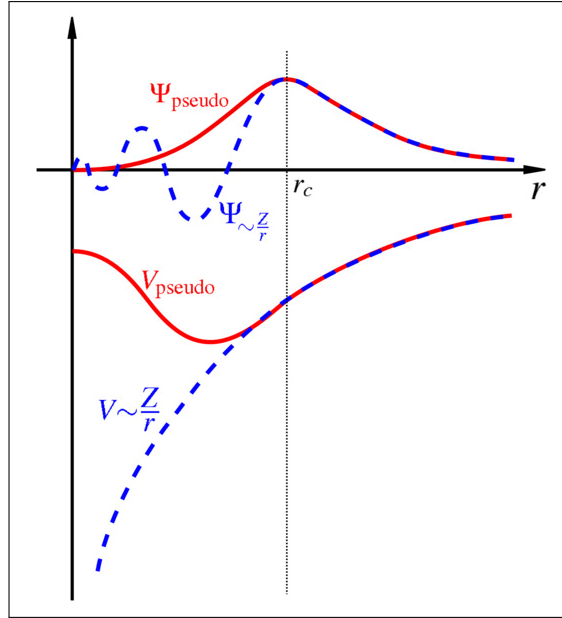


**Figure 1.3:** Figure showing pseudopotentials.

price to pay when using pseudopotentials is that all information on the charge density and the wavefunctions near the nucleus is lost. An efficient alternative to FLAPW and PP approaches is the PAW method.

The PAW method which was first introduced by Blöchl is a combination of the augmented plane wave methods and the pseudopotential approach, which incorporates their fundamental aspects into a unified electronic structure method.

As already mentioned, the valence wavefunctions tend to have rapid oscillations near the ion cores due to the requirement that they have to be orthogonal to the core states. This is problematic because many Fourier components are required to describe the one-elctron wavefunctions accurately. In the PAW

method, the problem is addressed by transforming these rapidly oscillating wave-functions into smooth wavefunctions that are more computationally convenient. The all-electron wavefunction is written as a linear transformation of a pseudo wavefunction (PS WF) and the linear transformation that transforms the pseudo wavefunction $|\tilde{\psi}\rangle$ to the all-electron wavefunction $|\psi\rangle$ is given as,

$$|\psi\rangle = T|\tilde{\psi}\rangle \tag{1.99}$$

and transformation $T$ is given as,

$$T = 1 + \sum_{\mathbf{R}} \hat{T}_{\mathbf{R}} \tag{1.100}$$

where $\hat{T}_{\mathbf{R}}$ is non-zero only within some spherical augmentation $\Omega_{\mathbf{R}}$ enclosing atom $\mathbf{R}$. The true wavefunction is written in terms of partial waves and for each partial wave $\phi_i$, a pseudo partial wave $\tilde{\phi}_i$. '$i$' refers to the atomic site $\mathbf{R}$, the angular quantum numbers $(l,m)$ with an additional index that labels the different partial waves at that site. Within the augmentation region, every pseudo wavefunction is expanded into pseudo partial waves:

$$|\tilde{\psi}\rangle = \sum_i |\tilde{\phi}_i\rangle c_i \tag{1.101}$$

$$|\phi_i\rangle = T|\tilde{\phi}_i\rangle \tag{1.102}$$

The all-electron WF is expressed as

$$|\psi\rangle = |\tilde{\psi}\rangle + \sum_i |\phi_i\rangle c_i - \sum_i \tilde{\phi}_i c_i \tag{1.103}$$

where $c_i$ is to be determined. $c_i$ is given as

$$c_i = \langle \tilde{p}_i|\tilde{\psi}\rangle \tag{1.104}$$

where $\langle \tilde{p}_i|$ represents the projector functions . According to Blöch's formulation, the projector function is defined as

$$\langle \tilde{p}_i| = \sum_j \left( \left[ \langle f_{\mathbf{k}}|\tilde{\phi}_l\rangle \right] \right)^{-1}_{ij} \langle f_j| \tag{1.105}$$

The all-electron partial waves $|\phi_i\rangle = T|\tilde{\phi}_i\rangle$ are typically chosen to be solutions to the KS SE for an isolated atom. The transformation $T$ is thus specified by

a set of all-electron partial waves $|\phi_i\rangle$, set of pseudo partial waves $|\tilde{\phi}_i\rangle$ and a set of projector functions $\langle\tilde{p}_i|$. Outside the augmentation region, the pseudo partial waves are equal to the all-electron partial waves and inside they could be any smooth function such as combination of polynomials or Bessel's functions.

### 1.9.1   VASP2WANNIER90 interface

In this section, we will discuss the practical instructions for the use of VASP2WANNIER90. VASP uses WANNIER90 in library mode to generate all ingredients which are required to run the wannier90 code as a post-processing tool. The main input file for wannier90 code is the wannier90.win. Apart from this file, the other main input files are (i) the overlaps between the cell periodic parts of the Bloch states (wannier90.mmn), (ii) the projections of the Bloch states onto the trial localized orbitals (wannier90.amn) and (iii) the eigenvalues file (wannier90.eig). These files are generated by VASP by setting LWANNIER90 = .TRUE. in the main VASP input file (INCAR). These files are generated provided that the instructions for a given problem is specified in the wannier90.win file. If the wannier90.win file is not already present, then VASP generates the file wannier90.win and this has to be then modified according to the problem under consideration following the instructions given in the wannier90 code manual and then on rerunning VASP with the modified wannier90.win file, the other input files for the wannier90 run (i-iii) are generated. To construct the UNK files (the periodic part of the Bloch states represented on a regular real space grid) that are required in order to plot the MLWFs, it is necessary to set LWRITE_UNK = .TRUE. in the IN-CAR file. In a spin-polarized calculation two sets of input files are generated. VASP2WANNIER90 is employed only once to generate the files wannier90.mmn, wannier90.amn and wannier90.eig.

An example of the input wannier file wannier90.win (LaMnO$_3$ Experimental *Pbnm* structure (majority spin channel) ) is given below:

```
num_wann=4

num_bands=112

Begin Projections

f=0.5,0.0,0.25:l=2,mr=1,4:z=0,0,1:x=1,1,0

f=0.0,0.5,0.25:l=2,mr=1,4:z=0,0,1:x=1,1,0

End Projections
```

```
dis_win_min =8.2
dis_win_max = 11.3
dis_num_iter = 1000
guiding_centres=true
# BS flags
bands_plot = true
begin kpoint_path
T -0.5 0.0 0.5 Z 0.0 0.0 0.5
Z 0.0 0.0 0.5 G 0.0 0.0 0.0
G 0.0 0.0 0.0 M 0.5 0.5 0.0
M 0.5 0.5 0.0 A 0.5 0.5 0.5
end kpoint_path
begin unit_cell_cart
5.5391978 0.0000000 0.0000000
0.0000000 5.6990978 0.0000000
0.0000000 0.0000000 7.7174968
end unit_cell_cart
begin atoms_cart
La 2.8048792 3.0974585 3.8587484
La 0.0352803 5.4511882 0.0000000
La 2.7343187 2.6016393 0.0000000
La 5.5039176 0.2479096 3.8587484
Mn 2.7695989 0.0000000 1.9293742
Mn 0.0000000 2.8495489 1.9293742
Mn 2.7695989 0.0000000 5.7881226
Mn 0.0000000 2.8495489 5.7881226
O 2.3635790 5.6381181 3.8587484
O 5.1331779 2.9105287 0.0000000
O 3.1756188 0.0609798 0.0000000
O 0.4060199 2.7885691 3.8587484
O 4.0197981 1.7177092 2.2264940
```

```
O 1.2501992 1.1318397 1.6322544
O 1.5193997 3.9813886 6.0852424
O 4.2889981 4.5672582 5.4910028
O 1.5193997 3.9813886 1.6322544
O 4.2889981 4.5672582 2.2264940
O 4.0197981 1.7177092 5.4910028
O 1.2501992 1.1318397 6.0852424
end atoms_cart

mp_grid = 4 4 4
begin kpoints
0.0000000 0.0000000 0.0000000
0.2500000 0.0000000 0.0000000
0.5000000 0.0000000 0.0000000
0.0000000 0.2500000 0.0000000
 .
 .
 .
-0.2500000 -0.5000000 -0.5000000
end kpoints
```

We have so far discussed the underlying theory for this thesis work i.e. Combination of FP and MH via MLWFs (FP $\Rightarrow$ MLWFs $\Rightarrow$ TB (MH)). We will discuss the application of the theory to LaMnO$_3$ and then to RMnO$_3$ in the subsequent chapters.

# Chapter 2

# FP+MH study: LaMnO$_3$

We discussed the theory part behind this work (PBE, Hybrid Functionals, GW method, LDA+U), MLWFs, TB method and the combination of the FP and MH in the previous chapter. In this chapter, we will discuss the application of the FP $\Rightarrow$ MLWFs $\Rightarrow$ MH approach (Refer to the schematic representation (Fig. 1.2) given in Chapter 2) to the widely studied antiferromagnetic insulator, LaMnO$_3$.

## 2.1    Introduction

A prototypical textbook example of perovskite TMOs is the antiferromagnetic insulator LaMnO$_3$. The ground state electronic structure of LaMnO$_3$ is characterized by the crystal-field induced breaking of the degeneracy of the Mn$^{3+}$ 3$d^4$ manifold in the high-spin configuration $(t_{2g})^3(e_g)^1$, with the $t_{2g}$ orbitals lying lower in energy than the two-fold degenerate $e_g$ ones. Due to the non-spherical symmetric crystal field (surrounding oxygen octahedra), the point charges of the ligands interact with the $d$-metal ions and therefore the degeneracy of the 3$d$ orbitals is lifted. As a general rule of thumb, the electrostatic energy is increased for the $d$ orbitals oriented towards the region of high electron density and vice versa. The $e_g$ orbitals are directly pointing towards the oxygen ligands whereas the $t_{2g}$ electrons are pointing between the oxygen ligands so that these electrons have an energy which is less affected by the Coulomb interactions between the Mn$^{3+}$ $3d$ electrons and the oxygen $2p$ electrons than the $e_g$ electrons. Thus, the $e_g$ electrons have an energy raised by this Coulomb interaction. Due to the strong Hund's rule coupling, the spins of the fully occupied majority $t_{2g}$ orbitals (S=3/2) are aligned

parallel with the spin of the singly occupied majority $e_g$ states (S=1/2) on the same site. The orbital degeneracy in the $e_g$ channel is further lifted via cooperative Jahn-Teller (JT) distortions [61, 62, 63, 64], manifested by long and short Mn-O octahedral bonds alternating along the conventional orthorhombic basal plane (See Fig.2.3), which are accompanied by GdFeO$_3$-type (GFO) checkerboard tilting and rotations of the oxygen octahedra [65, 66, 67]. As a result, the ideal cubic perovskite structure is strongly distorted into an orthorhombic structure with *Pbnm* symmetry [65, 66] and it has been experimentally confirmed that the orbital ordering is of C-type where two kinds of orbitals are alternately aligned in the $xy$-plane and the planes are stacked along the $z$ axis [68]. The corresponding occupied $e_g$ orbital can be written as $|\theta\rangle = \cos\frac{\theta}{2}|3z^2-r^2\rangle + \sin\frac{\theta}{2}|x^2-y^2\rangle$ [54, 69, 70, 71], with the sign of $\theta \sim 108°$ alternating along $x$ and $y$ and repeating along $z$. This particular orbital ordering is responsible for the observed A-type antiferromagnetic arrangement below $T_N = 140$ K [65, 72]. It was found that long-range order disappears above 750 K, whereas a local JT distortion (without long-range order) remains (dynamically) active up to $> 1150$ K [63, 64, 70]. Figure 2.1 shows the various structural distortions as mentioned above. The ideal cubic perovskite structure (Fig.2.1(a)) requires a single unit cell whereas the other structures (JT, GFO and experimental *Pbnm*) (Fig.2.1(b)-(d)) requires two unit cells. The orbital and the spin-ordering features along the $c$ axis corresponding to the orthorhombic structure of LaMnO$_3$ (taken from Ref.[9]) is shown in Fig.2.1(e). It could be seen that the orbital and the spin ordering along the $c$ axis is of staggered and uniform order.

To get an overall picture of the electronic structure of LaMnO$_3$, an orbital energy diagram representation of the Mn(3$d$) states and O($p$) states in LaMnO$_3$ is presented in Fig.2.2(a). HSE bandstructure and the corresponding PDOS with Mn ($e_g$), Mn($t_{2g}$) and O($p$) characters are presented in Fig.2.2(b). The splitting of the Mn$^{3+}$ 3$d^4$ manifold into $t_{2g}$ and $e_g$ is shown in the non-spin polarized case (Fig.2.2(a)) and there is also a hybridization between the $e_g$ and O($p$) states. In the spin-polarized case, we show the Jahn-Teller distortion which reduces the symmetry from octahedral to tetragonal and breaks the degeneracy of the $e_g$ orbitals (both high and low spins) and opens a gap. In Fig.2.2(b), the orbital diagram representation is reflected in the HSE bandstructure and the corresponding PDOS. The four $e_g$ bands (represented by red filled area on the left panel) that lie near the Fermi level represent the local majority spin bands out of which 2 bands that lie below the Fermi level are occupied and the other 2 above the

**(a)** Ideal cubic perovskite structure

**(b)** Jahn-Teller distorted structure

**(c)** GdFeO$_3$ (GFO) distorted structure

**(d)** Experimental Pbnm structure

**(e)** Orbital and spin ordering in Experimental structure of LaMnO$_3$.
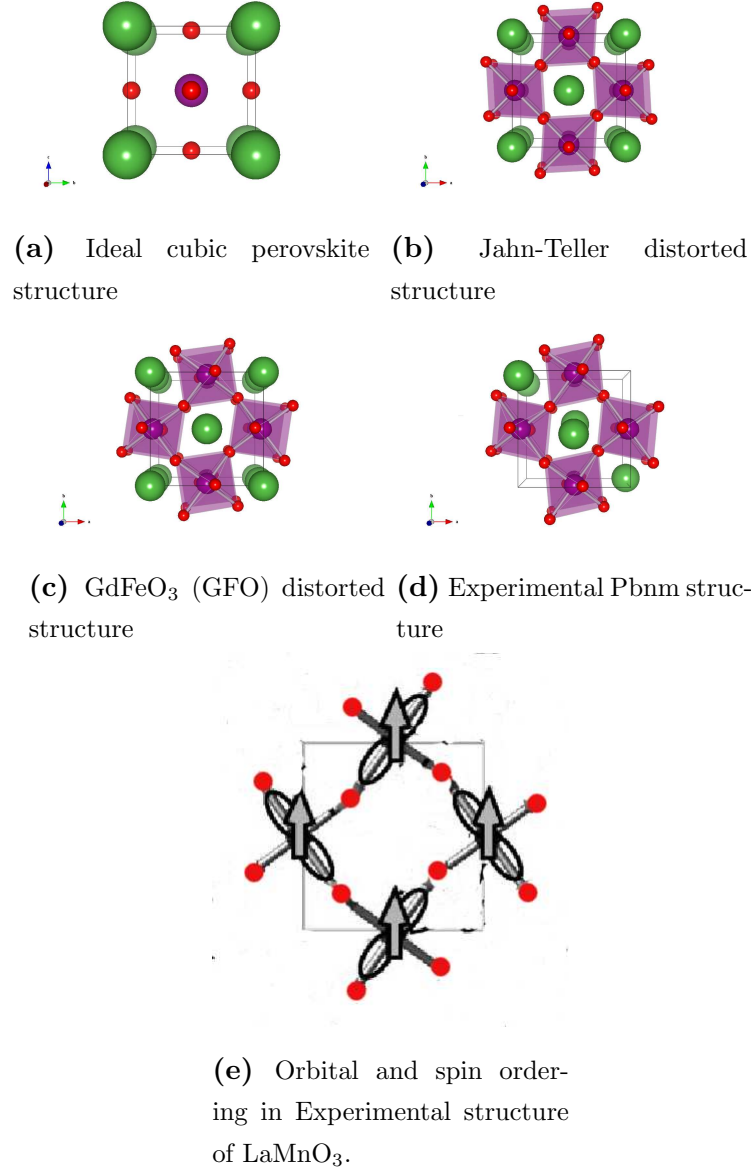
**Figure 2.1:** Different structural modifications of LaMnO$_3$ viewed along the z-direction. Ideal perovskite structure (a) requires a single unit cell, other structures ((b)-(d)) requires 2 unit cells. Pictures generated using VESTA [73]. (e) The orbital and the spin ordering as seen along the $c$ axis for the Experimental orthorhombic structure of LaMnO$_3$ (taken from Ref.[9]).

Fermi level are unoccupied (2 unit cells). It could be observed that the unoccupied local minority $e_g$ bands (red-filled area on the right panel) are strongly hybridized with the $t_{2g}$ bands (green lines) which is due to the tilting and rotation of the oxygen octahedra. There is obviously hybridization that is observed between the Mn($d$) and O($p$) (blue lines) states. A very elaborate discussion of the $ab-initio$ electronic bands at various levels of calculation follows later in this chapter. This picture has been presented to give an overall idea of the electronic states of LaMnO$_3$.

The question of whether the origin of orbital ordering should be attributed to a superexchange mechanism (O-mediated virtual hopping of electrons between nearest neighbor $S = 2$ Mn cations, associated with a local Coulomb electron-electron interaction: $d_i^4 d_j^4 \rightleftharpoons d_i^3 d_j^5$) or to an electron-lattice coupling effect (structural-induced splitting of the degenerate $e_g$ levels) [69] has been the subject of numerous studies [6, 54, 70, 74, 75, 76, 77, 78, 79, 80]. Considering that there is no clear experimental evidence to support one mechanism over the other, the employment of theoretical models and computer simulations has become an essential tool to explain the complicated coupling between structural and electronic degrees of freedom and to interpret the experimental observations. On the basis of model calculations, it has been recognized that the simultaneous inclusion of both superexchange and JT interactions is crucial to provide, to some extent, a satisfactory description of the observed transition temperatures $T_{\mathrm{N}}$, $T_{\mathrm{OO}}$ and $T_{\mathrm{JT}}$ [54, 70, 74]. This approach typically relies on a suitable mapping between a realistic band structure calculated e.g. via DFT [51] and an effective many-body Hamiltonian, which is often achieved by downfolding the relevant bands and constructing a localized Wannier basis [8, 32, 54, 70, 81].

As discussed in the previous chapter, the MLWFs can be used to extract an effective TB description of the $e_g$ subspace in LaMnO$_3$ [8, 81]. The calculated TB parameters can then be used to construct a simplified TB Hamiltonian in the form that is very often used for the description of manganites, $\hat{H}_{\mathrm{TB}} = \hat{H}_{\mathrm{kin}} + \hat{H}_{\mathrm{Hund}} + \hat{H}_{\mathrm{JT}} + \hat{H}_{\mathrm{e-e}}$, which then provides a very accurate representation of the underlying KS band structure.

In the following sections, we will describe the construction of the TB Hamiltonian for LaMnO$_3$ and we will present and interpret the obtained results.
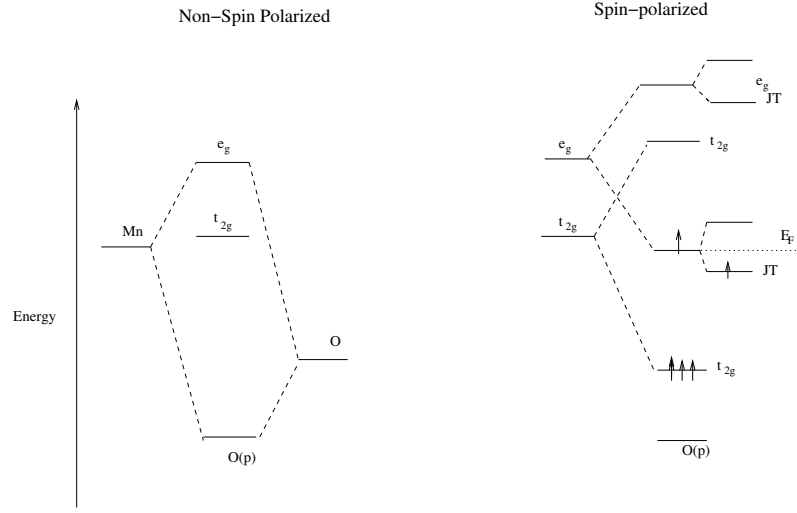
**(a)**
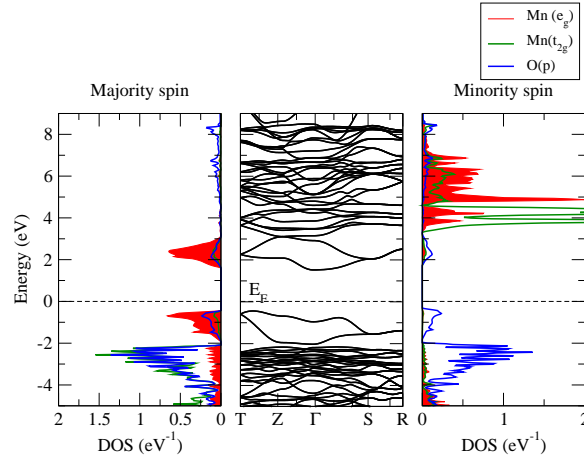


**(b)**

**Figure 2.2:** (a) An orbital diagram representation of the Mn($3d$) states and O($2p$) states in the experimental structure. (b) HSE bandstructure (black lines) and associated normalized PDOS (to the left and right of the band structure plots) of LaMnO$_3$ corresponding to Mn($e_g$) (red-filled areas), Mn($t_{2g}$) (green lines) and O($p$) character (blue dots). In the left/right PDOS plots, Mn($d$) PDOSs correspond to the local majority/minority Mn sites while the O($p$) PDOS is calculated as an average over all the sites.

## 2.2   TB Hamiltonian

The effective electronic Hamiltonian for the e$_g$ manifold in manganites is generally described within the TB formalism as a sum of the Kinetic energy $\hat{H}_{kin}$ and several local interaction terms such as the Hund's rule coupling to t$_{2g}$ core spin $\hat{H}_{Hund}$, the JT coupling to the oxygen octahedra distortion $\hat{H}_{JT}$, and eventually the *el-el* interaction $\hat{H}_{e-e}$, which can be written as,

$$\hat{H}_{\text{kin}} = -\sum_{a,b,\mathbf{R},\Delta\mathbf{R},\sigma} \hat{c}^{\dagger}_{\sigma,a(\mathbf{R}+\Delta\mathbf{R})} t_{\sigma,a(\mathbf{R}+\Delta\mathbf{R})b(\mathbf{R})} \hat{c}_{\sigma,b(\mathbf{R})} , \tag{2.1}$$

$$\hat{H}_{\text{Hund}} = -J_{\text{H}} \sum_{\mathbf{R}} \mathbf{S}_{\mathbf{R}} \sum_{a,\sigma,\sigma'} \hat{c}^{\dagger}_{\sigma,a(\mathbf{R})} \tau_{\sigma\sigma'} \hat{c}_{\sigma',a(\mathbf{R})} , \tag{2.2}$$

$$\hat{H}_{\text{JT}} = -\lambda \sum_{a,b,\mathbf{R},i,\sigma} \hat{c}^{\dagger}_{\sigma,a(\mathbf{R})} Q^{i}_{\mathbf{R}} \tau^{i}_{ab} \hat{c}_{\sigma,b(\mathbf{R})} , \tag{2.3}$$

$$\hat{H}_{\text{e-e}} = \frac{1}{2} \sum_{a,b,c,d,\sigma,\sigma'} U_{abcd} \hat{c}^{\dagger}_{\sigma,a(\mathbf{R})} \hat{c}^{\dagger}_{\sigma',b(\mathbf{R})} \hat{c}_{\sigma',d(\mathbf{R})} \hat{c}_{\sigma,c(\mathbf{R})} . \tag{2.4}$$

1.  $\hat{H}_{kin}$. It represents the kinetic part which describes the electron hopping between orbital $|a\rangle$ at site $\mathbf{R}$ and orbital $|b\rangle$ at site $\mathbf{R}+\Delta\mathbf{R}$. It is assumed that the sites are translationally equivalent so that the hopping amplitudes $t_{ab}(\Delta\mathbf{R})$ depend only on the relative positions of the two sites. Representing the $e_g$ orbital subspace within the usual basis $|1\rangle = |3z^2\text{-}r^2\rangle$ and $|2\rangle = |x^2\text{-}y^2\rangle$, and assuming cubic symmetry, the nearest-neighbour hopping along the three Cartesian coordinates has the following form:

$$\mathbf{t}(\pm a_c \hat{\mathbf{z}}) = \begin{pmatrix} t & 0 \\ 0 & t' \end{pmatrix} \tag{2.5}$$

$$\mathbf{t}(\pm a_c \hat{\mathbf{x}}) = t \begin{pmatrix} \frac{1}{4} & -\frac{\sqrt{3}}{4} \\ -\frac{\sqrt{3}}{4} & \frac{3}{4} \end{pmatrix} + t' \begin{pmatrix} \frac{3}{4} & \frac{\sqrt{3}}{4} \\ \frac{\sqrt{3}}{4} & \frac{1}{4} \end{pmatrix} \tag{2.6}$$

$$\mathbf{t}(\pm a_c \hat{\mathbf{y}}) = t \begin{pmatrix} \frac{1}{4} & \frac{\sqrt{3}}{4} \\ \frac{\sqrt{3}}{4} & \frac{3}{4} \end{pmatrix} + t' \begin{pmatrix} \frac{3}{4} & -\frac{\sqrt{3}}{4} \\ -\frac{\sqrt{3}}{4} & \frac{1}{4} \end{pmatrix} \tag{2.7}$$

$a_c$ is the lattice constant of the underlying cubic perovskite structure. $t'$ represents the hopping between two neighbouring $|x^2\text{-}y^2\rangle$-type orbitals along $\hat{\mathbf{z}}$ and the value is small due to the planar shape of the orbital and it is

therefore often neglected. So, the nearest neighbour hopping depends only on a single parameter $t$, the hopping along $\hat{\mathbf{z}}$ between $|3z^2\text{-}r^2\rangle$-type orbitals. In matrix notation, $\mathbf{t}(\pm\hat{\mathbf{z}})$, $\mathbf{t}(\pm\hat{\mathbf{x}})$ and $\mathbf{t}(\pm\hat{\mathbf{y}})$ are given as,

$$\mathbf{t}(\pm\hat{\mathbf{z}}) = -\frac{1}{2}\mathrm{t}(\mathbf{1} + \tau^z), \tag{2.8}$$

$$\mathbf{t}(\pm\hat{\mathbf{x}}) = -\frac{1}{4}\mathrm{t}(2\cdot\mathbf{1} - \sqrt{3}\cdot\tau^x - \tau^z), \tag{2.9}$$

(and analogously for $\mathbf{t}(\pm\hat{\mathbf{y}})$), where $\tau^z$, $\tau^x$ represent the corresponding Pauli matrices. These Hamiltonian matrix elements could be obtained from the two-center integrals given in the Slater-Koster table 1.1 (Refer to Chapter 1).

$$\mathrm{E}_{3z^2-r^2,3z^2-r^2} = [n^2 - (l^2 - m^2)/2)]^2 V_{dd\sigma} + 3n^2(l^2 + m^2)V_{dd\pi} + \frac{3}{4}[l^2 + m^2]V_{dd\delta} \tag{2.10}$$

$$\mathrm{E}_{x^2-y^2,3z^2-r^2} = \sqrt{3}[(l^2-m^2)[n^2-(l^2-m^2)/2]V_{dd\sigma}/2 + n^2(m^2-l^2)V_{dd\pi} + (1+n^2)(l^2-m^2)/4V_{dd\delta}] \tag{2.11}$$

$$\mathrm{E}_{x^2-y^2,x^2-y^2} = \frac{3}{4}(l^2-m^2)V_{dd\sigma} + [l^2+m^2-(l^2-m^2)^2]V_{dd\pi} + [n^2+(l^2-m^2)^2/4]V_{dd\delta} \tag{2.12}$$

2. $\hat{H}_{Hund}$. It represents the effect of the strong Hund's rule coupling between the $t_{2g}$ spin and the $e_g$ spin. $J_H$ is the Hund's rule coupling strength. In order to simplify the model, $S_{\mathbf{R}}$ which represents the $t_{2g}$ spin (S=3/2) at site $\mathbf{R}$ is normalized as $|S_{\mathbf{R}}| = 1$. $\mathbf{s}_{\mathbf{R}} = \sum_{a,\sigma,\sigma'} c^{\dagger}_{\sigma,a(\mathbf{R})}\tau_{\sigma\sigma'}c_{\sigma',a(\mathbf{R})}$ is the corresponding $e_g$ valence spin and $\tau_{\sigma\sigma'}$ are the Pauli matrices.

3. $\hat{H}_{JT}$. It represents the JT coupling to the oxygen octahedra. $\lambda$ is the JT coupling constant which describes the strength of the JT coupling. There are 2 types of JT distortion modes ($Q^z$ and $Q^x$). The distortion mode called $Q^x$ distorts the octahedron resulting in two long, two short and two medium Mn-O bonds. $Q^z$ distortion mode distorts the octahedron, resulting in two long, four short (or four long and two short) Mn-O bonds. If $Q_{\mathbf{R}}^i$ denotes the amplitude of a particular JT mode (i=x,z) and $\tau_{ab}^i$ represents the

**(a)** $Q^x$        **(b)** $Q^z$
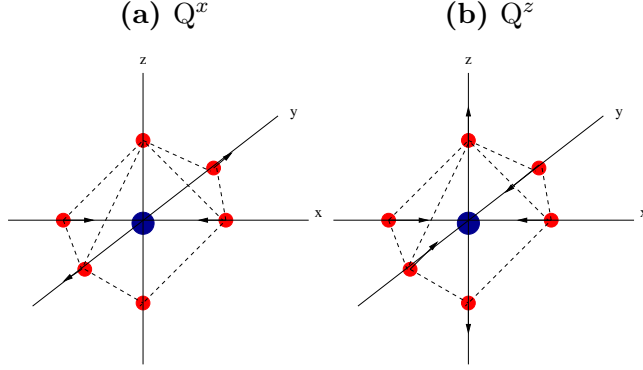


**Figure 2.3:** Different JT distortion modes $Q^x$ and $Q^z$. Red solid circles denote oxygen anions and the blue one denotes the Mn$^{3+}$ cation.

corresponding Pauli matrices, then the quantities $Q_{\mathbf{R}}^x$ and $Q_{\mathbf{R}}^z$ that describe the distortion of the oxygen octahedron surrounding the site $\mathbf{R}$ are given as,

$$Q_{\mathbf{R}}^x = \frac{1}{2\sqrt{2}}(d_{\mathbf{R}}^x - d_{\mathbf{R}}^y) \tag{2.13}$$

$$Q_{\mathbf{R}}^z = \frac{1}{2\sqrt{6}}(2d_{\mathbf{R}}^z - d_{\mathbf{R}}^x - d_{\mathbf{R}}^y) \tag{2.14}$$

where $d_{\mathbf{R}}^x$, $d_{\mathbf{R}}^y$ and $d_{\mathbf{R}}^z$ represent the O-O distances along the x,y and z directions, corresponding to the oxygen octahedron located at site $\mathbf{R}$ (shown in Fig. 2.3).

4. $\hat{H}_{e-e}$. This represents the Coulomb interaction between four orbitals $a$, $b$, $c$ and $d$ which raises the energy by U$_{abcd}$.

The general expression for the Coulomb matrix element U$_{abcd}$ as represented in Eqn.2.4 is given as,

$$U_{abcd} = \int\int d\mathbf{r}d\mathbf{r}'\phi_{a\sigma_1}^*(\mathbf{r})\phi_{b\sigma_2}^*(\mathbf{r}')g_{\mathbf{r}-\mathbf{r}'}\phi_{c\sigma_1}(\mathbf{r})\phi_{d\sigma_2}(\mathbf{r}') \tag{2.15}$$

where $g_{\mathbf{r}-\mathbf{r}'}$ is the screened Coulomb potential, and $\phi_{a\sigma}(\mathbf{r})$ is the Wannier function for an electron with spin $\sigma_1$ in the $a$-orbital at position $\mathbf{r}$. In Eqn.2.4, we have spin $\sigma_1$ associated with $a$ and $c$ orbitals and spin $\sigma_2$ associated with $b$ and $d$ orbitals.

In our TB analysis, we will only consider the *el-el* interaction within a mean-field approximation and use a simplified version of Eq. (2.4) corresponding to $U_{aaaa} = U_{abab} = U_W$ and all other interaction matrix elements set to zero, which is consistent with the PBE+$U$ treatment according to Dudarev *et al.* [34]. The resulting shift in the one-electron potential due to the *el-el* interaction then becomes

$$V_{\sigma,ab} = U_W \left( \frac{1}{2} \delta_{ab} - n_{\sigma,ab} \right) \tag{2.16}$$

where $U_W$ is the Hubbard parameter in the basis of MLWFs and $n_{\sigma,ab}$ are the corresponding occupation matrix elements.

## 2.3 Calculation of MH parameters

The various structural distortions as shown in Fig. 2.1 include: (a)Ideal cubic perovskite strcuture (b) Jahn-Teller distorted structure (c) GdFeO$_3$ (GFO) distorted structure (d) Experimental *Pbnm* structure.

In the work by Kovaçik *et al.* [8] it was shown that, at least at the PBE level, the influence of the individual structural distortion (JT or GFO) on the Hamiltonian matrix elements $h_{nm}^{\Delta R}$ expressed in the basis of $e_g$-like MLWFs is, to a great extent, independent from the other distortion, and that furthermore the magnetic configuration has only a weak influence in the resulting model parameters. The TB parameterization was therefore based on the various model structures with both FM (which always leads to a metallic system) and A-AFM order, with individual structural distortion modes frozen in. We will call this as **Model A**. Due to the significantly increased computational cost of the HSE and GW$_0$ methods in comparison with PBE (in particular for the metallic state for which a dense $k$-point mesh is required to achieve a well-converged solution), it is desirable to derive the TB parameters from as few (and if possible insulating) model structures as possible. Unlike Model A, TB parametrization in Model B is constructed from only two crystal structures: the purely JT ($Q^x$) distorted structure and the experimental *Pbnm* structure, in both the cases with A-AFM order, which then yields an insulating solution. As we will see, the results of Model B are essentially identical to those of Model A, at PBE level.

### 2.3.1 Model A - Model parameters in effective e$_g$ basis (PBE)

The model parametrization which we call "*Model A*" has been proposed by Kovàcik *et al.* [8]. In their work, MLWFs corresponding to Mn$^{3+}$ e$_g$ states of LaMnO$_3$ has been constructed based on GGA. The real-space Hamiltonian matrix elements in the MLWF basis for different structural modifications as shown in Fig. 2.3 are calculated and the obtained results are compared with assumptions made in commonly used two-band TB models for manganites. The authors have shown that the MLWF approach automatically leads to a TB parametrization of the relevant bands so that the parameters of the model can be simply "read-off" (from wannier90_hr.dat file) and no fitting procedure is required. We will discuss the work of Kovàcik *et al.* [8] in this section. The electronic Hamiltonian for Model A is given as,

$$\hat{H} = \hat{H}_{\text{kin}} + \hat{H}_{\text{Hund}} + \hat{H}_{\text{JT}} \tag{2.17}$$

(Refer to Sec. 2.2).

The parameters to be calculated are: Spin-dependent nearest-neighbour hopping ($t^{\uparrow\uparrow}$, $t^{\downarrow\downarrow}$), Next-nearest neighbour hopping $t^{xy}$ and $t^{2z}$, JT induced e$_g$ splitting $\tilde{\lambda}$, JT coupling strength ($\lambda^{\uparrow}$, $\lambda^{\downarrow}$), Hund's rule coupling strength ($J_H$), GFO reduction factor ($\eta^{\uparrow}$, $\eta^{\downarrow}$).

The procedure to calculate the parameters is given below:

1. $t^{\uparrow\uparrow}$. This parameter is the nearest-neighbour hopping amplitude of majority spin e$_g$ electrons $t$ as given in the Eqns.2.5, 2.6, 2.7 i.e. hopping of electron from the origin to its nearest-neighbour in the $\hat{z}$-direction. This parameter is read directly from the wannier_hr.dat file corresponding to FM majority spin channel of ideal cubic perovskite structure.

   $$h^z_{11} \rightarrow \quad 0 \quad 0 \quad 1 \quad 1 \quad 1 \quad -0.638466(t) \quad 0.000000$$
   $$h^z_{12} \rightarrow \quad 0 \quad 0 \quad 1 \quad 2 \quad 1 \quad \phantom{-}0.000000 \quad 0.000000$$
   $$h^z_{21} \rightarrow \quad 0 \quad 0 \quad 1 \quad 1 \quad 2 \quad \phantom{-}0.000000 \quad 0.000000$$
   $$h^z_{22} \rightarrow \quad 0 \quad 0 \quad 1 \quad 2 \quad 2 \quad \phantom{-}0.010314(t') \quad 0.000000$$

   It is to be noted that indexing is site-based i.e. h$^0$ denotes onsite matrix elements ($\Delta\mathbf{R}$=0), h$^x$ represents the hopping in x-direction ($\Delta\mathbf{R}$=±a$_c\hat{x}$), h$^z$ represents the hopping in z-direction ($\Delta\mathbf{R}$=±a$_c\hat{z}$) and h$^{xz}$ denotes hopping
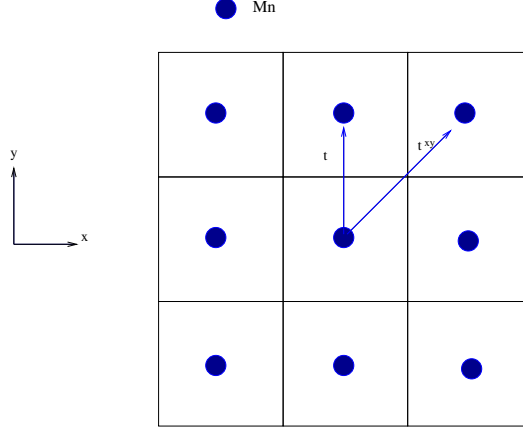
**Figure 2.4:** Representation of the first nn and second nn hoppings corresponding to the case of an ideal cubic perovskite structure within the $xy$ plane. Mn atoms are represented by filled blue circles, the hopping $t$ and $t^{xy}$ refer to hopping between the $e_g$ orbitals.

between the second nearest neighbours ($\Delta\mathbf{R}$=a$_c(\pm\hat{x}\pm\hat{z})$). As it has been already mentioned, t$'$ is much smaller than t and could be neglected.

Fig.2.4 represents the hopping directions in the case of ideal cubic perovskite structure. If each Mn site has $e_g$ orbitals labelled as 1,2 then the hopping amplitudes could be read-off from the wannier_hr.dat file as shown above ($h^z_{11}$, $h^z_{12}$, $h^z_{21}$ and $h^z_{22}$).

2. $t^{\downarrow\downarrow}$. This parameter is the nearest-neighbour hopping amplitude of minority spin e$_g$ electrons which is read directly from the wannier_hr.dat file corresponding to FM minority spin channel of cubic perovskite structure.

```
0  0  1  1  1  -0.516465(t)   0.000000
0  0  1  2  1    0.000000     0.000000
0  0  1  1  2    0.000000     0.000000
0  0  1  2  2  -0.002043(t')  0.000000
```

3. $t^{xy}$. This parameter represents the next-nearest neighbour hopping i.e. hopping between the $|3z^2\text{-}r^2\rangle$-type orbitals along the $\pm a_c\hat{\mathbf{x}}\pm a_c\hat{\mathbf{y}}$ directions. $t^{xy}$ is taken as spin average over the corresponding MLWF matrix elements $h^{xy}_{11}$ calculated for the ideal cubic perovskite structure.

```
h^{xy}_{11}(↑)  →   1   1   0   1   1   -0.021083   0.000000
h^{xy}_{11}(↓)  →   1   1   0   1   1   -0.015174   0.000000
```

4. $t^{2z}$. This parameter represents the hopping between second nearest neighbours along the coordinate axes $[\mathbf{t}(\pm 2a_c\hat{\mathbf{x}}), \mathbf{t}(\pm 2a_c\hat{\mathbf{y}}), \mathbf{t}(\pm 2a_c\hat{\mathbf{z}})]$ that has been included according to the ideal cubic symmetry relations given by Eqns. 2.5, 2.6, 2.7 with $a_c$ replaced by $2a_c$ ($t=t^{2z}$ and $t'$) where $t^{2z}$ is calculated from the purely GFO distorted structure.

```
h^{2z}_{11}(↑)  →   0   0   1   1   1   -0.020686   0.000000
h^{2z}_{11}(↓)  →   0   0   1   1   1   -0.021812   0.000000
```

5. $\eta$ ($\eta^\uparrow$ and $\eta^\downarrow$). This parameter represents the reduction of the hopping amplitudes (reduction factor) due to GdFeO$_3$ distortion. The main effect of GFO distortion is a systematic reduction of all hopping amplitudes by $\approx$ 20-30 %, which is consistent with the report [7]. Even though there is a significant spread in the reduction factors for the various hopping parameters, the overall reduction is approximately described as $\mathbf{h}^{x/z}(\alpha_{GFO}) = \mathbf{h}^{x/z}(0)(1-\eta\alpha^2_{GFO})$ where $\alpha_{GFO}$ refers to the amount of GFO distortion. $\mathbf{h}^{x/z}$ and $\mathbf{h}^{x/z}(0)$ refer to MLWF Hamiltonian matrix elements (hopping in $\hat{\mathbf{x}}$- or $\hat{\mathbf{z}}$-directions) corresponding to GFO distorted and ideal cubic perovskite structures respectively.

6. $\tilde{\lambda}$. This parameter represents the JT-induced splitting of the non-diagonal elements of the hopping matrix within the x-y plane and it is determined from the average splitting over all hopping amplitudes in the purely JT-distorted structure.

7. $\lambda^\uparrow$, $\lambda^\downarrow$. This parameter represents the JT coupling strength. The effect of the JT distortion ($Q^x_{\mathbf{R}}$, $Q^z_{\mathbf{R}}$) in the model is a linear coupling to the on-site terms at site $\mathbf{R}$ according to the equation,

$$\mathbf{t}^0 = \begin{pmatrix} e_0 - \lambda Q^z_{\mathbf{R}} & -\lambda Q^x_{\mathbf{R}} \\ -\lambda Q^x_{\mathbf{R}} & e_0 + \lambda Q^z_{\mathbf{R}} \end{pmatrix} \tag{2.18}$$

Where $Q^z_{\mathbf{R}}=0$ and $Q^x_{\mathbf{R}}=\pm\alpha_{JT}Q^x_0$ and $e_0$ is the on-site energy of the $e_g$ orbitals.

8. $J_H$. This parameter represents the Hund's rule coupling strength. It is calculated from the ideal cubic structure considering the fact that the energy

difference between the majority and the minority spin channel configuration equals to $2J_H$.

## 2.3.2 Model B

Model B could be constructed in two ways: (1) An effectively 'non-interacting' case in which the term $\hat{H}_{e-e}$ is neglected and the influence of the more sophisticated beyond-PBE treatment of the exchange-correlation kernel on the hopping, JT and the GFO-related parameters is treated 'implicitly'. We will call this as *Model B-1.* (2) An explicit treatment of $\hat{H}_{e-e}$ in the model Hamiltonian within the mean-field approximation. This allows us to obtain estimates for the corresponding on-site interaction parameters, by keeping the conventional PBE description as reference. We will call this *Model B-2.*

1. $t^{ss}$ ($t^{\uparrow\uparrow}$, $t^{\downarrow\downarrow}$, where 's' denotes the spin) - This parameter represents the nearest-neighbour hopping amplitude. It is calculated using the MLWF Hamiltonian matrix elements corresponding to the purely JT ($Q^x$)-distorted A-AFM structure. The formula is given as,

$$t^{ss} = \left( \frac{1}{2} h^x_{11} - \frac{3}{2} h^x_{22} \right)^s \qquad (2.19)$$

Where $h^x_{11}$ and $h^x_{11}$ represents $|3z^2\text{-}r^2\rangle$ - $|3z^2\text{-}r^2\rangle$ hopping and $|x^2\text{-}y^2\rangle$-$|x^2\text{-}y^2\rangle$ hopping in the x-y plane respectively. The Hamiltonian matrix elements are denoted by a notation $h^{\Delta\mathbf{R}}_{ab}$, where $a$ and $b$ correspond to two effective $e_g$ orbitals centered at individual Mn sites separated by $\Delta\mathbf{R}$. To further simply the notation, one Mn site is chosen as the origin and $\hat{x}$ and $\hat{y}$ axes are aligned with the directions corresponding to the long and short Mn-O bonds of the JT ($Q^x$) mode. The vectors $\hat{x}$, $\hat{y}$ and $\hat{z}$ are defined according to the nearest-neighbour spacing of the Mn sites along the respective axes.

Fig.2.5 shows the representation of the hoppings (for the two unit cell structure (JT)). If 1,2 and 3,4 represent the orbitals at different sites as shown in the figure, the value of $t^{\uparrow\uparrow}$ and $t^{\downarrow\downarrow}$ are calculated by the matrix elements from the wannnier_hr.dat file.
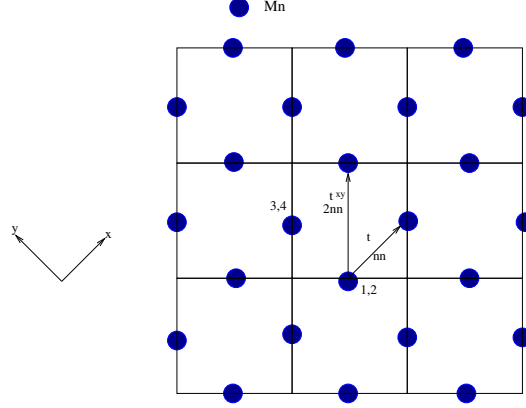
**Figure 2.5:** Representation of the first nn and second nn hoppings in the JT and Experimental *Pbnm* structures. Here one Mn site is chosen as the origin and the $\hat{x}$ and $\hat{y}$ axes are aligned with the directions corresponding to long and short Mn-O bonds of the JT ($Q^x$) mode. 1,2 and 3,4 represent the $e_g$ orbitals (majority spin) within a single unit cell. The minority spin $e_g$ orbitals which are not shown in the figure are labelled as 5,6 and 7,8.

$$
\begin{array}{llllllllll}
h^x_{11}(\uparrow) & \to & 1 & 0 & 0 & 1 & 3 & -0.147887 & 0.000000 \\
h^x_{22}(\uparrow) & \to & 1 & 0 & 0 & 2 & 4 & -0.463337 & 0.000000 \\
h^x_{11}(\downarrow) & \to & 1 & 0 & 0 & 5 & 7 & -0.118779 & 0.000000 \\
h^x_{22}(\downarrow) & \to & 1 & 0 & 0 & 6 & 8 & -0.377113 & 0.000000 \\
\end{array}
$$

2. $t^{xy}$ and $t^{2z}$- These parameters represent the second nearest-neighbour hopping amplitudes. The second nearest-neighbour hoppings $t^{xy}$ in the x-y plane are determined by the JT-distorted structure. It is given as,

$$\mathbf{t}(\pm\hat{x}\pm\hat{z}) = -t^{xy}\begin{pmatrix} -2 & \sqrt{3} \\ \sqrt{3} & 0 \end{pmatrix} \tag{2.20}$$

$$\mathbf{t}(\pm\hat{x}\pm\hat{y}) = -t^{xy}\begin{pmatrix} 1 & 0 \\ 0 & -3 \end{pmatrix} \tag{2.21}$$

The matrices related to $t^{2z}$ parameter take the same form as equations 2.9. Both $t^{xy}$ (second nn hopping) and $t^{2z}$ (second nn hopping along the x, y and z axes) are determined as,

$$t^{xy} = -\frac{1}{2}\left[(h^{xy}_{11})^{\uparrow} + (h^{xy}_{11})^{\downarrow}\right] \tag{2.22}$$

$$t^{2z} = -\frac{1}{2}\left[(h_{11}^{2z})^{\uparrow} + (h_{11}^{2z})^{\downarrow}\right] \tag{2.23}$$

3. $\tilde{\lambda}$. This parameter (as explained in Model A) determines the magnitude of the JT induced $e_g$ level splitting. The formula to calculate this parameter is given as,

$$\Delta\mathbf{t}^{ss}(\pm\hat{x}) = \tilde{\lambda}Q_{\mathbf{R}}^x \begin{pmatrix} 0 & 1 \\ 1 & 0 \end{pmatrix} \tag{2.24}$$

(And analogously for $\Delta\mathbf{t}(\pm\hat{y})$).

Thus $\tilde{\lambda}$ is given as,

$$\tilde{\lambda} = \frac{1}{2Q^x}\left(\frac{1}{2}(h_{12}^x - h_{21}^x)^{\uparrow} + \frac{1}{2}(h_{12}^x - h_{21}^x)^{\downarrow}\right) \tag{2.25}$$

Where the MLWF Hamiltonian matrix elements are read from the purely JT ($Q^x$) distorted structure (A-AFM).

4. $\lambda^s$ ($\lambda^{\uparrow}$, $\lambda^{\downarrow}$).This parameter (as already explained) represents the JT coupling strength which are determined from the splitting of the eigenvalues of the onsite Hamiltonian and the JT amplitude $Q^x$ for the purely JT($Q^x$) distorted structure. They are spin-dependent and are calculated using the formula given as,

$$\lambda^s = \frac{\Delta\varepsilon^s}{2|Q^x|} \tag{2.26}$$

The JT induced eigenvalue splitting $\Delta\varepsilon$ of the $e_g$ subspace $2 \times 2$ onsite matrix calculated as,

$$\Delta\varepsilon = \left[(h_{11}^0 - h_{22}^0)^2 + (2h_{12}^0)^2\right]^{1/2} \tag{2.27}$$

5. $\eta_t^s$ ($\eta_t^{\uparrow}$, $\eta_t^{\downarrow}$). These parameters represent the reduction in the hopping amplitudes due to GdFeO$_3$ distortion. As a result of the GFO distortion, the hopping amplitudes t$^{\uparrow\uparrow}$ and t$^{\downarrow\downarrow}$ are reduced by a factor (1-$\eta_t^s$), where $\eta_t^s$ is calculated from the ratio of the $t^{ss}$ calculated for the Pbnm and the JT($Q^x$) structures. The equations are shown below:

$$\eta_t^s = 1 - \frac{t^{ss}[Pbnm]}{t^{ss}[JT(Q^x)]} \tag{2.28}$$

Where t$^{ss}$[Pbnm] is the nearest-neighbour spin dependent hopping ampli-
tude calculated for the experimental Pbnm structure and the term t$^{ss}$[JT(Q$^x$)]
is the hopping amplitude calculated for the JT distorted structure.

6. $\eta_\lambda$. This parameter represents the reduction of the Jahn-Teller coupling
   strength due to GdFeO$_3$ distortion. Similar to the hopping amplitudes, $\lambda^s$
   is reduced by a factor (1-$\eta_\lambda^s$) due to the GFO distortion, $\eta_\lambda^s$ is determined
   as shown below:

$$\eta_\lambda = 1 - \frac{\Delta\varepsilon^\uparrow[Pbnm]}{\Delta\varepsilon^\uparrow[JT(Q^x)]} \frac{|\mathbf{Q}[JT(Q^x)]|}{|\mathbf{Q}[Pbnm]|} \tag{2.29}$$

Where $|\mathbf{Q}| = \sqrt{(Q^x)^2 + (Q^z)^2}$.

7. $J_H$. This parameter represents the Hund's rule coupling strength. This
   value is calculated from the experimental *Pbnm* structure using the formula,

$$J_H = \frac{1}{4}\left[(h_{11}^0 + h_{22}^0)^\downarrow - (h_{11}^0 + h_{22}^0)^\uparrow\right] \tag{2.30}$$

8. $U_W$. As already mentioned, this parameter describes the *el-el* interaction
   and it is calculated in the Model B, where the modifications induced by the
   beyond-PBE methods are treated as perturbation to the "non-interacting"
   PBE description by explicitly considering the *el-el* interaction and using
   the simplified mean-field approximation in the TB Hamiltonian U$_{aaaa}$ =
   U$_{abab}$ = U$_W$ and all the other interaction matrix elements set to zero, which
   is consistent with the PBE+U treatment according to Dudarev *et al.* The
   resulting shift in the one-electron potential due to the *el-el* interaction then
   becomes

$$\Delta V_{\sigma,ab} = U_W \left(\frac{\delta_{ab}}{2} - n_{\sigma,ab}\right) \tag{2.31}$$

where U$_W$ is the Hubbard parameter in the basis of MLWFs and $n_{\sigma,ab}$
are the corresponding occupation matrix elements. The occupation matrix
elements are calculated in the MLWF basis as,

$$n_{mm'}^{MLWF} = \int_{-\infty}^{E_F} d\epsilon \int_{BZ} d\mathbf{k} \sum_l (U_{lm}^{(\mathbf{k})})^* \delta(\epsilon - \epsilon_{l\mathbf{k}}) U_{lm'}^{(\mathbf{k})} \tag{2.32}$$

We will now discuss the two alternative ways to evaluate $U_W$ by using 2 different parametric expressions involving $J_H$, $\lambda^\uparrow$, $\lambda^\downarrow$ and the occupation matrix elements $n_{mm'}^{MLWF}$.

(A) Since it is not straightforward to parametrize the hopping amplitudes in terms of $U_W$, we will limit ourselves to analyzing the effect of Eqn. 2.31 on the local Hamiltonian, which is represented as 2×2 matrix in terms of the two local $e_g$ states in the following form:

$$\hat{H}_{local}^s = \tilde{\tilde{H}}_0^s - U_W \hat{n}^s \tag{2.33}$$

with

$$\tilde{\tilde{H}}_0^s = \mathbf{1} \left( \frac{1}{2} U_W - J_H \cdot s \right) - \lambda^s Q^x \hat{\tau}^x - \lambda^s Q^z \hat{\tau}^z \tag{2.34}$$

$\hat{n}^s \rightarrow$ Occupation matrix.

We calculate the local spin splitting by identifying Eqn.2.33 with the corresponding MLWF matrix. The Hamiltonian $\hat{H}_{local}^s$ could be written as:

$$\hat{H}_{local}^s = \begin{pmatrix} \frac{1}{2}U_W - J_H \cdot s - \lambda^s Q^z & -\lambda^s Q^x \\ -\lambda^s Q^x & \frac{1}{2}U_W - J_H \cdot s + \lambda^s Q^z \end{pmatrix} - U_W \begin{pmatrix} n_{aa}^s & n_{ab}^s \\ n_{ba}^s & n_{bb}^s \end{pmatrix} \tag{2.35}$$

For majority spin,

$$\hat{H}_{local}^\uparrow = \begin{pmatrix} \frac{1}{2}U_W - J_H - \lambda^\uparrow Q^z & -\lambda^\uparrow Q^x \\ -\lambda^\uparrow Q^x & \frac{1}{2}U_W - J_H + \lambda^\uparrow Q^z \end{pmatrix} - U_W \begin{pmatrix} n_{aa}^\uparrow & n_{ab}^\uparrow \\ n_{ba}^\uparrow & n_{bb}^\uparrow \end{pmatrix} \tag{2.36}$$

For minority spin,

$$\hat{H}_{local}^\downarrow = \begin{pmatrix} \frac{1}{2}U_W + J_H - \lambda^\downarrow Q^z & -\lambda^\downarrow Q^x \\ -\lambda^\downarrow Q^x & \frac{1}{2}U_W + J_H + \lambda^\downarrow Q^z \end{pmatrix} - U_W \begin{pmatrix} n_{aa}^\downarrow & n_{ab}^\downarrow \\ n_{ba}^\downarrow & n_{bb}^\downarrow \end{pmatrix} \tag{2.37}$$

By identifying $\hat{H}_{local}^s$ with the MLWF Hamiltonian, the local spin splitting from the MLWF matrix elements is readily obtained from Eqns. 2.36 and 2.37 as:

$$(h_{aa}^0)^\downarrow - (h_{aa}^0)^\uparrow = U_W(n_{aa}^\uparrow - n_{aa}^\downarrow) + 2J_H + (\lambda^\uparrow - \lambda^\downarrow)Q^z \tag{2.38}$$

Since U$_W$ calculated using the above equation is predominantly determined by the on-site Hund's rule coupling parameter J$_H$ i.e. from the difference between the majority and the minority on-site matrix elements, we call it U$_W^{(J)}$. The term $\Delta\lambda_W^{(J)} = (\lambda^\uparrow\text{-}\lambda^\downarrow)Q^z$ is a correction term of the order of $\approx$ 0.1 eV. Note that J$_H$, $\lambda^\uparrow$ and $\lambda^\downarrow$ is calculated at the PBE level.

(B) Since the bandgap in LaMnO$_3$ is largely controlled by the JT-induced splitting between occupied and unoccupied majority spin e$_g$ bands $\lambda^\uparrow$, the Hubbard parameter U$_W$ can also be calculated from the total JT induced splitting within the majority spin e$_g$ orbital manifold:

$$\Delta\epsilon^\uparrow = 2\lambda^\uparrow\sqrt{(Q^x)^2 + (Q^z)^2} + U_W\Delta n^\uparrow \tag{2.39}$$

where

- $\Delta\epsilon^\uparrow = \sqrt{((h_{aa}^0)^\uparrow - (h_{bb}^0)^\uparrow)^2 + 4((h_{ab}^0)^\uparrow)^2}$ represents the difference in eigenvalues of the local majority spin Hamiltonian as computed at beyond-PBE level,

- $2\lambda^\uparrow\sqrt{(Q^x)^2 + (Q^z)^2}$ is the corresponding PBE value ($\Delta\epsilon^{\uparrow(PBE)}$),

- $U_W\Delta n^\uparrow$ is the U$_W$-induced correction with $\Delta n^\uparrow = \sqrt{((n_{aa}^0)^\uparrow - (n_{bb}^0)^\uparrow)^2 + 4((n_{ab}^0)^\uparrow)^2}$ representing the difference in the majority spin eigenvalues of the MLWF occupation matrix.

The observation that both $\tilde{\hat{H}}_0$ and $\hat{n}$ can be diagonalized by the same Unitary transformation, has been used. If $\tilde{\hat{H}}_0$ and $\hat{n}$ can be diagonalized by the same Unitary transformation, then their eigenvalue difference could be related as given by Eqn.2.39 with $U_W$ being the slope. This parameter U$_W$ is calculated from the MLWF Hamiltonian of the *Pbnm* structure.

In this case, U$_W$ is determined as a correction to the JT gap ($\lambda^\uparrow$), so we call it U$_W^\lambda$. Since the correlation-induced increase of the spin-splitting is only partially covered by the *el-el* term, this is corrected by introducing an empirical correction to the Hund's rule coupling:

$$\Delta J_W^{(\lambda)} = J_H - J_H^{(PBE)} - \frac{1}{4}U_W^{(\lambda)} \tag{2.40}$$

If the correction $\Delta J_W^{(\lambda)}$ is neglected, the local majority spin bands around the band gap are still described quite well, even though the splitting with respect to the local minority spin bands will be underestimated, which might be acceptable for certain applications.

Summing up, we have shown that we can parametrize $U_W$ either by $U_W^{(J)}$ and $\Delta\lambda_W^{(J)}$ (i.e. by deriving the el-el interaction through the difference between the majority and minority on-site matrix elements), and suitably introducing an appropriate correction $\Delta\lambda_W^{(J)}$, or by using $U_W^{(\lambda)}$ and $\Delta J_W^{(\lambda)}$ (i.e., employing the JT-induced splitting between the occupied and the unoccupied $e_g$ bands) plus an appropriate correction $\Delta J_W^{(\lambda)}$.

The results obtained by these two alternative procedures will be discussed for the case of LaMnO$_3$ in this chapter. However, we emphasize that, since the fundamental band gap in $R$MnO$_3$ (early series) ($R = $ La-Gd) is largely controlled by the JT-induced splitting between occupied and unoccupied $e_g$ bands, and since in a TB model for $R$MnO$_3$ it seems most desirable to describe the band gap correctly, $U_W^{(\lambda)}$ has been chosen to model the el-el interactions at TB level for the whole $R$MnO$_3$ series (Chapter 3).

## 2.4 First-principles results

In the following sections, we will discuss the electronic and magnetic ground states obtained within the various levels of approximation (PBE, PBE+$U$, HSE and GW$_0$), results of TB parameterizations corresponding to effective $e_g$ models, either with or without explicit *el-el* interaction term and implications of the different underlying band-structures.

### 2.4.1 Computational details

The calculations presented in this chapter are based on DFT within the PBE approximation to the exchange-correlation energy. The one-particle Kohn-Sham orbitals are computed within a plane-wave basis employing 2 different codes : ultrasoft PP based PWscf and PAW method based VASP. The PWscf program is used to benchmark the implementation of the VASP2WANNIER90 interface at the PBE and PBE+U level. PWscf calculations have been performed in collaboration with Kovačik and Ederer [82].
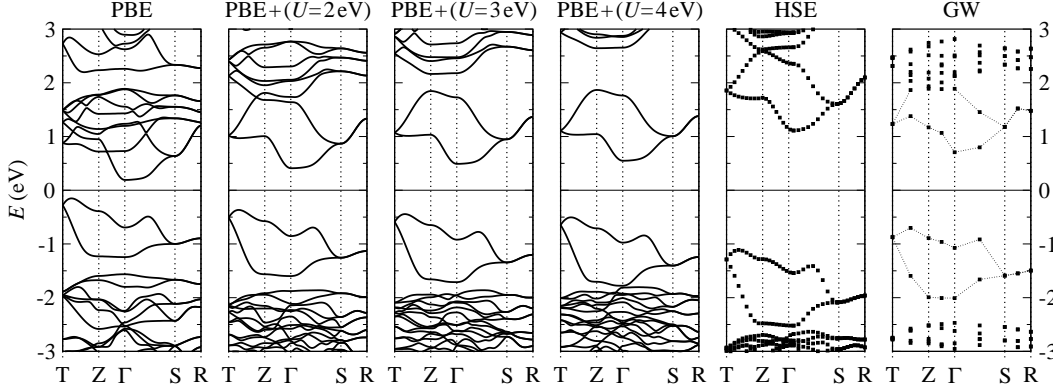
**Figure 2.6:** Calculated band structure along certain high-symmetry directions within the BZ. Each panel reports results obtained by a different method, as specified in the panel title. E=0 is aligned to the middle of the gap.

An identical setup is adopted for VASP and PWscf calculations. All ground state electronic and magnetic properties are calculated for the experimental low temperature *Pbnm* structure reported in [65] using a regular $\Gamma$-centered $7 \times 7 \times 5$ and $6 \times 6 \times 6$ $k$-point mesh in PWscf and VASP respectively (reduced to $4 \times 4 \times 4$ at the GW$_0$ level), and a plane wave energy cutoff of 35 Ryd ($\approx 476$ eV) and 300 eV in PWscf and VASP, respectively. Spin-polarized calculations were performed within a collinear setup without the inclusion of spin-orbit effects. The PBE and PBE+U results shown in this chapter correspond to PWscf except where otherwise noted, whereas HSE and GW$_0$ results are obtained using VASP. In both PWscf and VASP, the Mn(3s), Mn(3p), La(5s) and La(5p) semi-core states in the valence. In PWscf, the unoccupied La(4f) states are excluded from the ultrasoft pseudopotential, whereas they are present in the corresponding VASP PAW potential.

### 2.4.2 Results and discussion

The calculated band structures are displayed in Fig.2.6 and the corresponding indirect ($E_i$) and smallest direct ($E_d$) band gaps are listed in Tab.2.1. The calculated valence and conduction band spectra and the PDOS (corresponding to Mn($e_g$), Mn($t_{2g}$), and O($p$) states), are represented in the Fig. 2.7 and Fig.2.8, respectively.

It can be seen from Fig.2.6 that the eigenvalue dispersion in LaMnO$_3$ is characterized by an insulating state with an indirect energy gap. By comparing with

| This Work | | | | | |
| --- | --- | --- | --- | --- | --- |
| | HSE | $GW_0$@PBE | PBE | PBE+$U$ | | |
| | | | | $U=2$ | $U=3$ | $U=4$ |
| $E_i$ | 2.25 | 1.41 | 0.38 | 0.82 | 0.98 | 1.10 |
| $E_d$ | 2.55 | 1.68 | 0.75 | 1.15 | 1.30 | 1.42 |
| Previous studies | | | | | |
| | B3LYP[87] | $G_0W_0$@LDA[88] | GGA[86] | GGA+$U$[86] | Expt. | |
| | | | | $U=2$ | | |
| $E_i$ | 2.3 | 0.82 | 0.27 | 0.81 | | |
| $E_d$ | | 1.00 | 0.70 | 1.18 | $1.1^a$, $1.9^b$, $2.0^{c,d}$, $1.7^e$ | |

**Table 2.1:** Collection of calculated (present work and previous studies) and experimental value for the indirect ($E_i$) and direct ($E_d$) band gap of LaMnO$_3$. The measured values refer to optical conductivity [89, 90, 91], Raman [92], and photoemission [93] experiments.

[a]Ref. [89], [b]Ref. [90], [c]Ref. [91], [d]Ref. [92], [e]Ref. [93],

the PDOS shown in Fig.2.8, it becomes clear that within all methods the Mott-Hubbard gap is opened between occupied and empty states with predominant Mn($e_g$) character. While the width of the band gap differs strongly between the various methods, each one is in good agreement with previous LDA/GGA [83, 84, 85, 86], (LDA/GGA)+$U$ [84, 86], and hybrid functionals [87], respectively (see Tab.2.1). The partially-self consistent $GW_0$ that has been employed in this work cannot be directly compared with the single-shot $G_0W_0$ results of Nohara *et al.*[88] since the latter depend much more on the initial LDA wavefunction and consequently convey a smaller bandgap.

Due to the inadequate treatment of exchange-correlation effects, conventional PBE-DFT leads to a significant underestimation of $E_d^{PBE} = 0.75$ eV compared to the experimental values obtained from optical conductivity measurements (1.1 eV [89], 1.9 eV [90], 2.0 eV [91]), Raman (2.0 eV [92]), and photoemission data (1.7 eV [93]). In addition, the uppermost filled Mn($e_g$) bands (with energies in the region between $-1.3$ eV and $0.0$ eV) are well separated from the lower-lying mostly Mn($t_{2g}$)- and O($p$)-like states (below $-1.5$ eV). In contrast,

while the lower part of the group of bands immediately above the gap (up to about 2 eV) exhibits predominant local majority spin $e_g$ character, these bands are strongly entangled with local minority spin $t_{2g}$ states at slightly higher energies (between approximately 1-2 eV). The inclusion of the on-site interaction term within the PBE+$U$ approach, separates these higher-lying local minority spin $t_{2g}$ states from the local majority $e_g$ bands directly above the gap for $U > 2$ eV. Furthermore, increasing $U$ also increases the band gap i.e. $E_d^{\text{PBE}+U}$ changes from 1.15 eV to 1.42 eV on changing U from 2 eV to 4 eV respectively and lowers the filled $e_g$ states relative to the bands with dominant Mn($t_{2g}$) and O($p$) character, which leads to an appreciable overlap between these sets of bands around the $\Gamma$ point for $U = 4$ eV.

Changing to a more elaborate treatment of the exchange-correlation kernel, it is seen that HSE provides a value of the bandgap ($E_d^{\text{HSE}} = 2.55$ eV) that is significantly larger (by $\approx 0.5$ eV) than the experimental measurements. This is in line with previous hybrid functional estimates based on the B3LYP approach implemented within a Gaussian basis set [87]. By comparing the PBE and HSE band gap one could argue that a smaller portion of exact HF exchange should be included in the hybrid functional framework in order to obtain a better agreement with experiment. Indeed, a reduced mixing parameter $a_{\text{mix}} = 0.15$ shrinks the direct gap down to 1.79 eV, almost on par with the photoemission measurements of Saitoh and coworkers [93], and with the more recent optical conductivity data of Jung *et al.*[90, 91], and Krüger *et al.*[92]. LaMnO$_3$ therefore seems to represent another example for which the one-quarter compromise (mixing 1/4 of exact exchange with 3/4 of DFT exchange) is not the ideal choice [94]. Finally, the parameter-free GW$_0$ technique leads to a quite satisfactory prediction of the band gap, $E_d^{\text{GW}_0} = 1.68$ eV, and about significantly larger than the only previous single-shot (i.e. perturbative) G$_0$W$_0$ study of Nohara *et al.* based on initial LDA wavefunctions [88]. Similarly to HSE and PBE+$U$ (for $U = 3$ eV), GW$_0$ deliver $e_g$ bands around E$_F$ well separated from the O($p$) and Mn($t_{2g}$) bands below and, to a lesser extent, above (there is an appreciable mixing of Mn($e_g$) and Mn($t_{2g}$) states along the T-Z-$\Gamma$ path around 2 eV), in clear contrast with the PBE picture which predicts a certain degree of overlap between the $e_g$ bands and the higher lying $t_{2g}$ bands.

In order to provide further assessment of the quality of the various methods in describing the electronic structure of LaMnO$_3$, the simulated valence and conduction band spectra is compared with the corresponding photoemission spectroscopy and X-ray absorption spectroscopy data [95] (See Fig. 2.7) . For negative
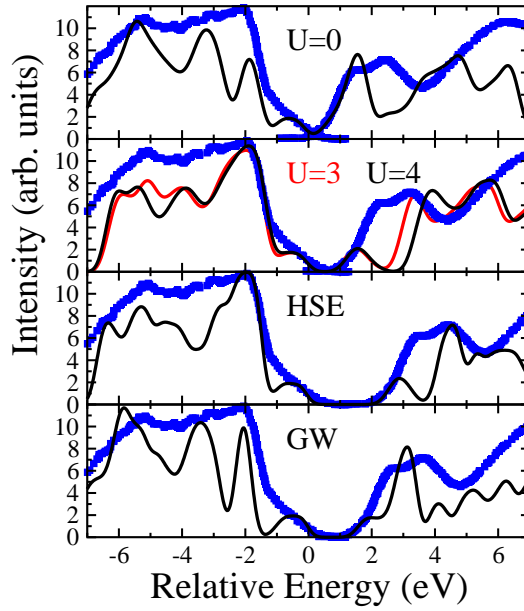
**Figure 2.7:** Comparison between experimental [95] (blue squares) and calculated valence and conduction band spectra for PBE, PBE+$U$ ($U = 3$ and 4 eV), HSE, and $GW_0$. The calculated and measured spectra have been aligned by overlapping the valence band maxima and conduction band minima.

energies (occupied states) none of the four methods differs dramatically from the experimental spectrum, even though the multi-peak structures in the range of $-7$ eV to $-4$ eV seen within PBE+$U$ and HSE do not have a clear experimental correspondence, whereas PBE and GW$_0$ profiles better follow the main three experimental peak/shoulders. The situation is more critical for the unoccupied region, since none of the methods is capable to correctly reproduce the two-peaks structure characterizing the onset of the conduction band right above E$_F$. These two peaks could be interpreted as formed by $e_g$ (lower one) and $t_{2g}$ (second ones) contributions and are described differently by the various schemes, following the corresponding band dispersions discussed in Fig. 2.6: (i) PBE both peaks merge in one single strong electronic signal, reflecting the large overlap between $e_g$ and $t_{2g}$ bands right above E$_F$; (ii) in PBE+U the two peak are much too separated, reflecting the wide $e_g$-$t_{2g}$ band splitting; (iii) HSE and GW$_0$ are rather similar. Their spectra are characterized by a lower $e_g$ small bunch of states (onset of the conduction band spectra) associated to a more intense $t_{2g}$-like peak, but the GW$_0$ $e_g/t_{2g}$ splitting ($\approx 1.4$ eV) better matches the experimental one ($\approx 1.1$ eV) as compared to the larger HSE splitting ($\approx 1.7$ eV). From these results it can be inferred that GW$_0$ and HSE convey the most satisfactory picture in terms of peak position and corresponding spectral weight for both occupied and unoccupied states, with GW$_0$ better reproducing the splitting between the two lower conduction peaks. However, it should be noted that the relative weights of the two lower conduction peaks do not match with experiment, indicating that it is necessary go beyond the GW approximation to obtain a refined agreement with experiment. It is underlined once more that unlike PBE+U and HSE (in which the proper adjustment of the parameters $U$ and $a_{\mathrm{mix}}$ can cure the bandgap problem and lead to values of the gap close to the experimental ones), the parameter-free GW$_0$ scheme is capable to provide a rather accurate picture without the need of any adjustable parameter.

Next, we will analyze the magnetic properties in terms of the nearest-neighbor magnetic exchange interactions within the orthorhombic $ab$ plane ($J_{ab}$) and along $c$ ($J_c$) [87, 96, 97]. This will provide further insights into the performance of the various methods with respect to energetic properties of LaMnO$_3$. By mapping the calculated total energies for different magnetic configurations onto a classical Heisenberg Hamiltonian $H = -\frac{1}{2}\sum_{i \neq j} J_{ij}\, S_i \cdot S_j$, the following equations for $J_{ab}$ and $J_c$ can be obtained (see also [87, 97]):

$$E_{\mathrm{FM}} - E_{\mathrm{AAF}} = -32 J_c \qquad\qquad (2.41)$$

$$E_{\text{CAF}} - E_{\text{FM}} = 64 J_{ab} \,. \tag{2.42}$$

Here, $E_{\text{FM}}$ corresponds to the total energy for the FM configuration, whereas $E_{\text{AAF}}$ and $E_{\text{CAF}}$ indicate the total energies associated with AFM ordering along $z$, and a two-dimensional checker-board like arrangement within the $xy$ plane, respectively [87]. The values of $J_{ab}$ and $J_c$ obtained using the various methods considered within this work are listed in Tab.2.2 along with the calculated magnetic moments at the Mn site. It is noted that, due to the neglect of orbital degrees of freedom which in LaMnO$_3$ are strongly coupled to spin degrees of freedom, it is not obvious whether a classical Heisenberg model is well suited to give a complete picture of the magnetic properties of LaMnO$_3$. Nevertheless it can still provide an accurate parameterization of the energy differences between the various magnetic configurations. However, the quantitative comparison with the experimental coupling constants derived from spin-wave spectra, i.e. small fluctuations around the AFM ground state, should be taken with care. In view of this, the following conclusions could be drawn about the efficiency of the various DFT and beyond-DFT methods employed in the present study: (i) the magnetic energy differences exhibit appreciable variation between VASP and PWscf leading to differences of about 1-2 meV in the magnetic coupling constants. This is most likely due to the different pseudopotential technique employed in the two codes (PAW method vs. ultrasoft pseudopotential), which lead to qualitative differences especially at PBE+$U$ level, as discussed below.

A more elaborate discussion on the performance of different functionals and methods in predicting the magnetic couplings is given in Refs. [86, 97], where it is concluded that the PAW values are very similar to the full potential FLAPW ones. (ii) In both codes PBE gives the correct A-AFM ground state, delivering a negative $J_c$ ($J_c^{\text{VASP}} = -2.13$ meV, $J_c^{\text{PWscf}} = -0.81$ meV) and a positive $J_{ab}$ ($J_{ab}^{\text{VASP}} = 3.22$ meV, $J_{ab}^{\text{PWscf}} = 4.56$ meV). (iii) The "+$U$" correction to PBE decreases the $E_{\text{FM}} - E_{\text{AAF}}$ energy difference and eventually leads to the prediction of a FM ground state for $U$ larger than a certain value. This critical value is rather different within the two codes used in this study: $J_c$ becomes positive for $U = 2$ eV and $U = 4$ eV, in PWscf and VASP, respectively. We note that this difference is almost entirely due to the difference in the corresponding PBE results. The $U$-induced changes in the magnetic coupling constant $J_c$ relative to the $U = 0$ reference are nearly identical within the two codes. (iv) While $J_c$ within HSE and PBE+$U$(VASP) are very similar for $U$ between 2-3 eV, the ratio

| | $J_{ab}$ | $J_c$ | $\mu$ |
|---|---|---|---|
| PWscf | | | |
| PBE | 4.56 | −0.81 | 3.67 |
| $U = 2$ eV | 5.02 | 0.37 | 3.82 |
| $U = 3$ eV | 5.30 | 0.98 | 3.89 |
| $U = 4$ eV | 5.63 | 1.55 | 3.96 |
| VASP | | | |
| PBE | 3.22 | −2.13 | 3.50 |
| $U = 2$ eV | 3.54 | −0.84 | 3.68 |
| $U = 3$ eV | 3.57 | −0.30 | 3.76 |
| $U = 4$ eV | 3.61 | 0.17 | 3.83 |
| HSE | 2.56 | −0.53 | 3.74 |
| GW$_0$ | | | 3.51 |
| Previous studies | | | |
| GGA+$U$ ($U = 2$ eV)[a] | | −1.30 | 3.46 |
| B3LYP[b] | 2.09 | −1.01 | 3.80 |
| Expt | 1.66[c] | −1.16[c] | 3.87[c], 3.7±0.1[d], 3.4[e] |
| | 1.67[f] | −1.21[f] | |

**Table 2.2:** PBE, PBE+$U$, HSE and GW$_0$ derived magnetic exchange parameters (meV) and magnetic moment at Mn sites $\mu$ ($\mu_B$). The experimental and previously published computed data are taken from: [a] Ref. [86], [b] Ref. [87], [c] Ref. [98], [d] Ref. [65], [e] Ref. [99], and [f] Ref. [100].

between $J_c$ and $J_{ab}$ is rather different within the two approaches. (v) Within the limitations regarding the applicability of a Heisenberg picture to $LaMnO_3$ stated above, HSE seems to be most consistent with the values of the magnetic coupling constants derived from neutron diffraction measurements of spin-wave spectra [98] and magnon data [100]. This further confirms the predictive power of HSE in describing exchange interactions in transition metal oxides, as compared to other available beyond-DFT schemes [101].

We can also see that all methods result in values for the local magnetic moments of the Mn cation that are within the range of variation of the experimental data. Generally, increasing $U$ within PBE+$U$ leads to a more localized magnetization density compared to PBE, and thus increases the local magnetic moments.

On the basis of the above analysis both of the electronic and magnetic properties of $LaMnO_3$, we can conclude that HSE and, when applicable, $GW_0$ (the calculation of magnetic energies at GW level to extract exchange coupling constants is presently not possible, or at least extremely difficult) are the most consistent with the available experimental data in terms of spectral properties, electronic structure and magnetic exchange interactions of $LaMnO_3$.

We can now proceed to the discussion of the Wannier-based description of the $e_g$ bands and the associated TB parameterization. In a TB picture, these ML-WFs can be seen as "antibonding" bands resulting from the $\sigma$-type hybridization between the $Mn(d)$ and $O(p)$ atomic orbitals. Note that in this and the following sections the discussion of the PBE+$U$ results refers to the representative value of $U = 3$ eV, unless explicitly stated otherwise.

Fig. 2.8 shows the PBE and beyond-PBE (PBE+$U$, HSE and $GW_0$) band structures and the corresponding PDOS with $Mn(e_g)$, $Mn(t_{2g})$, and $O(p)$ character. Apart from the obvious hybridization between $Mn(d)$ and $O(p)$ states, "$e_g$-like" orbitals at a certain site can hybridize with "$t_{2g}$-like" orbitals at a neighboring site as a result of the tilt and rotation of the oxygen octahedra. This leads to bands with mixed $e_g/t_{2g}$ character (note the bands around the gap with strong PDOS components of both $e_g$ and $t_{2g}$ character). Due to this strong mixing it is not possible to construct 8 $e_g$ character MLWFs within one energy window used in the disentanglement procedure. The corresponding energy window would inevitably also contain the local minority spin "$t_{2g}$" bands. Since due to the GFO distortion these bands can hybridize with the minority spin "$e_g$" bands, this would lead to MLWFs with strongly mixed $e_g/t_{2g}$ character. To circumvent this problem, two separate sets of 4 local majority and 4 local minority spin MLWFs using two different energy windows [8] are constructed. These energy

windows have to be chosen carefully for each individual method. (This problem is not present for the purely JT($Q^x$) distorted structure, from which we derive most of the model parameters. In this case we calculate a full set of 8 MLWFs).

To find a suitable energy window is quite straightforward for the local majority spin case. The upper bound of the energy window is determined by the upper bound of the highest (in energy) peak of the local majority spin Mn($e_g$) PDOS, while the lower bound of the energy window should be placed above the occupied bands with strong O($p$) and/or local majority spin Mn($t_{2g}$) character. It can be seen from Fig.2.8, that both the lower and the upper bound fall within small gaps separating the bands within the energy window from other bands at lower and higher energies. Furthermore, for PBE+U and HSE the MLWFs can be constructed from a completely isolated set of bands, whereas in the case of PBE and GW$_0$ additional bands with predominant minority spin Mn($t_{2g}$) character are included in the energy window. However, due to the different local spin projection, these latter bands have no noticeable effect on the final MLWFs.

For the local minority spin MLWFs, the upper bound of the energy window can be found in the same way as for the local majority spin bands. Within PBE the lower bound is also easily determined, since it falls within a small gap separating the local minority spin bands with predominant $e_g$ and $t_{2g}$ character. However, no such gap exists within PBE+$U$, HSE, and GW$_0$, and it is thus not possible to fully exclude the $t_{2g}$ character from the resulting MLWFs. Instead, the lower bound of the energy window has to be carefully adjusted by manually checking the $e_g$ character of the calculated MLWFs in real space.

The band dispersion of the so-obtained MLWFs is shown in Fig.2.8 as thick red lines. The 4 (energetically lower) local majority MLWF bands follow very closely the underlying PWscf/VASP bands and the overall dispersion is very similar for all methods. Despite the strong band-entanglement, the dispersion of the 4 (energetically higher) local minority MLWF bands is also very similar within all methods. Only the energetically lowest local minority spin band within PBE+$U$ and HSE exhibits strong deviations from the corresponding PBE and GW$_0$ case. This is due to the above-mentioned difficulty to exclude the $t_{2g}$ character in a controlled way. Conclusions drawn from such sets of MLWFs should therefore be taken with care. Overall, the similarities in the band structure and PDOS between PBE and GW$_0$ as well as between PBE+$U$ and HSE has been noted, regarding the degree of hybridization between Mn($e_g$), Mn($t_{2g}$) and O($p$) orbitals, that have been pointed out in the previous section, are also reflected in the MLWF bands.
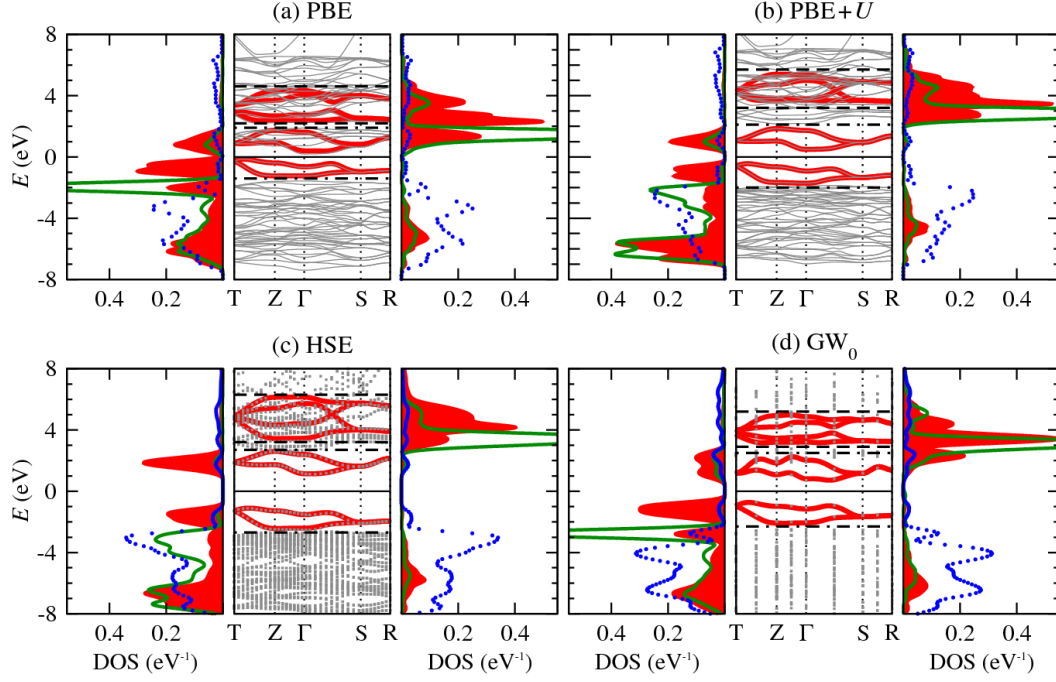
**Figure 2.8:** Effective $e_g$ MLWF bands (thick red lines) for LaMnO$_3$ superimposed to the *ab initio* electronic bands (gray thin solid/dotted lines) and associated normalized PDOS (to the left and right of the band structure plots) corresponding to Mn($e_g$) (red filled areas), Mn($t_{2g}$) (green lines), and O($p$) character (blue dots). In the left/right PDOS graphs, Mn($d$) PDOSs correspond to the local majority/minority Mn sites while the O($p$) PDOS is calculated as an average over all O sites. The two energy windows used in the wannier-downfolding are indicated by dashed and dot-dashed lines. The Fermi level (E=0 eV) is set in the middle of the gap. It is to be noted that Fig.2.2 (that was shown in the introduction section) corresponds to HSE bands and PDOS for room-temperature data whereas this plot corresponds to the optimized results.

To further demonstrate the similarities between MLWFs calculated at different levels of theory, the real space representation of the 2 MLWFs localized at a certain Mn site, projected on the $xy$ plane are shown in Fig.2.9. The dominant $e_g$ character at the central Mn site together with the "hybridization tails" of mostly $p$ character at the surrounding O sites is clearly visible for all MLWFs and methods. For the local majority spin MLWFs (first and third row), there is essentially no visible difference in orbital character between PBE and PBE+$U$, only the O($p$) tails are marginally stronger if the Hubbard $U$ correction is applied. At the HSE level, both local majority MLWFs exhibit significant $x/y$ asymmetry, leading to more pronounced O($p$) hybridization tails along the short and long Mn-O bond for the $|3z^2 - r^2\rangle$-like and $|x^2 - y^2\rangle$-like function, respectively. Within GW$_0$, the central $e_g$-like part as well as the O($p$) tails are less asymmetric than for HSE, and appear similar to PBE/PBE+$U$ for both local majority MLWFs. In comparison with the local majority MLWFs, the O($p$) hybridization tails of the local minority MLWFs (second and fourth row) are generally less pronounced. There is no significant difference between the local minority spin MLWFs calculated using the different methods. Even at the PBE+$U$ and HSE levels, for which the admixture of the $t_{2g}$ character could not be controlled systematically, there is no apparent difference in comparison with PBE.

The orbitally ordered states resulting from this set of MLWFs basis set is shown in Fig.2.10 in terms of charge density isosurfaces of the highest occupied and lower unoccupied orbitals associated to the $e_g$ bands below and above E$_F$ in the lower energy window as defined in Fig. 2.8. This plot clearly shows the staggered ordering at neighbouring Mn sites and the significant $p - d$ hybridization at the oxygen sites. As a comparison, the corresponding staggered ordering associated to the highest occupied $e_g$-like bands as obtained from the full *ab initio* self-consistent charge density (without downfolding) within the various methods employed in the present study is shown in Fig.2.11. The similarities between the *ab initio* and wannierized orbital ordering is a further demonstration of the quality and reliability of the wannierization procedure.
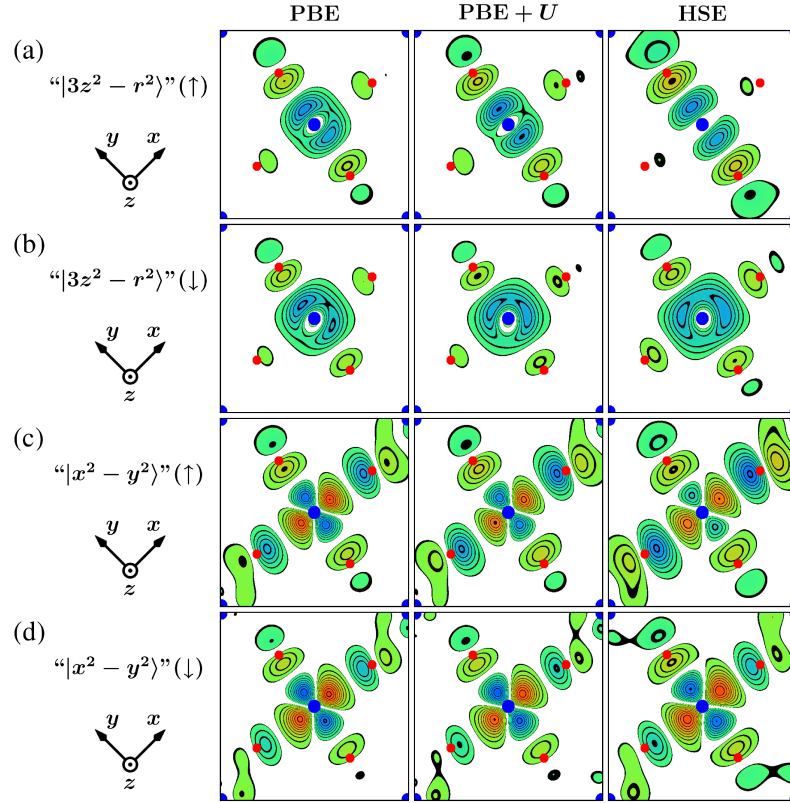
**Figure 2.9:** Real space representation of the four $e_g$ MLWFs corresponding to a certain Mn site, projected on the $xy$ plane cutting through the Mn site. Black iso-lines correspond to $\pm N/\sqrt{V}$ with integer $N \geq 1$, the white region is defined by values in the interval $[-1/\sqrt{V}, +1/\sqrt{V}]$, where $V$ is the volume of the unit cell. Blueish/reddish hue denotes negative/positive values of MLWFs and Mn and O atoms are shown as blue and red spheres, respectively.
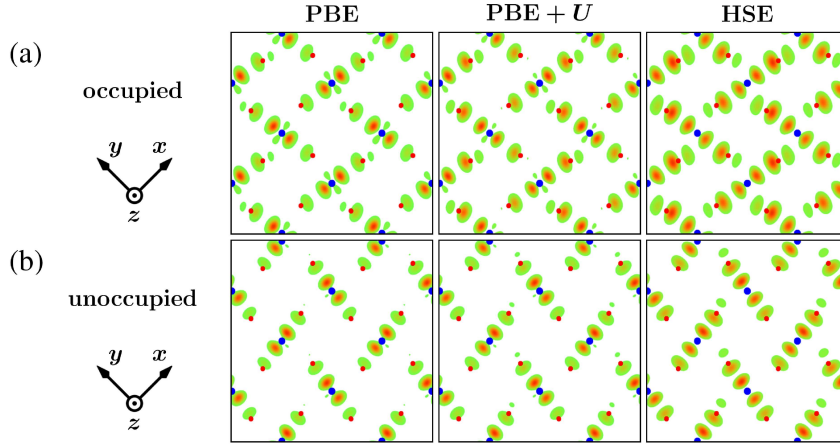
**Figure 2.10:** Charge density isosurfaces of the orbitally ordered states associated to the highest occupied (a) and lower unoccupied (b) MLWFs orbitals. Color coding and symbols are the same as in Fig. 2.9.
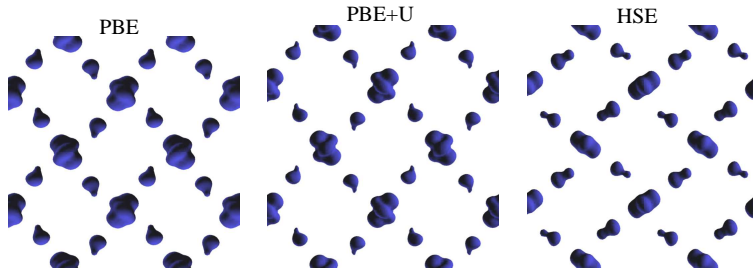


**Figure 2.11:** Charge density isosurfaces of the highest occupied $e_g$ orbitals (from $E_F$ to the lower energy bound as defined in Fig.2.8) showing the orbitally ordered state of LaMnO$_3$ obtained using the different methodologies employed in this study.

## 2.5 TB results

### 2.5.1 TB without $\hat{H}_{el-el}$: Model A

The TB model Hamiltonian to be parametrized is the following (i.e. MH without the *el-el* interaction term, $\hat{H}_{el-el}$):

$$\hat{H} = \hat{H}_{\mathrm{kin}} + \hat{H}_{\mathrm{Hund}} + \hat{H}_{\mathrm{JT}} \tag{2.43}$$

(Refer to Sec. 2.2).

We will discuss the TB parametrization (Model A) for the TB Hamiltonian presented above (as proposed by the authors of [8]) in detail in this section and also discuss the results obtained i.e. Model parameters in effective $e_g$ basis based on various model structures with both FM (which always leads to a metallic system) and A-AFM order, with individual structural distortion modes frozen in (using PBE). The TB parameters at PBE level obtained in [8] using the PWscf code and the VASP results will be compared in this section. This will serve as a benchmark for our computational machinery which will then be elaborated further for Model B.

As already introduced, the parameters to be determined are: Spin-dependent nearest-neighbour hopping ($t^{\uparrow\uparrow}$, $t^{\downarrow\downarrow}$), Next-nearest neighbour hopping $t^{xy}$ and $t^{2z}$, JT induced $e_g$ splitting $\tilde{\lambda}$, JT coupling strength ($\lambda^{\uparrow}$, $\lambda^{\downarrow}$), Hund's rule coupling strength ($J_H$), GFO reduction factor ($\eta^{\uparrow}$, $\eta^{\downarrow}$).

Starting from the ideal cubic perovskite structure, the effect of each distortion is analysed by gradually increasing the amount of distortion. A linear superposition of the Wyckoff postions in the cubic perovskite structure and the distortion (JT or GFO) is considered which is represented as

$$\mathbf{R}(\alpha_x) = (1 - \alpha_x)\mathbf{R}^{(i)} + \alpha_x\mathbf{R}^{(x)} \tag{2.44}$$

$\alpha_x$ is taken to vary between 0 to 1. $\mathbf{R}^i$ refers to the Wyckoff positions in the case of cubic structure and x= JT or GFO distortions.

We will now discuss the results obtained for the various structural distortions and also the role of the distortion in the computed TB parameters.

The effect of structural distortions on $e_g$ bands is compared in Fig. 2.12. All the bands shown in the Fig.2.12 refer to calculations performed on experimental unit-cell volume. Comparing the $e_g$ bands obtained using different structural modifications we observe the following: In the cubic structure, the $e_g$ bands
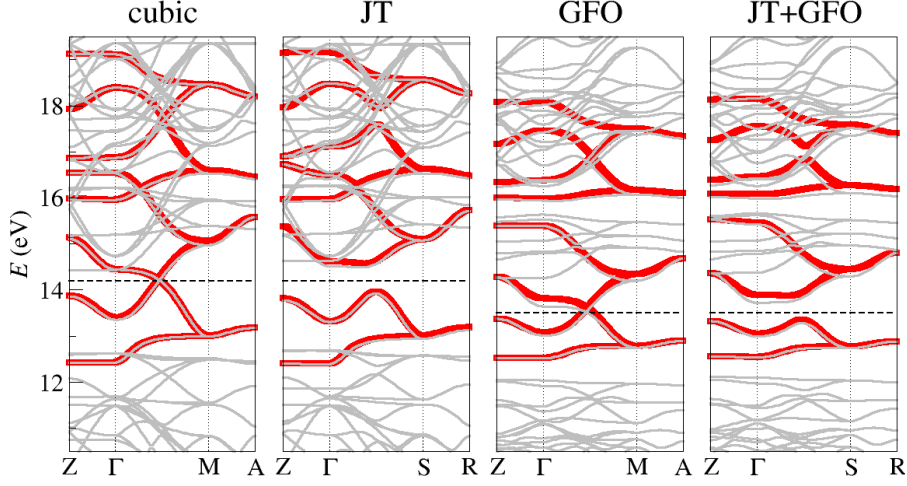
**Figure 2.12:** The effect of structural distortions on the band structure. These band structures were calculated by the authors of [8] wherein the calculations were performed using PwSCF (DFT at GGA level). It is seen in the figure that the JT opens up the gap and the GFO reduces the bandwidth.

exhibit a metallic character. In the JT distorted structure, a gap opens up. The GFO structure shows a metallic behaviour, and in the JT+GFO structure, an insulating gap opens up. It could also be observed that the bandwidth of the $e_g$ bands in the cubic and JT distorted structure are very similar in magnitude whereas the bandwidth in the GFO and JT+GFO structures decreases by around 16% when compared to the cubic and JT distorted structures.

In the ideal cubic perovskite structure, two $e_g$ MLWFs are constructed for the FM configuration (Fig. 2.13(a) and (b)) and 2 pairs of MLWFs, localized at the two Mn sites within the unit cell, are constructed for the AAFM magnetic configuration (see Fig.2.13(c)). In Fig.2.13(c), A-AFM cubic refers to the bands corresponding to an ideal cubic perovskite structure doubled in the $\hat{z}$ direction, whereas in Fig. 2.12, "cubic" refers to a cell in which a=b=a$_c\sqrt{2}$ (a$_c$ - ideal cubic perovskite cell lattice parameter) and doubled in $\hat{z}$ direction. To get an overall picture of all the hoppings in the MLWFs basis, the magnitudes of all hoppings in the case of FM majority spin channel cubic perovskite structure is shown in the Fig. 2.14. It could be seen that the hopping along the Cartesian axes are the most dominant and also it decays slowly with respect to the intersite distance $\Delta$R and as a result, the terms corresponding to intersite distances $\Delta$R = 2a$_c$ and 3a$_c$ are comparable with the second nearest neighbour hopping for which $\Delta$R = $\sqrt{2}$a$_c$.
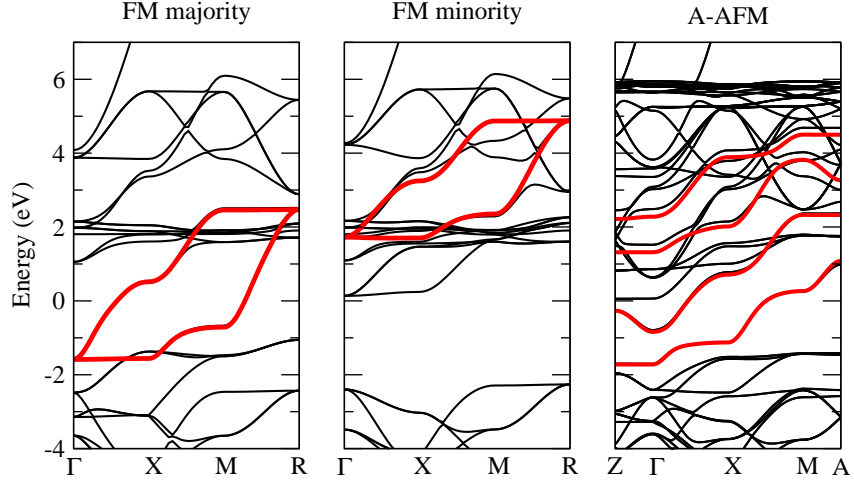
**Figure 2.13:** FM majority and minority and A-AFM bandstructures and $e_g$ ML-WFs. The A-AFM bandstructure has been constructed by considering an ideal cubic perovskite structure doubled in the $\hat{z}$-direction.
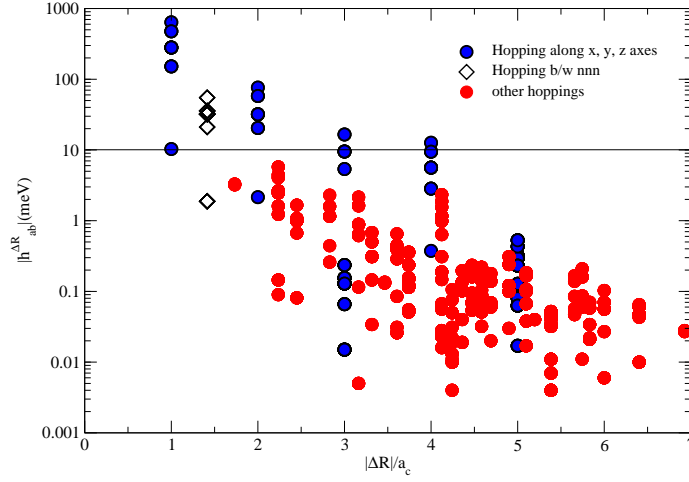


**Figure 2.14:** All the non-zero matrix elements plotted as a function of the intersite distance $|\Delta\mathbf{R}|$ in the ideal cubic perovskite structure (FM majority spin channel). Blue filled circles represent the hopping along the Cartesian axes. Diamond symbols represent the hopping between nnn, Red filled circles represent all the other hoppings.

In the JT distorted structure, 4 e$_g$ MLWFs are constructed for FM configuration (up and down) and 8 MLWFs for the AAFM configuration. The effect of the JT distortion is analysed by using the Eqn. 2.44 by varying $\alpha_{JT}$ from 0 (cubic) to 1 (fully JT distorted structure). As already introduced, the JT term in the TB Hamiltonian is given as,

$$\hat{H}_{JT} = \lambda \sum_{\mathbf{R},\sigma,a,b} \hat{c}^\dagger_{a\mathbf{R}\sigma}(Q^x_{\mathbf{R}}\tau^x_{ab} + Q^z_{\mathbf{R}}\tau^z_{ab})\hat{c}_{b\mathbf{R}\sigma} \tag{2.45}$$

Where $\tau^x$ and $\tau^z$ are the respective Pauli matrices. So, it could be seen that within the model, the effect of the JT distortion is a linear coupling to the onsite terms according to

$$\mathbf{t}^0 = \begin{pmatrix} e_0 - \lambda Q^z_{\mathbf{R}} & -\lambda Q^x_{\mathbf{R}} \\ -\lambda Q^x_{\mathbf{R}} & e_0 + \lambda Q^z_{\mathbf{R}} \end{pmatrix} \tag{2.46}$$

Where e$_0$ is the onsite energy. The variation of different matrix elements in the JT distorted structure are presented in the Fig. 2.15.

To find the parameter $\lambda$, the slope of linear variation of h$^0_{12}$ which is shown in Fig.2.15(a) is considered. The slope could be written as -$\lambda Q^x_0$ and it is identical for FM and AAFM majority spin channels whereas it is smaller in the case of minority spin channel, the reason for this could be attributed to the hybridization with the surrounding oxygen orbitals. When this value is compared with the previous results [7], it is observed that the value is atleast a factor of two larger. This could be explained by the strong linear splitting observed for the off-diagonal in-plane nn hopping as shown in Fig.2.15(c) and (d) that is caused by the JT distortion. This linear splitting is taken into account by the parameter which is represented as $\tilde{\lambda}$.

Next we consider the variation from the cubic to GFO distorted structure. As in the case of JT distorted structure, 4 e$_g$ MLWFs are constructed for FM configuration (up and down) and 8 MLWFs for the AAFM configuration. The effect of the GFO distortion is the reduction of the bandwidth (seen in the Fig. 2.12) and the reduction in the hopping parameters in the x-y plane could be observed in the Fig. 2.16. The hopping parameters along the $\hat{z}$ direction also varies similar to that of the variation in the xy plane. The parameter in the TB model which is introduced due to the GFO distortion is $\eta$ which is calculated from the ratio of the h$^{x/z}(\alpha_{GFO})$ to h$^{x/z}(\alpha_{GFO}=0)$ according to the equation,

$$h^{x/z}(\alpha_{GFO}) = h^{x/z}(0)(1 - \eta\alpha^2_{GFO}) \tag{2.47}$$
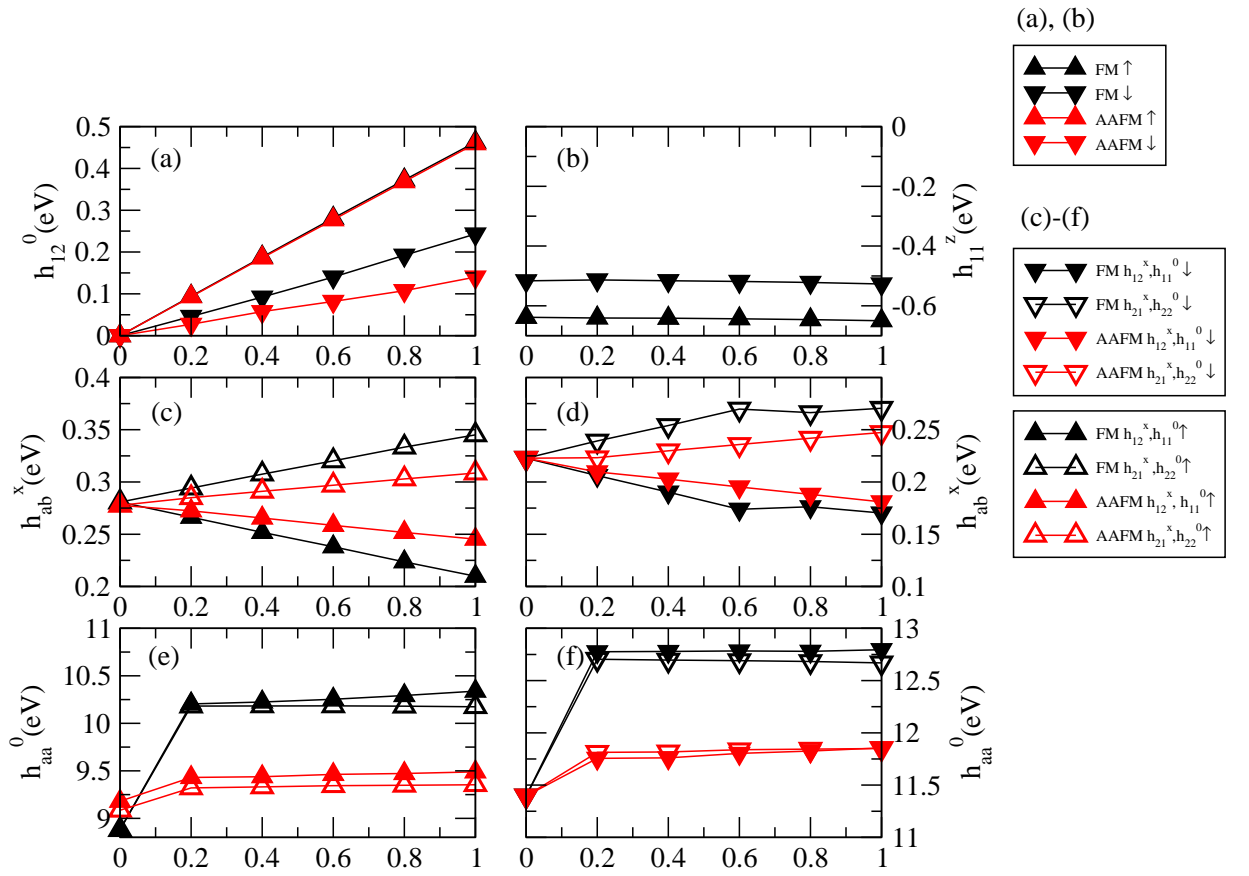
**Figure 2.15:** Variation of different matrix elements with the amount of disortion from cubic to JT.
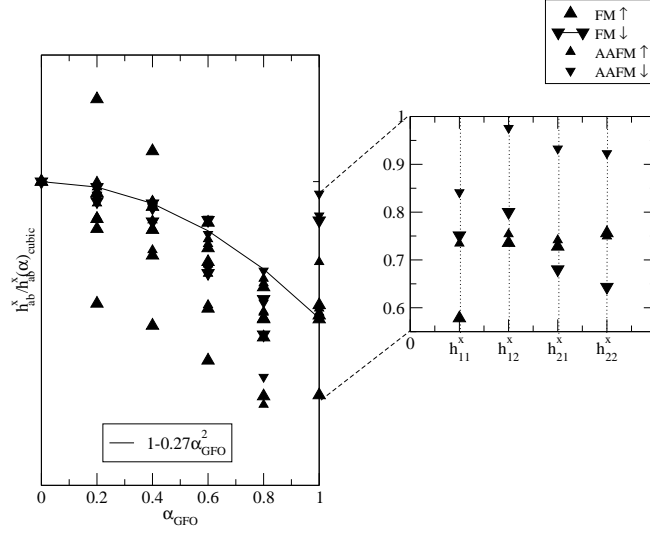
**Figure 2.16:** Variation of the matrix elements as a function of the amount of GFO disortion. The variation of the matrix elements are fitted using the function $(1\text{-}0.27\alpha_{GFO}^2)$ where 0.27 represents the value of $\eta$ (GFO reduction factor).The inset plot shows the matrix elements corresponding to $\alpha_{GFO} = 1$.
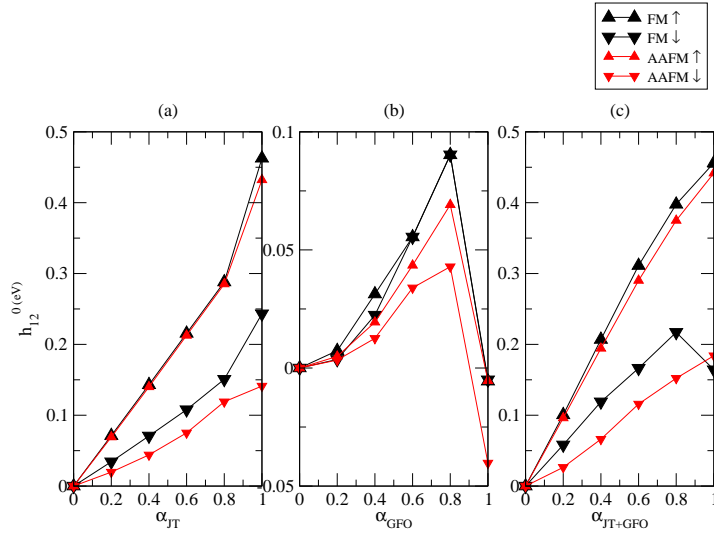


**Figure 2.17:** Variation of the on-site off-diagonal matrix elements with the amount of distortion from (a) cubic to JT (b) cubic to GFO (c) cubic to JT-GFO.

The parameter, Hund's rule coupling strength $J_H$ is calculated by noting the fact that Hund's coupling leads to an onsite splitting equal to $2J_H$. It could be calculated by taking the difference between the onsite terms in the case of FM majority and FM minority spin channels divided by 2. The value turns out to be nearly equal for each of the individual structural distortions which ranges from 1.3 to 1.5 eV.

The effects of the JT, GFO and the combined JT+GFO as a function of the amount of distortion is shown in Fig. 2.17. The plot shows the variation of the onsite off-diagonal elements as a function of the amount of distortion $\alpha_x$ (x = JT, GFO and JT+GFO). There is a strong linear dependence of the off-diagonal matrix elements $h_{12}^0$ seen on varying the amount of distortion from cubic to JT. On varying the distortions from cubic to GFO, $h_{12}^0$ increases and then drops at $\alpha_{GFO} = 1$ i.e. fully distorted GFO structure. Comparing Fig.2.17(a) and (c), it is seen that the GFO distortion reduces the on-site matrix elements which are otherwise proportional to the JT distortion. This is seen to be an evidence for the ligand-field nature of the JT coupling, that it is mediated by the Mn-O hybridization (which is reduced by the GFO distortion).

The TB parameters are compared with a simple model [7] that includes only the nearest-neighbours and the parameters of this model have been chosen by the typical simplified fitting procedure. The difference between the simplified model and the refined model (parameters from MLWFs) is that the simple model included only the hopping parameters $t(a_c)$, $\lambda$ and $J_H$ whereas the refined model includes the further nearest neighbours, the local spin-dependent and non-local terms, JT coupling terms and the reduction due to GFO disortion. The obtained parameters from the simple model and the refined model have been compared in Tab.2.3. It is seen that in the refined model, where the TB parameters are calculated from the MLWFs, the TB dispersion follows very closely the underlying $e_g$ MLWFs. The simple model, which does not take into account the GFO reduction factor ($\eta$) and the next-nearest-neighbour hoppings, deviates much stronger from the MLWF bands than the refined model, but still pretty much captures the overall band dispersion quite well.

Thus the authors of [8] have shown that the MLWFs proves to be an excellent tool to calculate the model parameters. It enables the refinement of the models to arbitrary accuracy towards MLWF description.

| | Refined [8] | Refined (VASP) | Simple [7] |
|---|---|---|---|
| t$^{\uparrow\uparrow}$ (eV) | -0.648 | -0.638 | -0.492 |
| t$^{\downarrow\downarrow}$ (eV) | -0.512 | -0.516 | -0.492 |
| t$^{\uparrow\downarrow}$ (eV) | -0.569 | -0.577 | -0.492 |
| $\eta$ | 0.26 | 0.25 | |
| $\tilde{\lambda}$ (eV/$\mathring{A}$) | 0.53 | 0.421 | 0 |
| $\lambda^{\uparrow}$ (eV/$\mathring{A}$) | 3.19 | 2.873 | 1.64 |
| $\lambda^{\downarrow}$ (eV/$\mathring{A}$) | 1.33 | 1.546 | 1.64 |
| t$^{xy}$ (eV) | -0.018 | -0.021 | 0 |
| t$^{2z}$ (eV) | -0.020 | -0.020 | 0 |
| J$_H$ (eV) | 1.5 | 1.257 | 1.805 |

**Table 2.3:** Collection of parameters obtained using a simple model [7] and Model A parameters and comparison between the PWscf results [8] with VASP.
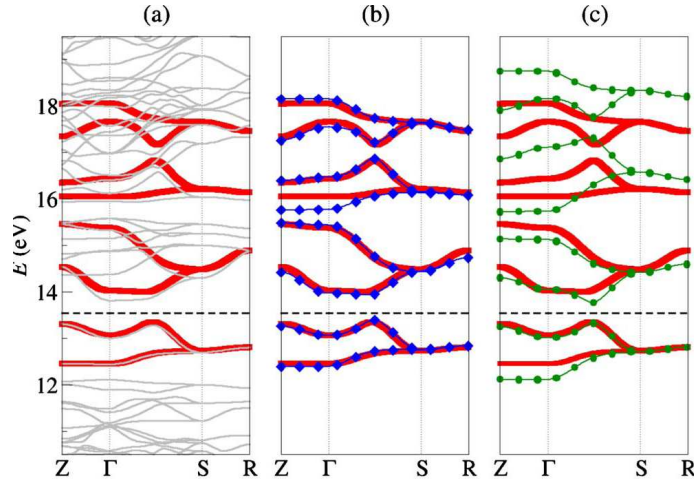


**Figure 2.18:** Figure from [8] showing (a) DFT and MLWFs bands for the A-AFM experimental Pbnm structure (b) Comparison of the MLWFs and the refined TB model (c) Comparison of the MLWFs and the simple TB model.
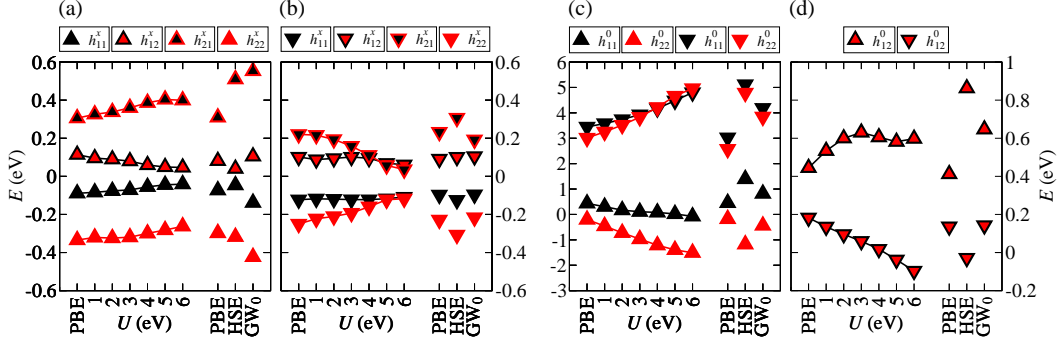
**Figure 2.19:** Hamiltonian matrix elements in the basis of MLWFs for the experimental *Pbnm* structure: nearest-neighbor terms corresponding to local majority (a) and minority (b) spin projection, diagonal (c) and off-diagonal (d) on-site terms. Local majority and minority spin projections are indicated by up and down triangles, respectively. Left/right parts of the horizontal axis corresponds to PWscf/VASP results.

## 2.5.2 TB without $\hat{H}_{el-el}$ :Model B-1

Under this model, we attempt to parametrize the Hamiltonian which is given as,

$$\hat{H} = \hat{H}_{\text{kin}} + \hat{H}_{\text{Hund}} + \hat{H}_{\text{JT}} \tag{2.48}$$

(Refer to Sec. 2.2). by constructing the TB parametrization from only two crystal structures: purely JT ($Q^x$) distorted structure and the experimental *Pbnm* structure, in both the cases with A-AFM order, which then yields an insulating solution. Within model, only two contributions to the on-site part of the TB Hamiltonian are considered: the Hund's rule coupling $\hat{H}_{\text{Hund}}$ and the JT coupling $\hat{H}_{\text{JT}}$. The strength of the Hund's rule coupling $J_{\text{H}}$ is determined from the spin splitting of the on-site diagonal matrix elements $h_{aa}^0$ for the *Pbnm* structure, averaged over both orbitals . The JT coupling strength $\lambda^s$ for local spin-projection $s$ is determined from the splitting of the eigenvalues of the on-site Hamiltonian matrix $\underline{\underline{h}}^0$ and the JT amplitude $Q^x$ for the purely JT($Q^x$) distorted structure. As can be seen from Fig.2.19(c,d), the corresponding matrix elements are strongly spin-dependent, leading to large differences in the corresponding JT coupling constants. Similar to the hopping amplitudes, $\lambda^s$ is reduced by a factor $(1 - \eta_\lambda^s)$ due to the GFO distortion, which is determined from the ratio between $\lambda^s$ calculated for the *Pbnm* and JT($Q^x$) structures.

Table 2.4 lists the obtained TB parameters corresponding to Model B-1 (TB without $\hat{H}_{el-el}$) calculated within the various levels of approximation. Both hopping amplitudes and JT coupling strength correspond to the case without GFO distortion. It can be seen from the first two rows of Tab.2.4 that the parameterization that is used in the present study yields only marginal differences for the PBE hopping parameters and Hund's rule coupling in comparison with [8]. This corroborates the quality of our TB parameterization based on only two structures (JT($Q^x$) and *Pbnm* with A-AFM order). Note, that a crystal structure derived from low-temperature measurements [65] has been used here, whereas in [8] the room temperature measurements of Ref. [66] have been used. The JT coupling parameters differ slightly more from [8] due to the revised definition of $\lambda^s$ used in the present study. Another important change arises from the use of 3 separate GFO reduction factors $\eta_t^\uparrow$, $\eta_t^\downarrow$, and $\eta_\lambda$, instead of using one averaged value as it was done in [8]), which provides a more accurate TB description of the MLWF bands. It can be also seen from Tab.2.4 that at the PBE level, there is essentially no difference between the hopping amplitudes calculated using PWscf and VASP. There is a 12 % difference in $J_H$ between PBE(VASP) and PBE(PWscf), which could be related to the noticeable differences in the energetics of the various magnetic configurations discussed earlier.

Comparing the parameters obtained from the beyond-PBE methods with the pure PBE case, it could be seen that the hopping parameter $t^{\uparrow\uparrow}$ is generally increased in all beyond-PBE methods. As was shown in [81], this can be understood within an extended nearest neighbor TB model including both Mn($d$) and O($p$) states, from which an effective $e_g$-only model can be derived in the limit of large energy separation $\varepsilon_{dp}$ between the $d$ and $p$ orbitals. The effective hopping $t_{dd}^{\mathrm{eff}}$ in the $e_g$ model is then given in terms of the nearest neighbor hopping amplitude $t_{dp}$ of the extended $d$-$p$ model as $t_{dd}^{\mathrm{eff}} = t_{dp}^2/\varepsilon_{dp}$ (Refer to Appendix for details on the $e_g$ model and $d$-$p$ model). The increase of $t^{\uparrow\uparrow}$ is therefore consistent with the observation that all beyond-PBE methods lower the $e_g$ bands relative to the lower-lying oxygen $p$ bands. The small decrease of $t^{\downarrow\downarrow}$ within PBE+$U$ (for small values of $U \lesssim 2$ eV) can be explained in the same way, since here the corresponding energy separation between O($p$) and Mn($e_g$) increases. The JT parameter $\widetilde{\lambda}$ is generally very similar for PBE, PBE+$U$, and GW$_0$, while a strong enhancement of $\widetilde{\lambda}$ can be seen for HSE, which is consistent with the strong $x/y$ asymmetry of the corresponding MLWFs seen in Fig. 2.9(c). Since the changes of the already rather small further-neighbor hoppings within the beyond-PBE methods are very small, the corresponding PBE values are used for simplicity. The GFO

| | Hopping parameters | | | | | | | On-site parameters | | | |
|---|---|---|---|---|---|---|---|---|---|---|---|
| | $t^{\uparrow\uparrow}$ | $t^{\downarrow\downarrow}$ | $\widetilde{\lambda}$ | $t^{xy}$ | $t^{2z}$ | $\eta_t^{\uparrow}$ | $\eta_t^{\downarrow}$ | $J_{\mathrm{H}}$ | $\lambda^{\uparrow}$ | $\lambda^{\downarrow}$ | $\eta_\lambda$ |
| | | | | | | PWscf | | | | | |
| PBE [8] | 648 | 512 | 530 | 18 | 30 | 0.26 | 0.26 | 1.50 | 3.19 | 1.33 | 0.26 |
| PBE | 632 | 512 | 523 | 12 | 51 | 0.28 | 0.39 | 1.56 | 3.35 | 1.07 | 0.22 |
| PBE+$U$ | 748 | 482 | 516 | 12 | 51 | 0.41 | (0.39) | 2.16 | 5.22 | (1.07) | 0.21 |
| | | | | | | VASP | | | | | |
| PBE | 630 | 503 | 516 | 13 | 50 | 0.35 | 0.42 | 1.33 | 3.21 | 1.02 | 0.23 |
| HSE | 750 | 497 | 707 | 13 | 50 | 0.40 | 0.20 | 2.42 | 10.25 | 0.96 | 0.28 |
| GW$_0$ | 746 | 469 | 490 | 13 | 50 | 0.24 | 0.41 | 1.90 | 4.43 | 0.88 | 0.04 |

**Table 2.4:** The TB model parameters as derived from PBE and beyond-PBE band structures (Model B-1, in PBE+U ,U=3 eV has been used). Since the PBE+$U$ values of $\eta_t^{\downarrow}$ and $\lambda^{\downarrow}$ are unreliable (see text), the corresponding PBE values (in brackets) to compute the TB bands displayed in Fig.2.20 are used. Units: $t^{\uparrow\uparrow}$, $t^{\downarrow\downarrow}$, $t^{xy}$, $t^{2z}$ in meV; $\widetilde{\lambda}$ in meV/Å; $J_{\mathrm{H}}$ in eV; $\lambda^{\uparrow}$, $\lambda^{\downarrow}$ in eV/Å; $\eta_t^{\uparrow}$, $\eta_t^{\downarrow}$, $\eta_\lambda$ are unit-less.

reduction factors for the hopping amplitudes, $\eta_t^{\uparrow}$ and $\eta_t^{\downarrow}$, are slightly decreased within GW$_0$, whereas $\eta_t^{\uparrow}$ is increased for PBE+$U$ and HSE, and $\eta_t^{\downarrow}$ is strongly decreased in HSE. Due to the strong mixing between minority spin $e_g$ and $t_{2g}$ bands within PBE+$U$ (see also Fig.2.20(b)), the determination of $\eta_t^{\downarrow}$ is rather unreliable in this case, and therefore the corresponding PBE value has been used. It could be noted that the same effect also leads to the strong changes in the local minority hopping matrix elements within the $xy$ plane calculated within PBE+$U$ for $U \gtrsim 3$ eV (see Fig.2.19(b)). Using the HSE and GW$_0$ methods this problem is not encountered.

For all beyond-PBE methods, a significant increase of $J_{\mathrm{H}}$ and $\lambda^{\uparrow}$ can be observed, which in the TB model gives rise to an increase of the spin splitting and the band gap, respectively. The change of $\lambda^{\downarrow}$ compared to PBE is very small for both HSE and GW$_0$. Due to the inaccurate treatment of the minority spin bands, PBE+$U$ gives an unrealistically small value of $\lambda^{\downarrow} = 0.30$ eV/Å, which is therefore substituted with the corresponding PBE value. While $\eta_\lambda$ does not change significantly for small values of the Hubbard $U$, a small increase (significant decrease) is observed for HSE (GW$_0$).
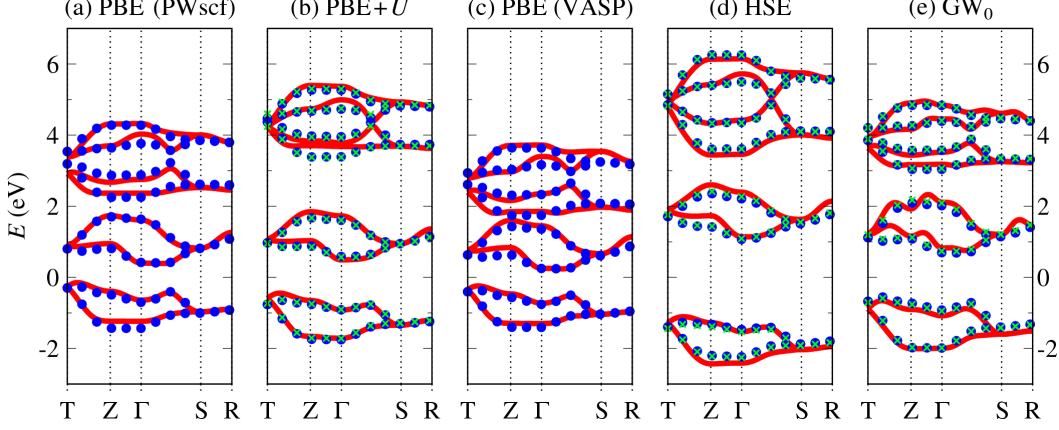
**Figure 2.20:** Comparison of the band dispersion corresponding to MLWFs (red lines), the TB Model B-1 using parameters given in Tab.2.4 (blue circles), and the TB Model B-2 with interaction parameters given in Tab.2.5 (green crosses).

To assess the quality of the parameterization, the TB parameters tabulated in Tab.2.4 to compute the resulting $e_g$ band structure is used. In Fig.2.20(a) and (c), the band dispersions of the TB model (blue filled circles) and the MLWFs (thick red lines) for the experimental *Pbnm* structure within the PBE approximation are compared. Despite the many simplifications made in the construction of the model parameters, the TB model can reproduce the MLWF bands to a remarkable accuracy (for both PWscf and VASP). The reliability of the beyond-PBE TB representation can be appreciated by the overall excellent match between the TB and MLWFs bands shown in Fig.2.20(b), (d) and (e), which exhibit the same quality as observed at the PBE level. This is particularly true for the band gap, whose method-dependent changes (see Tab.2.1) are perfectly reflected in the TB description.

## 2.5.3  TB with $\hat{H}_{el-el}$ : Model B-2

Now, we will discuss the alternative TB parameterization in which the modifications induced by the beyond-PBE methods are treated as a perturbation to the "noninteracting" PBE description by explicitly considering the *el-el* interaction and using the simplified mean-field approximation in the TB Hamiltonian.

We have already discussed the procedure for calculating U$_W$ ( this corresponds to that calculated in the Model B-2 which is different from U corresponding to PBE+U) under the section 2.3.2. We will discuss the results in this section.

| | $J_\mathrm{H}$ | $\Delta\varepsilon^\uparrow$ | $\Delta n^\uparrow$ | $U_\mathrm{W}^{(J)}$ | $U_\mathrm{W}^{(\lambda)}$ | $\Delta J_\mathrm{W}^{(\lambda)}$ |
|---|---|---|---|---|---|---|
| | | | | | Interaction parameters | |
| | | | PWscf | | | |
| PBE | 1.56 | 1.09 | 0.71 | - | - | - |
| PBE+$U$ | 2.16 | 1.66 | 0.80 | 2.40 | 0.70 | 0.42 |
| | | | VASP | | | |
| PBE | 1.33 | 1.04 | 0.70 | - | - | - |
| HSE | 2.42 | 3.10 | 0.89 | 4.37 | 2.31 | 0.51 |
| GW$_0$ | 1.90 | 1.80 | 0.70 | 2.30 | 1.09 | 0.30 |

**Table 2.5:** The interaction parameters determined in Model B-2. Note, that in Model B-2 the on-site parameters are set to the PBE values while the hopping parameters are set to the values given in Tab.2.4. Units: all quantities are in eV except $\Delta n^\uparrow$ which is unit-less.

It can be seen that within PBE+$U$, the parameter $U_\mathrm{W}^{(J)}$ is almost as large as the value of $U = 3$ eV used for the Hubbard parameter within the PBE+$U$ calculation, whereas the parameter $U_\mathrm{W}^{(\lambda)}$ is significantly smaller than that. We note that, as discussed in [81], the Hubbard correction within PBE+$U$ is applied to rather localized atomic-like orbitals, whereas the parameter $U_\mathrm{W}$ corresponds to more extended $e_g$-like Wannier orbitals. The JT splitting is strongly affected by hybridization with the surrounding oxygen ligands and is thus quite different for atomic-like and extended Wannier states [81]. As a result, $U_\mathrm{W}^{(\lambda)}$ is quite different from the $U$ value used within PBE+$U$, and the smaller value of $U_\mathrm{W}^{(\lambda)}$ can thus be related to the fact that the *el-el* interaction is more screened in the more extended effective $e_g$ Wannier orbitals. On the other hand, the similarity between $U_\mathrm{W}^{(J)}$ and the $U$ value used within PBE+$U$ indicates that the local spin-splitting is more or less the same for both sets of orbitals, which is consistent with the view that this splitting is essentially an atomic property. A similar difference between $U_\mathrm{W}^{(J)}$ and $U_\mathrm{W}^{(\lambda)}$ is also observed for HSE and GW$_0$. The large values of $U_\mathrm{W}$ delivered by HSE reflects the larger spin splitting and band gap in the corresponding band structure compared to PBE+$U$ and GW$_0$.

The large difference between the two parameters $U_\mathrm{W}^{(J)}$ and $U_\mathrm{W}^{(\lambda)}$ also indicates that it is not possible to map the electron-electron interaction effects manifested in the on-site matrix corresponding to effective $e_g$ orbitals to only one interaction

parameter while using PBE as "noninteracting" reference. Similar conclusions have already been reached in [81] for the PBE+$U$ case. From the current study we can conclude that the modification of the local spin splitting (described by $U_\mathrm{W}^{(J)}$) and the enhancement of the JT induced orbital splitting (described by $U_\mathrm{W}^{(\lambda)}$) that arise in the KS or GW$_0$ quasiparticle band structures due to the beyond-PBE treatment of exchange and correlation, are not compatible with a simple mean-field Hubbard-like correction to an otherwise "non-interacting" TB Hamiltonian with two effective $e_g$ orbitals per Mn site and only one parameter describing the *el-el* interaction. This leads to an important conclusion of the present study with regard to methods such as LDA+$U$ or LDA+DMFT, which supplement a "non-interacting" KS Hamiltonian with a Hubbard interaction between a strongly interacting subset of orbitals: using different methods for obtaining the noninteracting reference can lead to significant differences, and it is by no means clear whether PBE (GGA) or even LDA always provides the best starting point for a more sophisticated treatment of correlation effects. Our results also emphasize the importance of finding improved ways to account for the double counting correction when using different electronic structures as noninteracting reference.

In order to see how, within the limitations discussed in the preceeding paragraph, a TB Hamiltonian can reproduce the MLWF band dispersion, a modified parameterization using $U_\mathrm{W}^{(\lambda)}$ to model the *el-el* interactions is considered. Since in that way the correlation-induced increase of the spin splitting is only partially covered by the *el-el* term , it is corrected by introducing an "empirical" correction to the Hund's rule coupling:

$$\Delta J_\mathrm{W}^{(\lambda)} = J_\mathrm{H} - J_\mathrm{H}^{\mathrm{(PBE)}} - \frac{1}{4} U_\mathrm{W}^{(\lambda)} \tag{2.49}$$

Note, that as already discussed (Refer to Sec.2.3.2), we could choose $U_\mathrm{W}^{(J)}$ as the *el-el* interaction parameter and define an appropriate correction to $\lambda^\uparrow$.

Figure 2.20 also shows the dispersion calculated from such a modified TB model with explicit *el-el* interaction, where the correlation induced change of the spin splitting and band gap is described by two interaction parameters, $U_\mathrm{W}^{(\lambda)}$ and $\Delta J_\mathrm{W}^{(\lambda)}$, while $J_\mathrm{H}$, $\lambda^\uparrow$, $\lambda^\downarrow$, and $\eta_\lambda$ are fixed at their respective PBE values. In addition, the hopping amplitudes are set to the values given in Tab.2.4. The band dispersions using these sets of parameters (shown as green crosses in Fig.2.20) again almost perfectly follow the MLWF bands. The agreement between the bands calculated within the two parameterizations (Model B-1 and B-2) also reflects the transferability of the on-site parameters between the structures with and without the GFO distortion.

| | Hopping parameters | | | | | | | On-site parameters | | | |
|---|---|---|---|---|---|---|---|---|---|---|---|
| | $t^{\uparrow\uparrow}$ | $t^{\downarrow\downarrow}$ | $\tilde{\lambda}$ | $t^{xy}$ | $t^{2z}$ | $\eta^{\uparrow}$ | $\eta^{\downarrow}$ | $J_H$ | $\lambda^{\uparrow}$ | $\lambda^{\downarrow}$ | $\eta_{\lambda}$ |
| | PBE | | | | | | | | | | |
| $LaMnO_3$ | 0.621 | 0.506 | 0.544 | 0.013 | 0.052 | 0.27 | 0.37 | 1.34 | 3.082 | 0.941 | 0.21 |

**Table 2.6:** TB parameters corresponding to the room temperature structure of $LaMnO_3$ obtained by using *Model B-1* at PBE level.

## 2.6 Influence of each TB parameter on the bandstructure

Let us now discuss the influence of each TB parameter on the bandstructure. We will consider the bandstructure at PBE level of calculations. The TB bands calculated using the obtained values are shown in Fig. 2.21. The obtained values are tabulated in Tab.2.6.

1. Influence of $t^{\uparrow\uparrow}$, $t^{\downarrow\downarrow}$, $t^{xy}$, $t^{2z}$. It is a well known fact from the TB model that the bandwidth is related to the hopping amplitude i.e. as a thumb rule, the bandwidth is linearly proportional to the hopping amplitude. As per this relation, the variation of $t^{\uparrow\uparrow}$ and $t^{\downarrow\downarrow}$ leads to a linear variation in the bandwidth of the local majority bands and the bandwidth of the local minority bands respectively. This is graphically shown in Fig.2.21 in which the changes in the bandstructure upon decrease and increase of the hopping amplitudes (Fig.2.21(b)-(e)) as compared to the obtained values (Fig.2.21(a)). A plot of hopping amplitudes Vs. bandwidth and the effect of hopping amplitudes on the $e_g$ bands are shown in (f) and (g) of Fig. 2.21. The linear relation between band width and the hopping parameter $t$ is clearly evident from the plots. The obtained values of the second nearest-neighbour hoppings are already very small in magnitude, and therefore changing these values does not largely influence the bandstructure.

2. Influence of $\eta^{\uparrow}$ and $\eta^{\downarrow}$. Plots showing the effect of varying $\eta^s$ are shown in the Fig.2.22. We have seen in the Sec. 2.3.2 the formula to calculate $\eta^{\uparrow}$ and $\eta^{\downarrow}$ which is given as,

$$\eta_t^s = 1 - \frac{t^{ss}[\text{Pbnm}]}{t^{ss}[\text{JT}(Q^x)]}$$
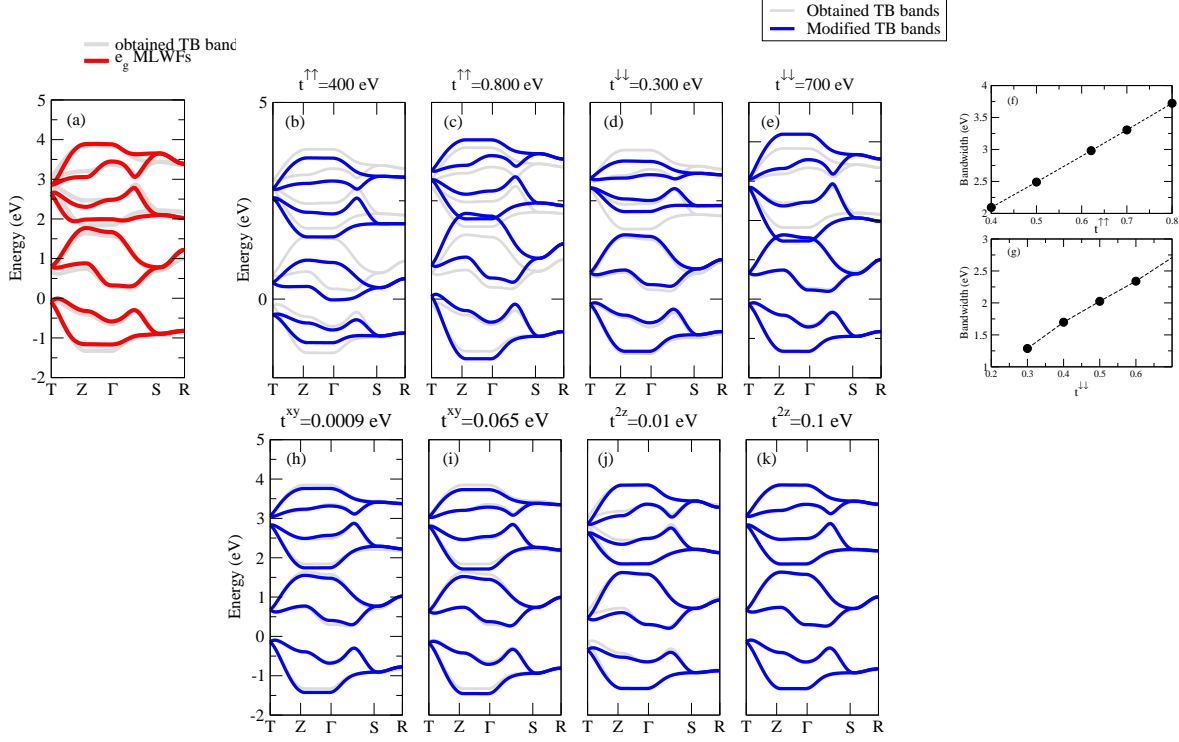
**Figure 2.21:** Influence of t$^{\uparrow\uparrow}$, t$^{\downarrow\downarrow}$, t$^{xy}$, t$^{2z}$ on the e$_g$ bands. Panel(a) shows the obtained TB bands (grey) and the MLWFs (red). In Panels (b)-(e), (h)-(k), the grey bands represents the obtained bands whereas the blue bands represent the modified TB bands by the decrease and increase of a given TB parameter. The obtained values of t$^{\uparrow\uparrow}$, t$^{\downarrow\downarrow}$, t$^{xy}$, t$^{2z}$ in the units of eV are 0.621, 0.506, 0.013 and 0.052 respectively.

Where 's' denotes up/down spin. Varying the value of $\eta$ basically means that we are varying the ratio between $t^{ss}[Pbnm]$ and $t^{ss}[JT(Q^x)]$. We have seen that the hopping amplitude is related to the bandwidth and therefore, increasing $\eta^s$ means that the ratio of the hopping amplitudes decreases. Since hopping amplitude is proportional to the bandwidth, decreasing $\eta^s$ should increase the bandwidth of the corresponding majority/minority group of bands and increasing $\eta^s$ should decrease the bandwidth and this is exactly what is seen in Fig.2.22.

3. Influence of $\tilde{\lambda}$. The effect of $\tilde{\lambda}$ on the e$_g$ bands is given in the Fig.2.23.

   In the model, $\tilde{\lambda}$ is calculated as,
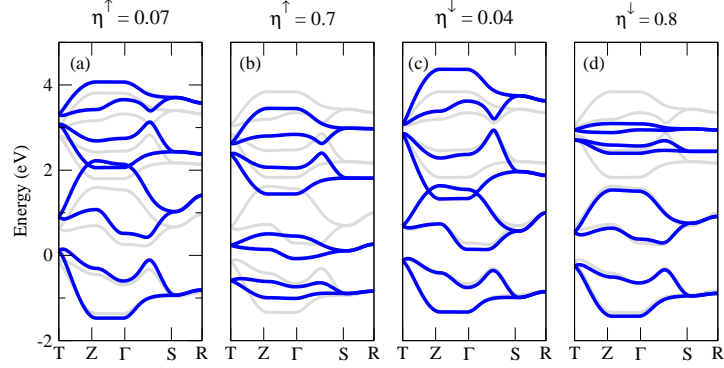
**Figure 2.22:** Effect of $\eta^s$ on the $e_g$ bands. The obtained values of $\eta^\uparrow$ and $\eta^\downarrow$ are 0.27 and 0.37 respectively.

$$\tilde{\lambda} = \frac{1}{2Q^x}\left( \frac{1}{2}(h_{12}^x - h_{21}^x)^\uparrow + \frac{1}{2}(h_{12}^x - h_{21}^x)^\downarrow \right)$$

$\tilde{\lambda}$ is defined as the JT-induced splitting of the non-diagonal elements of the hopping matrix, and in the model we calculate the value by taking into account the average of the splitting of the non-diagonal elements of both majority and minority spin channels. It is mentioned in [8] that within the TB model, when this splitting term $\tilde{\lambda}$ is taken into account, the effect of the on-site JT term on the band dispersion is cancelled i.e. including $\tilde{\lambda}$ reduces the JT gap. In the figure 2.23, we show a plot by considering $\tilde{\lambda}=0$, the bandgap in this case is 0.37 eV whereas, for the case when $\tilde{\lambda}$ is included, the value of the gap is 0.35. Therefore, the effect of $\tilde{\lambda}$ is mainly to correct the JT induced gap, but the size of the correction is almost negligible.

4. Influence of $J_H$. The effect of increasing and decreasing the value of $J_H$ is shown in Fig.2.24.

$J_H$ denotes the Hund's rule coupling of $t_{2g}$ spins to the $e_g$ spin. In the model, $J_H$ is calculated as,

$$J_H = \frac{1}{4}[(h_{11}^0 + h_{22}^0)^\downarrow - (h_{11}^0 + h_{22}^0)^\uparrow]$$

Where $h_{11}^0$ and $h_{22}^0$ denotes the Hamiltonian matrix elements in the $e_g$ basis where 1,2 denote the site indices. Variation of $J_H$ means that we are varying the difference between $(h_{11}^0 + h_{22}^0)^\downarrow$ and $(h_{11}^0 + h_{22}^0)^\uparrow$, i.e. it influences the

$\tilde{\lambda}$= 0.744 eV        $\tilde{\lambda}$= 0 eV

(a)        (b)

T  Z  Γ    S  R    T  Z  Γ    S  R
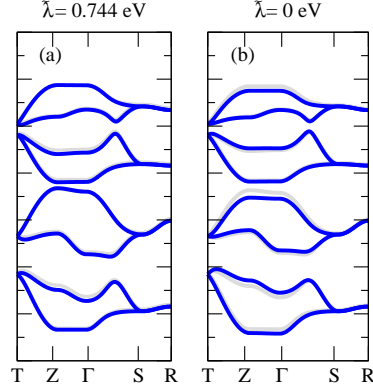
**Figure 2.23:** Effect of $\tilde{\lambda}$ on e$_g$ bands. The obtained value of $\tilde{\lambda}$ is 0.544 eV.

splitting between the majority spin channel bands and the minority spin channel bands. Indeed, Fig.2.24 shows that by decreasing J$_H$ from 1.34 to 0.7, the minority bands are pushed down and ultimately overlap with the majority bands. And, on increasing the value from 1.34 to 2.34, the two group of bands are further separated.

J$_H$ = 0.7 eV        J$_H$ = 2.34 eV

(a)        (b)

Energy (eV)

6

4

2

0

-2
T  Z  Γ    S  R    T  Z  Γ    S  R
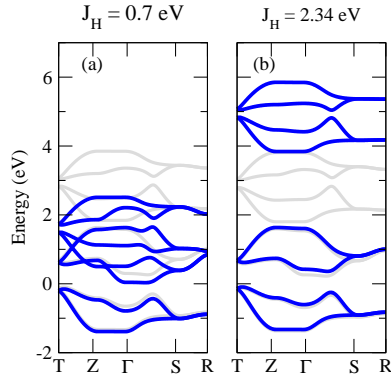
**Figure 2.24:** Effect of $J_H$ on the e$_g$ bands. The obtained value of J$_H$ is 1.34 eV.

5. Influence of $\lambda^s$ where s is ↑ or ↓. The effect on the e$_g$ bands with the variation of $\lambda^s$ is shown in the Fig. 2.25.

   $\lambda^s$ denotes the JT coupling strength which calculated in the model from the JT(AAFM) structure using the formula given as,

$$\lambda^s = \frac{\Delta\varepsilon^s}{2|Q^x|}$$

The JT induced eigenvalue splitting $\Delta\varepsilon$ of the e$_g$ subspace $2 \times 2$ onsite matrix calculated as,

$$\Delta\varepsilon = \left[(h_{11}^0 - h_{22}^0)^2 + (2h_{12}^0)^2\right]^{1/2}$$

Therefore, varying the value of $\lambda^s$ means that we are varying the JT induced eigenvalue splitting calculated in the model as $\Delta\varepsilon$ which means nothing but the bandgap. Similarly on increasing the value of $\lambda^\downarrow$ to a value similar in magnitude to $\lambda^\uparrow$, we notice a splitting in the local minority bands.
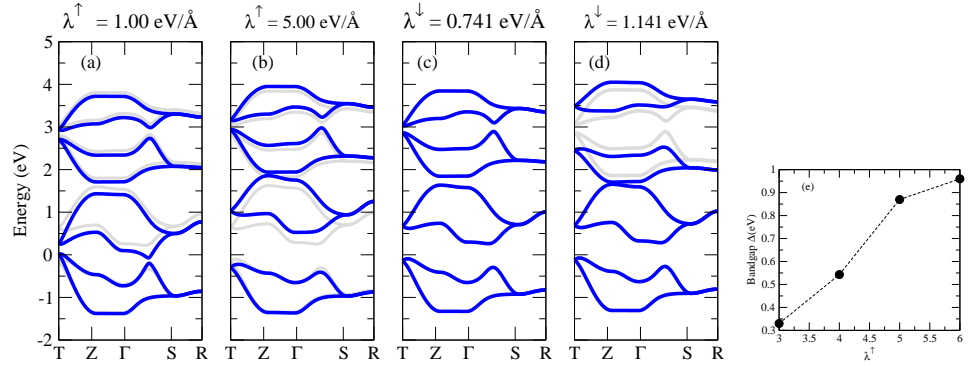


**Figure 2.25:** Effect of $\lambda^s$ on the e$_g$ bands. Panel (e) shows the plot of bandgap Vs. $\lambda^\uparrow$. The obtained values of $\lambda^\uparrow$ and $\lambda^\downarrow$ are 3.082 and 0.941 eV/$\mathring{A}$.

6. Influence of $\eta_\lambda$. The effect of $\eta_\lambda$ on the e$_g$ bands is shown in the Fig.2.26. $\eta_\lambda$ represents the reduction of the JT coupling strength due to GFO distortion. This on-site parameter enters the onsite Hamiltonian matrix elements as (1-$\eta_\lambda$) multiplied by the JT coupling constant $\lambda^\uparrow$. This value is calculated only for the spin-up case. The variation is similar to varying $\eta^s$ which influences the hopping. $\eta_\lambda$ is inversely proportional to the JT-induced splitting $\Delta\varepsilon$. Therefore, decreasing $\eta_\lambda$ increases the gap between the occupied local majority spin and the local minority spin bands (band gap) and vice versa.

7. Influence of U (U$_W^\lambda$). The effect of U$_W$ on the e$_g$ bands is shown in the Fig. 2.27. U$_W$ is the *el-el* Coulomb repulsion term which is calculated in the model from the total JT induced splitting within the majority spin e$_g$ orbital manifold, expressed as a difference in the eigenvalues of the local Hamiltonian corresponding to the *Pbnm* structure, which is given as,
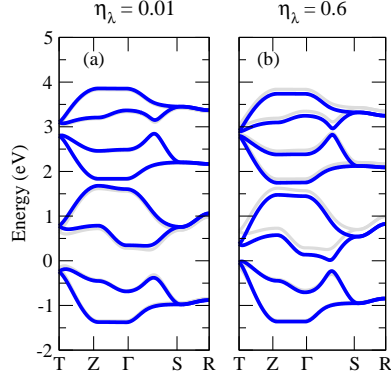
**Figure 2.26:** Effect of $\eta_\lambda$ on the e$_g$ bands. The obtained value of $\eta_\lambda$ is 0.21.

$$\Delta\varepsilon^\uparrow \;=\; \Delta\varepsilon^{\uparrow\mathrm{PBE}} + \mathrm{U}_\mathrm{W}^\lambda \Delta\mathrm{n}^\uparrow$$
$$\mathrm{U}_\mathrm{W}^\lambda \;=\; \frac{\Delta\varepsilon^\uparrow - \Delta\varepsilon^{\uparrow\mathrm{PBE}}}{\Delta\mathrm{n}^\uparrow}$$

Where $\Delta n^\uparrow$ is the difference in the majority spin eigenvalues of the MLWF occupation matrix. In accordance with the above equation, it could be seen that the variation of U$_W$ influences the splitting between the occupied and the unoccupied local majority bands. On increasing U from the obtained value of 2.34 to 3.34, we see the local majority bands splits and separates into 4 highly localized bands (evident from the DOS shown in Fig. 2.27). A decrease in U pushes down the unoccupied local majority bands along with the local minority bands.
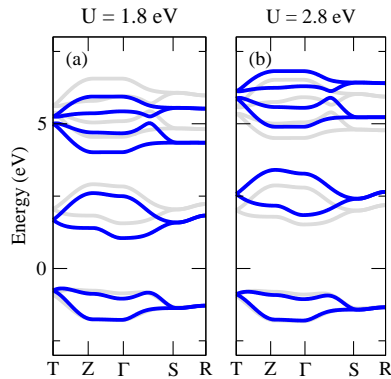


**Figure 2.27:** Effect of U (U$_W^\lambda$) on the e$_g$ bands. The obtained value is 2.34 eV.

## 2.7 Summary and Conclusions

In this chapter we have discussed the application of the FP $\Rightarrow$ MLWFs $\Rightarrow$ MH approach to LaMnO$_3$ and the following conclusions could be drawn from the studies:

(i) *Ab initio* electronic structure results. We find that all methods consistently find a orbitally-ordered (JT) insulating state. GW$_0$ provides the best agreement with experiments in terms of bandgap value, and both GW$_0$ and HSE convey a satisfactory description of valence and conduction band spectra. While in the PBE+$U$ and HSE cases a suitable adjustment of the parameters $U$ and $a_{\mathrm{mix}}$ can selectively improve the performance with respect to either bandgap or magnetic exchange interactions, a universal value that provides all quantities with good accuracy cannot be found. Even though the standard value $a_{\mathrm{mix}} = 0.25$ in HSE seems to provide rather accurate magnetic coupling constants, clearly a smaller $a_{\mathrm{mix}}$ is necessary to obtain a better Mott-Hubbard gap. While the two different codes used in the present study lead only to marginal differences in the KS band structure and the corresponding TB parameterization, the relative energies of different magnetic configurations depend on subtle details of the used methods, which hampers a concise comparison between the different energy functional (it should be noted however, that the PAW approach is usually considered superior to pure pseudopotential schemes). Within VASP a value for the Hubbard $U$ between 2-3 eV leads to similar magnetic coupling along $c$ as HSE, but somewhat stronger FM coupling within the $ab$ planes. Despite all its well-known limitations when applied to strongly-correlated materials, PBE does not seem to perform too badly (of course the fact the experimental structure has been used, helps in that respect, since PBE is known to fail in properly reproducing the JT distortion in LaMnO$_3$ [86]).

(ii) MLWFs. Despite the difficulties to fully disentangle the effective $e_g$ bands from other bands with similar energies, which are most pronounced within PBE+$U$ and HSE, the resulting MLWFs and associated ordering (Fig.2.11) look rather similar and are in good agreement with the precedent plots of Yin[54]. This represents a further proof of the quality and reliability of the Wannier construction of the $e_g$ $|3z^2 - r^2\rangle$ and $|x^2 - y^2\rangle$ orbitals. Despite these similarities, the differences in the underlying band structures lead to distinct differences in the Hamiltonian matrix elements in reciprocal space,

and allow for an accurate quantitative analysis of the differences between the various approximations for the exchange-correlation kernel.

(iii) TB parameterization. We have discussed two types of model parametrizations: Model A and Model B (1 and 2). We have adopted the general scheme of calculating the parameters which is Model B which includes Model B-1 and Model B-2 and we have demonstrated the methods-derived changes in the TB parameters due to the different treatment of the *el-el* exchange-correlation kernel in conventional and beyond-PBE approaches for using these 2 routes: (a) TB without *el-el* interaction (Model B-1) ($\hat{H}_{\text{TB}} = \hat{H}_{\text{kin}} + \hat{H}_{\text{Hund}} + \hat{H}_{\text{JT}}$). In this model the TB Hamiltonian does not explicitly incorporate an *el-el* interaction term. All changes in the beyond-PBE band structure with respect to the "noninteracting" PBE bands are integrated in the hopping, JT and Hund parameters (in particular $t^{\uparrow\uparrow}$, $\lambda^{\uparrow}$, and $J_{\text{H}}$).

(b) TB with *el-el* interaction (Model B-2) ($\hat{H}_{\text{TB}} = \hat{H}_{\text{kin}} + \hat{H}_{\text{Hund}} + \hat{H}_{\text{JT}} + \hat{H}_{\text{e-e}}$). In this second type of parameterization the *el-el* term in the TB Hamiltonian has been treated explicitly. The *el-el* interaction effects are treated by parameterizing the on site Hund and JT parameters into a non-interacting (PBE) and interacting (dependent on $U_{\text{W}}^{(\lambda)}$ and $U_{\text{W}}^{(J)}$) part. Since it has been found that $U_{\text{W}}^{(\lambda)} \neq U_{\text{W}}^{(J)}$, in order to achieve a correct parameterization it is necessary to fix one $U_{\text{W}}$ channel ($U_{\text{W}}^{(\lambda)}$) and evaluate the changes on the remaining one ($\Delta J_{\text{W}}^{(\lambda)}$). Both the models, yield excellent TB bands, essentially overlapping with the underlying MLWFs ones.

It is to be noted that the different levels of approximation for the non-interacting band structure can lead to significant changes in the hopping amplitudes, which cannot easily be accounted for by a local double-counting correction. In addition, it has also been shown that the influence of the beyond-PBE treatment on the model parameters of the local Hamiltonian cannot be captured by a simple mean-field Hubbard term with only one interaction parameter. For an accurate many-body or effective model treatment of LaMnO$_3$ and similar materials it thus seems most desirable to start from the most realistic single particle band-structure (i.e. not necessarily LDA or GGA) and use an appropriate double counting correction. The exact form of such a correction term, however, is still unclear at this point.

# Chapter 3

# $R$MnO$_3$ ($R$ = La, Pr, Nd, Sm, Eu, Gd)

In the previous chapter, we discussed the electronic and magnetic properties of LaMnO$_3$ and discussed in detail the application of TB parametrization to LaMnO$_3$. In this chapter, we will discuss the electronic, structural and magnetic properties of the less investigated orthorhombic $R$MnO$_3$ ($R$ = La, Pr, Nd, Sm, Eu, Gd) and the application of TB parametrization to these compounds. Then, we will discuss the evolution of the structural, electronic and magnetic properties and the TB parameters as a function of the IR of $R^{3+}$ (r$_R$). To be consistent with the results, the room temperature structural data has been used for all the compounds including LaMnO$_3$ as no low temperature experimental data are available in the literature for the early series orthorhombic $R$MnO$_3$ compounds.

## 3.1  Introduction

Since the discovery of CMR phenomena in $R_{1-x}A_x$MnO$_3$ ($R$=rare-earth and $A$=Sr, Ca, Ba, Pb) [102, 103, 104, 105, 106], these compounds have become the subject of numerous studies. CMR phenomenon has been observed in materials like Pr$_{1-x}$Ca$_x$MnO$_3$, Pr$_{1-x}$Ba$_x$MnO$_3$, Pr$_{1-x}$K$_x$MnO$_3$ and Nd$_{0.5}$Sr$_{0.5}$MnO$_3$ apart from the well-known hole-doped LaMnO$_3$ [106, 107]. Interesting properties like switching from non-magneto electric to magneto electric by means of tuning the Mn$^{3+}$ magnetic structure through the changes of the rare earth cationic radius, have been observed in $R$MnO$_3$ ($R$=Nd, Sm, Eu) [9, 108]. The undoped

$R$MnO$_3$ compounds has also garnered special interest since the discovery of the large magneto electric effects in these compounds [109] and the studies on these compounds involve understanding the complex relationship between lattice distortion, magnetism etc. There are numerous studies available in the literature for the compound LaMnO$_3$ and studies on compounds with smaller $R^{3+}$ radii like TbMnO$_3$, DyMnO$_3$ that are said to exhibit multiferroic properties are also quite widely available [54, 61, 62, 63, 64, 65, 68, 70, 71, 74, 75, 76, 77, 78, 79, 80, 109]. However, experimental [63, 110, 111, 112, 113, 114, 115, 116, 117, 118] and theoretical [119, 120, 121, 122, 123] studies on early $R$MnO$_3$ are found in less number despite their interesting properties.
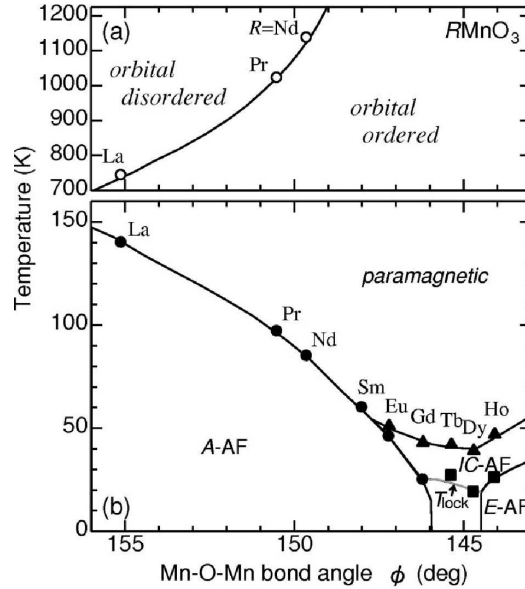


**Figure 3.1:** Phase diagram - $R$MnO$_3$ from [9](a) Orbital ordering temperature and (b) Spin ordering temperature as a function of the in-plane Mn-O-Mn bond angle

Kimura et al. [9] first reported a phase diagram of $R$MnO$_3$ (see Fig. 3.1) in which they showed the trends of the orbital and the spin ordering temperatures as a function of the Mn-O-Mn angle ($\phi$). This study was the first work which reported the multiferroic behaviour within the orthorhombic manganites followed by the work of T.Goto, Kimura et al [108]. The following could be understood from the report by Kimura et al. [9] and the phase diagram given in Fig. 3.1: When the La$^{3+}$ cation is replaced by the smaller cations, a successive increase in the orthorhombic distortion manifested by a decrease of $\phi$ (Mn-O-Mn bond angle) i.e. an increase of the GdFeO$_3$-type distortion is observed. The orbital

ordering temperature $T_{OO}$ monotonically increases with decreasing $r_R$ whereas the spin-ordering temperature $T_N$ decreases steadily from 140 K (for LaMnO$_3$) to 40 K (GdMnO$_3$) with decreasing $r_R$. Spin-ordering temperature or the Nèel temperature ($T_N$) Vs. $\phi$ (Mn-O-Mn bond angle) shows that the rare-earth manganites which have a larger $r_R$ ($R$ = La -Sm), exhibit only one magnetic phase transition (paramagnetic to A- AFM type ordering). The transition temperature decreases as the radius of the $R^{3+}$ ion decreases. The Mn-O-Mn bond angle is reduced by the smaller $R^{3+}$ ion which in turn increases the tilting of the oxygen octahedra thereby weakening the A-AFM ordering.

Particularly detailed and interesting theoretical findings for the $R$MnO$_3$ series have been reported by Kunihiko et al. in Ref.[119]. By adopting the fully optimized structure these authors have shown that the JT distortion is underestimated using DFT (LDA/GGA). However the situation improves only slightly when DFT+U is employed. In fact DFT+U works well for LaMnO$_3$, but for more distorted manganites the agreement with the experimental structural data get worse. In [82], it has been pointed out that the inclusion of U in the GGA functional partially cures this problem but it was found that for values of U larger than a certain value ( U $\geq$ 4 eV), the FM ordering becomes again the most favourable one. The deficiency of DFT in predicting the magnetic properties has also been pointed out. While the experiments have shown that at T=0, the A-AFM phase is the spin ground state even in GdMnO$_3$ (Refer to Fig.3.1), DFT shows a total energy trend where E-AFM and A-AFM phases are found to be degenerate in SmMnO$_3$ and E-AFM phase is shown to be the most stable ordering for GdMnO$_3$. The limitation in describing the magnetic ground state is also reflected in the exchange interactions: the nearest neighbour interplane coupling in LaMnO$_3$ is found to be weakly FM, in disagreement with the expected AFM behaviour. Therefore, the validity of a bare GGA treatment for LaMnO$_3$ is questionable as already been pointed out in [124].

Table 3.1 shows the experimental room-temperature Wycoff positions of $R$MnO$_3$ corresponding to different structural modifications (JT, GFO and Experimental structures). Let us now discuss the evolution of the various structural parameters (Refer to Fig. 3.2).

1. $r_R$ *Vs. Unit-cell parameters (a,b,c) and Volume (V)*. When the $r_R$ changes, the major effect is the shrinking of the volume due to the fact that we are adding protons to the nuclei (lanthanide contraction). The outermost $3d$ electrons remain unchanged which means that the screening remains almost
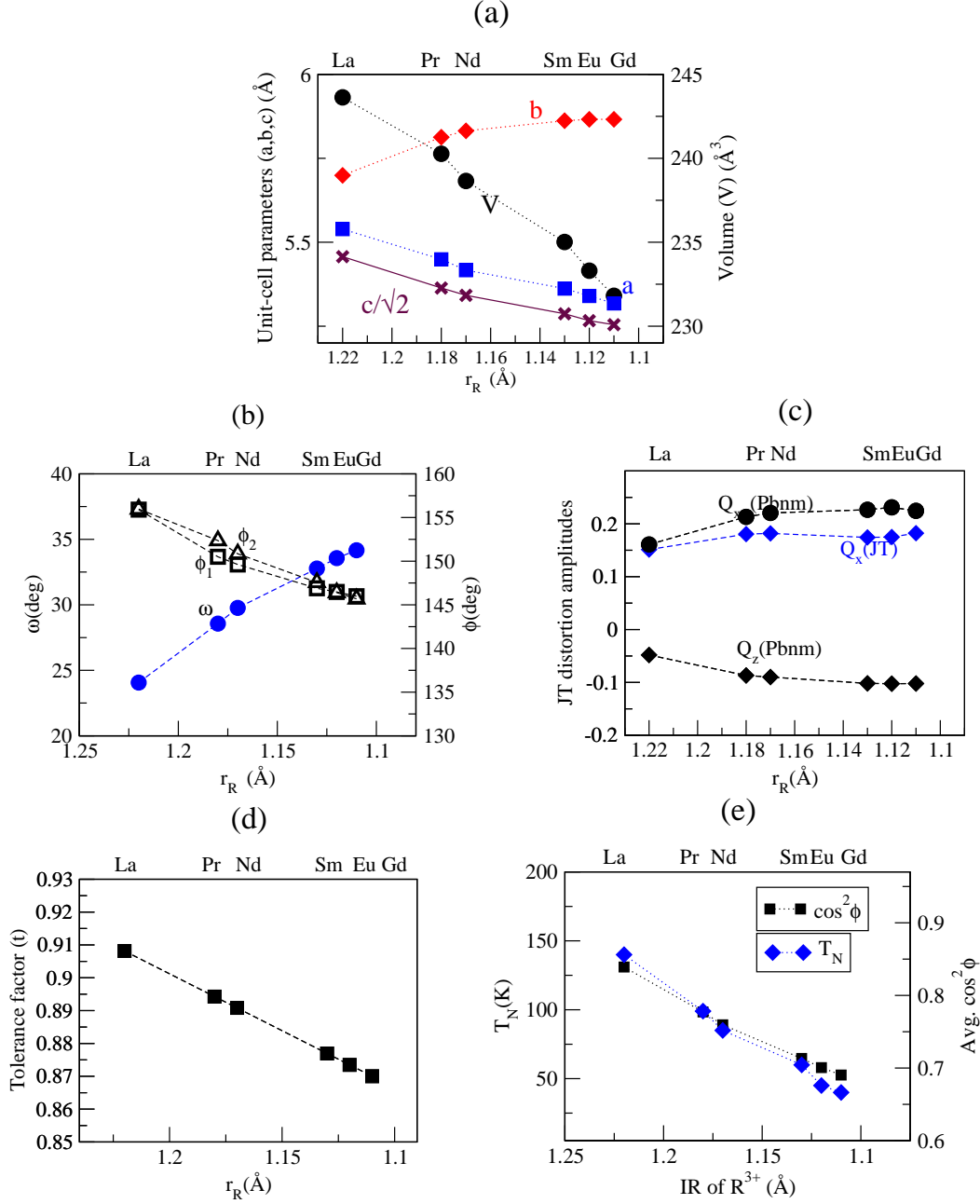
**Figure 3.2:** Plots of (a) $r_R$ Vs. Unit-cell parameters and Volume (b) $r_R$ Vs. Mn-O-Mn bond angles in ab plane ($\phi_1$, c-plane $\phi_2$)and octahedral tilting angle ($\omega$) (c) $r_R$ Vs. JT amplitudes $Q^x$ and $Q^z$ (d) $r_R$ Vs. tolerance factor (t) (e) $r_R$ Vs. Mn-O-Mn bond angles and $T_N$. The values are calculated using the room temperature structure experimental data.

Wyckoff Positions

| Compound | R, O(4c), O(8d) | Expt | JT | GFO |
|---|---|---|---|---|
| $LaMnO_3$ | $R$ | (0.9937,0.5436, 0.25) | (0.0, 0.5, 0.25) | (0.0, 0.5, 0.25) |
| | O(4c) | (0.0733,0.4893, 0.25) | (0.0, 0.0, 0.25) | (0.0733, 0.4893, 0.25) |
| | O(8d) | (0.7743,0.3014, 0.0385) | (0.2636,0.2636,0.0) | (0.2121,0.2879,0.0385) |
| $PrMnO_3$ | $R$ | (0.9911, 0.0639, 0.25) | (0.0, 0.5, 0.25) | (0.0, 0.5, 0.25) |
| | O(4c) | (0.0834,0.4819,0.25) | (0.0, 0.0, 0.25) | (0.0834, 0.4819, 0.25) |
| | O(8d) | (0.7151,0.3174,0.0430) | (0.2663,0.2663,0.0) | (0.1988,0.3012,0.0430) |
| $NdMnO_3$ | $R$ | (0.9886,0.0669,0.25) | (0.0, 0.5, 0.25) | (0.0, 0.5, 0.25) |
| | O(4c) | (0.0878,0.4790,0.25) | (0.0,0.0,0.25) | (0.0878,0.4790,0.25) |
| | O(8d) | (0.7141,0.3188,0.0450) | (0.26645,0.26645,0.0) | (0.19765,0.30235,0.0450) |
| $SmMnO_3$ | $R$ | (0.9850,0.0759,0.25) | (0.0, 0.5, 0.25) | (0.0, 0.5, 0.25) |
| | O(4c) | (0.097, 0.473,0.25) | (0.0, 0.0, 0.25) | (0.097,0.473,0.25) |
| | O(8d) | (0.7924,0.3241,0.0485) | (0.26585,0.26585,0.0) | (0.19175,0.30825,0.0485) |
| $EuMnO_3$ | $R$ | (0.9841, 0.0759, 0.25) | (0.0, 0.5, 0.25) | (0.0, 0.5, 0.25) |
| | O(4c) | (0.1,0.470,0.25) | (0.0,0.0,0.25) | (0.1,0.470,0.25) |
| | O(8d) | (0.7935,0.3254,0.0487) | (0.26595,0.26595,0.0) | (0.19055,0.30945,0.0487) |
| $GdMnO_3$ | $R$ | (0.9384, 0.0807, 0.25) | (0.0, 0.5, 0.25) | (0.0, 0.5, 0.25) |
| | O(4c) | (0.103,0.471,0.25) | (0.0,0.0,0.25) | (0.103,0.471,0.25) |
| | O(8d) | (0.7943,0.3246,0.0508) | (0.26665,0.26665,0.0) | (0.18905,0.31095,0.0508) |

**Table 3.1:** The table shows the Wyckoff positions corresponding to room temperature experimental structure, JT and GFO. x, y and z are the coordinates w.r.t. the orthorhombic lattice vectors. Experimental data corresponding to $LaMnO_3$ from [66], $RMnO_3$ ($R$ = Pr, Nd) from [125] and $RMnO_3$ ($R$ = Sm, Eu, Gd) from [126].

unchanged. In case the screening had changed, it would have contrast the shrinking of volume across the series. The plot shown Fig. 3.2(a) is very similar to the one shown in the work of Alonso et al. [125], though SmMnO$_3$, EuMnO$_3$ and GdMnO$_3$ are not discussed in their work. From the plot, it could be seen that variation of $b$ parameter is very small compared to that of $a$ and $c$. The reason has been attributed to the tilting scheme of MnO$_6$ octahedra in the Pbnm perovskites in which the distortion driven by a reduction of the $R^{3+}$ size leaves $b$ almost unchanged [125]. It is also seen that the decrease in the volume $V$ scales with the $R^{3+}$ size. In [125], it has been pointed out that the c/$\sqrt{2} < a <$ b is a characteristic of an orthorhombic structure, which has its origin in the strong cooperative JT effect, inducing an orbital ordering and distorting the MnO$_6$ octahedra. Going by the above points, it is seen that $R$MnO$_3$ ($R$ = La, Pr, Nd, Sm, Eu and Gd) exhibit the characteristics of an orthorhombic *Pbnm* structure as pointed out in the experimental work by Alonso et al.

2. $r_R$ *Vs. Mn-O-Mn bond angles (*$\phi_1$*, *$\phi_2$*) and tilting angle (*$\omega$*).* $\phi_1$ is the Mn-O-Mn bond angle taken in the ab-plane. $\phi_2$ is the angle in the c-direction. The tilting angle of the oxygen octahedra $\omega$ is calculated by the formula: $\omega$ = 180 - $\langle\phi\rangle$ where $\langle\phi\rangle$ is the average of $\phi_1$ and $\phi_2$. According to Zhou and Goodenough [127] the transition temperatures T$_{JT}$, T$_N$ and T$_{OO}$ should depend linearly on the average of the $\cos^2 \phi$. The T$_N$ Vs. $\phi$ plots are revised by incorporating the correct values for $\phi$ for Sm, Eu and Gd (which are now available in the literature [126]) and the expected linear behaviour is recovered as shown in Fig. 3.2(e).

3. $r_R$ *Vs. JT distortion amplitudes (*$Q^x$ *and *$Q^z$*).* The local JT distortion modes are defined as Q$^x$=(l-s)/$\sqrt{2}$ and Q$^z$=(*2m-l-s*)/$\sqrt{6}$ where *l*, *s* and *m* stand for long, short and medium Mn-O bond distances. With respect to the reference LaMnO$_3$ case, Q$^x$/Q$^z$ are found to be increased by about 30% in the other members of the $R$MnO$_3$ series, as a consequence of the progressive decrease of volume.

4. $r_R$ *Vs. Tolerance factor (*t*).* An important quantity in the physics of CMR manganites is the tolerance factor which gives indication on the octahedral tilting and distortions. It is defined as $t = \sqrt{2}(r_B + r_O)/r_A + r_O$ where $r_A$, $r_B$ and $r_O$ represent the ionic radii of A, B and O, respectively. Alternatively, it could be defined as $t = d_{A-O}/(\sqrt{2}d_{Mn-O})$, where $d_{A-O}$ is

the distance between the A site and the oxygen anions and $d_{Mn-O}$ is the distance between the Mn site and the oxygen anions. For an undistorted cube, $t$ is 1. In real systems, the A ions are too small to fill the space in the cube and the oxygen anions tend to move from their ideal positions and so the distances $d_{A-O}$ and $d_{Mn-O}$ vary and also the Mn-O-Mn bond angle becomes less than 180° resulting in tolerance factors of values less than 1 down the series from $R$=La to Gd. The trend of $t$ down the series is shown in the Fig.3.2. The trend of the tolerance factor $t$ is in accordance with the trend of the Mn-O-Mn bond angle $\phi$.

## 3.2   *Ab-initio* results

The ground state electronic and magnetic properties (PBE, HSE and $GW_0$(at PBE)) have been calculated from the experimental data taken from [66] for LaMnO$_3$, for $R$MnO$_3$ ($R$=Pr, Nd) taken from [125] and $R$MnO$_3$ ($R$=Sm, Eu, Gd) taken from [126]. A regular $\Gamma$-centered $6 \times 6 \times 6$ Monkhorst-Pack kpoint mesh has been used for all the PBE calculations whereas for HSE and $GW_0$ calculations, a $4 \times 4 \times 4$ kpoint mesh (Monkhorst Pack) has been employed. In the calculations, $R(5s)$, $R(5p)$, Mn($3s$, $3p$, $3d$, $4s$) are included. Unoccupied $R(4f)$ states have not been used for the calculations except for LaMnO$_3$. All the calculations are spin-polarized calculations.

The calculated band structures of $R$MnO$_3$ along with the corresponding e$_g$ MLWFs at different levels of calculations are shown in Fig. 3.3.

The eigenvalue dispersion for PBE, HSE and $GW_0$ level of calculations in $R$MnO$_3$ ($R$ = La, Pr, Nd, Sm, Eu, Gd) is characterized by an insulating state with an indirect energy gap. The band gaps of $R$MnO$_3$ and the magnetic moments of Mn$^{3+}$ at different levels of calculations are presented in the Tab.3.2 and the plot of the same has been shown in the Fig.3.4. Despite its known limitations, PBE is able to find the correct insulating state solution but the band gap is seriously underestimated. It could be seen that the magnetic moments calculated at the PBE and $GW_0$ level is comparable with that of the experimental results, whereas the tendency of HSE to overlocalize leads to larger values of the magnetic moment.

PDOS and the band structures corresponding to PrMnO$_3$ are shown in the Fig. 3.5. The PDOS and band structures for the other compounds have been included in the appendix since they display qualitatively very similar features. It is seen clearly in the Fig. 3.5 that within all methods the Mott-Hubbard gap is
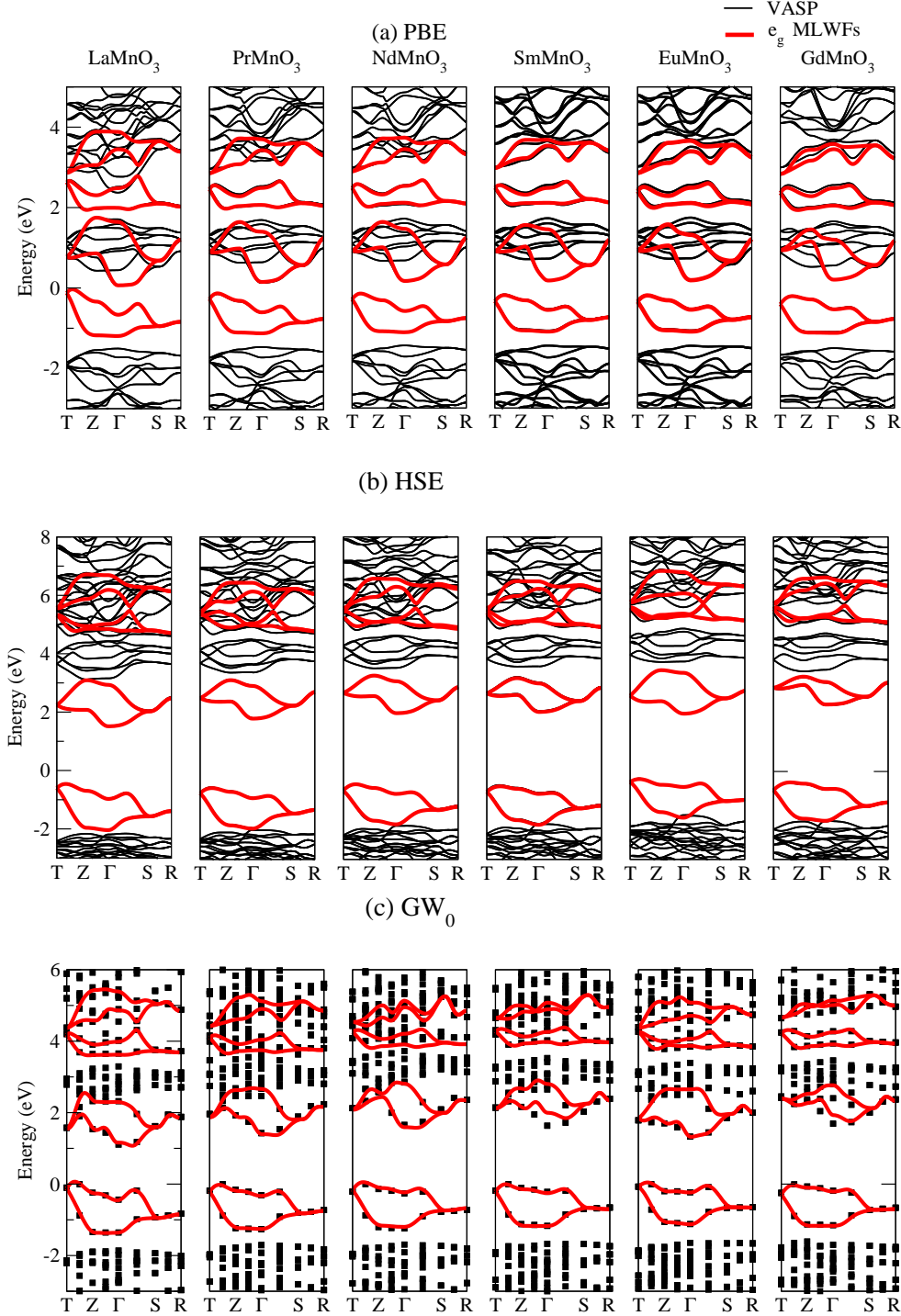
**Figure 3.3:** VASP band structure (black) and MLWFs (red) of $R$MnO$_3$ ($R$=La, Pr, Nd, Sm, Eu, Gd) (a) PBE (b)HSE and (c) GW$_0$.
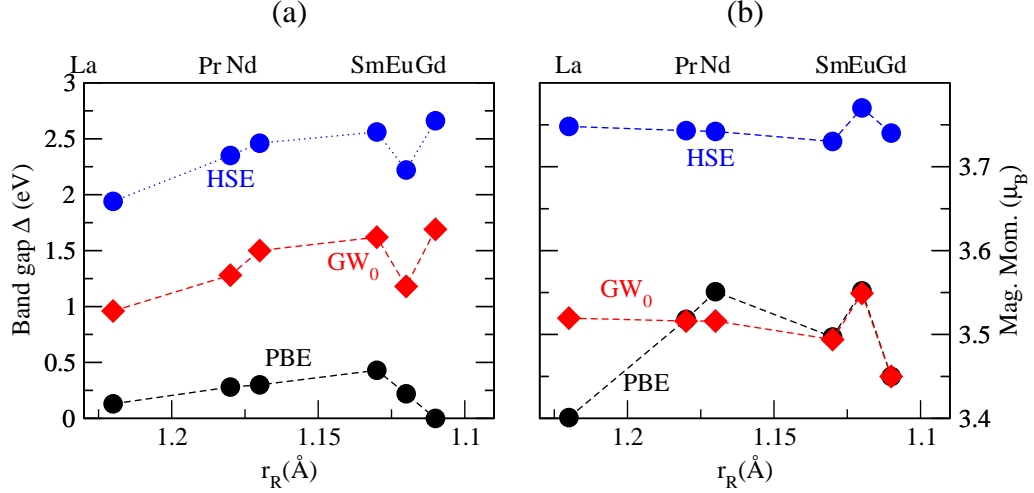
**Figure 3.4:** Figure showing the variation of (a) Band gap and (b) magnetic moment with $r_R$.

opened between occupied and empty states with predominant $Mn(e_g)$ character. In Fig.3.5 (which corresponds to $PrMnO_3$), it could be observed that '$e_g$-like' orbitals at a certain site hybridize with '$t_{2g}$-like' orbitals at a neighbouring site as a result of the tilt and rotation of the oxygen octahedra. This leads to bands with mixed $e_g/t_{2g}$ character in the early series of $RMnO_3$ ($R$ = Pr, Nd, Sm, Eu, Gd). This mixing makes the construction of eight $e_g$ character MLWFs within one energy window used in the disentanglement procedure quite difficult. This is because the single energy window contains strongly mixed $e_g/t_{2g}$ character due to the GFO distortion. This problem is overcome by constructing two separate sets of four local majority and four local minority spin MLWFs using two different energy windows. The problem of finding suitable energy windows has already been discussed in the previous chapter for the case of $LaMnO_3$. In the band structure and MLWFs plot corresponding to $PrMnO_3$ (as shown in the Fig. 3.5), it is seen that the four (energetically lower) local majority MLWF bands and the local minority bands follow very closely the underlying VASP bands (despite the strong band entanglement). At HSE level, the bandwidth of the local minority bands reduces when compared with that of PBE and the band gap increases. The wavy character that is observed in the dispersion of the local minority $e_g$ bands within $GW_0$ could be due to the size of the k-point mesh ($4 \times 4 \times 4$). With a larger mesh, the band dispersion could be improved at the cost of huge time for the computations.

103

| RMnO$_3$ | Band gap (eV) | | | | Magnetic moment ($\mu_B$) | | | |
| --- | --- | --- | --- | --- | --- | --- | --- | --- |
| | PBE | HSE | GW$_0$ | Expt. | PBE | HSE | GW$_0$ | Expt. |
| LaMnO$_3$ | 0.13 | 1.94 | 0.96 | 1.1 [89], 1.9 [90], 2.0 [91, 92], 1.7 [93] | 3.401 | 3.748 | 3.5195 | 3.65 [128], 3.87 [98], 3.7±0.1 [65], 3.4 [99] |
| PrMnO$_3$ | 0.28 | 2.35 | 1.28 | 1.75 [21] | 3.518 | 3.743 | 3.516 | 3.5 [115] |
| NdMnO$_3$ | 0.3 | 2.46 | 1.5 | 1.75 [21] | 3.551 | 3.742 | 3.516 | 3.22 [112] |
| SmMnO$_3$ | 0.43 | 2.56 | 1.62 | | 3.497 | 3.73 | 3.494 | 3.3 [129], 3.5 [130] |
| EuMnO$_3$ | 0.22 | 2.22 | 1.18 | | 3.552 | 3.77 | 3.549 | |
| GdMnO$_3$ | 0.397 | 2.66 | 1.69 | | 3.45 | 3.74 | 3.45 | |

**Table 3.2:** Table showing the values of band gap and magnetic moment of $R$MnO$_3$.
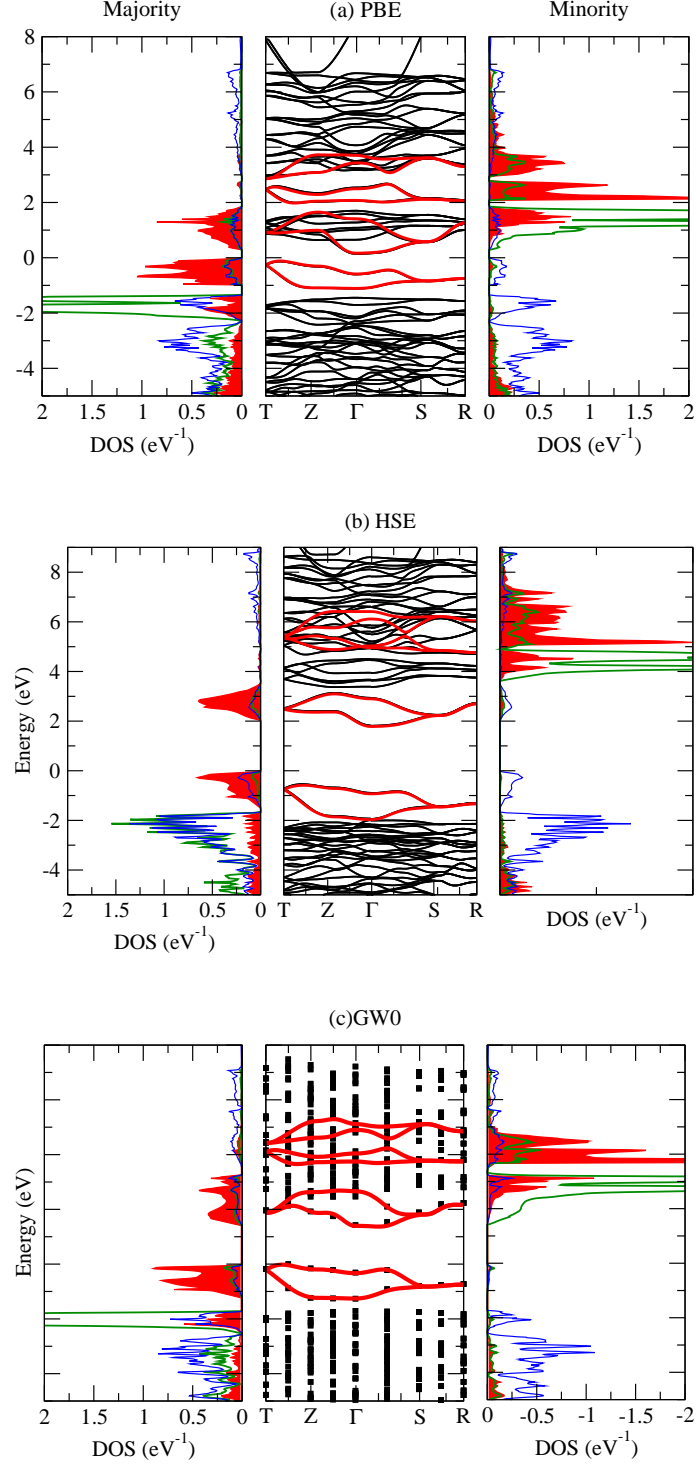
**Figure 3.5:** Effective e$_g$ MLWF bands (thick red lines) for PrMnO$_3$ and the VASP bands and the associated normalized PDOS (Mn (e$_g$ red-filled areas), Mn (t$_{2g}$ green lines) and O(p) blue dots. Left/right PDOSs correspond to local majority/minority Mn sites while O(p) PDOS is calculated as an average over all the O sites.

(a) PBE          (b) HSE
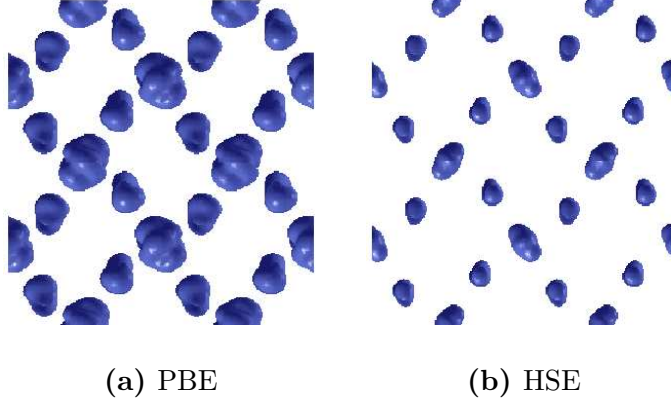
**Figure 3.6:** Charge density isosurfaces of the highest occupied e$_g$ orbitals (from the fermi energy to the lower bound of the e$_g$ bands) showing the orbitally ordered state of PrMnO$_3$ obtained using the different levels of calculations (PBE and HSE).

In Fig.3.6, the staggered ordering associated with the highest occupied $e_g$-like bands as obtained from the full ab-initio self-consistent charge density (without downfolding) at various levels of calculations are shown.

We will now analyze the magnetic properties in terms of the nearest-neighbour magnetic exchange interactions within the orthorhombic $ab$ plane ($J_{ab}$) and along $c$ direction ($J_c$) [87, 96, 97]. As we know from the work of Kunihiko et al. [119] that DFT does not provide a good prediction for the exchange parameters, they have been calculated at HSE level. The calculated HSE total energies are mapped onto a classical Heisenberg Hamiltonian $H$=-$\frac{1}{2}\sum_{i\neq j} J_{ij}S_i \cdot S_j$ (for S=2) and the following equations are obtained:

$$E_{FM} - E_{AAF} = -32J_c \tag{3.1}$$
$$E_{CAF} - E_{FM} = 64J_{ab} \tag{3.2}$$
$$\tag{3.3}$$

Where $E_{FM}$, $E_{CFM}$ and $E_{AFM}$ corresponds to the total energy for the ferromagnetic, C-type antiferromagnetic (a 2D checker board like arrangement within the $xy$ plane) and A-type antiferromagnetic configurations((1,0,0) planes of ferromagnetically aligned Mn ions are coupled antiferromagnetically to each other) respectively. The obtained $J$ are shown in Tab.3.3 and graphically represented in Fig. 3.7. Fig.3.7 shows the sum of the $J_{ab}$ and $J_c$: this energy is said to be proportional to T$_N$ within the mean-field approximation and indeed the trend is

| | $J_c$ | $J_{ab}$ |
|---|---|---|
| LaMnO$_3$ | 0.21 | 3.92 |
| LaMnO$_3$ (lowT) | -0.26 | 2.92 |
| PrMnO$_3$ | -0.26 | 2.25 |
| NdMnO$_3$ | -0.28 | 2.00 |
| SmMnO$_3$ | -0.26 | 1.55 |
| EuMnO$_3$ | -0.12 | 1.53 |

**Table 3.3:** Table showing magnetic exchange interactions within the orthorhombic $ab$ plane ($J_{ab}$) and along $c$ direction $J_c$ calculated at HSE level. For LaMnO$_3$, both room temperature and low temperature results are reported.

in good agreement with the experimental results showing a steep decrease of T$_N$ down the series.

Within a mean-field picture, the T$_N$ can be expressed in terms of the sum of the J, as:

$$\text{T}_{\text{N}_{\text{mean-field}}} = \frac{2\text{S}(\text{S}+1)}{3\text{k}_\text{B}}(J_{ab} + J_c) \tag{3.4}$$

Where $s$ denotes orthorhombic $ab$ plane and $c$-direction. By using the HSE values, mean-field T$_N$ have been obtained, which are in very good agreement with the experiment, as shown in the Fig. 3.7 and the values follow well the steep decrease from La to Eu.

We will now discuss the plot of dielectric function for $R$MnO$_3$ as shown in Fig.3.8(a)-(e). The dielectric function contains information about the direct or indirect optical transitions or fundamental excitations in a solid like phonons, polarons, magnons etc. The dielectric function is a complex function: $\epsilon(\omega) = \epsilon_1(\omega) + i\epsilon_2(\omega)$. The real and imaginary parts of the dielectric function are directly related to each other through Kramers-Kronig transformation. In Fig.3.8(a)-(e) the real and imaginary parts ($\epsilon_1$ and $\epsilon_2$) of the dielectric function calculated from the GW$_0$ routines by fixing the screened Coulomb interaction term W$_0$ to PBE level. The computed values are compared with the experimental data obtained from the spectroscopic ellipsometry measurements [121]. The coloured dashed lines shows the theoretical results whereas the corresponding coloured square symbols represents the experimental data taken from Ref. [121].
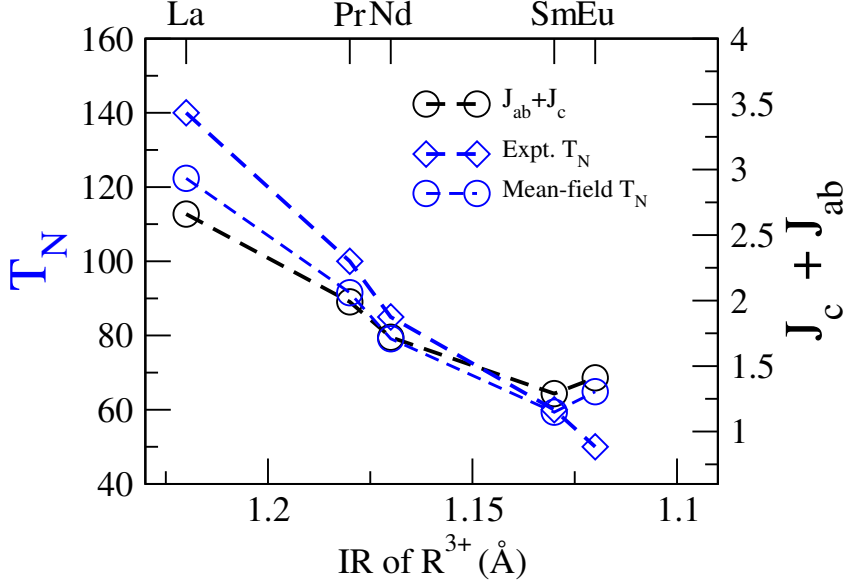
**Figure 3.7:** Plot showing the variation of $J_{ab}$ and $J_c$ and the calculated $T_N$ as a function of the ionic radii of $R^{3+}$.

The experimental plot of the dielectric function which was measured at a range of energy between 0.5 to 5.5 eV shows two intensive, broad optical features peaked at 2 eV and 4.5 eV respectively for LaMnO$_3$ (Fig.3.8(a)). For the other $R$MnO$_3$ compounds (Fig.3.8(b)-(e)), the intensive broad peak is peaked at 2.2 eV. While the authors of [77, 131] assign the peaks to $d$-$d$ charge transfer excitations, the authors of [121] argue that the peaks are due to the interplay of both $p$-$d$ and $d$-$d$ transitions. The same two peaks are suppressed by a factor of 1.5 in the case of other RMnO$_3$ (R = Pr, Nd, Sm, Eu) compounds. These experimental results also correspond with the results of Kim *et al.* [21]. The PBE results show the supression that is being observed experimentally, but the intensity at zero photon energy is quite high when compared with that of the experimental results. A better agreement with experiment could be achieved by treating the screened exchange at beyond-PBE level (i.e. within a fully self-consistent GW framework) but this is beyond the scope of the present study (as the corresponding calculation would be computationally very demanding).
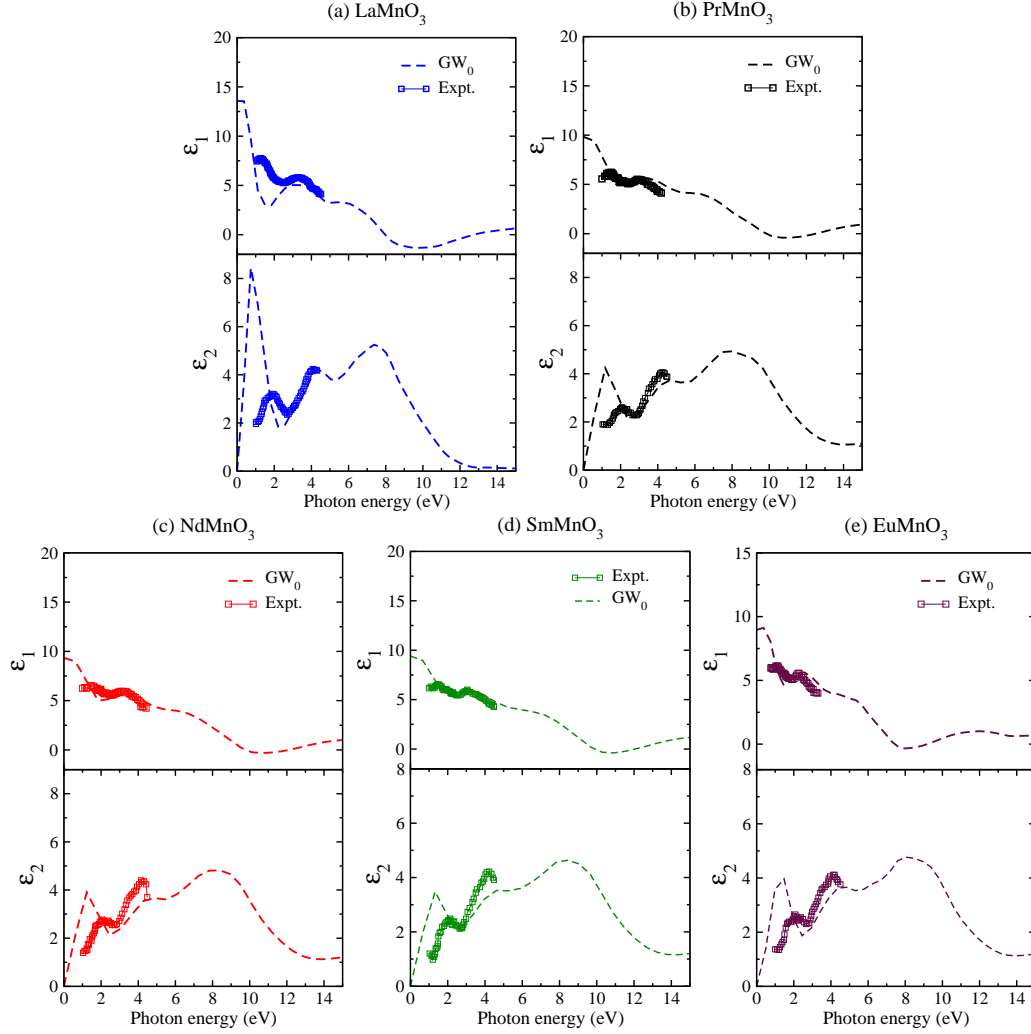
**Figure 3.8:** Plot showing the real and imaginary parts $\epsilon_1$ and $\epsilon_2$ of the dielectric function. The dashed lines indicate the data obtained from $GW_0$ at PBE calculations and the coloured squares indicate the experimental data taken from Ref. [121].

## 3.3 Tight-binding parametrization

### 3.3.1 Model B-1

Let us now discuss the results of Model B-1 in which the term $\hat{H}_{e-e}$ is neglected i.e. the electron-electron interaction is implicitly accounted for in the tight-binding model.

Table 3.4 gives the obtained TB parameters corresponding to Model B-1 calculated within the various levels of approximation and Fig. 3.9 shows the TB obtained using the Model B-1 along with the MLWFs.

($i$) *PBE*- The TB band dispersion and the MLWFs match closely in the case of LaMnO$_3$, the bandwidth of the local majority and local minority TB bands are slightly increased when compared to that of the MLWFs. In the case of PrMnO$_3$, the TB band dispersion of the local majority e$_g$ bands match closely with the MLWFs whereas the bandwidth of the local minority bands is increased by around 32 % when compared with the MLWFs. In the case of NdMnO$_3$, the local minority TB bands matches very well with the MLWFs whereas the bandwidth of the local majority TB bands is lesser than the bandwidth of the corresponding MLWFs by around 8 %. In the case of SmMnO$_3$, the bandwidth of both the local majority and the local minority TB bands decreases by around 10 % as compared to that of the corresponding MLWFs. The same trend as SmMnO$_3$ is observed in EuMnO$_3$. In the case of GdMnO$_3$, the local minority TB bands matches very closely with the MLWFs whereas there is around 10 % decrease in the bandwidth of the local majority TB bands when compared to the corresponding MLWFs.

($ii$) *HSE* - The reason for the increase in the values of t$^{\uparrow\uparrow}$ in all-beyond PBE methods has been explained in the previous chapter. It has been shown that the increase in t$^{\uparrow\uparrow}$ could be understood within an extended nearest-neighbour TB model including both Mn(d) and O(p) states, from which an effective e$_g$-only model could be derived in the limit of large energy separation $\epsilon_{dp}$ between the d and the p orbitals [81]. Comparing with PBE, it could be seen that the values of J$_H$ and $\lambda^\uparrow$ have increased in the case of HSE and this is reflected in the TB model by the increase in spin-splitting and the band gap respectively. In the case of HSE, overall, the TB band dispersion and the MLWFs matches reasonably good. The main observation is that in all the compounds the bandwidth of the occupied local majority TB bands are slightly lesser when compared to the corresponding

MLWFs and the band width of the local minority TB bands is reduced when compared with the corresponding MLWFs.

($iii$) $GW_0$ - At $GW_0$ level of calculations, TB bands follow the MLWFs quite well. There is a decrease in the bandwidth of the local minority bands that is observed starting from $PrMnO_3$ and also slight mismatch in the bandwidth of the local majority TB bands in the case of $LaMnO_3$, $SmMnO_3$ and $EuMnO_3$.

Overall, at all the levels of calculations, the TB bands obtained using Model B-1 follows reasonably quite closely the MLWFs. For details on the influence of each TB parameter on the $e_g$ band dispersion, refer to Sec.2.6 of the previous chapter.

### 3.3.2 Model B-2

Let us discuss the results of the alternative TB parametrization in which the modifications induced by the beyond-PBE methods are treated as perturbation to the 'non-interacting' PBE description by explicitly considering the el-el interaction and using the simplified mean-field approximation. As discussed in the previous chapter, this parametrization applies only for the beyond-PBE methods. The value of $U_W^\lambda$ is explicitly calculated and to correct the correlation-induced increase of the spin splitting, we calculate an empirical correction to the Hund's rule coupling $\Delta J_W^{(\lambda)}$. The onsite parameters are set to the corresponding PBE values. All the parameters calculated using Model B-2 are listed in the Tab.3.5. The dispersion of the $e_g$ states calculated from this model and the corresponding MLWFs for $RMnO_3$ are shown in the Fig.3.10. The interaction parameters $J_H$, $\Delta\epsilon^\uparrow$, $\Delta n^\uparrow$ that are used in the calculation of $U_W^\lambda$ are given in the Tab.3.6. A more detailed discussion of the evolution of the various TB parameters is given in the next section.

**Table 3.4:** TB parameters - $R$MnO$_3$ (*Model B-1*).

| | Hopping parameters | | | | | | | On-site parameters | | | |
|---|---|---|---|---|---|---|---|---|---|---|---|
| | $t^{\uparrow\uparrow}$ | $t^{\downarrow\downarrow}$ | $\tilde{\lambda}$ | $t^{xy}$ | $t^{2z}$ | $\eta^{\uparrow}$ | $\eta^{\downarrow}$ | $J_H$ | $\lambda^{\uparrow}$ | $\lambda^{\downarrow}$ | $\eta_\lambda$ |
| **PBE** | | | | | | | | | | | |
| LaMnO$_3$ | 0.621 | 0.506 | 0.544 | 0.013 | 0.052 | 0.27 | 0.37 | 1.34 | 3.082 | 0.941 | 0.21 |
| PrMnO$_3$ | 0.623 | 0.508 | 0.550 | 0.011 | 0.052 | 0.40 | 0.48 | 1.32 | 3.156 | 1.138 | 0.28 |
| NdMnO$_3$ | 0.664 | 0.514 | 0.380 | 0.013 | 0.027 | 0.45 | 0.51 | 1.32 | 3.202 | 1.288 | 0.29 |
| SmMnO$_3$ | 0.638 | 0.528 | 0.476 | 0.012 | 0.045 | 0.58 | 0.60 | 1.36 | 3.239 | 1.204 | 0.33 |
| EuMnO$_3$ | 0.643 | 0.531 | 0.684 | 0.012 | 0.052 | 0.49 | 0.57 | 1.32 | 3.266 | 1.246 | 0.31 |
| GdMnO$_3$ | 0.645 | 0.535 | 0.535 | 0.011 | 0.052 | 0.52 | 0.59 | 1.32 | 3.298 | 1.303 | 0.28 |
| **HSE** | | | | | | | | | | | |
| LaMnO$_3$ | 0.707 | 0.524 | 1.07 | 0.013 | 0.056 | 0.27 | 0.40 | 2.483 | 10.049 | 0.989 | 0.16 |
| PrMnO$_3$ | 0.704 | 0.530 | 1.050 | 0.011 | 0.056 | 0.38 | 0.69 | 2.442 | 9.286 | 0.412 | 0.25 |
| NdMnO$_3$ | 0.708 | 0.533 | 0.983 | 0.011 | 0.057 | 0.38 | 0.56 | 2.406 | 9.26 | 0.372 | 0.27 |
| SmMnO$_3$ | 0.723 | 0.558 | 1.047 | 0.011 | 0.057 | 0.45 | 0.62 | 2.415 | 9.653 | 0.435 | 0.31 |
| EuMnO$_3$ | 0.731 | 0.563 | 1.036 | 0.011 | 0.056 | 0.46 | 0.80 | 2.426 | 9.684 | 0.397 | 0.33 |
| GdMnO$_3$ | 0.734 | 0.565 | 1.009 | 0.011 | 0.057 | 0.48 | 0.65 | 2.421 | 9.547 | 0.263 | 0.28 |
| **GW$_0$** | | | | | | | | | | | |
| LaMnO$_3$ | 0.746 | 0.469 | 0.488 | 0.022 | 0.073 | 0.20 | 0.36 | 1.874 | 4.438 | 0.881 | 0.09 |
| PrMnO$_3$ | 0.781 | 0.380 | 0.489 | 0.035 | 0.065 | 0.27 | 0.42 | 1.805 | 4.556 | 0.826 | 0.13 |
| NdMnO$_3$ | 0.752 | 0.405 | 0.535 | 0.036 | 0.07 | 0.24 | 0.45 | 1.805 | 4.682 | 1.011 | 0.18 |
| SmMnO$_3$ | 0.746 | 0.493 | 0.574 | 0.013 | 0.063 | 0.34 | 0.66 | 1.797 | 4.525 | 1.271 | 0.15 |
| EuMnO$_3$ | 0.942 | 0.516 | 0.617 | 0.019 | 0.080 | 0.53 | 0.65 | 1.802 | 6.505 | 1.303 | 0.38 |
| GdMnO$_3$ | 0.759 | 0.515 | 0.561 | 0.017 | 0.051 | 0.46 | 0.66 | 1.828 | 4.568 | 1.401 | 0.03 |
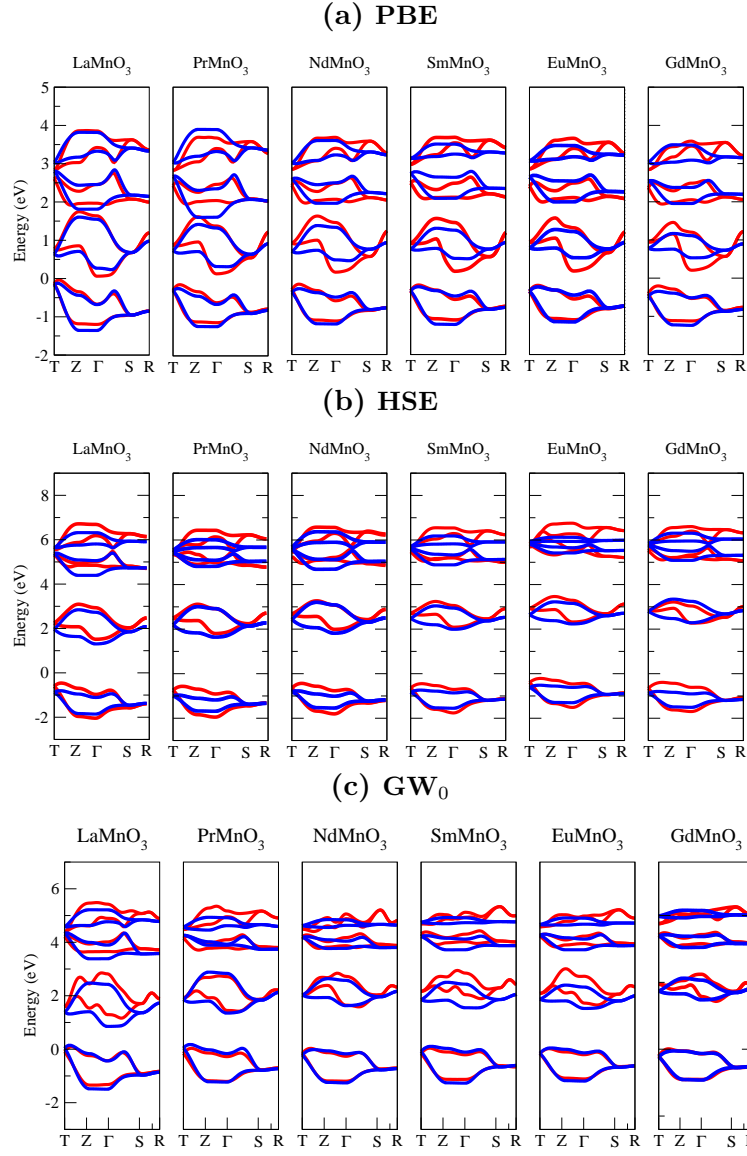
**Figure 3.9:** Figure showing $e_g$ TB bands (blue) obtained using *Model B-1* parametrization and the $e_g$ MLWFs(red).

**Table 3.5:** TB parameters - $R$MnO$_3$ (*Model B-2*).

| | Hopping parameters | | | | | | | On-site parameters | | | | Interaction terms | |
| | $t^{\uparrow\uparrow}$ | $t^{\downarrow\downarrow}$ | $\tilde{\lambda}$ | $t^{xy}$ | $t^{2z}$ | $\eta^{\uparrow}$ | $\eta^{\downarrow}$ | $J_H$ | $\lambda^{\uparrow}$ | $\lambda^{\downarrow}$ | $\eta_\lambda$ | $U^\lambda_W$ | $\Delta J$ |
|---|---|---|---|---|---|---|---|---|---|---|---|---|---|
| **HSE** | | | | | | | | | | | | | |
| LaMnO$_3$ | 0.707 | 0.524 | 1.07 | 0.013 | 0.056 | 0.26 | 0.40 | 1.34 | 3.082 | 0.941 | 0.21 | 2.34 | 0.56 |
| PrMnO$_3$ | 0.704 | 0.530 | 1.050 | 0.011 | 0.056 | 0.38 | 0.69 | 1.32 | 3.156 | 1.138 | 0.28 | 2.392 | 0.52 |
| NdMnO$_3$ | 0.708 | 0.533 | 0.983 | 0.011 | 0.057 | 0.38 | 0.56 | 1.32 | 3.202 | 1.288 | 0.29 | 2.407 | 0.49 |
| SmMnO$_3$ | 0.723 | 0.558 | 1.047 | 0.011 | 0.057 | 0.45 | 0.62 | 1.36 | 3.239 | 1.204 | 0.33 | 2.398 | 0.45 |
| EuMnO$_3$ | 0.731 | 0.563 | 1.036 | 0.011 | 0.056 | 0.46 | 0.80 | 1.315 | 3.266 | 1.246 | 0.31 | 2.343 | 0.526 |
| GdMnO$_3$ | 0.734 | 0.565 | 1.009 | 0.011 | 0.057 | 0.48 | 0.65 | 1.318 | 3.298 | 1.303 | 0.28 | 2.422 | 0.498 |
| **GW$_0$** | | | | | | | | | | | | | |
| LaMnO$_3$ | 0.746 | 0.469 | 0.488 | 0.022 | 0.073 | 0.20 | 0.36 | 1.34 | 3.082 | 0.941 | 0.21 | 0.882 | 0.313 |
| PrMnO$_3$ | 0.781 | 0.380 | 0.489 | 0.035 | 0.065 | 0.27 | 0.42 | 1.32 | 3.156 | 1.138 | 0.28 | 1.08 | 0.22 |
| NdMnO$_3$ | 0.752 | 0.405 | 0.535 | 0.036 | 0.07 | 0.24 | 0.45 | 1.32 | 3.202 | 1.288 | 0.29 | 1.006 | 0.27 |
| SmMnO$_3$ | 0.746 | 0.493 | 0.574 | 0.013 | 0.063 | 0.34 | 0.66 | 1.36 | 3.239 | 1.204 | 0.33 | 1.314 | 0.107 |
| EuMnO$_3$ | 0.942 | 0.516 | 0.617 | 0.019 | 0.080 | 0.53 | 0.65 | 1.315 | 3.266 | 1.246 | 0.31 | 1.143 | 0.20 |
| GdMnO$_3$ | 0.759 | 0.515 | 0.561 | 0.017 | 0.051 | 0.46 | 0.66 | 1.318 | 3.298 | 1.303 | 0.28 | 1.293 | 0.19 |
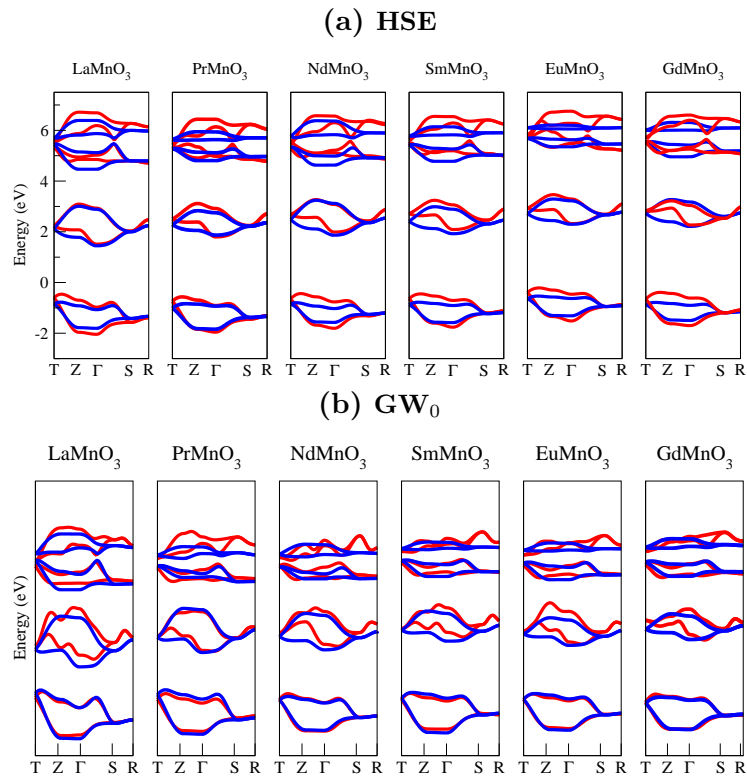
**Figure 3.10:** Figure showing e$_g$ TB bands (blue) obtained using *Model B-2* parametrization and the e$_g$ MLWFs(red).

| RMnO$_3$ | J$_H$ | $\Delta\epsilon^\uparrow$ | $\Delta$n$^\uparrow$ |
|---|---|---|---|
| HSE | | | |
| LaMnO$_3$ | 2.483 | 2.852 | 0.87 |
| PrMnO$_3$ | 2.442 | 3.206 | 0.906 |
| NdMnO$_3$ | 2.406 | 3.267 | 0.910 |
| SmMnO$_3$ | 2.415 | 3.310 | 0.919 |
| EuMnO$_3$ | 2.426 | 3.292 | 0.92 |
| GdMnO$_3$ | 2.421 | 3.411 | 0.927 |
| GW$_0$ | | | |
| LaMnO$_3$ | 1.874 | 1.362 | 0.616 |
| PrMnO$_3$ | 1.805 | 1.832 | 0.737 |
| NdMnO$_3$ | 1.753 | 2.011 | 0.751 |
| SmMnO$_3$ | 1.797 | 2.093 | 0.75 |
| EuMnO$_3$ | 1.802 | 2.027 | 0.778 |
| GdMnO$_3$ | 1.828 | 2.195 | 0.796 |

**Table 3.6:** Table showing the values of J$_H$, $\Delta$n$^\uparrow$, $\Delta\epsilon^\uparrow$ obtained at HSE and GW$_0$ level of calculations.

# 3.4 Evolution of the TB parameters as a function of r$_R$

The evolution of various TB parameters are shown in the Figs. 3.11, 3.12, 3.13. In general, an overall consistent qualitative description of the TB bands has been found for the compounds down the series at PBE, HSE and GW$_0$ level of calculations. However, in some cases, some quantitative deviations are observed in the GW$_0$, which could be attributed to the difficulties in achieving well-converged results at GW level (for instance, the upper local minority bands are not well reproduced in the case of Nd and Sm).

1. Hopping parameters *first nn hoppings* $t^{\uparrow\uparrow}$, $t^{\downarrow\downarrow}$, *second nn hoppings* $t^{xy}$, $t^{2z}$ *and ( $\eta^{\uparrow}$, $\eta^{\downarrow}$, $\tilde{\lambda}$).* There is not much variation seen in the magnitude of the nearest-neighbour hopping parameter (t$^{\uparrow\uparrow}$) at PBE, HSE and GW$_0$ levels of calculations. At GW$_0$ level, t$^{\downarrow\downarrow}$ is pretty much a constant down the series at PBE and HSE levels, whereas at GW$_0$ level, the value of t$^{\downarrow\downarrow}$ decreases by about 0.1 eV in the case of Pr and Nd. The variation of $\tilde{\lambda}$ down the series is pretty much a constant from La to Gd at PBE, HSE and GW$_0$. The magnitude of the next-nearest neighbours (t$^{xy}$ and t$^{2z}$) is already quite small in magnitude, and so the variation of this value down the series could be considered as negligible. t$^{\uparrow\uparrow}$, t$^{\downarrow\downarrow}$ calculated for the *Pbnm* structure shows a decrease in the values down the series. $\eta^{\uparrow}$ and $\eta^{\downarrow}$ are calculated from the ratio of the $t$(Pbnm) to $t$(JT). Therefore as $t$(Pbnm)($\uparrow$ and $\downarrow$) decreases down the series, the values of $\eta$($\uparrow$ and $\downarrow$) are expected to increase, and this could be seen from the plots of $\eta^{\uparrow}$ and $\eta^{\downarrow}$ Vs. r$_R$. It is a fact that the hopping amplitude is proportional to cos $\phi$ where $\phi$ is the Mn-O-Mn bond angle [132]. Comparing the trends of t$^{\uparrow\uparrow}$(Pbnm) and t$^{\downarrow\downarrow}$(Pbnm) down the series explains the observed rapid drop of the T$_N$ which is also proportional to cos$^2\phi$. The trend also is in very good agreement with the fact that the hopping amplitudes are monotonically related to the tolerance factor.

2. Onsite parameters ($J$, $\lambda^{\uparrow}$, $\lambda^{\downarrow}$, $\eta_\lambda$). The onsite parameters J (Hund's rule coupling strength) calculated at PBE, HSE and GW is nearly constant down the series. Even when the volume decreases down the series, the J and $\lambda^{\uparrow}$ (except for EuMnO$_3$) are nearly constants, this leads to an interesting conclusion that the Hund's rule coupling strength and the Jahn-Teller coupling constants could be considered as universal constants in the RMnO$_3$ series

although at GW$_0$ level of calculations a higher value of $\lambda^\uparrow$ is obtained for EuMnO$_3$ (43 % increase) when compared with the average of the $\lambda$ values obtained for the other $R$MnO$_3$ compounds. The value of $\lambda^\downarrow$ is less in the case of HSE when compared with that of PBE and GW$_0$. Unlike $\lambda^\uparrow$, $\lambda^\downarrow$ does not show a constant behaviour down the series. The value of $\lambda^\downarrow$ decreases by about 75 %. The value of $\eta_\lambda$ is pretty much a constant down the series.

3. Interaction parameters ($U^\lambda_W$). The value of U$^\lambda_W$ is constant down the series. If the screening remains unchanged, the band gap and U is expected to be unchanged. This shows the compounds of the early $R$MnO$_3$ series remains an orbitally-ordered JT insulator.
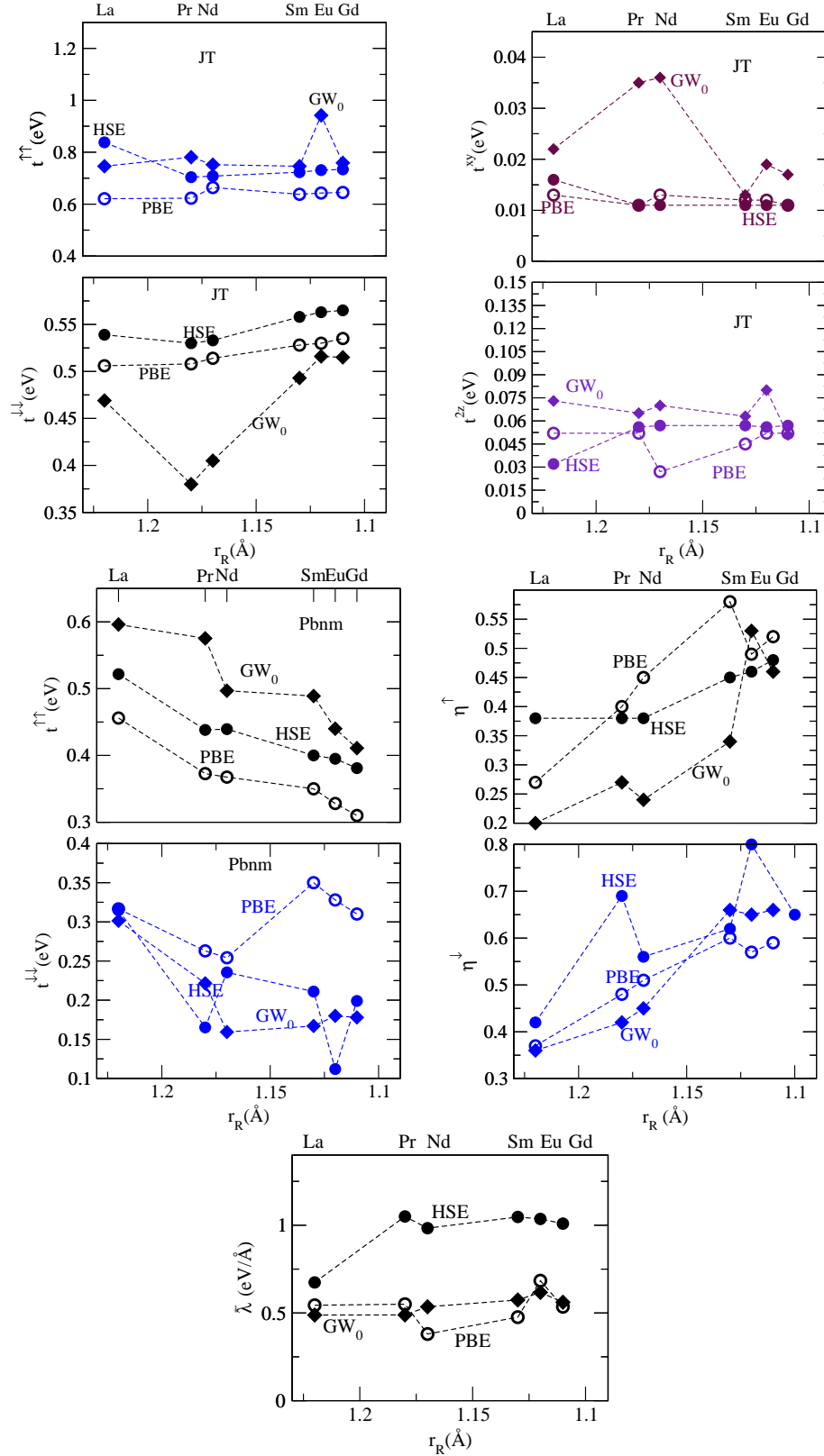
**Figure 3.11:** $r_R$ Vs. tight-binding hopping parameters (First nn hoppings $t^{\uparrow\uparrow}$ and $t^{\downarrow\downarrow}$, second nn hoppings $t^{xy}$ and $t^{2z}$, JT splitting $\tilde{\lambda}$, GFO reduction factors- $\eta^{\uparrow}$ and $\eta^{\downarrow}$.
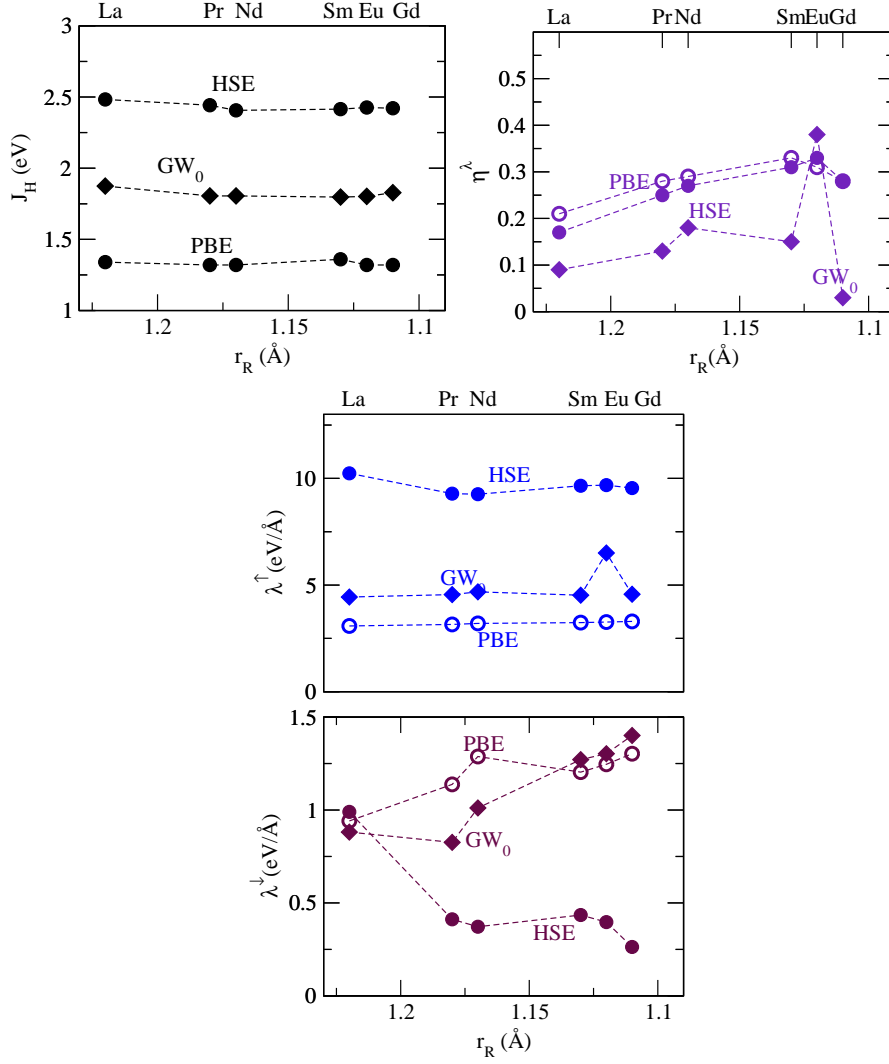
**Figure 3.12:** $r_R$ Vs. onsite parameters (J, $\lambda^\uparrow$, $\lambda^\downarrow$, $\eta_\lambda$).
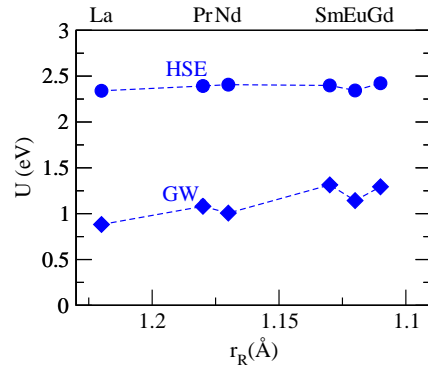


**Figure 3.13:** Plot of $r_R$ Vs. $U_W^\lambda$.

# Chapter 4

# Summary and Conclusions

In this thesis, the combination of first-principles and tight-binding model Hamiltonian via Maximally localized Wannier functions (MLWFs) has been applied to the parent compounds of manganites, $RMnO_3$ ($R$=La, Pr, Nd, Sm, Eu, Gd). The $e_g$ MLWFs have been obtained using VASP2WANNIER90 interface. The tight-binding parameters corresponding to the model Hamiltonian have been obtained and analyzed. We have discussed 2 different ways to obtain the TB parameters: (i) Model A - the tight-binding parametrization is based on the various model structures with both FM (which always leads to a metallic system) and A-AFM order [8, 81] (ii) Model B - TB parametrization is constructed from only two crystal structures: purely JT distorted structure and the experimental *Pbnm* structure, in both of which yield an insulating solution (A-AFM). We could obtain the parameters in 2 ways: (a) Considering an effectively non-interacting case in which the term $\hat{H}_{e-e}$ is neglected and the influence of the beyond PBE are considered implicitly within the model. We have called this model as Model B-1. (b) The alternative model in which the term $\hat{H}_{e-e}$ is treated explicitly by calculating the Hubbard-U using a mean-field treatment.

We have first discussed the case of LaMnO$_3$ in Chapter 3, the results of which have been published in [82]. We have employed four of the *ab-initio* methods to study LaMnO$_3$ : PBE , PBE+U, HSE and GW$_0$ (at PBE). The structural data for LaMnO$_3$ in Chapter 3 correspond to the optimized structure. All the methods consistently produce an orbitally-ordered JT insulating state. GW$_0$ produces values for the band gap comparable with the experiments while both GW$_0$ and HSE provide satisfactory description of valence and conduction band spectra. Inspite of the limitations within PBE approach, it does not perform too

badly. The proof of the quality and the reliability of the Wannier construction of the $e_g$ $|3z^2\text{-}r^2\rangle$ and $|x^2\text{-}y^2\rangle$ orbitals is represented by the resulting MLWFs, inspite of the difficulties to fully disentangle the effective $e_g$ bands from the other bands with similar energies which are most pronounced in the case of PBE+U and HSE. The different TB routes used in this study (Model-A and Model-B) yield very good TB bands, overlapping with the underlying MLWFs. Overall, it has been demonstrated that the MLWFs could be efficiently used to accurately interpolate the HSE and $GW_0$ band structure from the coarse uniform $k$-point mesh to the desirable symmetry lines thereby remedying the fundamental practical limitation of HSE and $GW_0$ scheme in computing the energy eigenvalues for selected $k$-points.

Using the same methodology we have studied the early series of the parent compounds of manganites $R\text{MnO}_3$ ($R$ = La, Pr, Nd, Sm, Eu, Gd). For qualitative and quantitative comparison, we have used the room temperature lattice constants and structures for all the compounds including $\text{LaMnO}_3$. The phase diagram shown by Kimura et al. [9] has been used as the basis for the work. We have attempted to investigate this phase diagram which shows the trend of the transition temperatures ($T_{OO}$ and $T_N$) by studying the evolution of the structural, electronic and magnetic properties and the tight-binding parameters. The plots of structural properties such as volume (V), unit-cell parameters (a, b, c), Mn-O-Mn bond angles ($\phi_1$, $\phi_2$) and the octahedral tilting angle $\omega$, JT distortion amplitudes ($Q^x$, $Q^z$) and the tolerance factor has been shown as a function of the ionic radii of $R^{3+}$. When the ionic radii of $R^{3+}$ decreases, the major effect is the shrinking of the volume because of the fact that we are adding protons to the nuclei (Lanthanide contraction). The decrease of the Mn-O-Mn bond angles, the tolerance factor and the Volume follow the same trend as the experimental $T_N$. All the methods produce a consistent Mott-Hubbard insulating state for all $R\text{MnO}_3$ ($R$ = La -Gd). Despite the difficulties in the disentanglement of the $e_g$ states mainly at HSE level, the obtained MLWFs are in very good agreement with the underlying VASP bands and also at PBE and $GW_0$ level, the MLWFs are in very good agreement with the underlying VASP bands. The exchange interaction parameters namely $J_{ab}$ and $J_c$ have been calculated at HSE level and the sum has been employed to estimate $T_N$ within a mean-field approach. The trend matches very well with the experimental $T_N$. The theoretical dielectric function matches fairly well with the experimental dielectric function.

Like in the case of $\text{LaMnO}_3$, the method-derived changes in the TB parameters due to the different treatment of the el-el exchange-correlation kernel at PBE,

HSE and $GW_0$ has been demonstrated and has been accounted for using Model B-1 and B-2. In general, an overall consistent qualitative description of the TB trend has been found for the compounds down the series at PBE, HSE and $GW_0$ level of calculations. However, certain deviations are observed when $GW_0$ is employed (for Pr and Nd) and this could be attributed to the difficulties in achieving well-converged results. Also the upper local minority $e_g$ bands are not very well described for the case of $NdMnO_3$ and $SmMnO_3$. The trends of the hopping parameters ($t^{\uparrow\uparrow}$, $t^{\downarrow\downarrow}$ (JT and Pbnm), $\tilde{\lambda}$, $\eta^{\uparrow}$ amd $\eta^{\downarrow}$) have been shown. The trends of hopping amplitudes $t^{\uparrow\uparrow}$ (Pbnm) , $t^{\downarrow\downarrow}$ (Pbnm) are comparable with that of the volume, tolerance factor, $\phi$ and $T_N$. The fact that the hopping amplitudes and the tolerance factor are monotonically related has been proven. Another interesting result is that of $J_H$ (Hund's rule coupling strength) which remains practically a constant at all levels of calculations. Also U and $\lambda^{\uparrow}$ remains pretty much a constant except for $EuMnO_3$ at $GW_0$ level. Thus $J_H$, $\lambda^{\uparrow}$ and U can be regarded as universal constants.

# Appendix A

## A.1  Model parameters in the extended $p-d$ basis

In this section we will briefly review the results based on p-d TB model and compare it with the e$_g$ model as discussed in the work by Kovačik *et al.* in [81]. Unlike the e$_g$-only model which only includes the e$_g$ states, the d-p model includes atomic-like orbitals corresponding to both Mn(d) and O(p) states in the TB basis.

The effect of Jahn-Teller distortions within the $d$-$p$ model has been studied and then the TB representations for both the models obtained from GGA+U calculations (with different values of the Hubbard parameter U) has been compared. The on-site energy splitting is given as $\delta = \sqrt{(\varepsilon_1 - \varepsilon_2)^2 + 4q^2}$, where $\varepsilon$ and q are onsite diagonal and onsite off-diagonal matrix elements respectively. The plots from [81] are shown in fig. A.1. In fig. A.1, it is observed that the onsite diagonal matrix elements are constant with the increase of the $Q^x/Q_0^x$ while $\delta$ (splitting of e$_g$ states) and the value of the onsite off-diagonal matrix elements are found to increase linearly. There is also difference in the values corresponding to the majority/minority spin channels and this has been attributed to the admixture of other states. It could be attributed to the combined crystal-field and ligand-field effect.

In the $d$-$p$ model, it has been found that the effect of $U$ is mostly local and this leads to U-dependent shifts of the on-site energies and an increase in the JT splitting, whereas the corresponding hopping amplitudes are only weakly affected by $U$ (See fig.A.2). The change of the onsite energies and the JT splitting calculated for the different values of $U$, are distinctly different from the corresponding mean-field model Hamitlonian. It is important to see how the GGA+U and the U-dependence of the onsite matrix elements are related. For each value of $U$ *(GGA+U)* using the occupation matrix elements obtained from the corresponding *GGA+U* calculations, the potential shift according to Dudarev et al. [34] which is given as

$$\Delta V_{mm'} = U \left( \frac{\delta_{mm'}}{2} - n_{mm'} \right) \tag{A.1}$$

is evaluated, and it is shown in the study that the *GGA+U* potential shifts and the *U*-dependence on the onsite MLWF matrix elements correspond well with each other. The reason for this is attributed to the fact that the MLWFs of the extended $d$-$p$ model are rather similar to the atomic orbitals used as projector
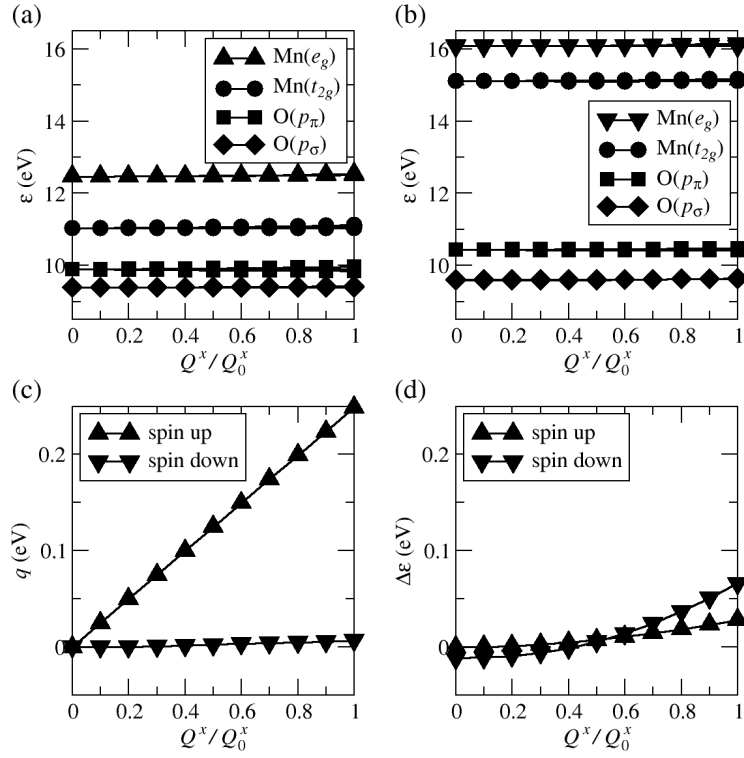
**Figure A.1:** Figure from [81] showing (a)/(b) Onsite energies of the d-p model for the majority/minority spins (c) Onsite off-diagonal element $q$ (d) Splitting $\Delta\varepsilon$ between on-site energies of the two $e_g$-like MLWFs

**(a)** Onsite energy (d-p)   **(b)** JT splitting (d-p)

**(c)** Onsite energy ($e_g$)   **(d)** JT splitting
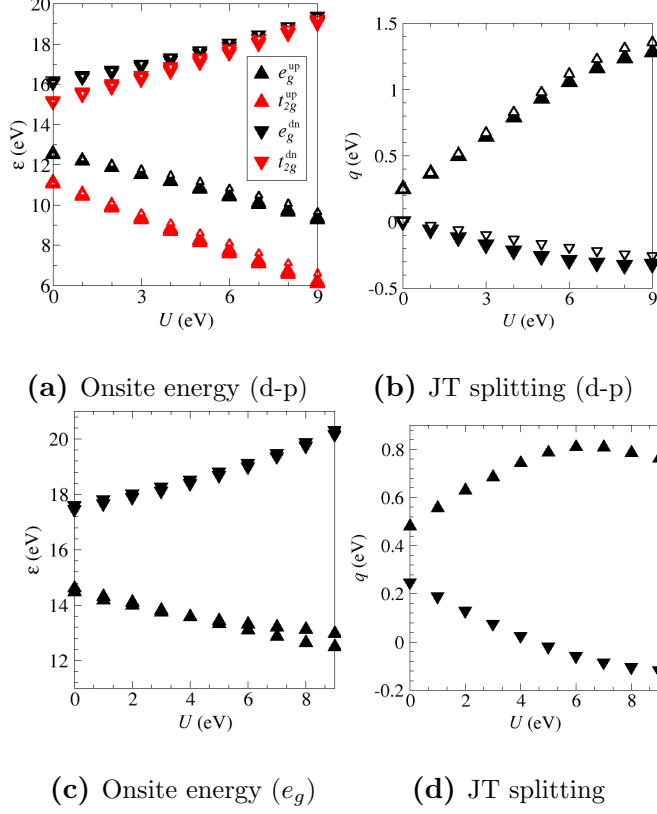
**Figure A.2:** Plots from [81] showing the variation of onsite energies and the JT splitting in both $d$-$p$ and $e_g$ models

functions within the $GGA+U$ approach. The similarity is further demonstrated by comparing the occupation of the corresponding MLWFs which is given as,

$$\mathrm{n}_{mm'}^{MLWF} = \int_{-\infty}^{\mathrm{E}_F} d\epsilon \int_{BZ} d\mathbf{k} \sum_{l} (U_{lm}^{(\mathbf{k})})^* \delta(\epsilon - \epsilon_{l\mathbf{k}}) U_{lm'}^{(\mathbf{k})} \tag{A.2}$$

The effect of U within the effective $e_g$ model shows that the U-dependence is weaker than in the $d$-$p$ model. This indicates that the $U$ dependence of the onsite energies for the effective $e_g$ MLWFs is still determined by the $GGA+U$ potential shifts, but is renormalized by the extent of the overlap between the extended MLWFs and the corresponding $e_g$ atomic orbital. It is seen that the effect of $U$ on the hopping amplitudes is strongly enhanced in the case of $e_g$ only.

In summary, the authors of [81] have discussed the differences in the MLWF-derived TB parametrization of LaMnO$_3$ that result from different values of the

Hubbard $U$ used in the $GGA+U$ calculations from which the MLWFs are obtained. Two different models ($d$-$p$ and $e_g$-only models) have been discussed. A similarity between the "+U" correction to the GGA functional and the mean-field approximation of the el-el interaction in the corresponding model Hamiltonian. This similarity explains the observed trends in the MLWF TB parameters and the difference between the two different TB models. The authors have noted the fact that the similarity between DFT and the mean-field Hubbard model is not present if the electronic structure is calculated using other "beyond LDA/GGA" methods like SIC, Hybrid functionals or the GW approximation.

**A.**

# Appendix B

## B.1  Bandstructures and PDOS - $R\text{MnO}_3$

In this appendix, PDOS, bandstructures (PBE, HSE and $GW_0$) and the $e_g$ ML-WFs corresponding to both JT-distorted structure (A-AFM) and experimental *Pbnm* structure for all $R\text{MnO}_3$ are presented.

# B.2   LaMnO$_3$

| h$^{\Delta \mathbf{R}}$ | PBE | HSE | GW$_0$ |
|---|---|---|---|
| h$_{11}^x(\uparrow)$ | -0.147887 | -0.242665 | -0.22265 |
| h$_{22}^x(\uparrow)$ | -0.463337 | -0.639777 | -0.571604 |
| h$_{11}^x(\downarrow)$ | -0.118779 | -0.135318 | -0.13223 |
| h$_{22}^x(\downarrow)$ | -0.377113 | -0.404526 | -0.356921 |
| h$_{12}^x(\uparrow)$ | 0.171214 | 0.258705 | 0.270957 |
| h$_{21}^x(\uparrow)$ | 0.382034 | 0.513952 | 0.490653 |
| h$_{12}^x(\downarrow)$ | 0.155312 | 0.146439 | 0.170482 |
| h$_{21}^x(\downarrow)$ | 0.273032 | 0.298212 | 0.245432 |
| h$_{11}^{xy}(\uparrow)$ | -0.012782 | -0.019338 | -0.025599 |
| h$_{11}^{xy}(\downarrow)$ | -0.012507 | -0.01268 | -0.01781 |
| h$_{11}^{2z}(\uparrow)$ | -0.051763 | -0.029109 | -0.030363 |
| h$_{11}^{2z}(\downarrow)$ | -0.05156 | -0.03583 | -0.116522 |
| h$_{11}^0(\uparrow)$ | 9.596297 | 9.000637 | 6.992145 |
| h$_{12}^0(\uparrow)$ | 0.432207 | 1.483219 | 0.637367 |
| h$_{22}^0(\uparrow)$ | 9.250851 | 8.128786 | 6.578301 |
| h$_{11}^0(\downarrow)$ | 11.874463 | 13.311348 | 9.950342 |
| h$_{12}^0(\downarrow)$ | 0.141168 | -0.144577 | 0.115559 |
| h$_{22}^0(\downarrow)$ | 11.841471 | 13.387414 | 10.082227 |

**Table B.1:** Matrix elements obtained from PBE, HSE and GW$_0$ corresponding to the JT-distorted (A-AFM) structure of LaMnO$_3$.

| $h^{\Delta\mathbf{R}}$ | PBE | HSE | $GW_0$ |
|---|---|---|---|
| $h_{11}^x(\uparrow)$ | -0.074443 | -0.075828 | -0.154411 |
| $h_{22}^x(\uparrow)$ | -0.328799 | -0.373085 | -0.44891 |
| $h_{11}^x(\downarrow)$ | -0.097383 | -0.127387 | -0.099391 |
| $h_{22}^x(\downarrow)$ | -0.243554 | -0.252342 | -0.234014 |
| $h_{11}^0(\uparrow)$ | 9.783282 | 8.735374 | 6.785627 |
| $h_{12}^0(\uparrow)$ | 0.373543 | 0.964386 | 0.568115 |
| $h_{22}^0(\uparrow)$ | 9.449427 | 6.634623 | 6.035349 |
| $h_{11}^0(\downarrow)$ | 12.459359 | 12.721685 | 10.261764 |
| $h_{22}^0(\downarrow)$ | 12.133419 | 12.580955 | 10.054899 |

**Table B.2:** Matrix elements obtained from PBE, HSE and $GW_0$ corresponding to the experimental *Pbnm* structure of LaMnO$_3$.
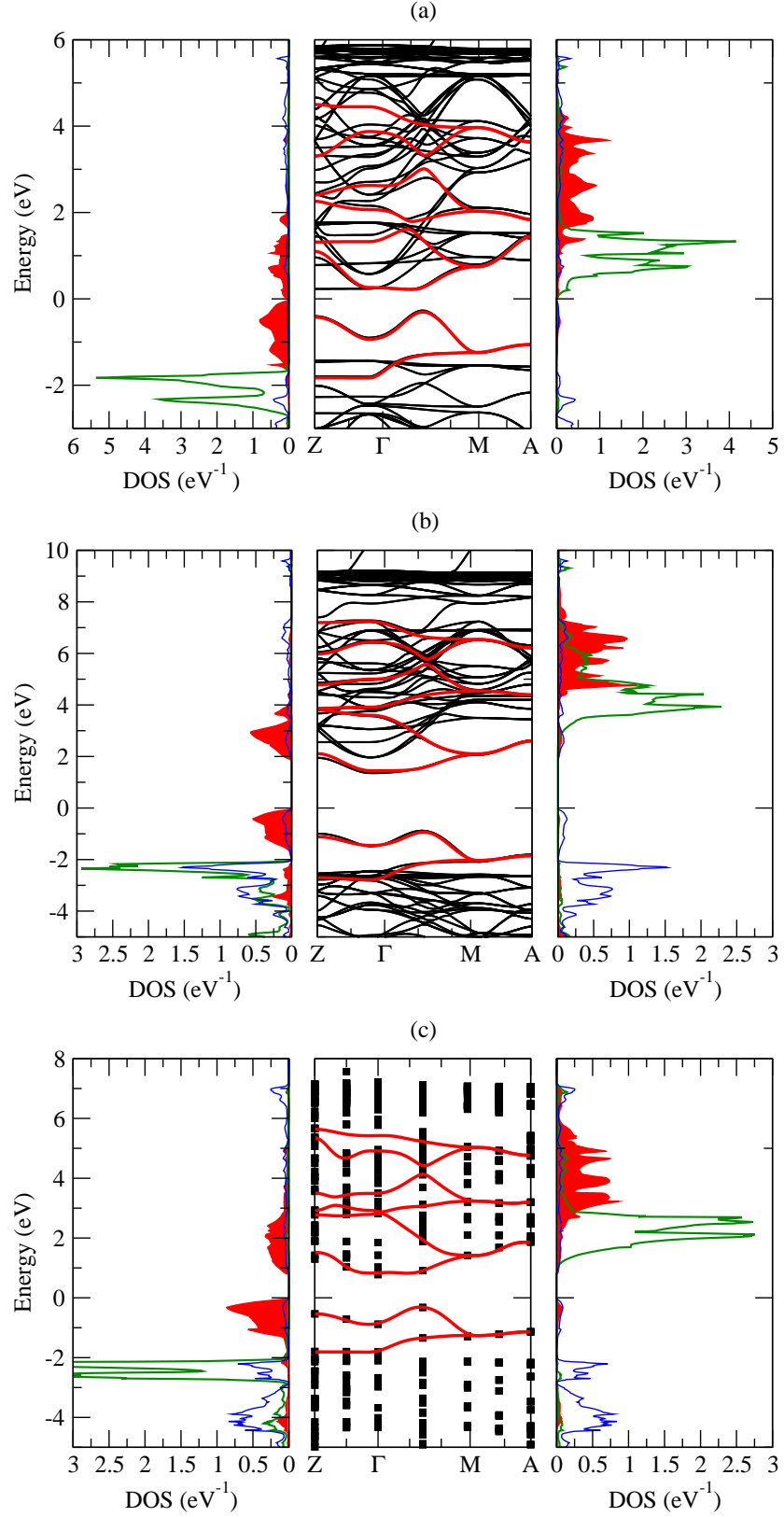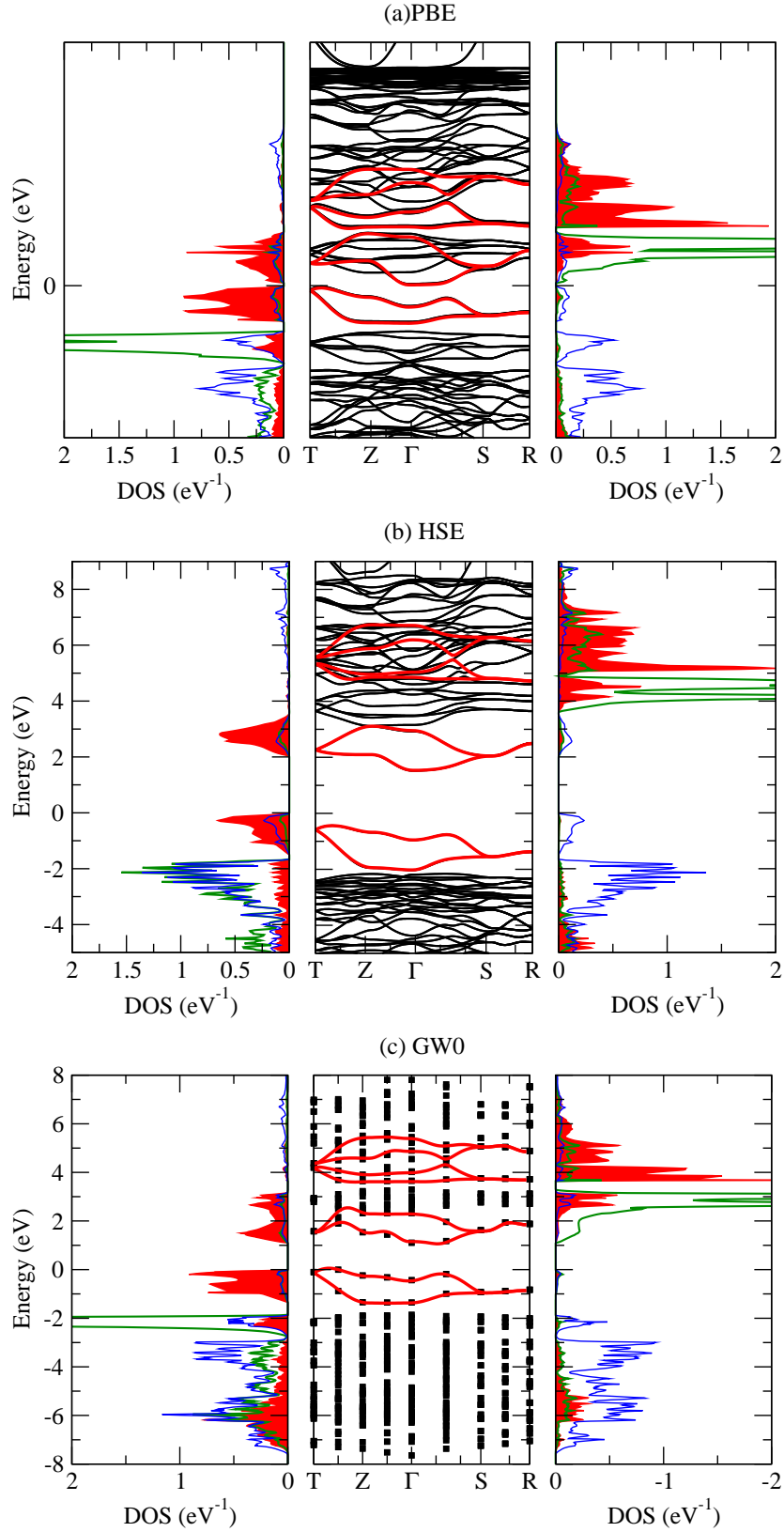
**Figure B.1:** VASP bandstructure (black) and MLWFs (red) of LaMnO$_3$ - JT distorted structure (A-AFM).

135

**Figure B.2:** VASP bandstructure (black) and MLWFs (red) of LaMnO$_3$ - Experimental *Pbnm* structure.

136

# B.3   PrMnO$_3$

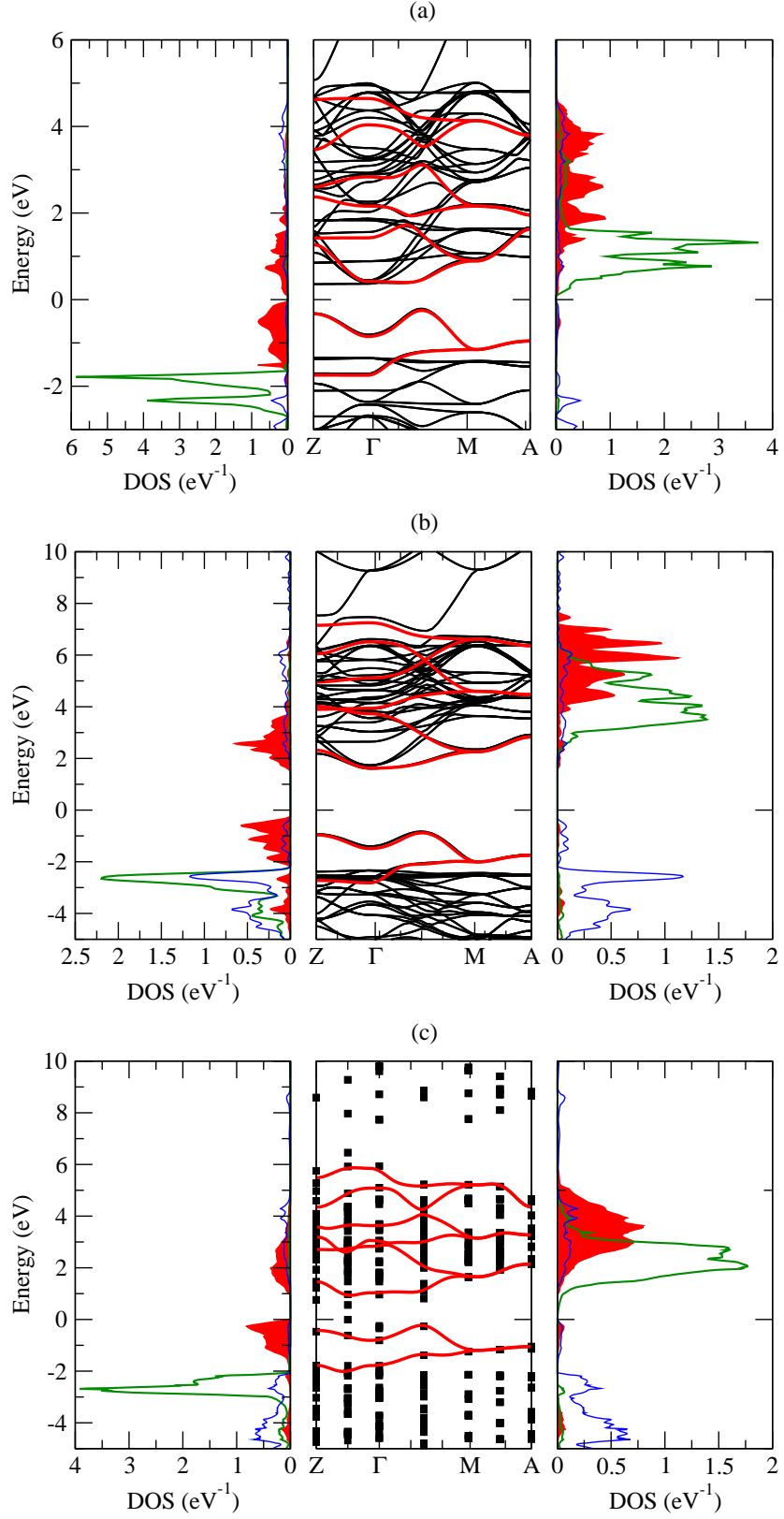| $h^{\Delta \mathbf{R}}$ | PBE | HSE | GW$_0$ |
|---|---|---|---|
| $h_{11}^{x}(\uparrow)$ | -0.143484 | -0.136679 | -0.220591 |
| $h_{22}^{x}(\uparrow)$ | -0.462969 | -0.514964 | -0.594461 |
| $h_{11}^{x}(\downarrow)$ | -0.115414 | -0.119939 | -0.12003 |
| $h_{22}^{x}(\downarrow)$ | -0.377134 | -0.393028 | -0.293243 |
| $h_{12}^{x}(\uparrow)$ | 0.159159 | 0.088998 | 0.288149 |
| $h_{21}^{x}(\uparrow)$ | 0.395107 | 0.651933 | 0.516809 |
| $h_{12}^{x}(\downarrow)$ | 0.137391 | 0.131907 | 0.107527 |
| $h_{21}^{x}(\downarrow)$ | 0.297312 | 0.325052 | 0.230764 |
| $h_{11}^{xy}(\uparrow)$ | -0.011922 | -0.008874 | -0.041828 |
| $h_{11}^{xy}(\downarrow)$ | -0.010732 | -0.012615 | -0.027929 |
| $h_{11}^{2z}(\uparrow)$ | -0.051776 | -0.055852 | -0.046466 |
| $h_{11}^{2z}(\downarrow)$ | -0.051931 | -0.05707 | -0.08388 |
| $h_{11}^{0}(\uparrow)$ | 7.206051 | 7.237943 | 8.035657 |
| $h_{12}^{0}(\uparrow)$ | 0.525828 | 1.307839 | 0.786964 |
| $h_{22}^{0}(\uparrow)$ | 6.775836 | 5.156393 | 7.575524 |
| $h_{11}^{0}(\downarrow)$ | 9.474095 | 10.88187 | 10.732289 |
| $h_{12}^{0}(\downarrow)$ | 0.200397 | -0.07418 | 0.128232 |
| $h_{22}^{0}(\downarrow)$ | 9.389982 | 10.880788 | 10.882625 |

**Table B.3:** Matrix elements obtained from PBE, HSE and GW$_0$ corresponding to the JT-distorted (A-AFM) structure of PrMnO$_3$.

| $h^{\Delta \mathbf{R}}$ | PBE | HSE | GW0 |
|---|---|---|---|
| $h_{11}^x(\uparrow)$ | -0.041079 | -0.054348 | -0.161338 |
| $h_{22}^x(\uparrow)$ | -0.262187 | -0.310247 | -0.437342 |
| $h_{11}^x(\downarrow)$ | -0.085787 | -0.117547 | -0.066355 |
| $h_{22}^x(\downarrow)$ | -0.203873 | -0.149344 | -0.169829 |
| $h_{11}^0(\uparrow)$ | 6.135555 | 6.276391 | 8.515796 |
| $h_{12}^0(\uparrow)$ | 0.389847 | 0.902014 | 0.801047 |
| $h_{22}^0(\uparrow)$ | 5.448305 | 3.625999 | 7.62784 |
| $h_{11}^0(\downarrow)$ | 8.658983 | 9.886314 | 11.871325 |
| $h_{22}^0(\downarrow)$ | 8.205297 | 9.785574 | 11.492162 |

**Table B.4:** Matrix elements obtained from PBE, HSE and GW0 corresponding to the experimental *Pbnm* structure of PrMnO$_3$.

**Figure B.3:** VASP bandstructure (black) and MLWFs (red) of PrMnO$_3$ - JT (AAFM) distorted structure.

## B.4 NdMnO$_3$

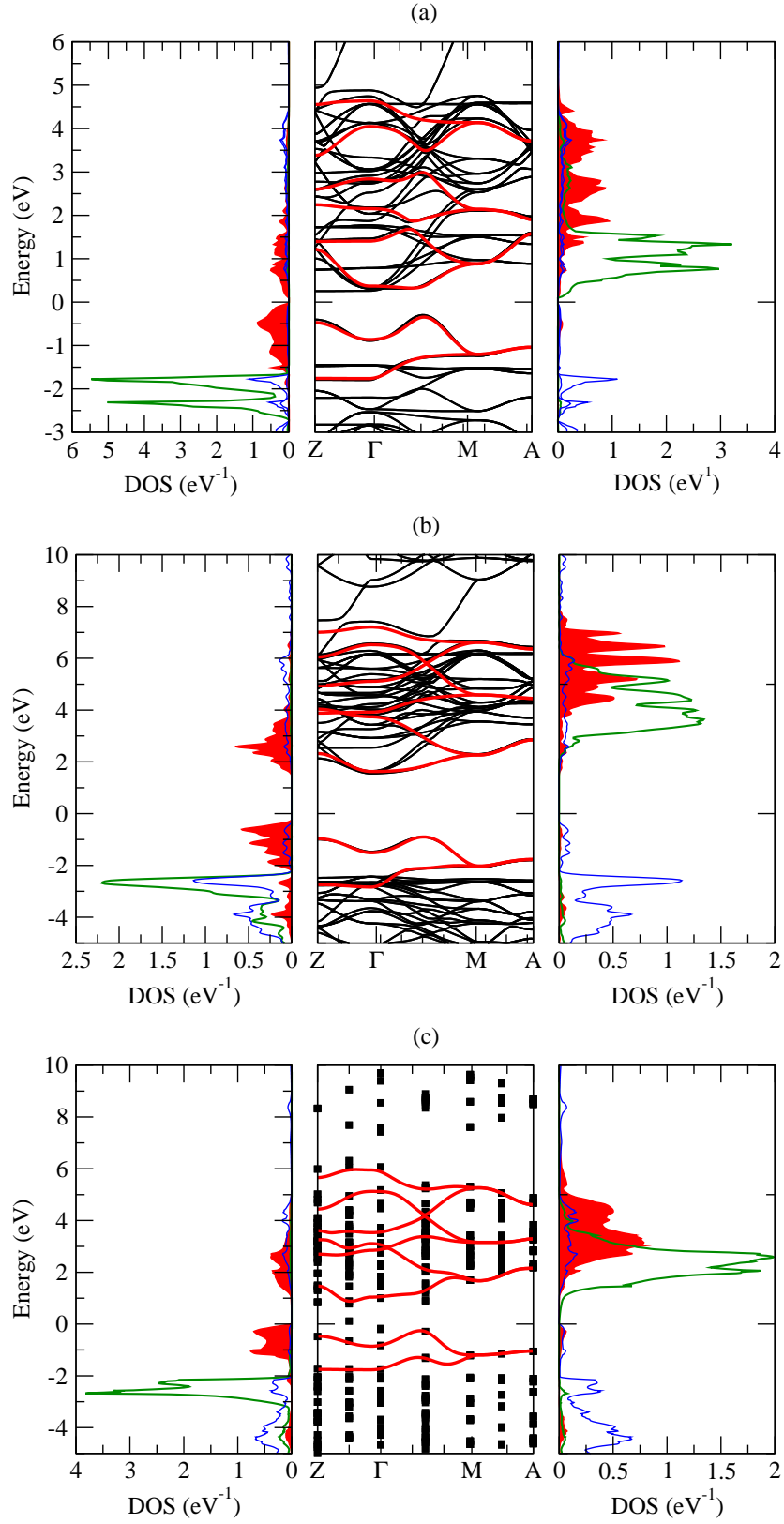| h$^{\Delta\mathbf{R}}$ | PBE | HSE | GW0 |
|---|---|---|---|
| h$_{11}^{x}(\uparrow)$ | -0.16864 | -0.137047 | -0.2181 |
| h$_{22}^{x}(\uparrow)$ | -0.498857 | -0.517797 | -0.574269 |
| h$_{11}^{x}(\downarrow)$ | -0.126805 | -0.12753 | -0.127403 |
| h$_{22}^{x}(\downarrow)$ | -0.385152 | -0.397951 | -0.312218 |
| h$_{12}^{x}(\uparrow)$ | 0.206304 | 0.091428 | 0.297574 |
| h$_{21}^{x}(\uparrow)$ | 0.364604 | 0.654064 | 0.544947 |
| h$_{12}^{x}(\downarrow)$ | 0.1577 | 0.15398 | 0.114424 |
| h$_{21}^{x}(\downarrow)$ | 0.275982 | 0.306741 | 0.256753 |
| h$_{11}^{xy}(\uparrow)$ | -0.013508 | -0.008531 | -0.037822 |
| h$_{11}^{xy}(\downarrow)$ | -0.012151 | -0.013518 | -0.033208 |
| h$_{11}^{2z}(\uparrow)$ | -0.025392 | -0.056323 | -0.056284 |
| h$_{11}^{2z}(\downarrow)$ | -0.028711 | -0.057195 | -0.083558 |
| h$_{11}^{0}(\uparrow)$ | 7.022166 | 7.241499 | 8.052973 |
| h$_{22}^{0}(\uparrow)$ | 6.711146 | 5.14978 | 7.550218 |
| h$_{12}^{0}(\uparrow)$ | 0.561618 | 1.321549 | 0.814227 |
| h$_{11}^{0}(\downarrow)$ | 9.338348 | 10.887348 | 10.739633 |
| h$_{22}^{0}(\downarrow)$ | 9.294104 | 10.862009 | 10.870879 |
| h$_{12}^{0}(\downarrow)$ | 0.233337 | -0.066553 | 0.171835 |

**Table B.5:** Matrix elements obtained from PBE, HSE and GW0 corresponding to the JT-distorted (A-AFM) structure of NdMnO$_3$.

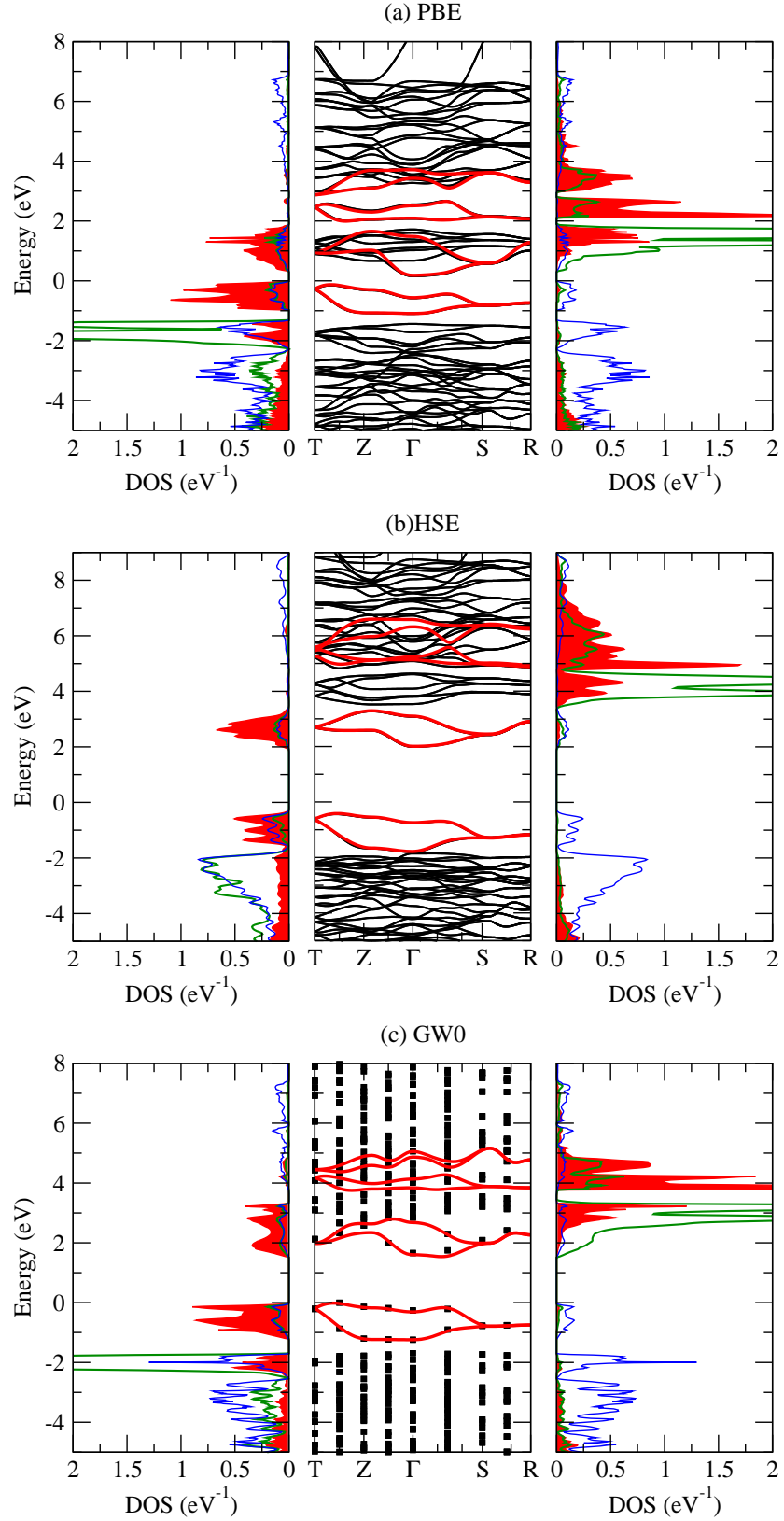| h$^{\Delta \mathbf{R}}$ | PBE | HSE | GW0 |
|---|---|---|---|
| h$_{11}^x(\uparrow)$ | -0.038422 | -0.068766 | -0.161338 |
| h$_{22}^x(\uparrow)$ | -0.257813 | -0.315873 | -0.437342 |
| h$_{11}^x(\downarrow)$ | -0.080705 | -0.106217 | -0.066355 |
| h$_{22}^x(\downarrow)$ | -0.196361 | -0.192411 | -0.169829 |
| h$_{11}^0(\uparrow)$ | 6.046113 | 6.144002 | 8.515796 |
| h$_{22}^0(\uparrow)$ | 5.325463 | 3.568329 | 7.62784 |
| h$_{12}^0(\uparrow)$ | 0.399448 | 1.004765 | 0.801047 |
| h$_{11}^0(\downarrow)$ | 8.55903 | 9.78862 | 11.871325 |
| h$_{22}^0(\downarrow)$ | 8.081982 | 9.547402 | 11.492162 |

**Table B.6:** Matrix elements obtained from PBE, HSE and GW0 corresponding to the experimental *Pbnm* structure of NdMnO$_3$.

**Figure B.4:** VASP bandstructure (black) and MLWFs (red) of NdMnO₃-JT-distorted structure (A-AFM).

**Figure B.5:** VASP bandstructure (black) and MLWFs (red) of NdMnO$_3$ - Experimental *Pbnm* structure.

143

## B.5   SmMnO$_3$

| h$^{\Delta \mathbf{R}}$ | PBE | HSE | GW0 |
|---|---|---|---|
| h$_{11}^{x}(\uparrow)$ | -0.148792 | -0.144406 | -0.222187 |
| h$_{22}^{x}(\uparrow)$ | -0.47518 | -0.53043 | -0.571119 |
| h$_{11}^{x}(\downarrow)$ | -0.126293 | -0.125711 | -0.128979 |
| h$_{22}^{x}(\downarrow)$ | -0.394062 | -0.413696 | -0.371814 |
| h$_{12}^{x}(\uparrow)$ | 0.171992 | 0.103332 | 0.260402 |
| h$_{21}^{x}(\uparrow)$ | 0.39442 | 0.65231 | 0.487537 |
| h$_{12}^{x}(\downarrow)$ | 0.172997 | 0.146003 | 0.135985 |
| h$_{21}^{x}(\downarrow)$ | 0.273961 | 0.325607 | 0.298862 |
| h$_{11}^{xy}(\uparrow)$ | -0.012381 | -0.008926 | -0.023488 |
| h$_{11}^{xy}(\downarrow)$ | -0.011974 | -0.013245 | -0.003007 |
| h$_{11}^{2z}(\uparrow)$ | -0.052123 | -0.056488 | -0.035757 |
| h$_{11}^{2z}(\downarrow)$ | -0.051999 | -0.056568 | -0.089837 |
| h$_{11}^{0}(\uparrow)$ | 7.06894 | 7.09751 | 7.948509 |
| h$_{22}^{0}(\uparrow)$ | 6.670591 | 5.077934 | 7.494789 |
| h$_{12}^{0}(\uparrow)$ | 0.527261 | 1.342226 | 0.73506 |
| h$_{11}^{0}(\downarrow)$ | 9.313243 | 10.779414 | 10.621519 |
| h$_{22}^{0}(\downarrow)$ | 9.279891 | 10.790282 | 10.734815 |
| h$_{12}^{0}(\downarrow)$ | 0.208825 | -0.075533 | 0.208521 |

**Table B.7:** Matrix elements obtained from PBE, HSE and GW0 corresponding to the JT-distorted (A-AFM) structure of SmMnO$_3$.
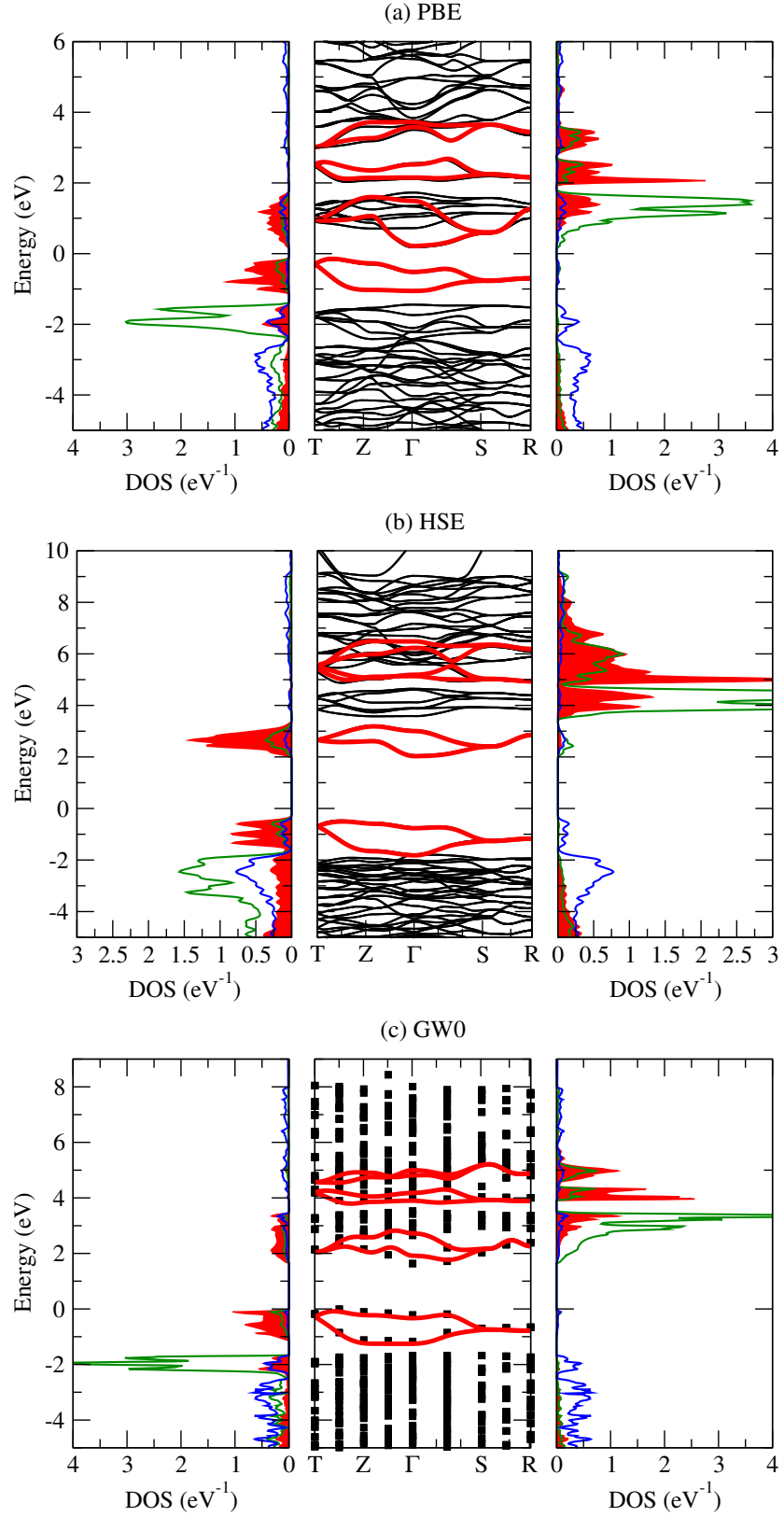
| h$^{\Delta\mathbf{R}}$ | PBE | HSE | GW0 |
|---|---|---|---|
| h$_{11}^x(\uparrow)$ | -0.033273 | -0.049174 | -0.148348 |
| h$_{22}^x(\uparrow)$ | -0.244358 | -0.282878 | -0.375663 |
| h$_{11}^x(\downarrow)$ | -0.089049 | -0.107945 | -0.056794 |
| h$_{22}^x(\downarrow)$ | -0.177362 | -0.176662 | -0.130018 |
| h$_{11}^0(\uparrow)$ | 5.754329 | 5.981308 | 7.014783 |
| h$_{22}^0(\uparrow)$ | 4.988071 | 3.145501 | 5.405091 |
| h$_{12}^0(\uparrow)$ | 0.399524 | 0.853958 | 0.668695 |
| h$_{11}^0(\downarrow)$ | 8.347355 | 9.504737 | 10.016262 |
| h$_{22}^0(\downarrow)$ | 7.837813 | 9.281237 | 9.591797 |

**Table B.8:** Matrix elements obtained from PBE, HSE and GW0 corresponding to the experimental *Pbnm* structure of SmMnO$_3$.
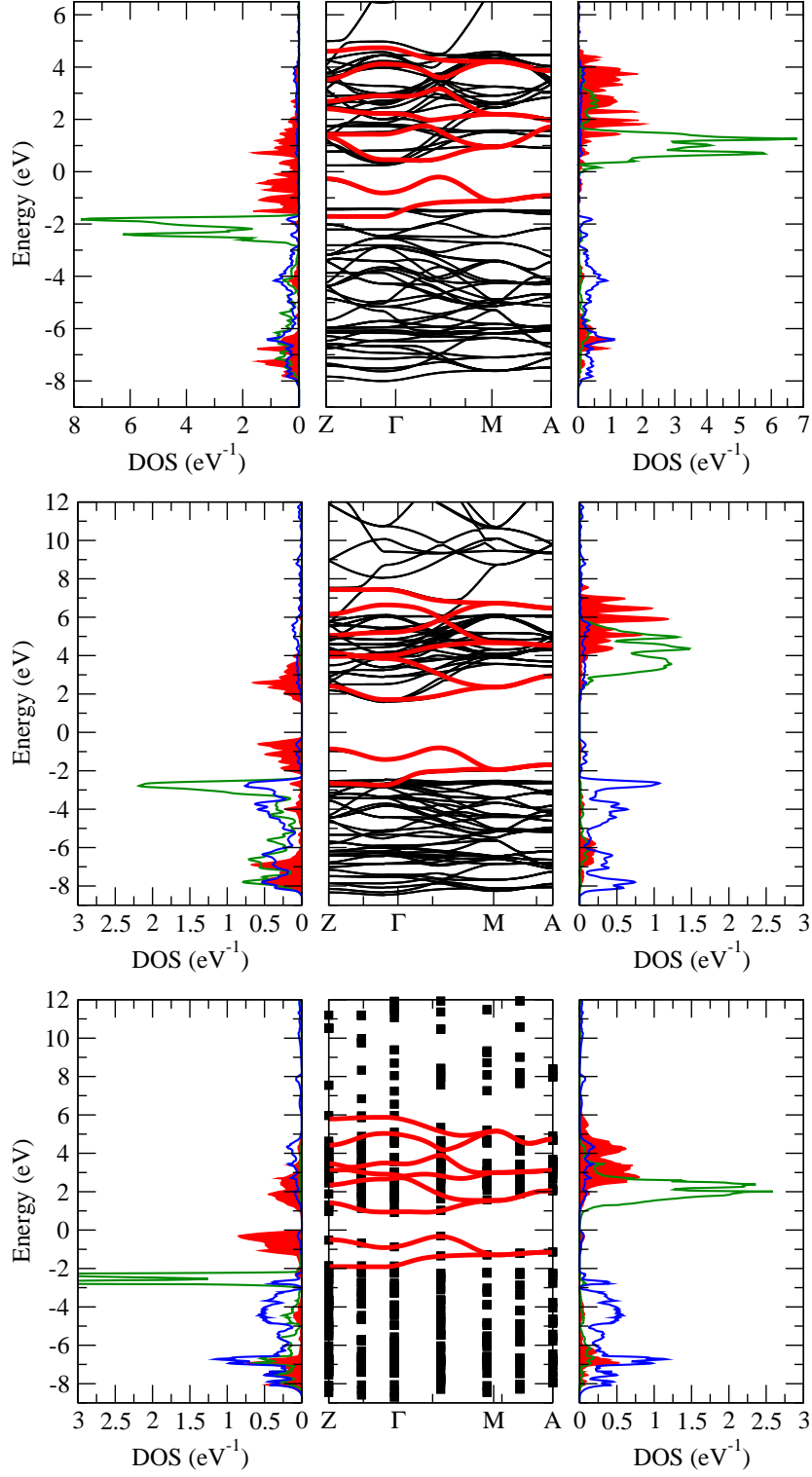
**Figure B.6:** VASP bandstructure (black) and MLWFs (red) of SmMnO$_3$-JT-distorted structure (A-AFM)

**Figure B.7:** VASP bandstructure (black) and MLWFs (red) of SmMnO$_3$-Experimental *Pbnm* structure

147

## B.6 EuMnO$_3$

| h$^{\Delta \mathbf{R}}$ | PBE | HSE | GW0 |
|---|---|---|---|
| h$_{11}^x(\uparrow)$ | -0.14947 | -0.147963 | -0.35679 |
| h$_{22}^x(\uparrow)$ | -0.478246 | -0.536403 | -0.747159 |
| h$_{11}^x(\downarrow)$ | -0.120906 | -0.126515 | -0.136764 |
| h$_{22}^x(\downarrow)$ | -0.39401 | -0.417446 | -0.389562 |
| h$_{12}^x(\uparrow)$ | 0.173521 | 0.107897 | 0.379587 |
| h$_{21}^x(\uparrow)$ | 0.39684 | 0.651522 | 0.672778 |
| h$_{12}^x(\downarrow)$ | 0.148604 | 0.147303 | 0.159093 |
| h$_{21}^x(\downarrow)$ | 0.302891 | 0.328876 | 0.298035 |
| h$_{11}^{xy}(\uparrow)$ | -0.012411 | -0.009193 | -0.022919 |
| h$_{11}^{xy}(\downarrow)$ | -0.011013 | -0.013249 | -0.015136 |
| h$_{11}^{2z}(\uparrow)$ | -0.052251 | -0.05654 | -0.057498 |
| h$_{11}^{2z}(\downarrow)$ | -0.052431 | -0.056452 | -0.104267 |
| h$_{11}^0(\uparrow)$ | 7.118311 | 7.204796 | 8.047724 |
| h$_{22}^0(\uparrow)$ | 6.71806 | 5.198054 | 7.44001 |
| h$_{12}^0(\uparrow)$ | 0.535423 | 1.3658 | 1.097081 |
| h$_{11}^0(\downarrow)$ | 9.376238 | 10.895284 | 11.26275 |
| h$_{22}^0(\downarrow)$ | 9.30569 | 10.902206 | 11.420105 |
| h$_{12}^0(\downarrow)$ | 0.215127 | -0.069327 | 0.213976 |

**Table B.9:** Matrix elements obtained from PBE, HSE and GW0 corresponding to the JT-distorted (A-AFM) structure of EuMnO$_3$.

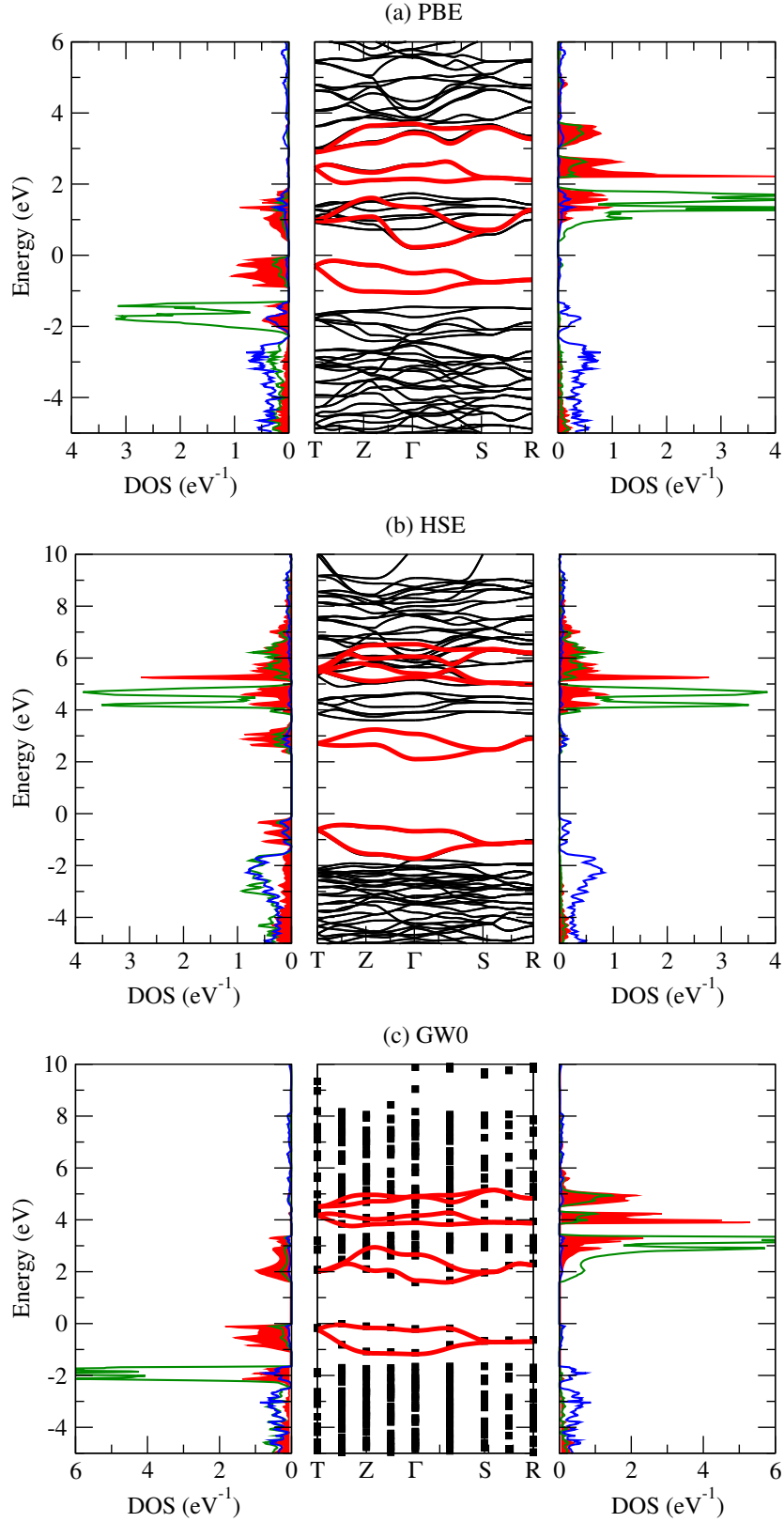| h$^{\Delta \mathbf{R}}$ | PBE | HSE | GW0 |
|---|---|---|---|
| h$_{11}^x(\uparrow)$ | -0.025256 | -0.046155 | -0.091573 |
| h$_{22}^x(\uparrow)$ | -0.227339 | -0.278408 | -0.323988 |
| h$_{11}^x(\downarrow)$ | -0.071666 | -0.101623 | -0.055141 |
| h$_{22}^x(\downarrow)$ | -0.175123 | -0.10882 | -0.138213 |
| h$_{11}^0(\uparrow)$ | 5.793459 | 5.849622 | 6.771829 |
| h$_{22}^0(\uparrow)$ | 4.928424 | 3.02166 | 5.093764 |
| h$_{12}^0(\uparrow)$ | 0.369338 | 0.842907 | 0.568721 |
| h$_{11}^0(\downarrow)$ | 8.256467 | 9.317415 | 9.747873 |
| h$_{22}^0(\downarrow)$ | 7.725225 | 9.259594 | 9.326106 |

**Table B.10:** Matrix elements obtained from PBE, HSE and GW0 corresponding to the experimental *Pbnm* structure of EuMnO$_3$.

(c)
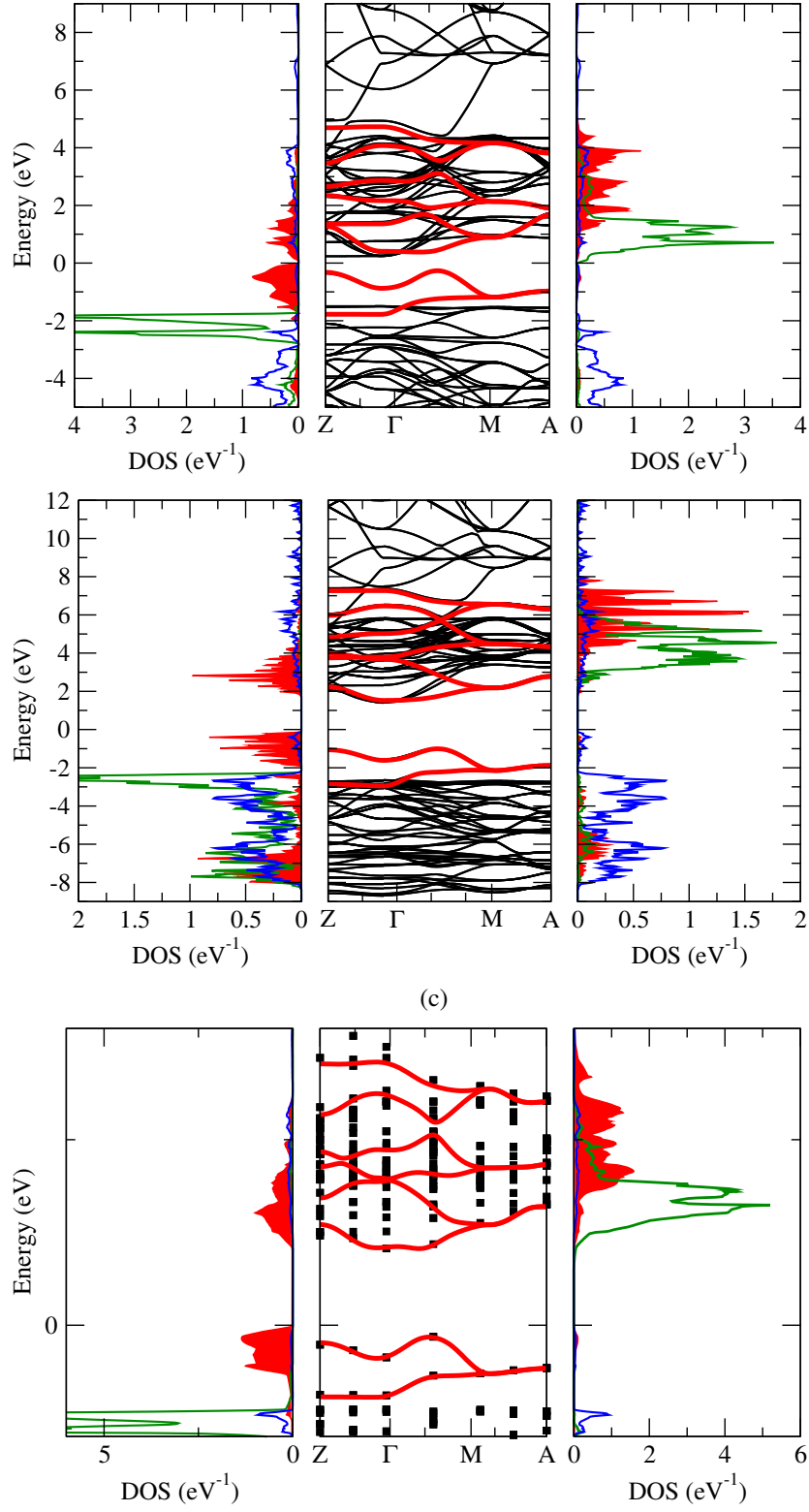
**Figure B.8:** VASP bandstructure (black) and MLWFs (red) of EuMnO$_3$-JT-distorted structure (A-AFM)

**Figure B.9:** VASP bandstructure (black) and MLWFs (red) of EuMnO$_3$-Experimental *Pbnm* structure
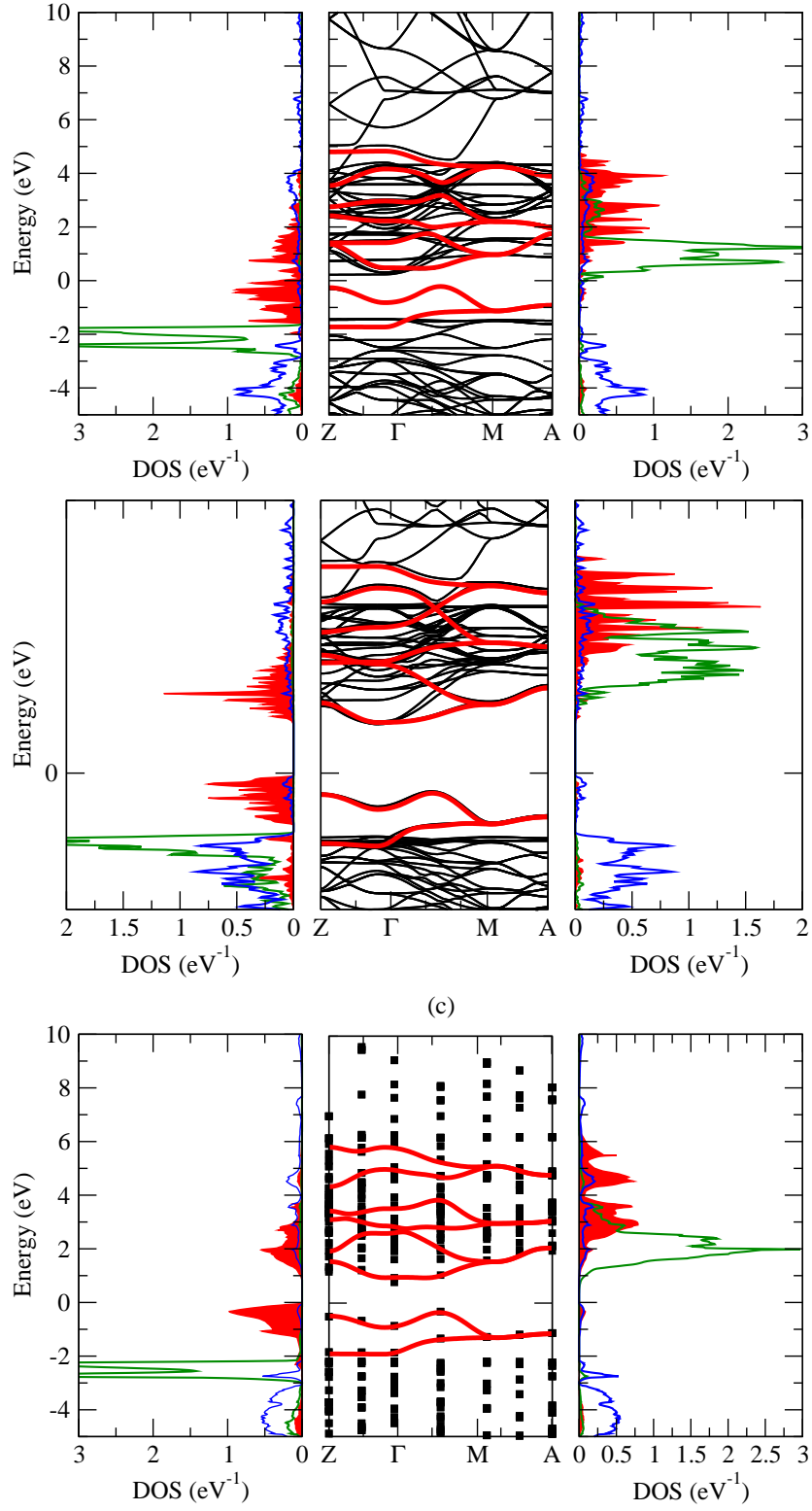
## B.7 GdMnO$_3$

| h$^{\Delta \mathbf{R}}$ | PBE | HSE | GW0 |
|---|---|---|---|
| h$_{11}^{x}(\uparrow)$ | -0.148679 | -0.147827 | -0.225868 |
| h$_{22}^{x}(\uparrow)$ | -0.479834 | -0.538303 | -0.581533 |
| h$_{11}^{x}(\downarrow)$ | -0.120739 | -0.126021 | -0.125482 |
| h$_{22}^{x}(\downarrow)$ | -0.397134 | -0.418775 | -0.385391 |
| h$_{12}^{x}(\uparrow)$ | 0.171505 | 0.107892 | 0.260729 |
| h$_{21}^{x}(\uparrow)$ | 0.401356 | 0.653903 | 0.497362 |
| h$_{12}^{x}(\downarrow)$ | 0.147766 | 0.145456 | 0.14227 |
| h$_{21}^{x}(\downarrow)$ | 0.307212 | 0.33373 | 0.313797 |
| h$_{11}^{xy}(\uparrow)$ | -0.012167 | -0.009125 | -0.020378 |
| h$_{11}^{xy}(\downarrow)$ | -0.010791 | -0.01291 | -0.012909 |
| h$_{11}^{2z}(\uparrow)$ | -0.052324 | -0.056513 | -0.030976 |
| h$_{11}^{2z}(\downarrow)$ | -0.052248 | -0.056706 | -0.070578 |
| h$_{11}^{0}(\uparrow)$ | 7.370674 | 7.478384 | 8.189757 |
| h$_{22}^{0}(\uparrow)$ | 6.947569 | 5.424153 | 7.695851 |
| h$_{12}^{0}(\uparrow)$ | 0.561695 | 1.401407 | 0.793921 |
| h$_{11}^{0}(\downarrow)$ | 9.624017 | 11.14847 | 10.913429 |
| h$_{22}^{0}(\downarrow)$ | 9.541347 | 11.137289 | 10.969709 |
| h$_{12}^{0}(\downarrow)$ | 0.233526 | -0.047579 | 0.25342 |

**Table B.11:** Matrix elements obtained from PBE, HSE and GW0 corresponding to the JT-distorted (A-AFM) structure of GdMnO$_3$.

| h$^{\Delta \mathbf{R}}$ | PBE | HSE | GW0 |
|---|---|---|---|
| h$_{11}^x(\uparrow)$ | -0.029476 | -0.062886 | -0.108061 |
| h$_{22}^x(\uparrow)$ | -0.216817 | -0.275215 | -0.310108 |
| h$_{11}^x(\downarrow)$ | -0.080031 | -0.105673 | -0.06752 |
| h$_{22}^x(\downarrow)$ | -0.172734 | -0.167832 | -0.140862 |
| h$_{11}^0(\uparrow)$ | 5.906388 | 6.131504 | 7.203631 |
| h$_{22}^0(\uparrow)$ | 4.946926 | 3.137636 | 5.275897 |
| h$_{12}^0(\uparrow)$ | 0.330352 | 0.817002 | 0.524399 |
| h$_{11}^0(\downarrow)$ | 8.350782 | 9.618906 | 10.15595 |
| h$_{22}^0(\downarrow)$ | 7.774725 | 9.335723 | 9.635297 |

**Table B.12:** Matrix elements obtained from PBE, HSE and GW0 corresponding to the experimental *Pbnm* structure of GdMnO$_3$.

**Figure B.10:** VASP bandstructure (black) and MLWFs (red) of GdMnO$_3$-JT distorted structure

(a) PBE

(b) HSE

(c) GW0
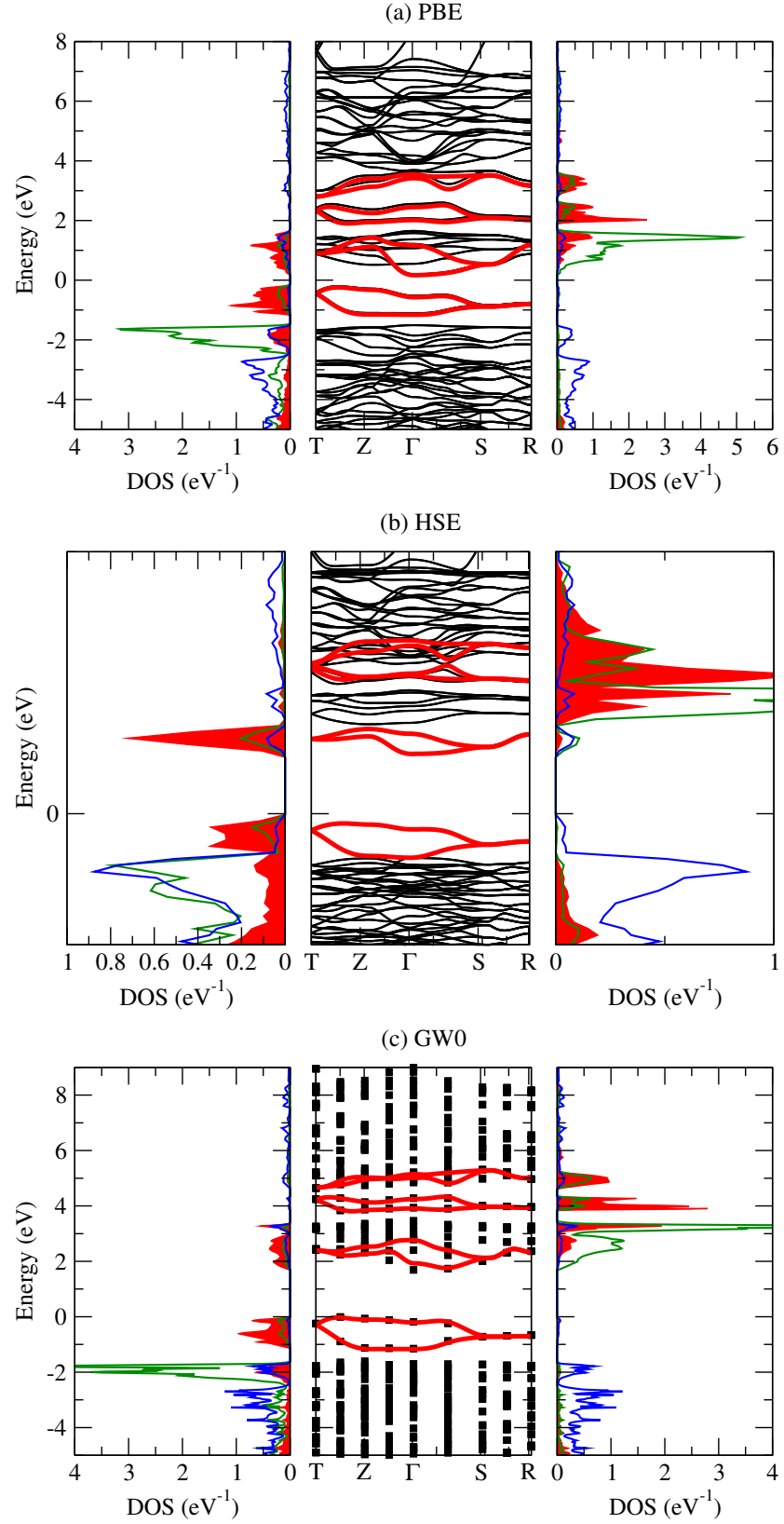
**Figure B.11:** VASP bandstructure (black) and MLWFs (red) of GdMnO$_3$-Experimental *Pbnm* structure 155

# References

[1] Fujimori A Imada M and Tokura Y. "Metal-insulator transitions". *Rev. Mod. Phys. 70 1039*, 1998. 1, 32

[2] Salamon M B and Jaime M. "The Physics of manganites:structure and transport". *Rev. Mod. Phys. 73 583*, 2001. 1

[3] Hotta T Dagotto E and Moreo A. "Colossal Magnetoresistant Materials: The Key Role of Phase separation". *Physics Reports 344 1*, 2001. 1

[4] Coey J.M.D. and Viret M. "Mixed-Valence manganites". *Advances in Physics 48 167-293*, 1999. 1

[5] Jonker G.H. and Van Santen J.H. "Ferromagnetic compounds of manganites with perovskite structure". *Physica 16 337*, 1950. 2

[6] Lin C and Millis J. "Theoretical description of pseudocubic manganites". *Phys. Rev. B 78 174419*, 2008. 3, 44

[7] Lin C Ederer C. and Millis A. "Structural distortions and model Hamiltonian parameters: From LSDA to a tight-binding description of $LaMnO_3$". *Phys. Rev. B 76 155105*, 2007. 3, 52, 76, 79, 80

[8] R.Kovačik and C. Ederer. "Calculation of model Hamiltonian parameters for $LaMnO_3$ using MLWFs". *Phys. Rev. B 81, 245108 (2010)*, 2010. 3, 44, 49, 50, 67, 73, 74, 79, 80, 82, 83, 89, 121

[9] T.Kimura *et al.* "Distorted perovskite with $e_g^1$ configuration as a frustrated spin system". *PRB 68, 060403 (R) (2003)*, 2003. 3, 42, 43, 95, 96, 122

[10] J. Kanamori. "Electron Correlation and Ferromagnetism of Transition Metals". *Prog. Theor. Phys. 30, 275*, 1963. 5

## REFERENCES

[11] J.Hubbard. "Electron Correlations in Narrow Energy Bands". *Proc. R. Soc. London, Ser. A 276, 238*, 1963. 5

[12] Anderson P.W. "New Approach to the Theory of Superexchange Interactions". *Phys. Rev. 115, 2*, 1959. 5

[13] Born M. and Oppenheimer J.R. "Zur Quantentheorie der Molekeln". *Ann. Physik 84:457*, 1954. 6

[14] V.Fock. "Näherungsmethode zur Losung des quanten-mechanischen Mehrkörperprobleme". *Z. Phys. 61:126*, 1930. 7

[15] Hohenberg P. and Kohn W. "Inhomogenous electron gas". *Phys. Rev. 136 (1964) B864*, 1964. 9

[16] Wilk L. Vosko S. H. and Nusair M. "Accurate spin-dependent electron liquid correlation energies for local spin density calculations: a critical analysis". *Can. J. Phys. 58 (8): 1200*, 1980. 13, 15

[17] Perdew J.P. and Alex Zunger. "Self-interaction correction to density-functional approximations for many-electron systems". *Phys. Rev. B 23, 5048*, 1981. 13

[18] Lee A. Cole and Perdew J.P. "Calculated electron affinities of the elements". *Phys. Rev. A 25, 1265*, 1982. 13

[19] John P. Perdew and Yue Wang. "Accurate and simple analytic representation of the electron-gas correlation energy". *Phys. Rev. B 45, 13244*, 1992. 13

[20] Axel D. Becke. "A new mixing of Hartree-Fock and local density-functional theories". *J. Chem. Phys. 98 1372*, 1993. 13

[21] Kim M.W. *et al.* "Effect of Orbital Rotation and Mixing on the Optical Properties of Orthorhombic RMnO$_3$ (R=La, Pr, Nd, Gd, and Tb)". *PRL 96, 247205*, 2006. 15, 104, 108

[22] C. F. Chabalowski P.J. Stephens, F. J. Devlin and M. J. Frisch. "Ab Initio Calculation of Vibrational Absorption and Circular Dichroism Spectra Using Density Functional Force Fields". *J. Phys. Chem. 98 (45): 11623*, 1994. 15

[23] Axel D. Becke. "Density-functional exchange-energy approximation with correct asymptotic behavior". *Phys. Rev. A 38 (6) 3098*, 1988. 15

[24] Weitao Yang Chengteh Lee and Robert G. Parr. "Development of the Colle-Salvetti correlation-energy formula into a functional of the electron density". *Phys. Rev. B 37 (2) 785*, 1988. 15

[25] Axel D. Becke. "Density-functional thermochemistry. III. The role of exact exchange". *J. Chem. Phys. 98 (7): 56485652*, 1993. 15

[26] Matthias Ernzerhof and Gustavo E. Scuseria. "Assessment of the Perdew-BurkeErnzerhof exchange-correlation functional". *J. Chem. Phys. 110, 5029*, 1999. 15

[27] Matthias Ernzerhof John P. Perdew and Kieron Burke. "Rationale for mixing exact exchange with density functional approximations". *J. Chem. Phys. 105, 9982*, 1996. 15, 32

[28] Scuseria G E Heyd J and Ernzerhof M. "Hybrid functionals based on a screened Coulomb potential". *J. Chem. Phys. 124 219906*, 2006. 15

[29] Marsman M *et al.* "Hybrid functionals applied to extended systems". *J. Phys.: Condens. Matter 20 064201*, 2008. 15

[30] Zaanen J. Anisimov V.I. and Anderson O.K. "Band theory and Mott insulators: Hubbard U instead of Stoner I". *PRB 44, 943*, 1991. 17

[31] Anisimov V.I. *et al.* "Density-functional theory and NiO photoemission spectra". *PRB 48, 16929*, 1993. 17

[32] Dederichs P.H. Solovyev I.V. and Anisimov V.I. "Corrected atomic limit in the local-density approximation and the electronic structure of d impurities in Rb". *PRB 50, 16861*, 1994. 17, 44

[33] Anisimov V.I. Liechtenstein A.I. and Zaanen J. "Density-functional theory and strong interactions: Orbital ordering in Mott-Hubbard insulators". *PRB 52, R5467*, 1995. 17

[34] Dudarev S.L. *et al.* "Electron-energy-loss spectra and the structural stability of nickel oxide:An LSDA+U study". *PRB 57, 1505*, 1998. 18, 49, 126

# REFERENCES

[35] Hedin L. "New Method for Calculating the One-Particle Green's Function with Application to the Electron-Gas Problem". *Phys. Rev. 139 A796*, 1965. 19

[36] Marsman M Franchini C, Sanna A and Kresse G. "Structural, vibrational, and quasiparticle properties of the Peierls semiconductor BaBiO$_3$: A hybrid functional and self-consistent GW+vertex-corrections study". *Phys. Rev. B 81 085213*, 2010. 19

[37] Aryasetiawan F. and Gunnarsson O. "The GW method". *Rep. Prog. Phys. 61 237*, 1998. 19

[38] Jonsson L. Aulbur W.G. and Wilkins J.W. "Quasiparticle Calculations in Solids". *Solid State Phys. 54 1*, 1999. 19

[39] Lundquist B.I. "Single-particle spectrum of the degenerate electron gas - I. The structure of the spectral weight function". *Phys. Kondens. Mater. 6 193*, 1967. 19

[40] Hybertson M.S. and Louie S.G. "First-Principles Theory of Quasiparticles: Calculation of Band Gaps in Semiconductors and Insulators". *Phys. Rev. Lett. 55 1418*, 1985. 19

[41] Aryasetiawan F. "Self-energy of ferromagnetic nickel in the GW approximation". *Phys. Rev. B 46 13051*, 1992. 19

[42] Aryasetiawan F. and Gunnarson O. "Electronic Structure of NiO in the GW Approximation". *Phys. Rev. Lett. 74 3221*, 1995. 19

[43] Bloch F. "über die quantenmechanik der elektronen in kristallgittern". *Z. Physik 52, 555*, 1928. 21, 26

[44] Slater J.C. and Koster G.F. "Simplified LCAO Method for the periodic potential problem". *Phys. Rev. 94,6*, 1954. 21, 24, 25

[45] Marzari N and Vanderbilt D. "Maximally localized generalized Wannier functions for composite energy bands". *Phys. Rev. B 56 12847*, 1997. 27, 31, 33

[46] J. des Cloizeaux. "Orthogonal Orbitals and Generalized Wannier Functions". *Phys. Rev. 129, 554*, 1963. 27

[47] J. des Cloizeaux. "Energy Bands and Projection Operators in a Crystal: Analytic and Asymptotic Properties". *Phys. Rev. 135, A685*, 1964. 27

[48] J. des Cloizeaux. "Analytical Properties of n-Dimensional Energy Bands and Wannier Functions". *Phys. Rev. 135, A698*, 1964. 27

[49] Blount E.I. "Formalisms of Band theory". *Solid State Phys. 13, 305*, 1962. 28

[50] Marzari N Souza I and Vanderbilt D. "Maximally localized Wannier functions for entangled energy bands". *Phys. Rev. B 65 035109*, 2001. 30, 31

[51] Kohn W and Sham L J. "Self-Consistent Equations Including Exchange and Correlation Effects". *Phys. Rev. 140 A1133*, 1965. 32, 44

[52] Krauth W Rozenberg M J Georges A, Kotliar G. "Dynamical Mean Field theory of strongly correlated fermion systems and the limit of infinite dimensions". *Rev. Mod. Phys. 68 13*, 1996. 32

[53] Karolak M *et al.* "Double counting in LDA + DMFTThe example of NiO ". *J. Electron Spectrosc. Relat. Phenom 181 11*, 2010. 32

[54] Volja D Yin W-G and Ku W. "Orbital Ordering in LaMnO$_3$: Electron-Electron versus Electron-Lattice Interactions". *Phys. Rev. Lett. 96 116405*, 2006. 33, 42, 44, 93, 96

[55] Kresse G and Joubert D. "From ultrasoft pseudopotentials to the projector augmented wave method". *Phys. Rev. B 59 1758*, 1999. 34

[56] Kresse G and Furthmüller J. "Efficient iterative schemes for ab initio total-energy calculations using a plane-wave basis set". *Phys. Rev. B 54 11169*, 1996. 34

[57] Kresse G and Furthmüller J. "Efficiency of ab-initio total energy calculations for metals and semiconductors using a plane-wave basis set". *Comput. Mat. Sci. 6 15*, 1996. 34

[58] Blöchl P E. Projector augmented-wave method. *Phys. Rev. B 50 17953*, 1994. 34

## REFERENCES

[59] Chadi D.J and Cohen M.L. "Special Points in the Brillouin Zone". *Phys. Rev. B 8, 5747*, 1973. 35

[60] Monkhorst H.J. and Pack J.D. "Special points for Brillouin-zone integrations". *Phys. Rev. B 13, 5188*, 1976. 35

[61] Rodrìguez-Carvajal J. et. al. "Neutron Diffraction Study of the Jahn-Teller Transition in Stoichiometric LaMnO₃". *Phys. Rev. B 57 3189(R)*, 1998. 42, 96

[62] Chatterji T *et al.* "Volume collapse in LaMnO₃ caused by an orbital order-disorder transition". *Phys. Rev. B 68 052406*, 2003. 42, 96

[63] Sànchez M C *et al.* "Cooperative Jahn-Teller Phase Transition in LaMnO₃ Studied by X-Ray Absorption Spectroscopy". *Phys. Rev. Lett. 90 045503*, 2003. 42, 96

[64] Qiu X *et al.* "Orbital Correlations in the Pseudocubic O and Rhombohedral R Phases of LaMnO₃". *Phys. Rev. Lett. 94 177203*, 2005. 42, 96

[65] Elemans Jacqueline B A A et. al. "The crystallographic and magnetic structures of $La_{1-x}Ba_xMn_{1-x}Me_xO_3$ (Me = Mn or Ti)". *J Solid State Chem. 3 238*, 1971. 42, 60, 66, 82, 96, 104

[66] Krogh Anderson I G Norby P and Krogh Anderson E. "The crystal structure of lanthanum manganate(iii), LaMnO₃, at room temperature and at 1273 K under N₂". *J. Sol. State Chem. 119, 191*, 1995. 42, 82, 99, 101

[67] Woodward P M. "Octahedral Tilting in Perovskites. I. Geometrical Considerations". *Acta Cryst B53 32*, 1997. 42

[68] Murakami Y et. al. "Resonant X-Ray Scattering from Orbital Ordering in LaMnO₃". *Phys. Rev. Lett. 81 582*, 1998. 42, 96

[69] Kanamori J. "Crystal Distortion in Magnetic Compounds". *J. Appl. Phys. 31 S14*, 1960. 42, 44

[70] Pavarini E. and Koch E. "Origin of Jahn-Teller Distortion and Orbital Order in LaMnO₃". *Phys. Rev. Lett. 104 086402*, 2010. 42, 44, 96

[71] Sikora O. and Olès A M. "Origin of the Orbital Ordering in LaMnO₃". *Acta Phys. Pol. B 34 861*, 2002. 42, 96

[72] E. O. Wollan and W. C. Koehler. "Neutron Diffraction Study of the Magnetic Properties of the Series of Perovskite-Type Compounds [(1-x)La, xCa]MnO₃". *Phys. Rev 100 545*, 1955. 42

[73] Momma K and Izumi F. "VESTA: a three-dimensional visualization system for electronic and structural analysis". *J. Appl. Crystallogr. 41 653*, 2008. 43

[74] Feiner L F and Olès A M. "Electronic origin of magnetic and orbital ordering in insulating LaMnO₃". *Phys. Rev. B 59 3295*, 1999. 44, 96

[75] Malvezzi A L Hotta T and Dagotto E. "Charge-Orbital Stripe Structure in La$_{1-x}$Ca$_x$MnO$_3$ ( x = 1/2,2/3)". *Phys. Rev. B 62 9432*, 2000. 44, 96

[76] Bala J and Olès A. "Jahn-Teller effect on orbital ordering and dynamics in ferromagnetic LaMnO₃". *Phys. Rev. B 62 6085(R)*, 2000. 44, 96

[77] Ahn K H and Millis A J. "Effects of magnetic ordering on the anisotropy and temperature dependence of the optical conductivity in LaMnO₃: A tight-binding approach". *Phys. Rev. B 61 13545*, 2000. 44, 96, 108

[78] Ishihara S Okamoto S and Maekawa S. "Orbital ordering in LaMnO₃: Electron-electron and electron-lattice interactions". *Phys. Rev. B 65 144403*, 2002. 44, 96

[79] Tyer R *et al.* "Ab initio charge, spin and orbital energy scales in LaMnO₃". *Europhys. Lett. 65 519*, 2004. 44, 96

[80] Gehring G A Zenia H and Temmerman W M. "Orbital ordering in cubic LaMnO₃ from first principles calculations". *New J. Phys. 7 257*, 2005. 44, 96

[81] R.Kovačik and C. Ederer. "Effect of Hubbard U on the construction of low-energy Hamiltonians for LaMnO₃ via MLWFs". *Phys. Rev. B 84, 075118 (2011)*, 2011. 44, 82, 85, 86, 110, 121, 126, 127, 128

[82] C.Franchini *et al.* "MLWFs in LaMnO₃ within PBE+U, hybrid functionals and partially self-consistent GW: an efficient route to construct ab-initio tight-binding parameters for e$_g$ perovskites". *J.Phys. Condensed Matter 24 235602 (2012)*, 2012. 59, 97, 121

# REFERENCES

[83] Pickett W E and Singh D J. "Electronic structure and half-metallic transport in the $La_{1-x}Ca_xMnO_3$ system". *Phys. Rev. B 53 1146*, 1996. 61

[84] Terakura K Sawada H, Morikawa Y and Hamada N. "Jahn-Teller distortion and magnetic structures in $LaMnO_3$". *Phys. Rev. B 56 12154*, 1997. 61

[85] Fjellvag Delin A Ravindran P, Kjekshus A and Erikson O. "Ground-state and excited-state properties of $LaMnO_3$ from full-potential calculations". *Phys. Rev. B 65 064445*, 2002. 61

[86] Ishibashi S Hashimoto T and Terakura K. "Jahn-Teller distortion and magnetic structure in $LaMnO_3$: A first-principles theoretical study with full structure optimizations". *Phys. Rev. B 82 045124*, 2010. 61, 65, 66, 93

[87] Harrison N M Muñoz D and Illas F. "Electronic and magnetic structure of $LaMnO_3$ from hybrid periodic density-functional theory". *Phys. Rev. B 69 085115*, 2004. 61, 62, 64, 65, 66, 106

[88] Kobayashi S Nohara Y, Yamasaki A and Fujiwara T. "Electronic structure of antiferromagnetic $LaMnO_3$ and the effects of charge polarization". *Phys. Rev. B 74 064417*, 2006. 61, 62

[89] Tokura Y Arima T and Torrance J B. "Variation of optical gaps in perovskite-type 3d transition-metal oxides". *Phys. Rev. B 48 17006*, 1993. 61, 104

[90] Jung J H *et al.* "Determination of electronic band structures of $CaMnO_3$ and $LaMnO_3$ using optical-conductivity analyses". *Phys. Rev. B 55 15489*, 1997. 61, 62, 104

[91] Jung J H *et al.* "Midgap states of $La_{1-x}Ca_xMnO_3$:Doping-dependent optical-conductivity studies". *Phys. Rev. B 57 R11043*, 1998. 61, 62, 104

[92] Krüger R *et al.* "Orbital ordering in $LaMnO_3$ investigated by Resonance Raman Spectroscopy". *Phys. Rev. Lett. 92 097203*, 2004. 61, 62, 104

[93] Saitoh *et al.* "Electronic structure of $La_{1-x}Sr_xMnO_3$ studied by photoemission and x-ray-absorption spectroscopy". *Phys. Rev. B 51 13942*, 1995. 61, 62, 104

[94] Franchini C *et al.* "Exceptionally strong magnetism in the 4d perovskites $RTcO_3$ (R=Ca, Sr, Ba)". *Phys. Rev. B **83**, 220402(R)*, 2011. 62

[95] Park J H *et al.* "Electronic Aspects of the Ferromagnetic Transition in Manganese Perovskites". *Phys. Rev. Lett. 76 4215*, 1996. 62, 63

[96] Hamada N Solovyev I and Terakura K. "Crucial Role of the Lattice Distortion in the Magnetism of LaMnO$_3$". *Phys. Rev. Lett. 76 4825*, 1996. 64, 106

[97] Evarestov R A *et al.* "Comparative density-functional LCAO and plane-wave calculations of LaMnO$_3$ surfaces". *Phys. Rev. B 72 214411*, 2005. 64, 65, 106

[98] Moussa F *et al.* "Spin waves in the antiferromagnet perovskite LaMnO$_3$: A neutron-scattering study". *Phys. Rev. B 54 15149*, 1996. 66, 67, 104

[99] Fjellvag H Hauback B C and Sakai N. "Effect of Nonstoichiometry on Properties of La$_{1t}$MnO$_{3+}$: III. Magnetic Order Studied by Powder Neutron Diffraction". *J. Solid State Chem. 124 43*, 1996. 66, 104

[100] Nishizawa A Hirota K, Kaneko N and Endoh Y. "Two-Dimensional Planar Ferromagnetic Coupling in LaMnO$_3$". *J. Phys. Soc. Jpn. 65 3736*, 1996. 66, 67

[101] Archer T. *et al.* "Exchange interactions and magnetic phases of transition metal oxides: Benchmarking advanced ab initio methods". *Phys. Rev. B 84 115114*, 2011. 67

[102] Khomskii D.I. and Sawatzky G.A. "Interplay between spin, charge and orbital degrees of freedom in magnetic oxides". *Solid State Commun. 102 87*, 1997. 95

[103] Kusters R.M.*et al.* "Magnetoresistance measurements on the magnetic semiconductor Nd$_{0.5}$Pb$_{0.5}$MnO$_3$". *Physica B 155, 362*, 1989. 95

[104] von Helmolt *et al.* "Giant negative magnetoresistance in perovskitelike La$_{2/3}$Ba$_{1/3}$MnO$_x$ ferromagnetic films". *Phys. Rev. Lett. 71, 2331*, 1993. 95

[105] Jin S. *et al.* "Thousandfold change in resistivity in magnetoresistive la-ca-mn-o films". *Science 64, 413*, 1994. 95

[106] Tokura Y *et al.* "Giant magnetotransport phenomena in filling-controlled Kondo lattice system: La$_{1-x}$Sr$_x$MnO$_3$". *Science 63, 3931*, 1994. 95

# REFERENCES

[107] Zener C. "Interaction between the d-Shells in the Transition Metals. II. Ferromagnetic Compounds of Manganese with Perovskite Structure". *Physical Review 82, 403*, 1951. 95

[108] Goto T. et al. "Ferroelectricity and Giant Magnetocapacitance in Perovskite Rare-Earth Manganites". *Phys. Rev. Lett. 92, 257201*, 2004. 95, 96

[109] Kimura T. *et al.* "Magnetoelectric phase diagrams of orthorhombic $RMnO_3$ (R = Gd, Tb and Dy) ". *PRB 71, 224425*, 2005. 96

[110] Ferreira W.S. *et al.* "spin-phonon coupling and magnetoelectric properties:$EuMnO_3$ vs. $GdMnO_3$. *PRB 79, 054303*. 96

[111] Tapan Chatterji *et al.* "Direct evidence for the Nd magnetic ordering in $NdMnO_3$ from the hyperfine field splitting of Nd nuclear levels". *J. Phys.: Condens. Matter 21 126003*, 2009. 96

[112] Munõz *et al.* "Magnetic structure evolution of $NdMnO_3$ derived from neutron diffraction data". *J. Phys. Condens. Matter 12, 1361*, 2000. 96, 104

[113] Kamegashira and Miyazaki. "Jahn-Teller transitions in $NdMnO_3$". *Phys. Stat. Sol. (a) 76, K39*, 1983. 96

[114] Dabrowski B. *et al.* "Structural, transport, and magnetic properties of RMnO3 perovskites (R=La, Pr, Nd, Sm, Eu, Dy)". *J. Solid State Chem. 178, 629*, 2005. 96

[115] Laverdière J. *et al.* "Spin-phonon coupling in orthorhombic $RMnO_3$ (R=Pr,Nd,Sm,Eu,Gd,Tb,Dy,Ho,Y): A Raman study". *PRB 73, 214301*, 2006. 96, 104

[116] Iliev M.N. *et al.* "Distortion-dependent Raman spectra and mode mixing in $RMnO_3$ perovskites (R = La, Pr, Nd, Sm, Eu, Gd, Tb, Dy, Ho, Y)". *PRB 73, 064302*, 2006. 96

[117] Lee J.S. *et al.* "Systematics of electromagnons in the spiral spin-ordered states of $RMnO_3$". *PRB 79, 180403(R)*, 2009. 96

[118] Ayato Iyama *et al.* "High magnetic field effect on interplay between Sm 4f and Mn 3d moments in $SmMnO_3$". *J. Phys. Soc. Japan 81, 013703*, 2012. 96

[119] Kunihiko Yamakuchi *et al.* "Magnetically induced ferroelectricity in orthorhombic manganites: Microscopic origin and chemical trends". *PRB 78, 014403 (2008)*, 2008. 96, 97, 106

[120] Kim *et al.* "Nearest and next-nearest superexchange interactions in orthorhombic perovskite manganites RMnO₃ (R = rare-earth)". *PRB 80, 064416*, 2009. 96

[121] Moskvin A.S. *et al.* "Interplay of p-d and d-d charge transfer transitions in rare-earth perovskite manganites". *PRB 82, 035106*, 2010. 96, 107, 108, 109

[122] Dong S. *et al.* "Double-exchange model study of multiferroic RMnO₃ perovskites". *Eur. Phys. J. B 71, 339-344*, 2009. 96

[123] Renu Choitrani *et al.* "Lattice Dynamics of manganites RMnO₃ (R = Sm, Eu, Gd) instabilities and coexistence of orthorhombic and hexagonal phases". *New J. Phys. 11, 073041*, 2009. 96

[124] Jiangang He *et al.* "Structural transitions and transport-half-metallic ferromagnetism in LaMnO₃ at elevated pressure". *PRB 85, 195135*, 2012. 97

[125] J.A.Alonso *et al.* "Evolution of the Jahn-Teller distortion of MnO₆ octahedra in RMnO₃ perovskites (R = Pr, Nd, Dy, Tb, Ho, Er, Y): a neutron diffraction study". *Inorg. Chem. 2000, 39, 917-923*, 2000. 99, 100, 101

[126] Takanori Mori *et al.* "Crystal growth and crystal structures of the LnMnO₃ peroskites:Ln=Nd, Sm, Eu and Gd". *Materials Letters 54 (2002) 238-243*, 2002. 99, 100, 101

[127] Zhou J.S. and J.B.Goodenough. "Orbital order-disorder transition in single-valent manganites". *Phys. Rev. B 68 144*, 2003. 100

[128] Huang Q. *et al.* "Structure and magnetic order in undoped lanthanum manganite". *PRB 55, 14987*, 1997. 104

[129] D.O'Flynn *et al.* "Multiferroic properties and magnetic structure of $Sm_{1-x}Y_xMnO_3$". *PRB 83, 174426*, 2011. 104

[130] Ivanov V.Yu. *et al.* "Phase transitions in $Sm_{1-x}Sr_xMnO_3$ single crystals ($0 \leq x \leq 0.8$)". *Phys. Status Solidi B 236, 445*, 2003. 104

[131] Kovaleva N N *et al.* "Spin-Controlled Mott-Hubbard Bands in LaMnO₃ Probed by Optical Ellipsometry". *PRL 93, 147204*, 2004. 108

[132] Harrison W.A. *Electronic Structure and the Properties of Solids.* Dover Publications, NewYork, 1989. 117

# Conferences and Publications

1. C Franchini, R Kováčik, M Marsman, S Sathyanarayana Murthy, J He, C Ederer and G Kresse, *"Maximally localized Wannier functions in LaMnO$_3$ within PBE + U, hybrid functionals and partially self-consistent GW: an efficient route to construct* ab-initio *tight-binding parameters for e$_g$ perovskites"*, J. Phys.: Condens. Matter **24** 235602 (2012).

2. A talk at internal project meeting titled "Calculation and comparison of model Hamiltonian parameters for LaMnO$_3$ using Maximally Localized Wannier Functions within PBE, HSE and GW", Trinity College, Dublin, Ireland.

3. Sowmya S.Murthy, Roman Kováčik, Martijn Marsman, Claude Ederer, Georg Kresse and Cesare Franchini, *"DFT and beyond-DFT derived tight-binding parameters for RMnO$_3$ (R = La, Pr, Nd, Sm, Eu) using VASP2WANNIER90"*, Deutsche Physikalische Gesellschaft (DPG) conference, Berlin, March 2012.

4. Sowmya S.Murthy, Roman Kováčik, Martijn Marsman, Claude Ederer, Georg Kresse and Cesare Franchini,Poster presentation titled *"DFT and beyond-DFT derived tight-binding parameters for RMnO$_3$ (R = La, Pr, Nd, Sm, Eu) using VASP2WANNIER90"*, ATHENA 2012, Kolkata, India, April 2012.

5. Sowmya S.Murthy, Roman Kováčik, Claude Ederer and Cesare Franchini, *"Combined First-principles and Model Hamiltonian study of RMnO$_3$ (R = La, Pr, Nd, Sm, Eu, Gd)"* (Ready for submission).

6. Seminar talk at the department group meeting (April 16, 2013).

# SOWMYA SATHYANARAYANA MURTHY

University of Vienna, Computational Materials Physics,
Sensengasse 8/12, 1090 Vienna
(43) 4277-73314, s.murthy@univie.ac.at

**EDUCATION**

**2007-2009 M.Sc. in Applied Physics**
National Institute of Technology,
Tiruchirapalli,
Tamilnadu,
India.

**2004-2007 B.Sc. (Hons.) in Physics**
Sri Sathya Sai University,
Anantapur Campus for Women,
Anantapur,
Andhra Pradesh,
India.

**May -July 2008** Summer Research student at Tata Institute of Fundamental Research (TIFR), Colaba, Mumbai.

**CONFERENCES AND TALKS**

- Talk at the internal project meeting (ATHENA) (Advanced theories for functional metal oxides (Dublin, June 2011).

- Attended the Psi-k/CECAM/CCP9 Biennial Graduate School in Electronic-Structure Methods (July 10, 2011 to July 15, 2011, Oxford, UK).

- A talk titled "DFT and beyond-DFT derived tight-binding parameters for $R$MnO$_3$ ($R$=La, Pr, Nd, Sm, Eu) using VASP2WANNIER90" at *Deutsche Physikalische Gesellschaft* (Berlin, March 2012).

- Poster titled "DFT and beyond-DFT derived tight-binding parameters for $R$MnO$_3$ ($R$=La, Pr, Nd, Sm, Eu) using VASP2WANNIER90" at ATHENA-An Advanced School on Modelling complex oxides (April 9-12, 2012).

**AWARDS AND HONOURS**

- Graduate student selected under EU-FP7 funded project- ATHENA (Advanced Theory for functional metal oxides (Feb. 2010-May 2012).

- Co-secretary of SPIE (Society for optics and Photonics), National Institute of Technology, Tiruchirapalli, Tamilnadu, India (2008-2009).

- Visiting summer research fellowship (May-July, 2008)
  Tata Institute of Fundamental Research, Colaba, Mumbai, India.

- Cultural secretary at the Sri Sathya Sai University (2007).

**COMPUTATIONAL SKILLS**

- Linux operating system (Ubuntu, OpenSuse)

- Basics of Web-designing (PHP, MySQL, HTML, Javascript)

- Basic shell-scripting.

- Computational science visualization tools like VESTA, Xcrysden

- FORTRAN 77/90, "Mathematica"(Basic), C, Latex, Python and perl scripting (basics), WWW.

**LANGUAGES**

- English, Basic German (A2 level), Tamil, Telugu.

**PUBLICATIONS**

- MLWFs in LaMnO$_3$ within PBE+U, hybrid functionals and partially self-consistent GW: an efficient route to construct ab-initio tight-binding parameters for e$_g$ perovskites, J.Phys. Condensed Matter 24 235602 (2012).